

**School of Molecular and Life Sciences**

**Reactivity of Natural Organic Matter in Advanced Oxidation  
Processes and Implications for Catalytic Ceramic Membrane  
Application**

**Suona Zhang**

**This thesis is presented for the Degree of  
Doctor of Philosophy  
of  
Curtin University**

**December 2019**

## **Declaration**

To the best of my knowledge and belief, this thesis contains no material previously published by any other person except where due acknowledgment has been made.

This thesis contains no material which has been accepted for the award of any other degree or diploma in any university.

Signature: Suona zhang

Date: 04/12/2019

# Acknowledgments

First and foremost, I would like to express my heartfelt gratitude to my supervisor, Professor Jean-Philippe Croué. I would not have experienced such a wonderful PhD journey if it were not for his exceptional scientific ideas, insightful guidance, constant supports, and cheerful encouragement. I have always felt lucky to work with him. His devotion to research, enthusiasm for adventures, and passion for life will have a life-time influence on me. I wish to extend my appreciation to Dr. Leonardo Gutierrez for all his professional instructions and invaluable help, and Dr. Franca Jones for her support during my PhD study. I also want to acknowledge Dr. Zhineng Hao and Professor Jingfu Liu at the Research Centre for Eco-Environmental Sciences, Chinese Academy of Sciences, for providing a platform to complete part of my research work and the assistance in data analysis.

Taking this opportunity, I acknowledge my colleagues and staff at the Curtin Water Quality Research Group and the Department of Chemistry for their companionship and help during my PhD track, in no particular order: Maolida Nihemaiti, Xizhi Niu, Wei Hu, Zuotong How, Rhys Carter, Valentin Rougé, Ionut Caraene, Luis Restrepo Vieira, Farid Sepanta, Amin Delfi, Manaswini Natarajan, Deborah Liew, Sebastian Allard, Yolanta Gruchlik, Ina Christiana, Cynthia Joll, Mark Hackett, Damien Arrigan, Peter Chapman, Ching Goh, Grant Cope, Marcus Tey, and Robert Herman.

I wish to thank the following organizations: China Scholarship Council (CSC) and Curtin University for providing the CSC-Curtin Joint Scholarship and Research Centre for Eco-Environmental Sciences, and the Chinese Academy of Sciences for the instrumental support.

Cordial gratitude from the deepest part of my heart goes to my family. I am enormously grateful to my parents for their pure love and unconditional support. I wouldn't have taken the step to postgraduate study without the influence of my elder brother. He has always set the best example for me since childhood. It is genuinely appreciable for me to have an amazing sister-in-law and lovely niece becoming my family. The four-year long-distance relation couldn't have survived without the love, patience, and support of my husband. I couldn't have imagined a life without him, who cherishes and cares about me more than himself.

# Abstract

The reaction of natural organic matter (NOM) with  $\cdot\text{OH}$  has been long-studied while less information is available regarding the reactivity of NOM with  $\text{SO}_4^{\cdot-}$ . Briefly, the more selective reactivity between  $\text{SO}_4^{\cdot-}$  and electron-rich NOM moieties as compared to  $\cdot\text{OH}$  has been widely acknowledged. However, the  $\text{SO}_4^{\cdot-}$ -induced reaction rate with NOM reactive moieties and their transformation products remain mostly unknown. Also, NOM has exhibited higher scavenging capacity to  $\cdot\text{OH}$  than  $\text{SO}_4^{\cdot-}$  due to the nonselective nature of the former during radical attack. The scavenging capacity is directly related to the reactivity of NOM, i.e., reaction rate of NOM with radicals. Considering the highly heterogeneous nature of NOM, a difference in reactive sites would be highly expected for the two radicals, leading to different reaction pathways as well as reaction rates. Therefore, a better understanding of the nature of reactive sites and reaction pathways would ultimately assist in elucidating the difference in reactivity and the selection of  $\cdot\text{OH}$ - or  $\text{SO}_4^{\cdot-}$ -based oxidation processes in water treatment (e.g., catalytic membrane process). Primarily due to the generation of reactive species (e.g.  $\cdot\text{OH}$ ), catalytic membrane has received increasing interests with its enhanced performance in organic contaminants degradation, NOM fouling mitigation and membrane cleaning.

To contribute to the above knowledge gaps, the doctoral thesis systematically investigated the reactivity of NOM in advanced oxidation processes; based on these findings, the performance of a novel  $\text{SO}_4^{\cdot-}$ -based catalytic ceramic membrane was also studied. Following a brief summary of the thesis content in Chapter 1, Chapter 2 studied the reactivity of DOM with  $\text{SO}_4^{\cdot-}$  with a specific focus on the reaction kinetics and the transformation of DOM. Four well-characterized hydrophobic DOM fractions

extracted from different surface water sources were selected as model CDOM.  $\text{SO}_4^{\bullet-}$  was produced through the activation of peroxymonosulfate (PMS) by Co(II) ions at pH 8 in borate buffer. As  $\text{SO}_4^{\bullet-}$  would selectively react with electron-rich moieties in DOM, i.e., known as chromophoric DOM (CDOM) due to its light-absorbing properties, the reactivity of NOM was studied based on the decrease in its ultraviolet absorbance at 254 nm ( $\text{UVA}_{254}$ ) as a function of time. The reactivity of CDOM changed with time where fast and slow reacting CDOMs (i.e.,  $\text{CDOM}_{\text{fast}}$  and  $\text{CDOM}_{\text{slow}}$ ) were clearly distinguished. A second-order rate constant of  $\text{CDOM}_{\text{fast}}$  with  $\text{SO}_4^{\bullet-}$  was calculated by plotting  $\text{UVA}_{254}$  decrease versus PMS exposure; where a  $R_{\text{ct}}$  value (i.e., ratio of sulfate radical to PMS exposure) was calculated using par-chlorobenzoic acid (*p*CBA) as a probe compound. The transformation of CDOM was studied through the analysis of the changes in  $\text{UVA}_{254}$ , electron-donating capacity, fluorescence intensity, and total organic carbon. A transformation pathway leading to a significant carbon removal was proposed. Although  $\text{SO}_4^{\bullet-}$  is considered a promising alternative in advanced oxidation processes (AOPs) for water treatment, little is known about its reactivity to the ubiquitous DOM in water bodies. Thus, the current study would ultimately assist in the development of  $\text{SO}_4^{\bullet-}$ -based catalytic membrane process.

Chapter 3 investigated the difference in reactivity between NOM and  $\cdot\text{OH}$  or  $\text{SO}_4^{\bullet-}$  using a state-of-the-art analytical technique, Fourier Transformation Ion Cyclotron Resonance Mass Spectrometry (FT-ICR MS). Specifically, the reactivities of three aquatic NOM isolates of different characteristics with  $\cdot\text{OH}$  and  $\text{SO}_4^{\bullet-}$  were explored through the calculation of the second-order rate constant of  $\text{UV}_{254}$  decay. NOM exhibited higher reactivity to  $\cdot\text{OH}$  than  $\text{SO}_4^{\bullet-}$ , although both were measured in the order of  $\sim 10^8 \text{ M}^{-1}\text{s}^{-1}$ . The reactive molecules detected with FT-ICR MS were identified to exert a difference. Although molecules with higher electron density and lower

degree of oxidation and saturation (i.e., with larger double bond equivalent (DBE), lower O/C and H/C) were observed as reactive to both radicals, exclusively reactive molecules accounting for 10–20% of the total radical species were also identified. Specifically, the exclusively  $\text{SO}_4^{\bullet-}$ -reactive molecules were considerably more enriched in electrons (i.e., higher DBE), larger in size (i.e. higher  $m/z$  or carbon number), and higher oxygen content (i.e., higher O/C with  $-\text{COOH}$  as a contributor); while  $\bullet\text{OH}$  could also exclusively attack more aliphatic structures (i.e., higher H/C and lower DBE) besides electron-rich centers. The different rates of reactions associated with these identified reactive sites supported the observed higher reactivity of NOM to  $\bullet\text{OH}$  than  $\text{SO}_4^{\bullet-}$ . The findings of this chapter would provide a detailed molecular-level understanding of the distinct reactivity of NOM between these two radical species and will assist in the selection of oxidants to be applied with catalytic membranes.

NOM-membrane interactions have a pivotal role in membrane fouling by governing the initial phase (i.e., conditioning film formation) as well as the availability of reactive sites. Therefore, detailed knowledge of the interactions between NOM and catalysts is critical, and will strongly assist in the selection of catalytic materials for improved catalytic performance. In Chapter 4, the interfacial interactions between DOM and  $\text{MnO}_2$  as a potential metal oxide for catalytic membrane applications were studied. The influence of DOM properties on its interfacial interactions with  $\text{MnO}_2$  (i.e., as a promising alternative material for catalytic membrane preparation) was studied by Time-Resolved Dynamic Light Scattering (TR-DLS) and Atomic Force Microscopy (AFM) under varied solution conditions. Four DOM fractions of different characteristics (e.g., SUVA, hydrophobic character, structural properties) were selected. Bare- $\text{MnO}_2$  nanoparticles readily aggregated in  $\text{NaCl}$  and  $\text{CaCl}_2$  solutions.

Classic DLVO Theory successfully described critical coagulation concentrations (CCC) and aggregation behaviors. In NaCl solution, DOM adsorbed on MnO<sub>2</sub> surface and provided electrostatic and steric stabilization. The two DOM fractions of higher hydrophobic (HPO) character were more efficient in decreasing the aggregation rates. Enhanced MnO<sub>2</sub> aggregation was observed at high Ca<sup>2+</sup> concentrations due to efficient charge screening and cation bridging between carboxyl groups in DOM structures. The addition of oxidant (H<sub>2</sub>O<sub>2</sub>) induced a high aggregation of bare-MnO<sub>2</sub> nanoparticles, possibly due to the release of Mn<sup>2+</sup> (i.e., complexation mechanisms) and generation of reactive species (e.g., O<sub>2</sub><sup>•-</sup>, HO<sub>2</sub><sup>-</sup>, H<sup>•</sup>). As opposed to their hydrophilic (HPI) counterparts, HPO isolates adsorbed on MnO<sub>2</sub> significantly decreased the catalytic oxidation processes between H<sub>2</sub>O<sub>2</sub> and MnO<sub>2</sub>, suggesting a more efficient and stronger DOM coating. Interfacial forces measured by AFM showed weaker interactions between HPI isolates and MnO<sub>2</sub>, indicating unfavorable polar interactions. Conversely, the high adhesion forces between MnO<sub>2</sub> and HPO isolate would be a direct indicator of the strength of the bond. As membrane fouling is originally driven by NOM-membrane interfacial interaction, this chapter contributes to drawing attention to the interfacial interactions between NOM and catalysts as an equally important criterion for catalyst selection besides its catalytic properties.

Based on the findings in previous chapters, MnO<sub>2</sub>-Co<sub>3</sub>O<sub>4</sub> was selected for the application of catalytic membranes due to its high efficiency in catalytically decomposing PMS into SO<sub>4</sub><sup>•-</sup>. The performance of the SO<sub>4</sub><sup>•-</sup>-based catalytic membrane was comprehensively explored in terms of the removal of organic contaminants, transformation of NOM, mitigation of fouling, and efficiency of self-cleaning. The catalytic membrane was prepared through the filtration of MnO<sub>2</sub>-Co<sub>3</sub>O<sub>4</sub> nanoparticle solution followed by sintering and sonication. Characterization results of the catalytic

membrane demonstrated the successful deposition of nanoparticles onto the membrane surface. In addition, the influence of  $0.06 \text{ mg/cm}^2$  coating on membrane permeability was negligible. The production of  $\text{SO}_4^{\bullet-}$  as the predominant radical species was confirmed using *p*CBA and nitrobenzene (NB) as probe compounds. Due to the reaction with  $\text{SO}_4^{\bullet-}$ , a higher NOM removal rate was observed with coated membrane as compared to the pristine membrane. Interestingly, fouling mitigation in terms of flux increase was not significant (i.e., 8% increase in normalized flux) in the PMS/coated membrane system, probably due to the formation of small molecules, and thus, leading to more fouling. Moreover, the PMS cleaning efficiency with the coated membrane was not only considerably higher than the pristine membrane, it was also stable within three cycles of membrane filtration. Due to the metal (especially Co) leaching issue, alternative efficient and environmentally-friendly catalysts would be highly required for the application of the catalytic membrane.

Chapters 6 presented the general conclusions, and future perspectives according to the major findings obtained throughout this PhD project.

# Table of Contents

Acknowledgments.....	I
Abstract .....	III
Table of Contents .....	VIII
List of Figures .....	XIII
List of Tables .....	XXVI
List of Equations .....	XXIX
List of Publications and Presentations Arising from this Thesis .....	XXXI
Chapter 1. Thesis Overview .....	1
Chapter 2. Reactivity of chromophoric dissolved organic matter (CDOM) to sulfate radicals: Reaction kinetics and structural transformation .....	5
2.1 Introduction .....	6
2.2 Materials and method .....	8
2.2.1 Chemical reagents and DOM fractions .....	8
2.2.2 Experimental setup and procedures .....	9
2.2.3 Analytical methods .....	10
2.3 Results and Discussion .....	12
2.3.1 Biphasic decrease of CDOM in Co(II)/PMS system .....	12

2.3.2	Evaluation of sulfate radical production .....	14
2.3.3	Reactivity of CDOM <sub>fast</sub> to SO <sub>4</sub> <sup>•-</sup> and its application.....	19
2.3.4	Sulfate radical-induced CDOM transformation .....	22
2.4	Summary.....	27
Chapter 3. Molecular Insights into the Reactivity of Aquatic Natural Organic Matter towards <sup>•</sup> OH and SO <sub>4</sub> <sup>•-</sup> Using FT-ICR MS .....		30
3.1	Introduction .....	31
3.2	Materials and Methods .....	33
3.2.1	Chemicals and NOM samples.....	33
3.2.2	UV-AOPs experimental procedure. ....	33
3.2.3	FT-ICR MS analysis. ....	35
3.2.4	Complementary analysis. ....	35
3.3	Results and discussion .....	36
3.3.1	Reactivity of NOM isolates with radicals. ....	36
3.3.2	Identification of reactive molecules. ....	38
3.3.3	Exclusively reactive molecules. ....	41
3.3.4	Reaction pathways of major reactive molecules.....	45
3.4	Summary.....	47

Chapter 4. Organic Matter interfacial interactions with MnO <sub>2</sub> and its influence on catalytic oxidation processes.....	49
4.1 Introduction .....	50
4.2 Materials and methods.....	52
4.2.1 Solution preparation and reagents .....	52
4.2.2 Preparation of MnO <sub>2</sub> nanoparticles.....	53
4.2.3 Origin and characteristics of the DOM isolates .....	53
4.2.4 Measurement of zeta potential, hydrodynamic diameter, and aggregation kinetics of MnO <sub>2</sub> nanoparticles in DOM-containing electrolyte solutions .....	54
4.2.5 Force measurements and data analysis .....	55
4.3 Results and discussion .....	56
4.3.1 Characteristics of MnO <sub>2</sub> particles .....	56
4.3.2 Aggregation kinetics of MnO <sub>2</sub> nanoparticles.....	57
4.3.3 Interfacial interactions between MnO <sub>2</sub> and DOMs.....	65
4.4 Summary.....	69
Chapter 5. SO <sub>4</sub> <sup>2-</sup> -based catalytic ceramic UF membrane for organics removal and flux restoration .....	71
5.1 Introduction .....	72

5.2	Experimental Section.....	75
5.2.1	Chemicals and materials .....	75
5.2.2	Preparation and characterization of MnO <sub>2</sub> -Co <sub>3</sub> O <sub>4</sub> coated ceramic membrane.....	76
5.2.3	Experimental procedures.....	77
5.2.4	Analytical methods .....	79
5.3	Results and Discussion .....	80
5.3.1	Characterization of MnO <sub>2</sub> -Co <sub>3</sub> O <sub>4</sub> nanoparticles and catalytic membrane.....	80
5.3.2	Catalytic performance of the coated membrane.....	83
5.3.3	Fouling behavior of catalytic membrane.....	85
5.3.4	Cleaning efficiency of catalytic membranes .....	92
5.3.5	Metal leaching.....	95
5.4	Summary.....	96
	Chapter 6. Conclusions and Future Perspectives .....	97
	Appendix 1 Supporting Information-Chapter 2 .....	100
	Appendix 2 Supporting Information-Chapter 3 .....	111
	Appendix 3 Supporting Information-Chapter 4 .....	127

Appendix 4 Supporting Information-Chapter 5 .....	136
Appendix 5 Permission from the Publisher .....	149
Appendix 6 Attribution Statements.....	150
List of References .....	154

# List of Figures

## Chapter 2–5

- Figure 2-1. UVA<sub>254</sub> decrease of different DOM fractions in Co(II)/PMS system as a function of time. Conditions: [PMS]<sub>0</sub> = 1.0 mM; Co(II) = 1.0 μM; DOM = 3.90 ± 0.11 mgC/L; pH = 8.00 ± 0.05 (10 mM borate buffer); T = 20°C ..... 13
- Figure 2-2. Correlation between pCBA decay and PMS exposure in Co(II)/PMS system with different DOM fractions. Conditions: [PMS]<sub>0</sub> = 1.00 mM; Co(II) = 1.00 μM; [pCBA]<sub>0</sub> = 1.00 μM; DOM = 3.90 ± 0.11 mgC/L; pH = 8.00 ± 0.05 (10 mM borate buffer); T = 20°C..... 18
- Figure 2-3. Correlation between CDOM<sub>fast</sub> decrease and PMS exposure in Co(II)/PMS system. Conditions: [PMS]<sub>0</sub> = 1.00 mM; Co(II) = 1.00 μM; [pCBA]<sub>0</sub> = 1.00 μM; DOM = 3.90 ± 0.11 mgC/L; pH = 8.00 ± 0.05(10 mM borate buffer); T = 20°C..... 19
- Figure 2-4. Correlation between normalized UVA<sub>254</sub> and EDC decrease of different DOM fractions in Co(II)/PMS reaction system. Conditions: PMS exposure = 0.00–8.04 M·s; Co(II) = 1.00 μM; DOM = 3.90 ± 0.11 mgC/L; pH = 8.00 ± 0.05 (10 mM borate buffer); T = 20°C. Areas a<sub>0</sub>, a<sub>1</sub>, and b illustrated the results obtained with a PMS exposure lower than 0.01, lower than 0.1, and larger than 0.1 M·s, respectively. R<sub>E</sub> and R<sub>U</sub> represented the normalized removal efficiency in EDC and UVA<sub>254</sub> ..... 22

Figure 2-5. TOC removal as a function of UVA<sub>254</sub> decrease. Conditions: PMS exposure = 0.00–8.04 M·s; Co(II) = 1.00 μM; DOM = 3.90 ± 0.11 mgC/L; pH = 8.00 ± 0.05 (10 mM borate buffer); T = 20°C. Red dashed line was drawn to differentiate the correlation between CDOM<sub>fast</sub> and CDOM<sub>slow</sub> with TOC removal..... 24

Figure 2-6. Normalized emission spectra by its respective maximum fluorescence intensity of (a) S-HPOA, (b) B-HPOA, (d) R-HPO, and (d) C-HPO at an excitation wavelength of 230nm. The legend in each figure represented various PMS exposures ..... 26

Figure 2-7. Proposed pathway of sulfate radical-induced DOM transformation 27

Figure 3-1. (a) UV<sub>254</sub> decrease of S-HPOA with time, and (b) second-order rate constants ( $k_{sec}$ ) of three NOM isolates with  $\cdot\text{OH}$  or  $\text{SO}_4^{\cdot-}$ . Conditions: Incident UV intensity = 0.9 mW·cm<sup>-2</sup>, [TOC]<sub>0</sub> = 3.89 ± 0.18 mgC·L<sup>-1</sup>, [H<sub>2</sub>O<sub>2</sub>]<sub>0</sub> or [PDS]<sub>0</sub> = 1.0 mM, at unadjusted pH ([pH]<sub>0</sub>=4.65 ± 0.09) and room temperature (20°C). ..... 36

Figure 3-2. (a, c) van Krevelen diagrams and (b, d) molecular compositions of S-HPOA after  $\cdot\text{OH}$  or  $\text{SO}_4^{\cdot-}$  treatment. The olive points/bars represent the radical-reactive moieties (formulas that disappeared after reaction), and wine points/bars reflect the radical-resistant structures (formulas remaining unchanged after reaction). ..... 38

Figure 3-3. van Krevelen diagram of molecules exclusively reactive to  $\cdot\text{OH}$  or  $\text{SO}_4^{\cdot-}$  within (a) S-HPOA, (b) R-HPO, and (c) C-HPO. Red points denote

<p>molecules exclusively reactive to <math>\cdot\text{OH}</math>; while olive points denote molecules exclusively reactive to <math>\text{SO}_4^{\cdot-}</math>.....</p>	42
<p>Figure 3-4. KMD (COO) of molecules exclusively reactive with <math>\cdot\text{OH}</math> or <math>\text{SO}_4^{\cdot-}</math> as a function of oxygen number in the NOM isolate of S-HPOA. The selected molecular formulas were presented as an illustration.....</p>	44
<p>Figure 3-5. DBE of molecules exclusively reactive to (a) <math>\cdot\text{OH}</math> or (b) or <math>\text{SO}_4^{\cdot-}</math> as a function of number of carbon atoms based on O/C in S-HPOA. The dashed line indicates the comparison at a DBE value of 15.66 (<math>\text{DBE}_{\text{wa}}</math> of the molecules exclusively reactive to <math>\text{SO}_4^{\cdot-}</math>) .....</p>	45
<p>Figure 3-6. Relationship between normalized <math>\text{UVA}_{254}</math> and EDC decrease of different NOM isolates in (a) <math>\cdot\text{OH}</math> and or (b) <math>\text{SO}_4^{\cdot-}</math> reaction processes. Conditions: Incident UV intensity = <math>0.9 \text{ mW}\cdot\text{cm}^{-2}</math>, <math>[\text{TOC}]_0 = 3.89 \pm 0.18 \text{ mgC}\cdot\text{L}^{-1}</math>, and <math>[\text{H}_2\text{O}_2]_0</math> or <math>[\text{PDS}]_0 = 0.00\text{--}0.10 \text{ mM}</math>, at unadjusted pH (<math>4.65 \pm 0.09</math>) and room temperature (<math>20^\circ\text{C}</math>). .....</p>	47
<p>Figure 4-1 Zeta potential of <math>\text{MnO}_2</math> of as a function of: a) solution pH 2-10, and b) ionic strength (<math>\text{Na}^+</math> and <math>\text{Ca}^{2+}</math>) ranging from 1-100 mM and at unadjusted pH. ....</p>	56
<p>Figure 4-2. Aggregation rate constants <math>\kappa_{11}</math> of <math>\text{MnO}_2</math> nanoparticles in <math>\text{Na}^+</math> or <math>\text{Ca}^{2+}</math> solutions at unadjusted pH (<math>5.8 \pm 0.3</math>).....</p>	57
<p>Figure 4-3. Aggregation rate constants <math>\kappa_{11}</math> of <math>\text{MnO}_2</math> in the presence of 10 mg C/L DOM in a) <math>\text{Na}^+</math> or b) <math>\text{Ca}^{2+}</math> solutions and at unadjusted pH.....</p>	60

Figure 4-4. Aggregation kinetic profiles of bared MnO<sub>2</sub> particles in 30mM NaCl solution. 1 mM H<sub>2</sub>O<sub>2</sub> were added after 1h of MnO<sub>2</sub> aggregation. .... 63

Figure 4-5. Aggregation profiles of MnO<sub>2</sub> particles in 10 mg C/L DOM-containing NaCl solutions, at unadjusted pH. 1mM H<sub>2</sub>O<sub>2</sub> was added after 1h of MnO<sub>2</sub> /DOM aggregation. .... 64

Figure 4-7. Representative approaching curve profiles between CRW-OC-HPO or JWW-HPO-coated silica colloidal probe and MnO<sub>2</sub> surface at 10 mM Na<sup>+</sup> and at unadjusted pH. .... 66

Figure 4-8. Maximum adhesion forces between MnO<sub>2</sub> and a) JWW-HPO, and b) CRW-OC-HPO in NaCl or CaCl<sub>2</sub> solution at different ionic strengths and unadjusted pH. .... 68

Figure 5-1. (a) Normalized flux decline, and (b) TOC retention rate for coated membranes with different MnO<sub>2</sub>-Co<sub>3</sub>O<sub>4</sub> loadings (0.0–4.0 mg). Fouling experiments were conducted with NOM-containing feed water (~5mgC/L NOM mixture with ~10% colloids and ~90% HPO fractions) at unadjusted pH of 6.3 ± 0.2 and operating pressure of 1bar. .... 82

Figure 5-2. (a) pCBA and (b) NB removal during filtration with pristine and coated membranes with or without PMS addition. Conditions: [pCBA]<sub>0</sub> = 2 μM, [NB]<sub>0</sub> = 2 μM, [PMS]<sub>0</sub> = 1 mM, TMP = 1.0 bar, temperature = 20 ± 1°C, pH = 5.20 ± 0.20 without PMS addition and 3.40 ± 0.10 with PMS addition without pH adjustment, pH was adjusted to 7.40 ± 0.20 with 0.01M NaOH for both sole and catalytic filtration process. .... 84

Figure 5-3. (a) Fouling profile and (b) TOC retention rate for both pristine and coated membranes caused by different NOM solutions: 4.28 mgC/L HPO-Blavet (pH 5.87), 2.78 mgC/L Colloids-Brittany (pH 6.74), and 2.76 mgC/L Colloids-Mery (pH 6.45) at a transmembrane pressure of 1 bar..... 85

Figure 5-4. (a) UV<sub>254</sub> and (b) TOC removal rate with pristine and coated membranes. NOM solution-B: 0.56 mgC/L Colloids-Brittany + 4.45 mgC/L HPO-SRNOM, and NOM solution-M: 0.55mgC/L Colloids-Mery + 4.45 mgC/L HPO-SRNOM. Experimental conditions: Operational pressure =1.0 bar, temperature 20±1°C, pH ~ 6 without PMS addition and 3.40±0.10 with 1 mM PMS addition..... 86

Figure 5-5. Normalized water flux of the pristine and coated membrane with or without PMS addition in (a) NOM solution-B and (b) NOM solution-M. NOM solution-B: 0.56 mgC/L Colloids-Brittany + 4.45 mgC/L HPO-SRNOM, NOM solution-M: 0.55 mgC/L Colloids-Mery + 4.45 mgC/ L HPO-SRNOM. Experimental conditions: Operational pressure =1.0 bar, temperature 20 ± 1 °C, pH ~ 6 without PMS addition, and 3.40 ± 0.10 with 1 mM PMS addition..... 89

Figure 5-6. Change in normalized water flux during fouling test and PMS cleaning for (a) NOM solution-B and (b) solution-M fouled membrane. Conditions: Fouling tests were conducted with 100 mL of feed water containing 0.56mgC/L Colloids-Brittany + 4.45 mgC/L HPO-SRNOM for (a) and 0.55mgC/L Colloids-Mery + 4.45 mgC/ L HPO-SRNOM for (b). Cleaning was performed with 100 mL of 10 mM PMS solution at pH 3.20 ± 0.10..... 92

Figure 5-7. Flux recovery rate with (a) multiple cleaning methods and (b) fouling profiles during filtration cycles with PMS cleaning applied between each fouling cycle for both pristine and coated membranes. Feedwater for fouling tests was prepared with a mixture of 0.55 mgC/L Colloids-Mery and 4.45 mgC/L HPO-SRNOM (pH 6.28). The black dash lines in Figure 5-7a indicate the range of the values in normalized water flux before cleaning.

..... 95

#### Appendix 1-4

Figure A1-1. Calibration curve for PMS determination ( $\text{PMS } (\mu\text{M}) = 99.92 A_{734} - 29.052, R^2=0.9998$ ) ..... 103

Figure A1-2.  $\text{UVA}_{254}$  decrease of different DOM fractions in the solely presence of PMS as a function of time. Conditions:  $[\text{PMS}]_0 = 1.0 \text{ mM}$ ;  $\text{DOM} = 3.90 \pm 0.11 \text{ mgC/L}$ ;  $\text{pH} = 8.00 \pm 0.05$  (borate buffer);  $T = 20^\circ\text{C}$ . ..... 104

Figure A1-3. Correlation between the reaction rate constant of  $\text{CDOM}_{\text{slow}}$  and SUVA for each DOM fraction. Conditions:  $[\text{PMS}]_0 = 1.0 \text{ mM}$ ;  $\text{Co(II)} = 1.0 \mu\text{M}$ ;  $\text{DOM} = 3.90 \pm 0.11 \text{ mgC/L}$ ;  $\text{pH} = 8.00 \pm 0.05$  (10 mM borate buffer);  $T = 20^\circ\text{C}$ . ..... 104

Figure A1-4. Removal of pCBA in the presence and absence of scavengers in PMS/Co(II) system. Conditions:  $[\text{PMS}]_0 = 1.0 \text{ mM}$ ;  $\text{Co(II)} = 1.0 \mu\text{M}$ ;  $[\text{pCBA}]_0 = 10 \mu\text{M}$ ;  $\text{pH} = 8.00 \pm 0.05$  (borate buffer) ;  $T = 20^\circ\text{C}$ . ..... 105

Figure A1-5. PMS decomposition in Co(II)/PMS system with or without DOM isolates. Conditions:  $[\text{PMS}]_0 = 1.00 \text{ mM}$ ;  $\text{Co(II)} = 1.00 \mu\text{M}$ ;  $\text{DOM} = 3.90 \pm 0.11 \text{ mgC/L}$ ;  $\text{pH} = 8.00 \pm 0.05$  (10 mM borate buffer);  $T = 20^\circ\text{C}$ . ..... 105

Figure A1-6. (a) PMS decomposition and (b) pCBA decrease in Co(II)/PMS system containing different DOM isolates. Conditions:  $[PMS]_0 = 1.00 \text{ mM}$ ;  $Co(II) = 1.00 \text{ }\mu\text{M}$ ;  $[pCBA]_0 = 1.0 \text{ }\mu\text{M}$ ;  $DOM = 3.90 \pm 0.11 \text{ mgC/L}$ ;  $pH = 8.00 \pm 0.05$  (10 mM borate buffer);  $T = 20^\circ\text{C}$ . ..... 106

Figure A1-7. Correlation between pCBA decay and PMS exposure ( $<0.1 \text{ M}\cdot\text{s}$ ) in Co(II)/PMS system containing different DOM fractions. Conditions:  $[PMS]_0 = 1.00 \text{ mM}$ ;  $Co(II) = 1.00 \text{ }\mu\text{M}$ ;  $[pCBA]_0 = 1.0 \text{ }\mu\text{M}$ ;  $DOM = 3.90 \pm 0.11 \text{ mgC/L}$ ;  $pH = 8.00 \pm 0.05$  (10 mM borate buffer);  $T = 20^\circ\text{C}$ .  $R_{ct0-0.01}$  and  $R_{ct0.01-0.1}$  represent the calculated Rct values at a PMS exposure of  $0-0.01\text{M}\cdot\text{s}$  and  $0.01-0.1\text{M}\cdot\text{s}$ , respectively. .... 106

Figure A1-8. EDC decrease of different DOM isolates in Co(II)/PMS system as a function of PMS exposures. Conditions: PMS exposure =  $0.00-8.04 \text{ M}\cdot\text{s}$ ;  $Co(II) = 1.0 \text{ }\mu\text{M}$ ;  $DOM = 3.90 \pm 0.11 \text{ mgC/L}$ ;  $pH = 8.00 \pm 0.05$ (borate buffer);  $T = 20^\circ\text{C}$ ..... 107

Figure A1-9.  $UVA_{254}$  decrease of different DOM samples in Co(II)/PMS system as a function of PMS exposures. Conditions: PMS exposure =  $0.00-8.04 \text{ M}\cdot\text{s}$ ;  $Co(II) = 1.0 \text{ }\mu\text{M}$ ;  $DOM = 3.90 \pm 0.11 \text{ mgC/L}$ ;  $pH = 8.00 \pm 0.05$ (borate buffer);  $T = 20^\circ\text{C}$ ..... 107

Figure A1-10. TOC removal of different DOM samples in Co(II)/PMS system as a function of PMS exposures. Conditions: PMS exposure =  $0.00-8.04 \text{ M}\cdot\text{s}$ ;  $Co(II) = 1.0 \text{ }\mu\text{M}$ ;  $DOM = 3.90 \pm 0.11 \text{ mgC/L}$ ;  $pH = 8.00 \pm 0.05$ (borate buffer);  $T = 20^\circ\text{C}$ ..... 108

Figure A1-11. EEM spectra of (a) S-HPOA, (b) B-HPOA, (c) R-HPO, and (d) C-HPO. DOC = $3.90 \pm 0.11$ mgC/L; pH = $8.00 \pm 0.05$ (10 mM borate buffered); T = 20°C.....	108
Figure A1-12. Correlation of fluorescence between Peak I and Peak II during Co(II)/PMS oxidation process. ....	109
Figure A1-13. FI decrease of different DOM samples in Co(II)/PMS reaction system as a function of PMS exposures. Conditions: PMS exposure = 0.00–8.04 M·s; Co(II) = 1.0 $\mu$ M; DOM = $3.90 \pm 0.11$ mgC/L; pH = $8.00 \pm 0.05$ (borate buffer); T = 20°C. ....	109
Figure A1-14. Correlation between the relative residual UV <sub>254</sub> and FI of different DOM samples in Co(II)/PMS system. Conditions: PMS exposure = 0.00–8.04 M·s; Co(II) = 1.0 $\mu$ M; DOM = $3.90 \pm 0.11$ mgC/L; pH = $8.00 \pm 0.05$ (borate buffer); T = 20°C. ....	110
Figure A2-1. Schematic representative of the collimated beam device (front view). ....	122
Figure A2-2. van Krevelen diagrams of the formulas assigned from FTICR-MS peaks of three NOM isolates: (a) S-HPOA, (b) R-HPO, and (c) C-HPO. Relative abundance of molecules containing respective CHO (blue), CHON (green), CHOS (orange) and CHONS (pink) groups were reflected by the height of stacked columns. Bubble sizes reflect the relative intensities of respective mass peaks. ....	122
Figure A2-3. UV <sub>254</sub> decrease of R-HPO (Ribou reservoir hydrophobic fraction) and C-HPO (Colorado river hydrophobic fraction) with $\cdot$ OH or SO <sub>4</sub> <sup>-</sup>	

treatment. Conditions: Incident UV intensity =  $0.9 \text{ mW}\cdot\text{cm}^{-2}$ ,  $[\text{TOC}]_0 = 3.89 \pm 0.18 \text{ mgC}\cdot\text{L}^{-1}$ ,  $[\text{H}_2\text{O}_2]_0$  or  $[\text{PDS}]_0 = 1.00 \text{ mM}$ , at unadjusted pH ( $[\text{pH}]_0(\text{H}_2\text{O}_2) = 4.65 \pm 0.09$ ,  $[\text{pH}]_0(\text{PDS}) = 4.66 \pm 0.18$ ) and room temperature ( $20^\circ\text{C}$ )..... 123

Figure A2-4. TOC change of three NOM isolates with  $\cdot\text{OH}$  or  $\text{SO}_4^{\cdot-}$  treatment for 30 min. Conditions: Incident UV intensity =  $0.9 \text{ mW}\cdot\text{cm}^{-2}$ ,  $[\text{TOC}]_0 = 3.89 \pm 0.18 \text{ mgC}\cdot\text{L}^{-1}$ ,  $[\text{H}_2\text{O}_2]_0$  or  $[\text{PDS}]_0 = 1.00 \text{ mM}$ , at unadjusted pH ( $[\text{pH}]_0(\text{H}_2\text{O}_2) = 4.65 \pm 0.09$ ,  $[\text{pH}]_0(\text{PDS}) = 4.66 \pm 0.18$ ) and room temperature ( $20^\circ\text{C}$ ). .. 123

Figure A2-5. (a,c) van Krevelen diagrams and (b,d) molecular compositions of R-HPO after  $\cdot\text{OH}$  or  $\text{SO}_4^{\cdot-}$  treatment. Green points/bars represent formulas disappeared after reaction (reactive), and red points/bars reflect formulas remaining unchanged after reaction (resistant)..... 124

Figure A2-6. (a,c) van Krevelen diagrams and (b,d) molecular compositions of C-HPO after  $\cdot\text{OH}$  or  $\text{SO}_4^{\cdot-}$  treatment. Green points/bars represent formulas disappeared after reaction (reactive), and red points/bars reflect formulas remaining unchanged after reaction (resistant)..... 124

Figure A2-7. KMD (COO) of molecules exclusively reactive with  $\cdot\text{OH}$  or  $\text{SO}_4^{\cdot-}$  as a function of oxygen number in the NOM isolate of (a) R-HPO and (b) C-HPO..... 125

Figure A2-8. DBE of molecules exclusively reactive to (a)  $\cdot\text{OH}$  or (b)  $\text{SO}_4^{\cdot-}$  as a function of carbon number in the NOM isolate of R-HPO. The dash line was drawn at approximately a DBE value of 11.86 ( $\text{DBE}_{\text{wa}}$  of the molecules exclusively reactive to  $\text{SO}_4^{\cdot-}$ ). ..... 125

Figure A2-9. DBE of molecules exclusively reactive to (a)  $\cdot\text{OH}$  or (b)  $\text{SO}_4^{\cdot-}$  as a function of carbon number in the NOM isolate of C-HPO. The dash line was drawn at approximately a DBE value of 11.53 ( $\text{DBE}_{\text{wa}}$  of the molecules exclusively reactive to  $\text{SO}_4^{\cdot-}$ ). ..... 125

Figure A2-10. Normalized decrease of (a), (b), and (c)  $\text{UVA}_{254}$  and (d), (e), and (f) EDC of different NOM isolates after reaction with  $\cdot\text{OH}$  and  $\text{SO}_4^{\cdot-}$ . Conditions: Incident UV intensity =  $0.9 \text{ mW}\cdot\text{cm}^{-2}$ ,  $[\text{TOC}]_0 = 3.89 \pm 0.18 \text{ mgC}\cdot\text{L}^{-1}$ , and  $[\text{H}_2\text{O}_2]_0$  or  $[\text{PDS}]_0 = 0.00\text{--}0.10 \text{ mM}$ , at unadjusted pH ( $[\text{pH}]_0(\text{H}_2\text{O}_2) = 4.65\pm 0.09$ ,  $[\text{pH}]_0(\text{PDS}) = 4.66\pm 0.18$ ) and room temperature ( $20^\circ\text{C}$ )..... 126

Figure A3-1. (a) XRD and (b) UV-Vis spectra of  $\text{MnO}_2$  particles ..... 131

Figure A3-2. Aggregation kinetics of  $\text{MnO}_2$  particles under different  $\text{Na}^+$  or  $\text{Ca}^{2+}$  concentrations at unadjusted pH (5.8) and at  $25^\circ\text{C}$ ..... 132

Figure A3-3. DLVO interaction energy profiles between bare  $\text{MnO}_2$  particles as a function of separation distance under different solution condition at unadjusted pH (5.8) ..... 132

Figure A3-4. Aggregation kinetics of  $\text{MnO}_2$  particles in the presence of 10 mg C/L DOM and in 30 mM NaCl solution at unadjusted pH (5.8) and at  $25^\circ\text{C}$  ..... 133

Figure A3-5. Mass spectra (left) and van Krevelen Diagrams (right) for JWW-HPO, CRW-OC-HPO, and RRW-HPI. Colors reflect the molecular series, i.e., CHO: blue, CHOS: green, CHNO: orange, and CHNOS: red. Bubble

areas reflect the relative average intensities of the respective mass peaks .....	133
Figure A3-6. Aggregation kinetics of MnO <sub>2</sub> particles in the presence of 10 mg C/L DOM and in 33.3 mM CaCl <sub>2</sub> solution at unadjusted pH (5.8) and at 25°C .....	134
Figure A3-7. Probability density function describing the mean hydrodynamic diameter ( $\mu$ ) and variance ( $\sigma$ ) of MnO <sub>2</sub> nanoparticles in the (a) absence of DOM in solution and in (b) GRW-HPO-containing solutions, after contact with H <sub>2</sub> O <sub>2</sub> . .....	134
Figure A3-8. Change of Zeta Potential of MnO <sub>2</sub> particles in 30 mM NaCl solution at unadjusted pH, before and after 1 mM H <sub>2</sub> O <sub>2</sub> addition .....	135
Figure A4-1. FTIR spectra of Colloids-mery.....	141
Figure A4-2. Schematic representative of membrane filtration set-up.....	141
Figure A4-3. Zeta potential of MnO <sub>2</sub> -Co <sub>3</sub> O <sub>4</sub> particles as a function of solution pH. .....	142
Figure A4-4. Optical pictures (a), topography (3D-height sensor) images (b) and phase images (c) of original (left) and MnO <sub>2</sub> -Co <sub>3</sub> O <sub>4</sub> -coated membranes (right). Images were acquired by AFM scan (tapping mode) in air with a scan area of 3 $\mu\text{m} \times 3 \mu\text{m}$ .....	143
Figure A4-5. XPS spectra of Co2p and Mn2p for coated membrane without (a, b) and with sonication (c, d).....	144

Figure A4-6. Comparison of original and coated ceramic membrane (1mg MnO<sub>2</sub>-Co<sub>3</sub>O<sub>4</sub> nanoparticles) for pure water permeability (TMP: 1 bar, Temperature: 20 ± 1 °C)..... 145

Figure A4-7. Flux decline for coated membranes with different MnO<sub>2</sub>-Co<sub>3</sub>O<sub>4</sub> loadings (0.0–4.0 mg). Fouling experiments were conducted with NOM-containing feed water (~5mgC/L NOM mixture with ~10% colloids and ~90% HPO fractions) at unadjusted pH of 6.3±0.2 and operating pressure of 1bar. .... 145

Figure A4-8. UV<sub>254</sub> and TOC removal rate after filtration of 100 mL NOM solution for both original and coated membranes. NOM solution: Colloids-Mery 0.55mgC/L + HPO SRNOM 4.45 mgC/L. Experimental conditions: Operational pressure =1.0 bar, temperature 20 ± 1 °C, pH was adjusted with NaOH to 7.40 ± 0.2..... 146

Figure A4-9. Normalized water flux of the original and coated membrane with or with PMS addition in NOM solution-M (Colloids-Mery 0.55 mgC/L + HPO SRNOM 4.45 mgC/ L). Experimental conditions: Operational pressure =1.0 bar, temperature 20 ± 1 °C, pH was adjusted with NaOH to 7.40±0.2. .... 146

Figure A4-10. Fluorescence EEM spectra of (a) NOM solution-B and (d) solution-M, permeate from pristine membrane with PMS added in (b) NOM solution-B and (e) solution-M, and permeate from coated membrane with PMS added in (c) NOM solution-B and (f) solution-M. Emission spectra of (g) NOM solution-B and (h) solution-M before and after filtration under different condtions at an excitation wavelength of 230 nm. .... 147

Figure A4-11. Flux recovery by soaking fouled membrane in 10 mM PMS solution (pH  $3.20 \pm 0.10$ ) for 10 min. Conditions: fouling tests were conducted with 100 mL of NOM solution-M (Colloids-Mery 0.55 mgC/L and HPO SRNOM 4.45 mgC/L)..... 148

# List of Tables

## Chapter 2–5

Table 2-1. Rct values in different DOM-containing systems under PMS exposure higher than 0.1 M·s

$$\left( \ln(pCBA / pCBA_0) = -A([PMS]_0 \int_0^t e^{-kt} dt) + B, R^2; R_{ct} = A / k_{SO_4^{\cdot-}, pCBA} \right) \dots\dots\dots 18$$

Table 4-1. Mean values ( $\mu$ ) of attracting forces (mN/m) measured during DOM-coated silica colloidal probe approaching to MnO<sub>2</sub> surface at different solution chemistries. Variance ( $\sigma$ ) are shown in parentheses. .... 67

Table 5-1. R<sup>2</sup> values from the fitting of the experimental data with filtration models (R<sup>2</sup>: coefficient of determination for different modelings; STDEV: Standard deviation in R<sup>2</sup> of duplicate modeling. The experimental data used for modeling was obtained from fouling tests using NOM solution-M) ... 91

## Appendix 1–4

Table A1-1. Characteristics of selected DOM fractions ..... 102

Table A1-2. Peak location and maximum fluorescence intensity of each peak for the DOM fractions..... 102

Table A1-3. Second order rate constants of pCBA, t-BuOH, and EtOH with ·OH and SO<sub>4</sub><sup>·-</sup> ..... 102

Table A1-4. Calculation of PMS exposures with an initial PMS concentration of 1 mM at different reaction time in S-HPOA containing system (PMS exposure (M·s) = $[PMS]_0 \int_0^t e^{-kt} dt$ ) .....	103
Table A1-5. Calculation of PMS exposures with different initial PMS concentrations in S-HPOA containing system (PMS exposure (M·s) = $[PMS]_0 \int_0^{t_c} e^{-kt} dt$ ) .....	103
Table A2-1. Bulk properties of NOM isolates .....	118
Table A2-2. Molecular characteristics of NOM isolates studied in the experiment .....	118
Table A2-3. Rate constant ( $k$ ) and correlation coefficient ( $R^2$ ) of pseudo-first-order kinetics of UV <sub>254</sub> decrease and steady-state radical concentration. (Conditions: Incident UV intensity = $0.9 \text{ mW}\cdot\text{cm}^{-2}$ , $[\text{TOC}]_0 = 3.89 \pm 0.18 \text{ mgC}\cdot\text{L}^{-1}$ , $[\text{H}_2\text{O}_2]_0$ or $[\text{PDS}]_0 = 1.00 \text{ mM}$ , $[\text{pCBA}]_0$ or $[\text{NB}]_0 = 1.00 \mu\text{M}$ at unadjusted pH ( $[\text{pH}]_0(\text{H}_2\text{O}_2) = 4.65 \pm 0.09$ , $[\text{pH}]_0(\text{PDS}) = 4.66 \pm 0.18$ ) and room temperature (20°C). ) .....	118
Table A2-4. Statistics on molecules reactive or resistant to $\cdot\text{OH}$ and $\text{SO}_4^{\cdot-}$ ....	119
Table A2-5. Removal efficiency of different NOM classes by $\cdot\text{OH}$ and $\text{SO}_4^{\cdot-}$ . .....	119
Table A2-6. Comparison of molecular characteristics between reactive and resistant molecules in $\cdot\text{OH}$ and $\text{SO}_4^{\cdot-}$ -based AOPs.....	120

Table A2-7. Percentage of molecules with different molecular compositions reactive to $\cdot\text{OH}$ and $\text{SO}_4^{\cdot-}$ .....	121
Table A2-8. Molecular characteristics of molecules exclusively reactive to $\cdot\text{OH}$ or $\text{SO}_4^{\cdot-}$ .....	121
Table A2-9. Characteristics of molecules produced through $\cdot\text{OH}$ or $\text{SO}_4^{\cdot-}$ oxidation.....	121
Table A3-1. Major characteristics of HPO and HPI DOM fractions.....	131
Table A4-1. Characteristics of original ceramic membranes.....	138
Table A4-2. Flux and resistance of membrane with different catalyst loadings (0–4mg) before ( $J_0$ and $R_0$ ) and after ( $J_f$ and $R_f$ ) fouling. Fouling experiments were conducted with NOM-containing feed water (~5mgC/L NOM mixture with ~10% colloids and ~90% HPO fractions) at unadjusted pH of $6.3 \pm 0.2$ and operating pressure of 1bar.....	138
Table A4-3. SUVA value ( $\text{m}^{-1}(\text{mg/L})^{-1}$ ) of feedwater and permeate under different experimental conditions: NOM solution-B: 0.56 mgC/L Colloids-Brittany + 4.45 mgC/L HPO-SRNOM, and NOM solution-M: 0.55mgC/L Colloids-Mery + 4.45 mgC/L HPO-SRNOM. Experimental conditions: Operational pressure = 1.0 bar, temperature $20 \pm 1^\circ\text{C}$ , pH ~ 6 without PMS addition and $3.40 \pm 0.10$ with 1 mM PMS addition.....	139
Table A4-4. Equations and descriptions of different filtration models.....	139
Table A4-5. Leaching of cobalt and manganese ions from the coated membrane under different conditions.....	140

# List of Equations

Equation 2.1 .....	15
Equation 2.2 .....	15
Equation 2.3 .....	15
Equation 2.4 .....	16
Equation 2.5 .....	16
Equation 2.6 .....	16
Equation 2.7 .....	17
Equation 2.8 .....	17
Equation 2.10 .....	19
Equation 2.11 .....	21
Equation 2.12 .....	21
Equation 5.1 .....	77
Equation 5.2 .....	78
Equation 5.3 .....	78
Equation 5.4 .....	78

Equation 5.5 ..... 79

**Appendix1–4**

Equation A 5-1 ..... 79

Equation A1-1 ..... 101

Equation A1-2 ..... 101

Equation A2-1 ..... 112

Equation A2-2 ..... 112

Equation A2-3 ..... 112

Equation A2-4 ..... 112

Equation A2-5 ..... 114

Equation A2-6 ..... 115

Equation A2-7 ..... 115

Equation A2-8 ..... 115

Equation A2-9 ..... 115

Equation A2-10 ..... 115

Equation A3-1 ..... 130

Equation A3-2 ..... 130

# List of Publications and Presentations Arising from this Thesis

## Peer-reviewed journal articles

Zhang, S.; Rouge, V.; Gutierrez, L.; Croué, J.-P. (2019). Reactivity of chromophoric dissolved organic matter (CDOM) to sulfate radicals: Reaction kinetics and structural transformation. *Water Research*, 163, 114846.

Zhang, S.; Gutierrez, L.; Niu, X-Z.; Qi F.; Croué, J.-P. (2018). Organic Matter interfacial interactions with MnO<sub>2</sub> and its influence on catalytic oxidation processes. *Chemosphere*, 209, 950–959.

Zhang, S.; Hao, Z.; Liu, J.; Gutierrez, L.; Croué, J.-P. (2019). Molecular Insights into the Reactivity of Aquatic Natural Organic Matter towards  $\cdot\text{OH}$  and  $\text{SO}_4^{\cdot-}$  Using FT-ICR MS. To be submitted to *Environmental Science & Technology*.

Zhang, S.; Gutierrez, L.; Qi, F.; Croué, J.-P. (2019).  $\text{SO}_4^{\cdot-}$ -based catalytic ceramic UF membrane for organics removal and flux restoration. To be submitted to *Chemical Engineering Journal*.

## Conference presentations

Zhang, S.; Gutierrez, L.; Qi, F.; Croué, J.-P. “Application of MnO<sub>2</sub>-Co<sub>3</sub>O<sub>4</sub> coated ceramic UF membrane for fouling mitigation and contaminant removal” 9th International Water Association (IWA) Membrane Technology Conference & Exhibition for Water and Wastewater Treatment and Reuse (IWA-MTC 2019). Toulouse, France, June 23-27, 2019 (Oral)

Zhang, S.; Hao, Z.; Liu, J.; Croué, J.-P. "Comparison of transformation of DOM with different characteristics with hydroxyl and sulfate radical in UV-AOPs" 2019 IUVA world congress. Sydney, Australia, February 10-13, 2019 (Oral)

Zhang, S.; Rouge, V.; Gutierrez, L.; Croué, J.-P. "Reactivity of sulfate radicals with chromophoric Dissolved Organic Matter: Reaction kinetics and structural transformation" 256th ACS conference. Boston, USA, August 18-22, 2018 (Oral)

Zhang, S.; Gutierrez, L.; Niu, X-Z.; Qi F.; Croué, J.-P. "Aquatic dissolved organic matter interfacial interactions with MnO<sub>2</sub>: Influence of DOM characteristics and solution chemistry" 2017 ICCE. Oslo, Norway, June 12-19, 2017 (Poster)

# Chapter 1. Thesis Overview

Currently, membrane technology has gained increasing interest in the water treatment field in an effort to meet the increasing demand for drinking water of quality. As a low-pressure membrane filtration technique, ultrafiltration has the capability to remove large substances in water (e.g., particulates, colloids, and microorganisms) at a relatively low cost. However, the removal of trace organic contaminants (TOrcs) is deficient due to their smaller size. More importantly, membrane fouling caused by natural/dissolved organic matter (NOM/DOM) (i.e., heterogeneous and complex product of biological and chemical decay of living organisms, and ubiquitous in aquatic environments) remains a substantial obstacle in its application. In the initial stage of fouling, the adsorption of foulants changes the characteristics of the membrane surface (i.e., conditioning film formation, NOM-membrane interfacial interactions); thus, affecting subsequent fouling behavior. The next fouling stage (i.e., cake layer formation) is mainly driven by NOM-NOM interaction as a function of solution conditions. Membrane fouling not only reduces productivity and permeate quality but also increases energy consumption and operational costs. To address these issues, the use of catalytic membranes, i.e., catalyst-modified membranes, has been proposed in recent years. When used in combination with oxidants (i.e.,  $O_3$  and  $H_2O_2$ ) or UV irradiation, catalytic membranes have shown enhanced performance in fouling mitigation as well as quality permeate production due to the generation of reactive oxygen species (ROS). Specifically, the reaction of TOrcs or NOM to these ROS (e.g.,  $\cdot OH$ ,  $O_2^{\cdot -}$ ,  $^1O_2$ ) plays a vital role in this improved performance. In addition, catalytic membranes exhibit an enhanced cleaning efficiency when specific oxidants are used as cleaning reagents. Remarkably, sulfate radical ( $SO_4^{\cdot -}$ )-based advanced oxidation

processes (AOPs) have recently attracted widespread attention as an alternative oxidation technology. This process is capable of degrading a wide variety of organic pollutants due to its high reduction potential. Therefore, the combination of the powerful  $\text{SO}_4^{\bullet-}$ -based oxidation process and the filtration performance of catalytic membranes is a promising concept worth of additional and extensive research.

This PhD project focused on the reactivity of natural organic matter in advanced oxidation processes, its interaction with metal oxide and the performance of  $\text{SO}_4^{\bullet-}$ -based catalytic ceramic membrane. The thesis includes 6 chapters. Chapter 1 presents the thesis outline. Chapter 2-5 give the results and corresponding discussions of four different research topics arising from the PhD project. The research output led to the publication of two peer-reviewed articles and two prepared manuscript ready for submission. The conclusions drawn from the PhD project, and future research perspectives are collated in Chapter 6. Supporting information for all the publications and manuscripts to be submitted are provided in Appendix 1-4. Publisher permission for the inclusion of the two published articles in this thesis are presented in Appendix 5.

Chapter 2 describes the  $\text{SO}_4^{\bullet-}$ -induced reactivity of CDOM with a focus on the reaction kinetics and CDOM transformation. A faster second order reaction rate of CDOM with  $\text{SO}_4^{\bullet-}$  (i.e.,  $\sim 10^8 \text{ M}^{-1}\text{s}^{-1}$ ) was measured as compared to that previously reported for bulk DOM (i.e.,  $\sim 10^7 \text{ M}^{-1}\text{s}^{-1}$ ). In addition, the major reaction pathways was presented with the use of traditional DOM characterization techniques. With the use of DOM isolates extracted from different natural sources, the study bears the advantage of providing solid evidence for the observations. The research findings was published in Water Research: “Zhang, S.; Rougé, V.; Gutierrez, L.; Croué, J.-P. (2019). Reactivity

of chromophoric dissolved organic matter (CDOM) to sulfate radicals: Reaction kinetics and structural transformation. *Water Research*, 163, 114846.”

Chapter 3 elucidates the difference in the reactivity of NOM between  $\cdot\text{OH}$  and  $\text{SO}_4^{\cdot-}$ , which leads to the long-acknowledged distinct scavenging capacity. Advanced analytic tool, i.e., Fourier Transformation Ion Cyclotron Resonance Mass Spectrometry (FT-ICR MS) was used to achieve the goal. With the accurate detection of NOM molecules and the unambiguous assignment of molecular formulas, reactive sites to respective radical species could be identified and the reaction pathways could be inferred. Different reactivity could be clarified with a distinct reaction rate associated with specific reaction pathways. The research findings would also assist in the selection of  $\cdot\text{OH}$  or  $\text{SO}_4^{\cdot-}$ -based AOPs in water treatment based on their reaction characteristics. The research work is to be submitted to *Environmental Science & Technology* for peer-review.

Chapter 4 presents a novel perspective regarding the selection of material for catalytic membrane preparation. Pursuit for highly efficient catalyst has sparked tremendous research focus on catalyst improvement. This Chapter is dedicated to drawn attention to the interaction between NOM and catalyst, which is critical in membrane fouling.  $\text{MnO}_2$  is selected as an alternative catalyst due to its natural-abundant and environmentally friendly nature. The interaction between NOM and  $\text{MnO}_2$  was investigated using Time-Resolved Dynamic Light Scattering (TR-DLS) and Atomic Force Microscopy (AFM) under varied solution conditions. The study would contribute to the better application of catalytic membrane by providing sights into the additional criteria for catalytic material selection. The research work was published in *Chemosphere*: “Zhang, S.; Gutierrez, L.; Niu, X-Z.; Qi, F.; Croué, J.-P. (2018).

Organic Matter interfacial interactions with MnO<sub>2</sub> and its influence on catalytic oxidation processes. *Chemosphere*, 209, 950–959.”

In Chapter 5, a comprehensive investigation on the performance of SO<sub>4</sub><sup>•-</sup>-based catalytic membrane was provided. The catalytic membrane was obtained through coating with MnO<sub>2</sub>-Co<sub>3</sub>O<sub>4</sub> nanoparticles, efficient for SO<sub>4</sub><sup>•-</sup> production through catalytic PMS decomposition. By providing information on the performance of the catalytic membrane in contaminants removal, NOM transformation, fouling mitigation, and self-cleaning efficiency, the study ultimately contributes to the application as well as optimisation of the novel SO<sub>4</sub><sup>•-</sup>-based catalytic membrane technology. The findings in this chapter will be submitted soon for peer-review.

A wrap up comes in Chapter 6 by providing the concluding remarks and future perspectives based on the findings in this thesis.

## **Chapter 2. Reactivity of chromophoric dissolved organic matter (CDOM) to sulfate radicals: Reaction kinetics and structural transformation**

Suona Zhang, Valentin Rougé, Leonardo Gutierrez, and Jean-Philippe Croué

Water Research, Volume 163, 15 October 2019, Pages 114846

<https://doi.org/10.1016/j.watres.2019.07.013>

## 2.1 Introduction

Sulfate radical ( $\text{SO}_4^{\bullet-}$ )-based advanced oxidation processes (AOPs) have gained increasing interest in water treatment at both fundamental and applied levels (Siegrist et al., 2011; Waclawek et al., 2017). Due to its comparable or even stronger oxidizing capabilities than  $\cdot\text{OH}$ ,  $\text{SO}_4^{\bullet-}$  is also capable of degrading a broad spectrum of trace organic contaminants (TOrcs) (e.g., pharmaceuticals, personal care products, and industrial chemicals) which are constantly detected in water bodies (Ghauch et al., 2017; Lutze et al., 2015a). A strong oxidation capacity, together with a high selectivity (i.e., lower scavenging of background organics) (Lutze et al., 2015a), multiple means of radical generation (Wang et al., 2014), and a favored storage/transport of stable solid precursors, make  $\text{SO}_4^{\bullet-}$  a promising alternative for contaminants removal.

Previous studies focusing on the removal of TOrcs by  $\text{SO}_4^{\bullet-}$  have provided key mechanistic and kinetic insights (Nihemaiti et al., 2018; Yang et al., 2019; Yang et al., 2017). However, little is known about the  $\text{SO}_4^{\bullet-}$ -induced reactivity and transformation of dissolved organic matter (i.e., DOM, a highly heterogeneous mixture of organic molecules ubiquitous in aquatic environments, and playing multiple key roles in water treatment) (Leenheer et al., 2003; Lutze et al., 2015a; Varanasi et al., 2018). Briefly, the presence of DOM is known to decrease the removal efficiency of TOrcs due to its radical scavenging effect. Also, DOM transformation or removal can control disinfection byproducts formation or membrane fouling by applying  $\text{SO}_4^{\bullet-}$ -based AOPs as a pretreatment strategy (Cheng et al., 2017a; Chu et al., 2015; Tian et al., 2018; Xie et al., 2015a). Therefore, an advanced knowledge on  $\text{SO}_4^{\bullet-}$ -induced reactivity and transformation of DOM is crucial to different water treatment processes considering its ubiquitous presence and the promising application of  $\text{SO}_4^{\bullet-}$ -based techniques.

The reactivity of DOM with oxidants such as chlorine, ozone, and  $\cdot\text{OH}$  has been extensively investigated. The difference in reactivity (i.e., faster reaction rate at the initial oxidation phase as compared to subsequent reaction phases) of different DOM isolates has been previously correlated with their structural variability and complexity (Chon et al., 2015; Westerhoff et al., 2004). Interestingly, while  $\cdot\text{OH}$  non-selectively reacts with target substances,  $\text{SO}_4^{\cdot-}$  mainly reacts with electron rich aromatic or conjugated double bond moieties (Varanasi et al., 2018). This reactive DOM fraction has been termed as chromophoric dissolved organic matter (CDOM) due to its light absorbing property (Lee et al., 2006; Leenheer et al., 2003). Therefore, the degradation rate of CDOM, as measured by ultraviolet absorbance at 254 nm ( $\text{UVA}_{254}$ ) (Westerhoff et al., 2007), could be used to determine its reactivity to  $\text{SO}_4^{\cdot-}$ .

A detailed study on the transformation of DOM, as a result of its reactivity to  $\text{SO}_4^{\cdot-}$ , remains challenging due to its structural complexity and a lack of analytical techniques. Alternatively, traditional DOM characterization techniques could be applied to provide some insights into  $\text{SO}_4^{\cdot-}$ -induced changes of typical DOM characteristics, e.g., electron donating capacity (EDC), optical property (chromophoric or fluorescent property), molecular weight, or organic content (Li et al., 2016; Wang et al., 2017). For instance, an investigation on the transformation of DOM with  $\cdot\text{OH}$  was conducted by tracking the changes in chromophoric and fluorescent properties (Sarathy et al., 2008). Specifically, the partial oxidation (i.e., no significant carbon removal) of DOM led to the breakdown of larger molecules, ring open of aromatic structures and the formation of small organics. Interestingly, due to the favorable decarboxylation mechanism driven by  $\text{SO}_4^{\cdot-}$ , a higher DOM mineralization would be expected (Madhavan et al., 1978; Varanasi et al., 2018).

To fill this knowledge gap, the objective of this study was to investigate the reactivity and transformation of CDOM with  $\text{SO}_4^{\cdot-}$ . The reactivity of CDOM was studied by following the decrease of its  $\text{UVA}_{254}$  with time. A second order rate constant of fast reacting CDOM was calculated based on an established correlation between  $\text{UVA}_{254}$  and radical exposure. By recording the changes in  $\text{UVA}_{254}$ , electron donating capacity (EDC), fluorescence intensity (FI), and total organic carbon (TOC), information on CDOM transformation was obtained. A Co(II)-activated peroxymonosulfate (PMS) process was used for the production of  $\text{SO}_4^{\cdot-}$  due to its high efficiency and simplicity. Four well characterized hydrophobic DOM fractions of different origins and characteristics were selected as model CDOM. This selection of organic isolates obtained from various sources shaping different characters represents a significant advance compared to model organics used in previous investigations.

## 2.2 Materials and method

### 2.2.1 Chemical reagents and DOM fractions

Peroxomonosulfate (Oxone,  $\text{KHSO}_5 \cdot 0.5\text{KHSO}_4 \cdot 0.5\text{K}_2\text{SO}_4$ ), 2,2'-azinobis (3-ethylbenzothiazoline-6-sulfonic acid) diammonium salt (ABTS;  $\geq 98\%$ ), cobalt(II) sulfate ( $\geq 99.0\%$ ), sodium tetraborate ( $\geq 99.5\%$ ), ethanol ( $\geq 99.5\%$ ), and *tert*-butanol (pure) were purchased from Sigma-Aldrich and prepared with Ultrapure water (PURELAB Ultra, ELGA). Sulfuric acid of HPLC grade and sodium thiosulfate ( $\text{Na}_2\text{S}_2\text{O}_3$ ) were purchased from UNIVAR. *p*-chlorobenzoic acid (pCBA, Acros Organics) was dissolved in ultrapure water to a concentration of 0.2 mM and used as a stock solution. A PMS stock solution of a high concentration (10 mM) was prepared and kept at 4°C due to its instability. The concentration of the stock solution was monitored on a daily basis prior to use.

Four DOM fractions previously isolated and characterized were selected for this study: Hydrophobic acids (i.e., DOM adsorbed onto XAD-8<sup>®</sup> resin at acid pH and eluted with sodium hydroxide) extracted from Suwannee River water (S-HPOA, USA) and Beaufort Reservoir (B-HPOA, France); hydrophobic DOM (i.e., similar protocol using a mixture of water and acetonitrile for resin elution) isolated from Ribou Reservoir NOM (R-HPO, France) and Colorado River (C-HPO, USA). The characteristics of the DOM isolates were summarized in Table A2-1.

### **2.2.2 Experimental setup and procedures**

Experiments were conducted in 40-mL amber glass vials with Teflon caps. A pre-determined amount of Co(II) as well as DOM stock solution were added into the 10 mM borate buffer to obtain a final composition of  $3.90 \pm 0.11$  mg C/L of DOM and 1  $\mu$ M of Co(II) at pH 8. Instead of phosphate buffer, tetraborate was used as a buffer solution due to the reported complexing ability of the former with cobalt. A pH 8 buffer was used due to its improved buffering capacity upon the addition of PMS at high concentrations.

The experiments for CDOM reaction kinetics were started by introducing 1 mM PMS. The use of a high initial PMS concentration would allow for a study under both low and high PMS exposure conditions, representative of different water treatment processes. Ethanol and *tert*-butanol at different concentrations (1 or 10 mM) were used as radical quenching agents, while *p*CBA (10  $\mu$ M) was used as a model compound to quantify primary reactive species. Samples were collected at specified time intervals and subjected to immediate measurement of PMS residual and UV absorbance at 254 nm (UVA<sub>254</sub>) without the addition of quenching agent. The value of UVA<sub>254</sub> was further corrected by subtracting the interferences from borate buffer (i.e., including

H<sub>2</sub>SO<sub>4</sub> for pH adjustment), CoSO<sub>4</sub>, and PMS. Also, the contribution of PMS at each sampling time was calculated based on the residual PMS concentration and its  $\epsilon_{254\text{nm}}$  measured in this study (12.3 M<sup>-1</sup>cm<sup>-1</sup>). For samples subjected to pCBA analysis, the reaction was stopped by adding 0.1 mL of ethanol (10 M) to 0.9 mL of sample. Sodium thiosulfate was found inefficient in quenching residual PMS with concentrations as high as 600 mM.

In order to avoid the interference of quenchers on Electron Donating Capacity (EDC) measurements, a new set of experiments was performed by using various initial PMS concentrations (i.e., from 0.00 to 1.00 mM) to achieve experimental conditions with different PMS exposures. PMS residual was periodically monitored, and all samples were analyzed after complete PMS consumption. All experiments were performed at room temperature (20°C) in glass bottles installed on a rotary shaker (Ika-Werke GMBH & Co. (KG), Labortechnik KS250 Basic) operated at 500 rpm.

### **2.2.3 Analytical methods**

#### ***2.2.3.1 Analysis of residual PMS***

The concentration of PMS was measured by an ABTS<sup>•+</sup>-based method described elsewhere (Zhang et al., 2016). In this method, ABTS<sup>•+</sup> is generated during the oxidation of ABTS by sulfate radical produced through the catalytic transformation of PMS, and then it was spectrophotometrically measured. Briefly, a solution containing 0.5 mL of ABTS (20 mM), 0.2 mL of CoSO<sub>4</sub> (20 mM), 10 mL of H<sub>2</sub>SO<sub>4</sub> (2%), and 1 mL of water sample was well mixed and measured at a 734 nm wavelength with a spectrophotometer (Cary 60, Agilent). The calibration curve for PMS determination was shown in Figure A1-1. Calibration curve for PMS determination (PMS (μM) = 99.92 A<sub>734</sub> - 29.052, R<sup>2</sup>=0.9998)Figure A1-1. A high concentration of CoSO<sub>4</sub> (20 mM)

was applied to accelerate the catalytic decomposition of PMS. However, this interference has been taken into consideration with the measurement of a blank sample with no PMS addition, as suggested by the calibration curve in Figure A1-1. Also, a background DOM would not be influential due to a measurement recorded at 734nm.

### ***2.2.3.2 Characterization of DOM transformation***

The EDC of DOM samples was analysed based on a method developed by Chon et al (Chon et al., 2015). Briefly, a size exclusion chromatography (SEC) coupled with post column reaction was used, where  $ABTS^{*+}$  was produced by the oxidation of ABTS with sodium persulfate in acidic environment. A TOYOPEARL HW-50S column (8mm×30cm) was selected for SEC using a 50 mM borate eluent (pH 7.8) at a flow rate of 0.2 mL/min. The post-column injection of  $ABTS^{*+}$  solution was operated at 0.05 mL/min from the helium pressurised generator. The reaction coil was connected to two UV detectors positioned in series (Agilent 1100 series, USA): the first one recording UV absorbance of DOM at 254 nm, and the second one recording the signal for ABTS/ $ABTS^{*+}$  at 405 nm.

A Cary 60 spectrophotometer (Agilent, USA) was used to collect absorbance data or to record the UV-vis spectra from 200 nm to 800 nm in 1cm path length quartz cell. The TOC concentration of each sample was measured with a Shimadzu TOC-L analyser (SHIDMAZU, Japan).

Fluorescence excitation and emission matrices (EEMs) were obtained using a Fluorescence spectrometer (Cary Eclipse, Varian). The operating parameters were adjusted based on the method from Chen et al (Chen et al., 2003). Briefly, the scan rate and excitation or emission slit bandwidth were set at 600 nm/min and 5nm, respectively. The spectra were recorded by scanning an emission spectra from 290 nm

to 550 nm at a 5nm increment with the excitation wavelength ranging from 220 nm to 400 nm at a 5 nm increment.

The concentration of *p*CBA was measured with a HPLC unit equipped with a UV detector (Agilent 1100 series, USA) recording absorbance at 238 nm and with a 250 mm\*4.6mm C18 5- $\mu$ m reverse phase column (Alltima<sup>TM</sup>, GRACE). The mobile phase consisted of 60% methanol and 40% phosphoric acid (0.1%, V/V). The *p*CBA calibration curve was built using gradually diluted stock solution.

## **2.3 Results and Discussion**

### **2.3.1 Biphasic decrease of CDOM in Co(II)/PMS system**

The reaction of CDOM with PMS led to an average decrease of 11% in UVA<sub>254</sub> within 60 min (Figure A1-2). However, the decrease of UVA<sub>254</sub> was remarkably faster in the presence of both PMS and Co(II) (Figure 2-1). Approximately 55% to 70% decrease in UVA<sub>254</sub> (depending on the DOM fraction) was observed in Co(II)-catalyzed PMS system within 60 min. This enhanced reaction was caused by the generation of reactive species (e.g., SO<sub>4</sub><sup>•-</sup>) in the Co(II)/PMS system, while the slight UVA<sub>254</sub> decrease in the absence of Co(II) catalyst was probably due to the reaction of quinones with PMS as previously reported (Zhou et al., 2015). The occurrence of quinones within humic substances has been widely acknowledged (Cory et al., 2005).

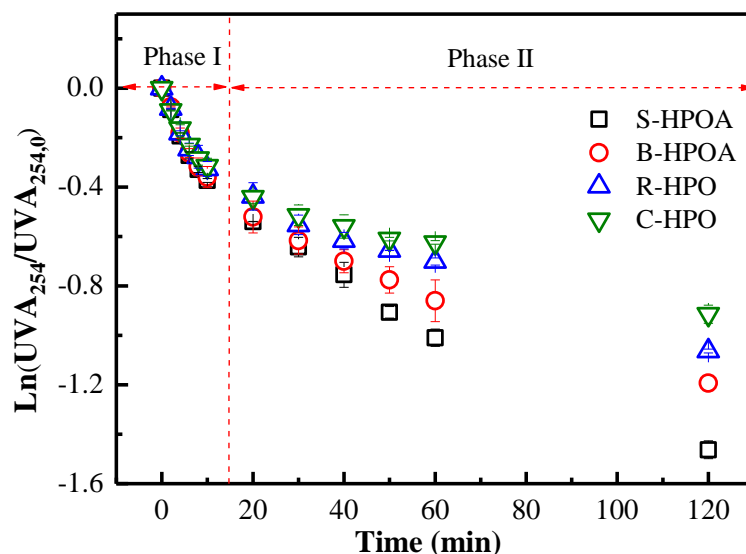


**Figure 2-1.** UVA<sub>254</sub> decrease of different DOM fractions in Co(II)/PMS system as a function of time. Conditions: [PMS]<sub>0</sub> = 1.0 mM; Co(II) = 1.0 μM; DOM = 3.90 ± 0.11 mgC/L; pH = 8.00 ± 0.05 (10 mM borate buffer); T = 20°C

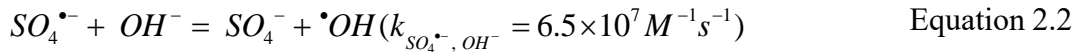
Noticeably, a fast and slow reaction phase could be distinguished for all DOM fractions throughout the oxidation process (Figure 2-1). Specifically, the pseudo-first-order rate constants of the fast reaction phase were 4.2 to 6.9 times higher than the rate constants of the slower reaction phase. These results showed a significant difference in the reactivity of CDOM with SO<sub>4</sub><sup>•-</sup> due to the heterogeneous structural property of the organic matter isolates. It has been previously reported that aromatic structures substituted with electron donating groups (i.e., -OH, -NH<sub>3</sub>, -OCH<sub>3</sub>) exhibited higher reactivity to SO<sub>4</sub><sup>•-</sup> (Luo et al., 2017); these structures could represent the main contributor to the fast reacting CDOM (i.e., CDOM<sub>fast</sub>). The slow reacting CDOM (i.e., CDOM<sub>slow</sub>) might include lower electron density moieties from the original CDOM constituents as well as the oxidation products of CDOM<sub>fast</sub> (Xiao et al., 2015; Zhang et al., 2012b).

The influence of the aromatic character of the DOM fractions on their reactivity with SO<sub>4</sub><sup>•-</sup> was highly expected based on previous findings (Luo et al., 2017; Westerhoff et

al., 2004). However, the difference in reactivity among the four DOM fractions was more significant during the slow reaction phase. The pseudo-first-order reaction rates of  $\text{CDOM}_{\text{slow}}$  (i.e.,  $\ln(\text{UVA}_{254}/\text{UVA}_{254,0})$  versus reaction time) were calculated as  $1.20 \times 10^{-2}$ ,  $0.84 \times 10^{-2}$ ,  $0.63 \times 10^{-2}$ , and  $0.46 \times 10^{-2} \text{ min}^{-1}$  for S-HPOA, B-HPOA, R-HPO and C-HPO, respectively. These  $\text{CDOM}_{\text{slow}}$  reactivities linearly increased with the SUVA values as shown in Figure A1-3. The  $\text{CDOM}_{\text{fast}}$  reactivity to  $\text{SO}_4^{\cdot-}$  of the four DOM fractions was further discussed in the following sections.

### 2.3.2 Evaluation of sulfate radical production

Anipsitakis and Dionysiou (Anipsitakis et al., 2003) reported the predominant role of  $\text{SO}_4^{\cdot-}$  (Equation 2.1) over  $\cdot\text{OH}$  in Co(II)-catalyzed PMS systems at pH 7. Because a pH 8 may promote a higher production of  $\cdot\text{OH}$  (Equation 2.2), the identification of major oxidizing species in the current system was conducted by following the degradation of *p*CBA as a probe compound under different scavenging conditions (Lutze et al., 2015b). The second-order rate constants of *p*CBA and radical scavengers (i.e., *t*-BuOH and EtOH) with  $\cdot\text{OH}$  and  $\text{SO}_4^{\cdot-}$  were summarized in Table A1-3. When 10 mM of radical scavenger (i.e., *t*-BuOH or EtOH, at a molar ratio of 1000:1 versus *p*CBA) was applied, the *p*CBA removal efficiency was decreased by approximately 10% in the presence of *t*-BuOH; while almost no *p*CBA decrease was observed with the addition of EtOH (Figure A1-4). Quantitatively, the ratio of the measured concentration of  $\cdot\text{OH}$  to  $\text{SO}_4^{\cdot-}$  was lower than 3%. These results indicated that  $\text{SO}_4^{\cdot-}$  was the predominant reactive species at pH 8. This is probably due to the competition for  $\text{SO}_4^{\cdot-}$  by either *p*CBA ( $3.6 \times 10^8 \text{ M}^{-1}\text{s}^{-1}$ ) or scavengers (i.e., DOM fractions, up to  $10^8 \text{ M}^{-1}\text{s}^{-1}$  as discussed below), leading to the unfavorable production of  $\cdot\text{OH}$  (Equation 2.2).



Therefore, the production of  $SO_4^{\bullet-}$  was investigated following the  $R_{ct}$  concept and the analysis of *p*CBA decay.  $R_{ct}$  (i.e., the ratio of radical exposure to oxidant exposure) (Elovitz et al., 1999) was used to present the production of  $SO_4^{\bullet-}$  with PMS exposure (Equation 2.4). According to Elovitz and von Gunten (Elovitz et al., 1999), the consumption of radicals by a probe compound (P) (e.g., *p*CBA in the current study) is considered insignificant as compared to major radical scavengers (S) (e.g., DOM in current study) if the probe compound is present at a considerably low concentration (i.e.,  $k_P[P] \ll k_S[S]$ , where  $k_P$  and  $k_S$  represents the rate constants of the probe compound and major radical scavengers with radicals, respectively). Therefore, a low *p*CBA concentration (i.e., 1  $\mu$ M) was applied to ensure an insignificant radical consumption by *p*CBA as compared to DOM. Specifically,  $k_{pCBA}[pCBA]$  was calculated as approximately 1.4% of  $k_{DOM}[DOM]$  under the current experimental condition, where  $k_{pCBA}$  and  $k_{DOM}$  represent the second order rate constants of *p*CBA ( $3.6 \times 10^8 M^{-1}s^{-1}$ ) and DOM ( $6.8 \times 10^3 LmgC^{-1}s^{-1}$ ) with  $SO_4^{\bullet-}$ , respectively. The  $R_{ct}$  value was only studied for the first 10 min of the reaction.  $CDOM_{fast}$  was observed reactive within this timeframe (Figure 2-1). The conversion from reaction time to PMS exposure was illustrated in Table A1-4.

Although no noticeable interference was observed with  $UVA_{254}$  or EDC measurements, the rate of catalytic PMS decomposition decreased due to the formation of cobalt-DOM complex. For instance, a 57% PMS decomposition was observed within 60 min in the DOM-free system. However, the PMS decomposition values for S-HPOA-, B-

HPOA-, R-HPO-, and C-HPO-containing system were 41%, 43%, 40%, and 43%, respectively. Specifically, approximately 80% of Co(II) was calculated as forming complexes with DOM under the current experimental conditions using the NICA-Donnan model with the constants adapted from Milne et al (Milne et al., 2003). In DOM-containing solutions with the addition of *p*CBA as probe compound, PMS decomposed following a pseudo-first-order reaction (Figure A1-6a), as described by (Equation 2.5), and *k* (i.e., pseudo-first-order rate constant) was measured as approximately  $3.0 \times 10^{-4} \text{s}^{-1}$  independent of DOM origins. The influence of *p*CBA addition (1  $\mu\text{M}$ ) on PMS decomposition was negligible. For instance, the averaged PMS residual measured in different DOM-containing systems within 10 min was 80% in the absence of *p*CBA (Figure A1-5) and 79% in the presence of *p*CBA (Figure A1-6a). The determined rate (within 10 min) was predominantly contributed by a catalytic decomposition since self-decomposition of PMS was found negligible within 2 hr at room temperature (20°C). The degradation of *p*CBA (Figure A1-6b) caused by  $\text{SO}_4^{\bullet-}$  was described by Equation 2.6 and Equation 2.7. By combining Equation 2.4 and Equation 2.5, *p*CBA degradation could be described using the  $R_{ct}$  concept (Equation 2.8).

$$R_{ct} = \frac{\int_0^t [\text{SO}_4^{\bullet-}] dt}{\int_0^t [\text{PMS}] dt} \quad \text{Equation 2.4}$$

$$[\text{PMS}] = [\text{PMS}]_0 e^{-kt} \quad \text{Equation 2.5}$$

$$-\frac{d[\text{pCBA}]}{dt} = k_{\text{SO}_4^{\bullet-}, \text{pCBA}} [\text{pCBA}] [\text{SO}_4^{\bullet-}] \quad \text{Equation 2.6}$$

$$\ln \frac{[pCBA]}{[pCBA]_0} = -k_{SO_4^{\bullet-}, pCBA} \int_0^t [SO_4^{\bullet-}] dt \quad \text{Equation 2.7}$$

$$\ln \frac{[pCBA]}{[pCBA]_0} = -k_{SO_4^{\bullet-}, pCBA} R_{ct} [PMS]_0 \int_0^t e^{-kt} dt \quad \text{Equation 2.8}$$

By plotting  $\ln (pCBA/pCBA_0)$  versus PMS exposure, linear correlations were observed as a function of PMS exposures (Figure 2-2). The  $R_{ct}$  value at PMS exposures higher than 0.1 M·s (i.e. a reaction time of 2–10 min, Table A1-4) for each system was determined from the slope of the linear regression line (Figure 2-2) and listed in Table 2-1; while the higher  $R_{ct}$  values at PMS exposures lower than 0.1 M·s (i.e. a reaction time of 0–2 min, Table A1-4) were shown in Figure A1-7. Higher  $R_{ct}$  values at the initial oxidation stage (PMS exposure < 0.1 M·s, results discussed in section 2.3.4.1) have also been reported during the ozonation of surface waters (Elovitz et al., 1999). The change of  $R_{ct}$  in the current study was likely due to the Co(II) regeneration process. Specifically, the conversion of Co(II) to Co(III) with a precipitate formation of the latter has been considered as a probable explanation for the slowing down of the catalytic rate with time at pH above 5.9 (Zhang et al., 1992). With a pH of 8 used in this study, Co(III) might have also precipitated out as  $Co(OH)_3$  ( $K_{sp} = 1.6 \times 10^{-44}$ ), leading to the retardation of the regeneration process and consequently to a slower  $SO_4^{\bullet-}$  production. Moreover, the additional PMS consumption during the regeneration of Co(II) (Equation 2.3), which inefficiently produced  $SO_5^{\bullet-}$  (Neta et al., 1988), would also lead to a decreased  $R_{ct}$ . A change in Co(II) catalytic behavior at different pH probably associated with Co(III) precipitation at higher pH has also been observed in previous studies. For instance, the degradation rate of 2,4-DCP in Co(II)/PMS system slowed down with reaction time at pH 7 (Anipsitakis et al., 2005), while it remained unaffected at pH 2 (Anipsitakis et al., 2003). Considering that no enhanced  $UVA_{254}$

decrease (explained in Section 2.3.4.1) was observed (Figure 2-1) in contrast to the significantly higher *p*CBA degradation (Figure A1-6b) at the initial oxidation stage (i.e., PMS exposure lower than 0.1 M·s), the relatively lower  $R_{ct}$  values (Table 2-1) determined after the initial short stage were used in the analysis of the following section.

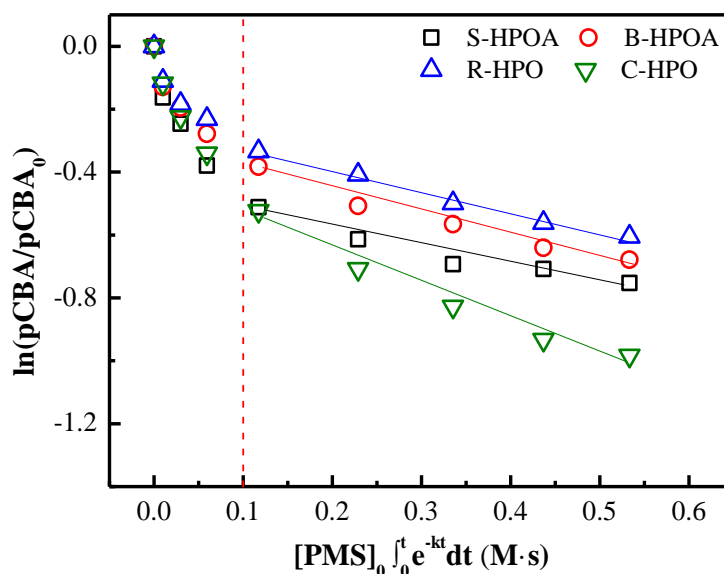


**Figure 2-2. Correlation between *p*CBA decay and PMS exposure in Co(II)/PMS system with different DOM fractions. Conditions:  $[PMS]_0 = 1.00$  mM;  $Co(II) = 1.00$   $\mu$ M;  $[pCBA]_0 = 1.00$   $\mu$ M; DOM =  $3.90 \pm 0.11$  mgC/L; pH =  $8.00 \pm 0.05$  (10 mM borate buffer); T = 20°C**

**Table 2-1.  $R_{ct}$  values in different DOM-containing systems under PMS exposure higher than 0.1 M·s**

$$\ln(pCBA/pCBA_0) = -A([PMS]_0 \int_0^t e^{-kt} dt) + B, R^2; R_{ct} = A/k_{SO_4^{\cdot-}, pCBA}$$

DOM fraction	A	$R_{ct}$	$R^2$
S-HPOA	0.588	$1.55 \times 10^{-9}$	0.935
B-HPOA	0.701	$1.95 \times 10^{-9}$	0.970
R-HPO	0.670	$1.86 \times 10^{-9}$	0.990

### 2.3.3 Reactivity of $\text{CDOM}_{\text{fast}}$ to $\text{SO}_4^{\cdot-}$ and its application

Following the procedures for establishing a relationship between  $\ln(p\text{CBA}/p\text{CBA}_0)$  and PMS exposure (Equation 2.8), i.e., obtained by combining Equation 2.4, Equation 2.5 and Equation 2.7, a similar correlation was also established between  $\ln(\text{UVA}_{254}/\text{UVA}_{254,0})$  of  $\text{CDOM}_{\text{fast}}$  and PMS exposure (Equation 2.9). This correlation was found linear when  $\ln(\text{UVA}_{254}/\text{UVA}_{254,0})$  of  $\text{CDOM}_{\text{fast}}$  was plotted against PMS exposure for all DOM fractions (Figure 2-3). The good linearity allowed the calculation of the reaction rate constant of  $\text{CDOM}_{\text{fast}}$  with  $\text{SO}_4^{\cdot-}$  using the  $R_{\text{ct}}$  value determined in Section 2.3.2.

$$\ln \frac{[\text{UVA}_{254}]}{[\text{UVA}_{254}]_0} = -k_{\text{SO}_4^{\cdot-}, \text{CDOM}} R_{\text{ct}} [\text{PMS}]_0 \int_0^t e^{-kt} dt \quad \text{Equation 2.9}$$

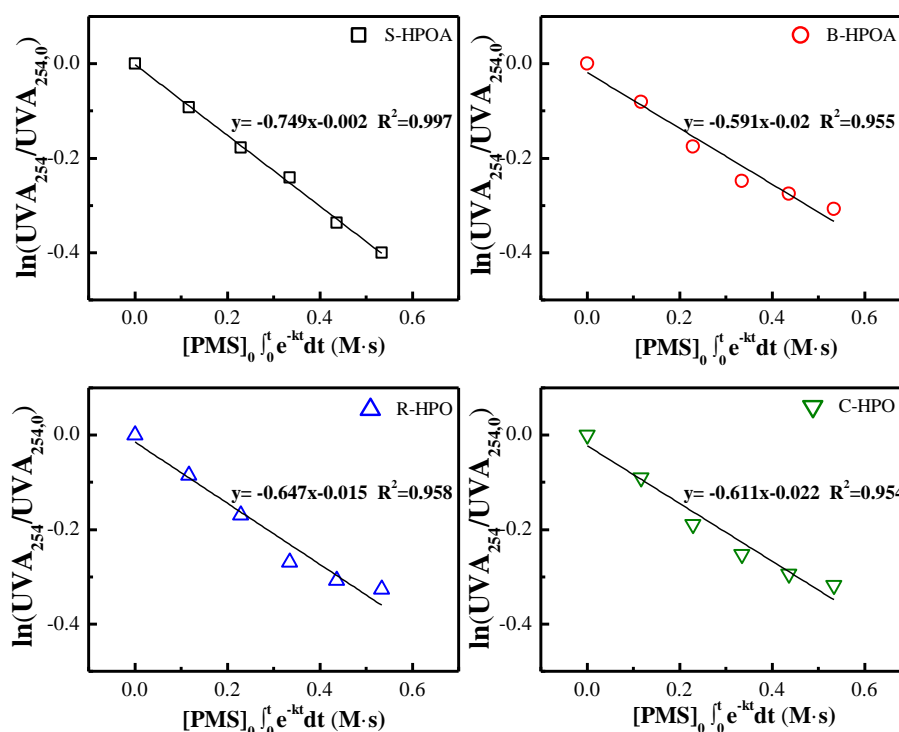


**Figure 2-3. Correlation between  $\text{CDOM}_{\text{fast}}$  decrease and PMS exposure in Co(II)/PMS system. Conditions:  $[\text{PMS}]_0 = 1.00$  mM;  $\text{Co(II)} = 1.00$   $\mu\text{M}$ ;  $[p\text{CBA}]_0$**

**= 1.00  $\mu\text{M}$ ; DOM = 3.90  $\pm$  0.11 mgC/L; pH = 8.00  $\pm$  0.05(10 mM borate buffer);  
T = 20°C**

Interestingly, the reaction rate constants of CDOM<sub>fast</sub> for all DOM fractions were at the same order of magnitude. The highest CDOM<sub>fast</sub> value was recorded for S-HPOA ( $4.59 \times 10^8 \text{ M}^{-1}\text{s}^{-1}$ ), also exhibiting the highest SUVA (4.78). The lowest CDOM<sub>fast</sub> value was observed for C-HPO ( $1.99 \times 10^8 \text{ M}^{-1}\text{s}^{-1}$ ), also showing lowest SUVA (2.14). However, B-HPOA (SUVA: 4.06) showed a lower  $k$  value than R-HPO (SUVA: 3.22), i.e.,  $3.04 \times 10^8 \text{ M}^{-1}\text{s}^{-1}$  versus  $3.48 \times 10^8 \text{ M}^{-1}\text{s}^{-1}$ , respectively. Therefore, the correlation between the reactivity of CDOM<sub>fast</sub> and SUVA of the corresponding DOM fraction would need additional investigation by including a larger pool of DOM fractions. These reaction rate constants were one order of magnitude higher than the data previously reported (i.e.,  $\sim 10^7 \text{ M}^{-1}\text{s}^{-1}$ ). For instance, Lutze et al. (2015a) observed a rate of  $6.8 \times 10^3 \text{ LmgC}^{-1}\text{s}^{-1}$  for humic acid (Depur from Carl Roth) using an indirect kinetic competition method; while Zhou et al. (2017) recorded a rate of  $1.86 \times 10^3 \text{ LmgC}^{-1}\text{s}^{-1}$  for Suwannee River fulvic acid using a direct laser flash photolysis method. The difference could be attributed to the fact that the value in this study was only measured for the conceptually isolated fast reacting moieties (i.e., CDOM<sub>fast</sub>) rather than for the bulk DOM (i.e., a combination of both fast and slow reacting moieties). However, the value was one order of magnitude lower than those reported for aromatic compounds ( $\sim 10^9 \text{ M}^{-1}\text{s}^{-1}$ ) (Fischer et al., 2001; Neta et al., 1977). This difference would be the result of stronger electrosteric repulsion between  $\text{SO}_4^{\bullet-}$  and structurally complex DOM as compared to simpler organic compounds. The higher reactivity of sulfate radicals to CDOM<sub>fast</sub> than to  $\text{OH}^-$  ( $\sim 10^7 \text{ M}^{-1}\text{s}^{-1}$ ) was expected to lead to an insignificant production of  $\cdot\text{OH}$  (Equation 2.2) due to its unfavorable formation kinetics. In addition, CDOM<sub>fast</sub> would be preferred to bulk DOM when evaluating the

scavenging property of dissolved organic matter in  $\text{SO}_4^{\bullet-}$ -based AOPs under lower PMS exposures, where  $\text{CDOM}_{\text{fast}}$  was the major reactive moieties (Figure 2-1).

The use of  $\text{UVA}_{254}$  as a surrogate indicator for the assessment of TOrCs removal efficiency has been extensively studied in ozone- and  $\cdot\text{OH}$ -based AOPs (Gerrity et al., 2012; Li et al., 2017; Rosario-Ortiz et al., 2010). This finding could also support its application in  $\text{SO}_4^{\bullet-}$ -based water treatment processes. The study on TOrCs removal efficiency could be achieved using either: i) the kinetics with second order reaction constants of TOrCs and radical exposure (Equation 2.10), or ii) the correlation established between  $\text{UVA}_{254}$  decrease and contaminants removal (Equation 2.11).

$$\ln \frac{[\text{TOrCs}]}{[\text{TOrCs}]_0} = -k_{\text{SO}_4^{\bullet-}, \text{TOrCs}} \int_0^t \text{SO}_4^{\bullet-} dt = -k_{\text{SO}_4^{\bullet-}, \text{TOrCs}} \ln \frac{[\text{UVA}_{254}]}{[\text{UVA}_{254}]_0} / -k_{\text{SO}_4^{\bullet-}, \text{CDOM}} \quad \text{Equation 2.10}$$

$$\ln \frac{[\text{TOrCs}]}{[\text{TOrCs}]_0} = \text{Slope} \times \ln \frac{[\text{UVA}_{254}]}{[\text{UVA}_{254}]_0} + \text{Intercept} \quad \text{Equation 2.11}$$

As compared to the direct measurement of TOrCs in a full-scale water treatment plant, the indirect monitoring of UV absorbing parameters using spectrophotometer would require lower capital/operating cost as well as time input. Especially, with the use of an on-line spectrophotometer, a quick track of the oxidation efficiency and consequently a rapid adjustment (i.e., oxidant dose or contact time) could also be expected. However, different correlation models should be established for different TOrCs due to the discrepancy in their reactivity. The successful application of this correlation could also be impacted by the fluctuation of water matrices (e.g.,  $\text{HCO}_3^-$ ,  $\text{NO}_3^-$ , or  $\text{Cl}^-$ ) or temperature due to seasonal changes.

The use of UV absorbing indices of humic substances in combination with their fluorescence properties has also been suggested as indicators in ozone-based water

treatment processes (Li et al., 2017). However, similar decreasing trend was observed in the current study between  $UVA_{254}$  and fluorescence intensity with increasing PMS concentration (Text A1-1). Consequently, the  $UVA_{254}$  parameter was sufficient as a single process indicator in this  $SO_4^{\cdot-}$ -based oxidation system.

### 2.3.4 Sulfate radical-induced CDOM transformation

#### 2.3.4.1 EDC decrease as a function of PMS exposures

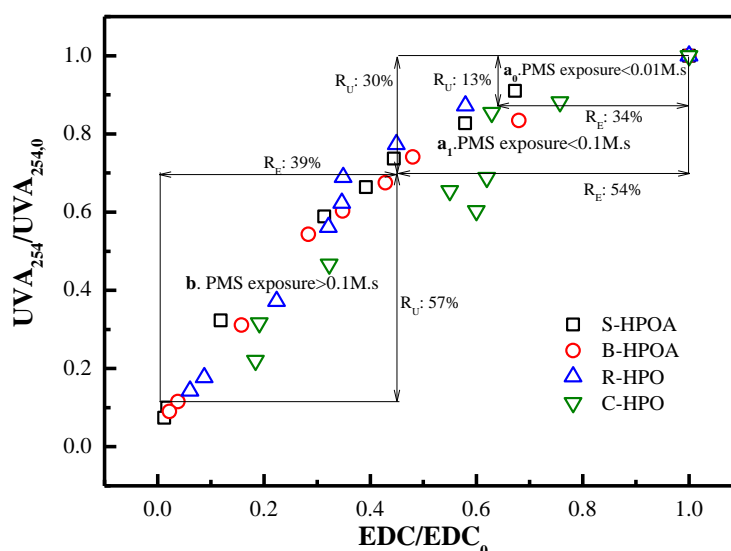


**Figure 2-4. Correlation between normalized  $UVA_{254}$  and EDC decrease of different DOM fractions in Co(II)/PMS reaction system. Conditions: PMS exposure = 0.00–8.04 M·s; Co(II) = 1.00  $\mu$ M; DOM =  $3.90 \pm 0.11$  mgC/L; pH =  $8.00 \pm 0.05$  (10 mM borate buffer); T = 20°C. Areas a<sub>0</sub>, a<sub>1</sub>, and b illustrated the results obtained with a PMS exposure lower than 0.01, lower than 0.1, and larger than 0.1 M·s, respectively. R<sub>E</sub> and R<sub>U</sub> represented the normalized removal efficiency in EDC and  $UVA_{254}$**

Electron donating capacity (EDC) associated with the presence of phenolic structures with different degree of substitution has been previously reported for aquatic humic substances (Aeschbacher et al., 2012). The change in EDC (Figure A1-8) was studied for each DOM fraction under various PMS exposures. The different PMS exposures were obtained by applying varying initial PMS concentrations for the same contact

time (i.e., 20 h) and the calculation of the PMS exposures was detailed in Text A1-2. In addition, the changes in normalized EDC and UVA<sub>254</sub> (Figure A1-9) of the four DOM fractions were plotted in Figure 2-4. This figure shows that for PMS exposures lower than 0.1 M·s (Area a<sub>1</sub>), an average of 54% decrease of EDC was recorded when only a 30% decrease of UVA<sub>254</sub> was observed. For PMS exposures higher than 0.1 M·s (Area b), the averaged normalized UVA<sub>254</sub> decreased from 70% to 13% (i.e., a 57% decrease), whereas the averaged normalized EDC decreased from 46% to 7% (i.e., a 39% decrease). The larger decrease of EDC than UVA<sub>254</sub> at PMS exposure lower than 0.1 M·s in this system indicated that the initial phase of SO<sub>4</sub><sup>•-</sup> reaction was the oxidation of phenolics into quinone-type structures with similar chromophoric properties (Ramseier et al., 2009). This reaction is thermodynamically favourable considering the very low oxidation potential of phenolic structures (0.153–0.620 V) (Bortolomeazzi et al., 2007) and the strong reduction potential of sulfate radicals (2.5–3.1V) (Anipsitakis et al., 2003). A similar observation has been previously reported during the treatment of humic substances by ClO<sub>2</sub> or HClO, where hydroquinone or catechol moieties (i.e., major EDC contributors (Chon et al., 2015)) were proposed as oxidized by HClO through electron transfer rather than electrophilic substitution (Wenk et al., 2013). Interestingly, a more pronounced decrease in EDC than in UVA<sub>254</sub> was observed with a PMS exposure lower than 0.01 M·s (Area a<sub>0</sub>, Figure 2-4), which was probably caused by the relatively higher R<sub>ct</sub> observed under this condition (Figure A1-7).

Due to a major SO<sub>4</sub><sup>•-</sup> consumption by the moieties with EDC at the initial oxidation phase (i.e., PMS exposure < 0.1 M·s), a UVA<sub>254</sub> decrease was not enhanced even under higher radical exposure (i.e., higher R<sub>ct</sub>) (Figure 2-3). This result supported the

selection of lower  $R_{ct}$  values (Figure 2-2) in the calculation of the second-order rate constants of  $CDOM_{fast}$  with  $SO_4^{\bullet-}$  as described in section 2.3.3.

#### 2.3.4.2 TOC removal efficiency at various PMS exposures

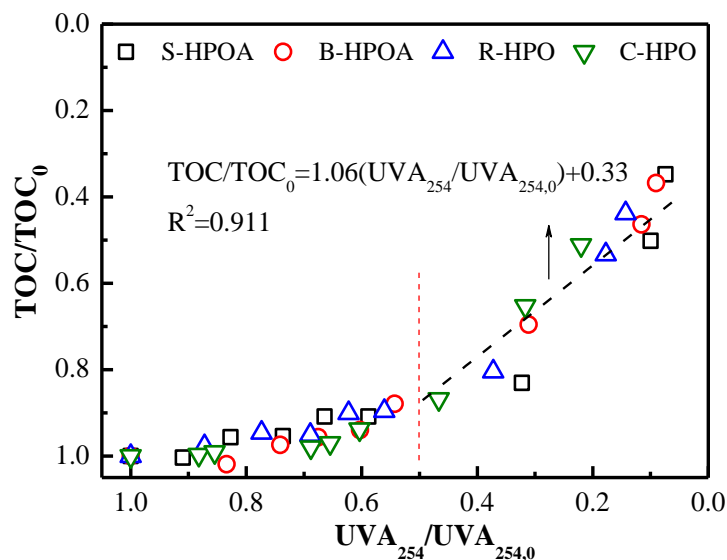


**Figure 2-5. TOC removal as a function of  $UVA_{254}$  decrease. Conditions: PMS exposure = 0.00–8.04 M·s; Co(II) = 1.00  $\mu$ M; DOM =  $3.90 \pm 0.11$  mgC/L; pH =  $8.00 \pm 0.05$  (10 mM borate buffer); T = 20°C. Red dashed line was drawn to differentiate the correlation between  $CDOM_{fast}$  and  $CDOM_{slow}$  with TOC removal**

In order to further explore the transformation of CDOM by sulfate radicals, the TOC content of the solution under different PMS exposures was measured. A significant TOC removal, 64%, 63%, 56%, 49% for S-HPOA, B-HPOA, R-HPO and C-HPO, respectively (i.e., 58% in average), was observed under a PMS exposure of 8.04 M·s (Figure A1-10). The relationship between  $UVA_{254}$  decrease and TOC removal was established and shown in Figure 2-5. Interestingly, the TOC removal was minor (i.e., less 10%) during the depletion of the UV absorbance of  $CDOM_{fast}$  (i.e.,  $UVA_{254}$  decrease within 50%, as indicated by the red dashed line in Figure 2-5). However, the decrease in the chromophoric property of  $CDOM_{slow}$  (i.e., observed when  $UVA_{254}$

decrease was larger than 50%, right side of the red dashed line in Figure 2-5) led to a considerable TOC removal. These results indicated that the reaction of CDOM<sub>fast</sub> would mainly lead to the breakdown of complex aromatic structures into small molecular weight fractions with insignificant mineralization. This transformation from larger molecules to smaller ones was evidenced by the blue shift or band contraction (Chen et al., 2002) in fluorescence emission spectra (Figure 2-6). Specifically, the decrease in the band width at 1/2 maximum fluorescence intensity was calculated as 24 nm, 24 nm, 33 nm, and 88 nm for S-HPOA, B-HPOA, R-HPO, and C-HPO, respectively. In contrast, the reaction of CDOM<sub>slow</sub> would mainly undergo through decarboxylation, which directly led to the observed carbon removal.

Interestingly, a good linearity between UVA<sub>254</sub> decrease and TOC removal during the CDOM<sub>slow</sub> decrease was observed (Figure 2-5). These results indicated that the change in CDOM<sub>slow</sub> could be used in the prediction of TOC removal for surface water during SO<sub>4</sub><sup>•-</sup>-based treatment. This may include water treatment processes targeting the removal of organics, e.g., pretreatment for the removal of disinfection byproducts precursors or membranes foulants, membrane cleaning, and the treatment of reverse osmosis concentrates. Nevertheless, under different water matrices this correlation might be affected by pH conditions, or the presence of radical scavengers HCO<sub>3</sub><sup>-</sup> or Cl<sup>-</sup>.

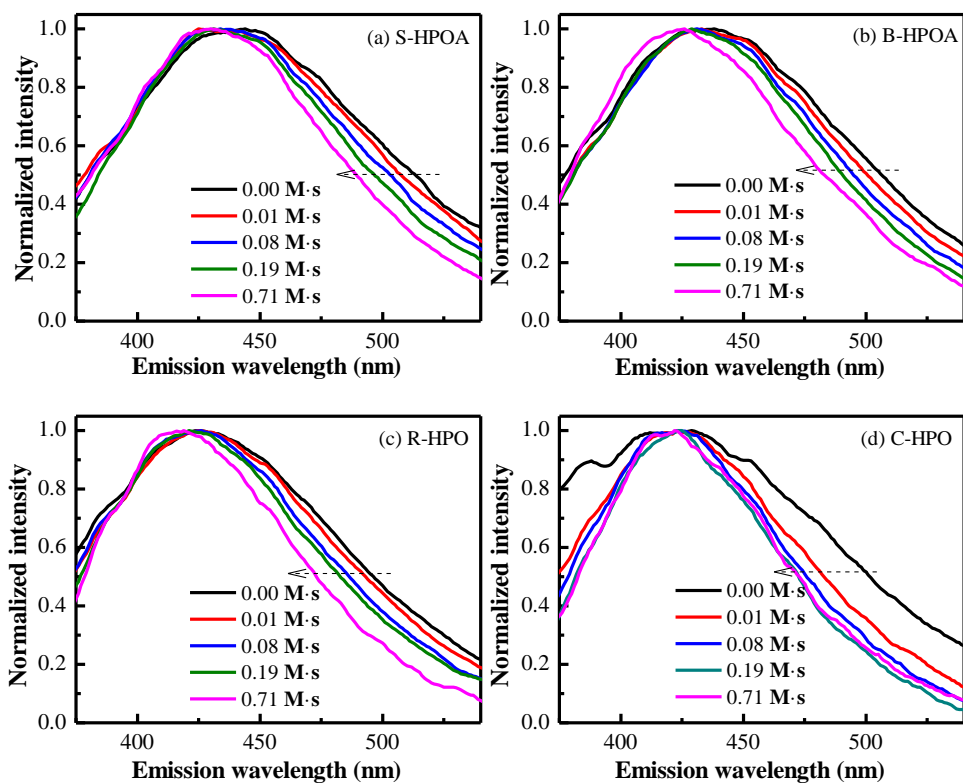


**Figure 2-6. Normalized emission spectra by its respective maximum fluorescence intensity of (a) S-HPOA, (b) B-HPOA, (d) R-HPO, and (d) C-HPO at an excitation wavelength of 230nm. The legend in each figure represented various PMS exposures**

#### 2.3.4.3 Evolution of CDOM transformation with sulfate radical

Based on the findings of this study (i.e., results obtained with the current characterization techniques), the evolution of the transformation of CDOM by sulfate radicals was summarized in Figure 2-7. The  $\text{SO}_4^{\cdot-}$ -induced reaction of  $\text{CDOM}_{\text{fast}}$ , (i.e., electron donating group substituted aromatic structures) was mainly initiated through single electron transfer or addition. The depletion of EDC would initially take place through the electron transfer from phenolic hydroxyl groups to sulfate radical as suggested by Reaction 1. Reaction 2 would produce hydroxylated C-centered radical cations and consequently lead to the formation of ring cleavage products (Anipsitakis et al., 2006). Remarkably, Reaction 4 would take place due to the high electron density

at R<sub>3</sub> site leading to the formation of smaller fluorescent molecules, as suggested by the blue shift of fluorescence emission spectra (Figure 2-6). The production of smaller molecules from complex structures could also be evidenced by the increased fluorescence signal (Figure A1-13) at lower PMS exposure, as the smaller aromatic moieties would be more fluorescent due to weaker intramolecular quenching effect. The decarboxylation of carboxyl groups (Reaction 3), i.e., newly formed or originally incorporated within DOM structures, would be the main reaction mechanism of CDOM<sub>slow</sub> transformation (Madhavan et al., 1978) leading to a significant removal of TOC. However, a more detailed study would be highly recommended for the optimization of process conditions for maximum carbon removal.

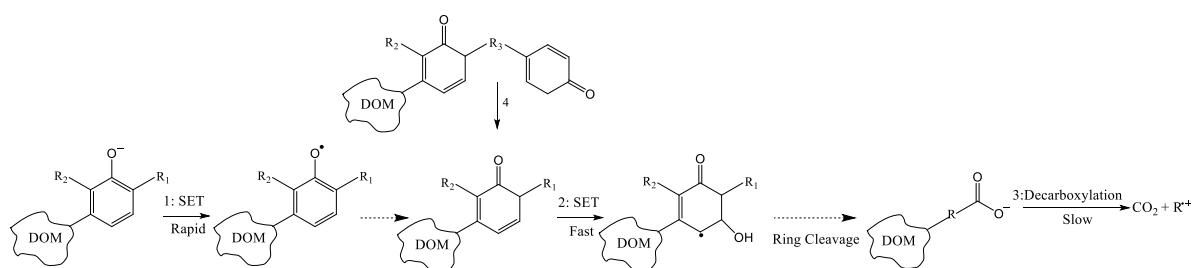


**Figure 2-7. Proposed pathway of sulfate radical-induced DOM transformation**

## 2.4 Summary

The current study provided systematic information on both the reactivity and fate of CDOM with sulfate radical. DOM fractions with different origins and characteristics were used in this investigation. The main conclusions included:

- Fast and slow reacting CDOM could be distinguished within all DOM fractions. Interestingly, the difference in the reactivity of CDOM<sub>fast</sub> among different organics were minor, while the reactivity CDOM<sub>slow</sub> were observed to increase with SUVA.

- The reactivity of CDOM<sub>fast</sub> to SO<sub>4</sub><sup>•-</sup> was calculated at an order of 10<sup>8</sup> M<sup>-1</sup>s<sup>-1</sup> from the observed linear correlation between CDOM<sub>fast</sub> decrease and sulfate radical exposure. The correlation also validated the potential application of UVA<sub>254</sub> as a surrogate indicator for TO<sub>r</sub>Cs removal efficiency.
- A faster decrease of EDC than UVA<sub>254</sub> at lower PMS exposure indicated a preferred oxidation of phenolic structures (i.e., preferential decrease of Electron Donating Capacity). Afterwards, the oxidation of CDOM<sub>fast</sub> would proceed with the formation of transient intermediates and ring cleavage products.
- The transformation products of CDOM<sub>fast</sub> together with the originally less reactive structures, i.e., CDOM<sub>slow</sub>, would undergo slow decarboxylation leading to a significant carbon removal. The linear relationship recorded between CDOM<sub>slow</sub> reduction and TOC removal could be used to predict carbon removal.

The findings in this work would highly assist in the design and operation of SO<sub>4</sub><sup>•-</sup>-based water treatment processes. Specifically, the scavenging capacity of background DOM could be better evaluated using the calculated reactivity of CDOM<sub>fast</sub> if the applied PMS exposure would mainly cause changes in CDOM<sub>fast</sub>. Also, the correlation established between CDOM and radical exposure would shed light on the applicability of UVA<sub>254</sub> as an indicator of TO<sub>r</sub>Cs removal efficiency in SO<sub>4</sub><sup>•-</sup>-based water treatment processes. However, further site-specific studies on the use of UVA<sub>254</sub> as an indicator are highly needed for its successful application.

SO<sub>4</sub><sup>•-</sup>-based advanced oxidation technique could be developed to address the need for DOM removal in varying water treatment scenarios, e.g., pretreatment for the removal

of disinfection by-products precursors or membrane foulants, application of catalytic membrane for organic fouling mitigation, membrane cleaning, or the treatment of reverse osmosis concentrate produced from reclaimed water treatment plants. Also, an increased PMS dose could be applied to increase the reaction rate of  $CDOM_{slow}$  and consequently increase carbon removal. In addition, carbon removal efficiency could be simply estimated based on the removal of  $CDOM_{slow}$  due to the observed good correlation.

# **Chapter 3. Molecular Insights into the Reactivity of Aquatic Natural Organic Matter towards $\cdot\text{OH}$ and $\text{SO}_4\cdot^-$ Using FT-ICR MS**

The contents of Chapter 3 & Appendix 2 are unable to be reproduced here as they are under embargo due to current consideration for publication in the journal *Environmental Science & Technology*.

### 3.1 Introduction

Hydroxyl radical ( $\cdot\text{OH}$ ) or sulfate radical ( $\text{SO}_4^{\cdot-}$ )-based advanced oxidation processes (AOPs) have received considerable research interest worldwide. The vast majority of the studies has focused on the removal of organic micropollutants (Miklos et al., 2018; Nihemaiti et al., 2018; Sun et al., 2019; Yang et al., 2014), while significantly less attention has been directed to the reactivity of natural organic matter (NOM) (Sarathy, 2009; Varanasi et al., 2018). NOM (i.e., the complex and heterogeneous product of decayed biological material) is ubiquitously present and plays multiple critical roles in both engineered and natural aquatic systems (Autin et al., 2013; Cabaniss, 2011; Croué et al., 2000; Guan et al., 2013; Guo et al., 2003; Hem et al., 2001; Le Roux et al., 2016; Lee et al., 2006; Lee et al., 2005; Zafiriou et al., 1984).

According to previous studies, the scavenging capacity of NOM to  $\cdot\text{OH}$  ( $\sim 10^4$  ( $\text{mgC/L})^{-1}\cdot\text{s}^{-1}$ ) is higher than that of  $\text{SO}_4^{\cdot-}$  ( $\sim 10^3$  ( $\text{mgC/L})^{-1}\cdot\text{s}^{-1}$ ) (Lutze et al., 2015a; Westerhoff et al., 2007). The reactivity of radical species with NOM depends on the nature and diversity of the reactive sites (i.e., molecules with specific composition and characteristics) and the reaction pathways (e.g., radical addition, electron transfer, or H-abstraction). Generally, the lower reactivity to  $\text{SO}_4^{\cdot-}$  has been attributed to its high selectivity toward electron-rich moieties and unfavorable/slower reaction with saturated structures (i.e., either through H-abstraction (Lutze et al., 2015a) or decarboxylation (Madhavan et al., 1978)). Nevertheless, additional research is highly required to clearly describe the difference in reactivity, especially with a focus on the reactive sites at the molecular level. Currently, the characterization of NOM in  $\cdot\text{OH}$  or  $\text{SO}_4^{\cdot-}$ -based AOPs has been mainly achieved through measurements of specific properties such as electron donating capacity (EDC), UV light absorbing property ( $\text{UV}_{254}$ ), fluorescent intensity (FI), molecular weight (MW), and total organic content

(TOC) (Sarathy et al., 2008; Zhang et al., 2019). Although these analytical tools provide insight into bulk properties, they prove unsuitable in revealing detailed information at the molecular level.

Ultra-high resolution mass spectroscopy, i.e., Fourier transform ion cyclotron resonance mass spectroscopy (FT-ICR MS), allows the detection of individual molecules within the complex natural organic mixtures based on which exact molecular formulas can be unambiguously assigned). As a result, molecular compositions and molecular characteristics can be readily obtained. This analytical technique has been widely used for the identification of newly-formed disinfection by-products, NOM components adsorbing onto minerals, and molecular characterization of NOM transformation in various processes (Gonsior et al., 2009; Lavonen et al., 2015; Lv et al., 2017; Lv et al., 2016; Varanasi et al., 2018; Yuan et al., 2017; Zhang et al., 2012a; Zhang et al., 2012b) (e.g., coagulation, disinfection, advanced oxidation, biological degradation, or sunlight-induced photochemical reaction). Based on the extensive and successful use of FT-ICR MS in these fields, a molecular-level investigation on the radical-induced reactivity of NOM will considerably advance our fundamental understanding of the preferential molecular target of radicals.

The objective of this investigation was to provide a molecular-level knowledge on the reactivity of NOM towards  $\cdot\text{OH}$  and  $\text{SO}_4^{\cdot-}$  (i.e., generated by UV/H<sub>2</sub>O<sub>2</sub> and UV/PDS, respectively) using FT-ICR MS. The NOM reactivity was investigated by calculating the second-order rate constant of the degradation of UV<sub>254</sub>-absorbing moieties using a modified method as previously reported (Zhang et al., 2019). Rather than analyzing radical-transformed NOM using Orbitrap mass spectrometer (Varanasi et al., 2018), the current study mainly focused on the identification of the reactive molecules susceptible to radical attack and their possible reaction pathways. Also, the analysis of

the bulk properties (i.e., EDC and UV<sub>254</sub>) was conducted. Three NOM isolates from different surface waters and varied physicochemical characteristics were selected. To the best of our knowledge, this is the first comprehensive study to elucidate the distinct reactivity of NOM towards  $\cdot\text{OH}$  and  $\text{SO}_4^{\cdot-}$  at the molecular level.

## **3.2 Materials and Methods**

### **3.2.1 Chemicals and NOM samples.**

Methanol and ethyl acetate of HPLC grade were purchased from Honeywell Burdick & Jackson. Sulfuric acid ( $\text{H}_2\text{SO}_4$ , 98%) and hydrochloric acid ( $\text{HCl}$ , 32%) were supplied by UNIVAR. All the solutions: peroxodisulfate (PDS;  $\geq 98\%$ , Sigma-Aldrich), hydrogen peroxide ( $\text{H}_2\text{O}_2$ , 30%, UNIVAR), p-chlorobenzoic acid (*p*CBA, Acros Organics) and nitrobenzene (NB, Sigma-Aldrich), were prepared with ultrapure water.

Three hydrophobic NOM fractions previously isolated from different surface waters were selected: Hydrophobic acid organic matter extracted from Suwannee River water (S-HPOA, USA), hydrophobic fraction from Ribou Reservoir NOM (R-HPO, France), and hydrophobic fraction from Colorado River (C-HPO, USA). The basic characteristics of the NOM samples were summarized in Table A2-1, Supporting Information (Text A2-1.).

### **3.2.2 UV-AOPs experimental procedure.**

$\cdot\text{OH}$  and  $\text{SO}_4^{\cdot-}$  were generated through UV irradiation of  $\text{H}_2\text{O}_2$  and PDS in unbuffered solutions, respectively. Buffer was not applied in the study to avoid the potential interference caused by the relevant produced radical species (e.g.,  $\text{CO}_3^{\cdot-}$ ). The UV-AOPs experiments were conducted with an LP-UV collimated beam device (CBD). The detailed information on the UV-CBD and the quantification of radical production were provided in the (Text A2-1.).

An incident UV intensity of  $\sim 0.9 \text{ mW}\cdot\text{cm}^{-2}$  was applied to a 250 mL NOM-containing ( $\sim 4 \text{ mgC}\cdot\text{L}^{-1}$ ) solution in a beaker with a diameter of 84 mm. Oxidants ( $\text{H}_2\text{O}_2$  or PDS: 1.0 mM, unless otherwise specified) were individually added into the solutions immediately prior to UV irradiation. The initial UV fluence varied among different NOM-containing solutions due to their difference in UV absorbance at 254 nm, and was calculated as 633, 760, and 886  $\text{mJ}\cdot\text{cm}^{-2}$  for S-HPOA-, R-HPO-, and C-HPO-containing solutions, respectively. A similar initial pH ( $\sim 4.65$ ) was recorded for UV/ $\text{H}_2\text{O}_2$  or UV/PDS experiments. The pH remained relatively stable in the UV/ $\text{H}_2\text{O}_2$  system; however, it decreased by approximately one pH unit in the UV/PDS system after 30 min of irradiation. Samples for FT-ICR MS analysis were acidified to  $\sim \text{pH } 2$  with HCl prior to solid phase extraction (SPE, Text A2-1.). Another set of experiments using 30 mL solution in a petri-dish was conducted to study the reaction pathways taking place for the major reactive molecules (Text A2-1.).

The study on the reactivity of NOM with radicals was performed by the use of *p*CBA and NB as probe compounds under the same experimental conditions as aforementioned. Samples were collected at specific time intervals for probe measurement with the addition of 1 M methanol as a radical quencher. Overall, the  $\cdot\text{OH}$  content was measured as below 10% in the UV/PDS system under all experimental conditions. The change in  $\text{UV}_{254}$  of the NOM solutions with time was immediately recorded without any quencher application. This recorded value was further corrected by subtracting the absorbance of oxidants and probe compounds and the contribution of sole UV irradiation. Specifically, the oxidant residue was analysed through modelling (Xie et al., 2015b) and the concentration of probe compounds were measured using HPLC. The absorbance was calculated using Lambert-Beer law. Specifically, the second-order rate constant of NOM was determined by normalizing

the degradation rate of UV<sub>254</sub>-absorbing moieties with steady-state radical concentration. The calculation of the steady-state radical concentration was detailed in Text A2-1. The samples collected for TOC measurements were acidified to pH ~2 with H<sub>2</sub>SO<sub>4</sub>.

### **3.2.3 FT-ICR MS analysis.**

A 15.0 T superconducting magnet equipped with a Bruker Solarix FT-ICR MS was used to collect the ultra-high-resolution mass spectra. Cartridge-extracted samples were diluted to approximately 500 mg/L with 1:1 methanol/water (v/v). Using a syringe pump at a flow rate of 120  $\mu\text{L}\cdot\text{h}^{-1}$ , the diluted sample was injected into the ESI unit with a voltage of -3.8 kV. An equilibrium time of 0.06 s was set to allow ion accumulation in the hexapole ion trap prior to injection into the ICR cell. A broadband mass scan ranging from 100–1000 Da was conducted, and a total of 200 mass spectra were accumulated per sample. Duplicate measurements were collected for each sample to ensure reproducibility and reliability. The injection syringe and lines were rinsed three times with a 1:1 methanol/water (v/v) solution between each sample injection. A blank sample (i.e., absence of NOM) was extracted and measured to exclude any signal interferences. Further information on data analysis was provided in Text A2-1.

### **3.2.4 Complementary analysis.**

A Cary 60 spectrophotometer (Agilent, USA) was used to measure the UV light absorbance of the NOM solutions at 254 nm (UV<sub>254</sub>). The total organic carbon concentration of the NOM solution was analysed with a Shimadzu TOC-L analyzer (SHIMADZU, Japan). The EDC of NOM samples was measured using a size exclusion chromatography (SEC) coupled with post a column reaction unit and two UV detectors, as previously reported. (Zhang et al., 2019) *p*CBA and NB concentrations were measured with an HPLC unit equipped with a 250 mm × 4.6 mm

C18 5- $\mu\text{m}$  reverse phase column (Alltima<sup>TM</sup>, GRACE) and UV detector (Agilent 1100 series, USA) by recording their absorbances at 238 nm and 270 nm, respectively.

### 3.3 Results and discussion

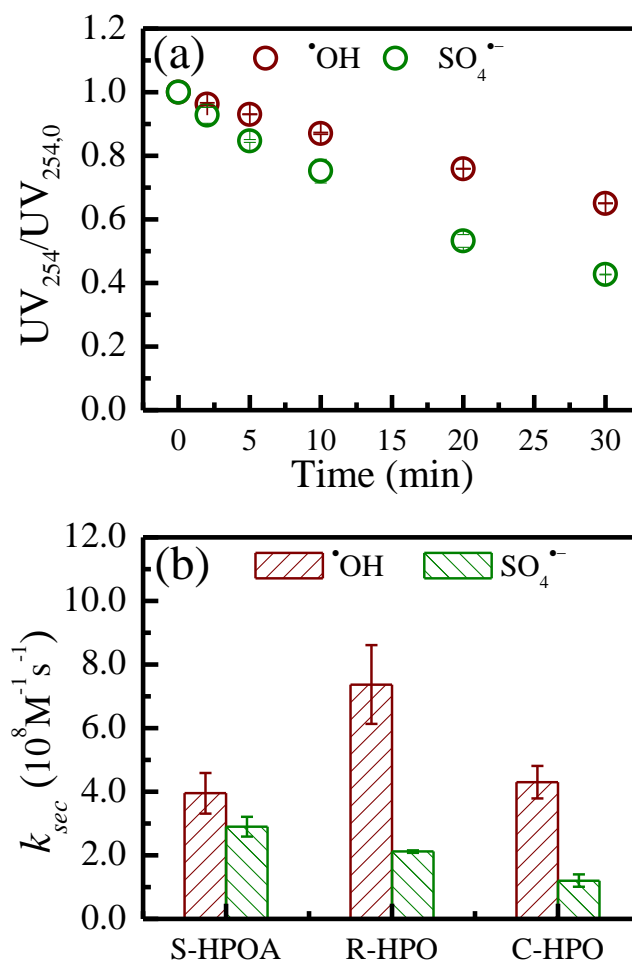


**Figure 3-1.** (a) UV<sub>254</sub> decrease of S-HPOA with time, and (b) second-order rate constants ( $k_{\text{sec}}$ ) of three NOM isolates with  $\cdot\text{OH}$  or  $\text{SO}_4^{\cdot-}$ . Conditions: Incident UV intensity =  $0.9 \text{ mW}\cdot\text{cm}^{-2}$ ,  $[\text{TOC}]_0 = 3.89 \pm 0.18 \text{ mgC}\cdot\text{L}^{-1}$ ,  $[\text{H}_2\text{O}_2]_0$  or  $[\text{PDS}]_0 = 1.0 \text{ mM}$ , at unadjusted pH ( $[\text{pH}]_0 = 4.65 \pm 0.09$ ) and room temperature ( $20^\circ\text{C}$ ).

#### 3.3.1 Reactivity of NOM isolates with radicals.

Due to the highly radical-active nature of chromophoric moieties in the selected NOM fractions (i.e., aromatic or phenolic structures (Fichot et al., 2016)), the reactivity of the NOM samples towards radicals was studied by following the change in UV<sub>254</sub> with

time. At a reaction time of 30 min and for all three NOM isolates (Figure 3-1a and Figure A2-3), the decrease in  $UV_{254}$  was in average 22% higher following  $SO_4^{\bullet-}$  oxidation as compared to that of  $\bullet OH$ , probably due to the higher production yield of  $SO_4^{\bullet-}$  under identical experimental conditions (Table A2-3). To validate a comparison in reactivity, the second-order rate constants ( $k_{sec}$ ) of the chromophores were investigated considering the radical quantity and using a modified method as previously reported (Zhang et al., 2019). Specifically, the rate constants were calculated using the pseudo-first-order rate constants of  $UV_{254}$  decay (Table A2-3) and steady-state radical concentration (Table A2-3). A higher  $k_{sec}$  ( $10^8 M^{-1}s^{-1}$ ) was obtained for  $\bullet OH$  than for  $SO_4^{\bullet-}$ , i.e., 3.955 versus 2.905, 7.372 versus 2.118, and 4.301 versus 1.205 for S-HPOA, R-HPO, and C-HPO, respectively (Figure 3-1b). This trend is in good agreement with those reported by Lutze et al. (2015a), i.e.,  $k(\bullet OH, \text{humic acids}) = 1.4 \times 10^4 L mgC^{-1} s^{-1}$ , and  $k(SO_4^{\bullet-}, \text{humic acids}) = 6.8 \times 10^3 L mgC^{-1} s^{-1}$ . Moreover, the difference in the reactivity between the radicals varied among different NOM isolates. Specifically, the  $k_{sec}$  of  $\bullet OH$  was calculated as 1.4, 3.5, and 3.6-fold of that of  $SO_4^{\bullet-}$  for S-HPOA, R-HPO, and C-HPO, respectively. Overall, the higher reactivity with  $\bullet OH$  than  $SO_4^{\bullet-}$  is in good agreement with the reported higher NOM scavenging capacity of hydroxyl radicals. Consistent with previous findings (Zhang et al., 2019), the reactivity with  $SO_4^{\bullet-}$  increased with the SUVA of untreated NOM samples (Table A2-1). However, no correlation could be established for  $\bullet OH$ , probably because  $\bullet OH$  could also non-selectively reacts with less electron-rich moieties. Interestingly, the TOC removal was negligible with  $\bullet OH$  oxidation (~10%) within 30 min, while a removal efficiency of approximately 35%, 48%, 43% for S-HPOA, R-HPO, and C-HPO, respectively, was achieved with  $SO_4^{\bullet-}$  oxidation (Figure A2-4). To

further study these observations, a molecular-level investigation was conducted for NOM samples with a reaction time of 30 min using FT-ICR MS.

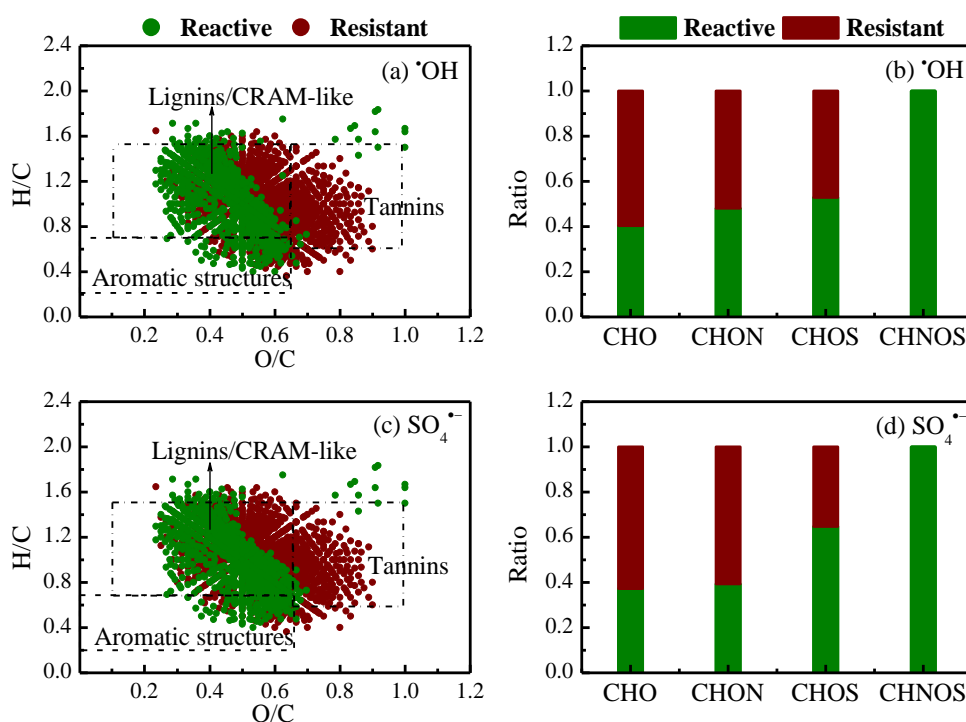


**Figure 3-2. (a, c) van Krevelen diagrams and (b, d) molecular compositions of S-HPOA after  $\cdot\text{OH}$  or  $\text{SO}_4^{\cdot-}$  treatment. The olive points/bars represent the radical-reactive moieties (formulas that disappeared after reaction), and wine points/bars reflect the radical-resistant structures (formulas remaining unchanged after reaction).**

### 3.3.2 Identification of reactive molecules.

The molecular formulas assigned through FT-ICR MS analysis for the untreated and the oxidized NOM fractions were compared to identify the radical-reactive moieties (formulas that disappeared after reaction) and radical-resistant moieties (formulas remaining unchanged after reaction) present in the three NOM isolates. Approximately 40%–50% of the total assigned formulas were identified as reactive, contributing to 15%–20% of the overall signal intensity (Table A2-4). The molecules also showing reactive to sole UV irradiation (ca. 20%) were not included in the following discussion due to the focus on  $\cdot\text{OH}$  or  $\text{SO}_4^{\cdot-}$  reaction of the current study. The distribution of the

reactive and resistant molecules was visualized in van Krevelen diagrams based on their respective H/C and O/C ratios (Figure 3-2). As shown in Figure 3-2a and Figure 3-2c, the majority of the reactive molecules within S-HPOA were assigned to lignins/carboxyl-rich alicyclic moieties (CRAM)-like structures, accounting for 83% and 82% in  $\cdot\text{OH}$ - and  $\text{SO}_4^{\cdot-}$ -based AOPs, respectively. Similar results were obtained with the other two NOM isolates, i.e., R-HPO and C-HPO (Figure A2-5 and Figure A2-6).

Higher removal efficiency was observed for aromatics and lignins/CRAM-like structures with  $\text{SO}_4^{\cdot-}$  oxidation (i.e., the ratio of reactive aromatics and lignins/CRAM-like structures to total assigned molecules of untreated NOM) (Table A2-5), and was consistent with the recorded higher decrease in  $\text{UV}_{254}$  (Figure 3-1). Moreover, the weight-averaged values (Equation A2-6–Equation A2-7) for various molecular characteristics (i.e.,  $m/z_{\text{wa}}$ ,  $\text{DBE}_{\text{wa}}$ ,  $\text{H/C}_{\text{wa}}$ , and  $\text{O/C}_{\text{wa}}$ ) between reactive and resistant molecules were calculated and compared (Table A2-6). The reactive molecules exhibited higher  $m/z_{\text{wa}}$ ,  $\text{C}_{\text{wa}}$ , and  $\text{DBE}_{\text{wa}}$ , but lower  $\text{H/C}_{\text{wa}}$  and  $\text{O/C}_{\text{wa}}$  as compared to resistant molecules (Table A2-6). Generally, the results indicated that larger molecules with a higher degree of unsaturation and electron density were more susceptible to  $\cdot\text{OH}$  and  $\text{SO}_4^{\cdot-}$  attacks. The  $\text{DBE}_{\text{wa}}$  of  $\text{SO}_4^{\cdot-}$  reactive molecules was the highest for S-HPOA (14.69, Table A2-6), also exhibiting the highest reactivity. However, the lowest  $\text{DBE}_{\text{wa}}$  of  $\text{SO}_4^{\cdot-}$  reactive molecules was observed with C-HPO (11.55, Table A2-6), also associated with the lowest reactivity (Figure 3-1). Interestingly, the molecules of S-HPOA reactive to  $\cdot\text{OH}$  were characterized by the highest  $\text{DBE}_{\text{wa}}$  (Table A2-6); however, the rate constant of the reaction between  $\cdot\text{OH}$  and S-HPOA was the lowest among the three NOM isolates (Figure 3-1). The highest reactivity was observed with R-HPO (Figure 3-1), showing a medium  $\text{DBE}_{\text{wa}}$  value for the reactive molecules

(Table A2-6). This result is probably associated with the molecular size of the reactive molecules within R-HPO; for instance, the  $m/z_{wa}$  (481.06) and  $C_{wa}$  (22.99) values of its reactive molecules were the lowest as compared to S-HPOA (537.65/26.13) or C-HPO (518.13/25.18) (Table A2-6). The correlation between the reactivity of NOM fractions and molecular size has been previously documented (Dong et al., 2010) where the reactivity increased with decreasing molecular size.

In addition, the reactive and resistant molecules were also plotted based on their molecular compositions, i.e., CHO, CHON, CHOS, and CHONS (Figure 3-2b and Figure 3-2d). Molecules only containing CHO (an average removal efficiency of 39%) were less reactive than those also containing N and S (an average removal efficiency of 44%, 59%, and 100% for CHON, CHOS, and CHONS, respectively). This trend was further confirmed by a similar observation for the other two N- or S-enriched NOM isolates, i.e., R-HPO and C-HPO (Figure A2-5 and Figure A2-6). Consistent with previous findings (Varanasi et al., 2018), these results indicated that molecules incorporating N- or S-containing functional groups (e.g.,  $-NH_2$ ,  $-NH-$ , or  $-S-$ ) are more reactive to both radical species (Yang et al., 2017; Ye et al., 2017). The increase in the reactivity caused by the presence of S or N would explain the observed trend in  $\cdot OH$ -induced reactivity (Figure 3-1). Besides the influence of molecular size, the highest reactivity of R-HPO to  $\cdot OH$  could also be attributed to the largest fraction of N- or S-containing reactive molecules, accounting for approximately 47% (Table A2-7). Similarly, the lower reactivity of S-HPOA, as compared to C-HPO, could be a result of the lower content of N or S in its reactive molecules (6% versus 37%, Table S7).

### 3.3.3 Exclusively reactive molecules.

#### 3.3.3.1 H/C.

The molecules degraded by  $\cdot\text{OH}$  and  $\text{SO}_4^{\cdot-}$  radicals were compared to identify specific reactive sites. The molecules that only reacted with  $\cdot\text{OH}$  or  $\text{SO}_4^{\cdot-}$  radicals accounted for approximately 10–20% of the total reactive molecules. The  $\text{H}/\text{C}_{\text{wa}}$  of the molecules only reactive towards  $\cdot\text{OH}$  were higher than that of  $\text{SO}_4^{\cdot-}$ , with the largest difference observed with S-HPOA (1.11 versus 0.86), medium difference with R-HPO (1.06 versus 1.02), and smallest difference with C-HPO (1.03 versus 1.02) (Table A2-8). To further elucidate the difference in the  $\text{H}/\text{C}_{\text{wa}}$  of exclusively reactive molecules, the respective number of reactive molecules located in Area I (i.e., with higher H/C: 1.2–1.6 and lower O/C: 0.2–0.5, Figure 3-3) were compared. Specifically, the percentage of molecules in Area I exclusively reactive towards  $\text{SO}_4^{\cdot-}$  was only 19% for S-HPOA and 33% for C-HPO, respectively. Interestingly, the exclusively  $\text{SO}_4^{\cdot-}$ -reactive molecules were more abundant in this region for R-HPO (i.e., up to 63%, Figure 3-3). However, the  $\text{DBE}_{\text{wa}}$  of the molecules exclusively reactive to  $\text{SO}_4^{\cdot-}$  (9.54) in Area I was higher than that of  $\cdot\text{OH}$  (7.86). The observation is in agreement with the high affinity of  $\text{SO}_4^{\cdot-}$  with electron-rich molecules. In addition, molecules exclusively reactive to  $\cdot\text{OH}$  falling in the same Area I were observed as more aliphatic, clearly indicated by their lower  $\text{DBE}_{\text{wa}}$  compared to the value determined for the total exclusively reactive molecules (i.e., 8.36 versus 10.86, 7.86 versus 11.06, and 6.69 versus 10.47 for S-HPOA, R-HPO, and C-HPO respectively, Table A2-8). The results indicated the intrinsic difference in reactive sites between the two radicals regardless of radical concentrations. Specifically,  $[\text{SO}_4^{\cdot-}]_{\text{ss}}$  was higher than  $[\cdot\text{OH}]_{\text{ss}}$  (Table A2-3) under identical experimental conditions arising from the higher quantum yield of PDS than  $\text{H}_2\text{O}_2$  (He et al., 2013). Due to a negligible carbon removal (Figure A2-4), a

reaction pathway of H-abstraction (Westerhoff et al., 2007) would be highly possible following the preferential targeting of these more aliphatic structures (i.e., molecules with higher H/C ratio and lower DBE) by  $\cdot\text{OH}$ . To test this hypothesis, the change in the  $\text{H}/\text{C}_{\text{wa}}$  of the produced molecules was also investigated. The produced molecules were only those extractable with SPE, partially representing the complete pool of produced species due to a decreased extraction efficiency following radical oxidation (i.e., 89%, 78%, and 56% for untreated S-HPOA,  $\cdot\text{OH}$  and  $\text{SO}_4^{\cdot-}$  treated samples, respectively). The newly formed molecules were characterized by a lower  $\text{H}/\text{C}_{\text{wa}}$  (5–10%, Table A2-9) in the  $\cdot\text{OH}$  oxidation system as compared to that in the  $\text{SO}_4^{\cdot-}$  oxidation system. This observation is supporting the hypothesis of a more prevalent H-abstraction from NOM molecules by  $\cdot\text{OH}$  than  $\text{SO}_4^{\cdot-}$ .

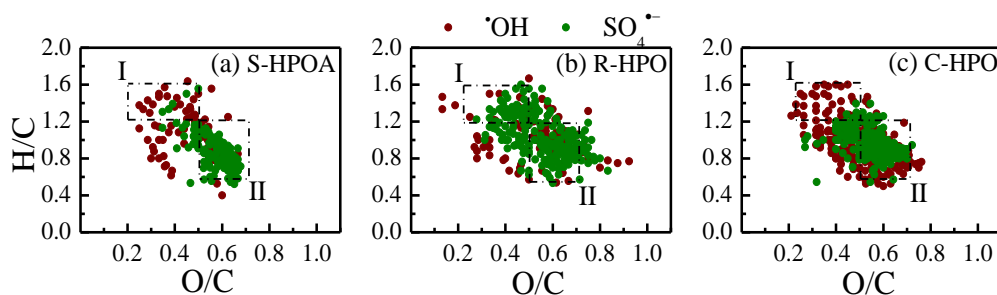


**Figure 3-3. van Krevelen diagram of molecules exclusively reactive to  $\cdot\text{OH}$  or  $\text{SO}_4^{\cdot-}$  within (a) S-HPOA, (b) R-HPO, and (c) C-HPO. Red points denote molecules exclusively reactive to  $\cdot\text{OH}$ ; while olive points denote molecules exclusively reactive to  $\text{SO}_4^{\cdot-}$ .**

### 3.3.3.2 O/C.

The  $\text{O}/\text{C}_{\text{wa}}$  of molecules exclusively reactive to  $\text{SO}_4^{\cdot-}$  was 10–22% higher than that of  $\cdot\text{OH}$  (Table A2-8). For instance, a larger fraction of molecules (i.e., 83%, 74%, and 75% for S-HPOA, R-HPO, and C-HPO respectively) located in Area II (higher O/C: 0.5–0.7, and lower H/C: 0.7–1.2, Figure 3-3) were observed to exclusively react with  $\text{SO}_4^{\cdot-}$ . Because the molecules were categorized as lignins/CRAM-like structures, one

of the probable contributors to the higher O/C would be the carboxyl group ( $-\text{COOH}$ ). Therefore, Kendrick Mass Defect (KMD) of homologous series with  $-\text{COOH}$  base (Sleighter et al., 2007), i.e., KMD (COO), were calculated (Equation A2-8–Equation A2-10) and plotted against the number of oxygen atoms (Figure 3-4, Figure A2-7). The results showed that the molecules exclusively reactive to  $\text{SO}_4^{\bullet-}$  presented a higher degree of  $-\text{COOH}$  functionalization than the  $\bullet\text{OH}$ -reactive compounds. For these reactive sites, a reaction pathway of  $\text{SO}_4^{\bullet-}$ -induced decarboxylation would be expected. Specifically,  $\text{SO}_4^{\bullet-}$  preferentially targeted the carboxyl-rich molecules, followed by decarboxylation, and eventually leading to higher carbon removal (i.e., as compared to  $\bullet\text{OH}$ , Figure 3-1b). For the exclusively reactive sites, the faster H-abstraction by  $\bullet\text{OH}$  ( $10^8\text{--}10^9 \text{ M}^{-1}\cdot\text{s}^{-1}$ ) (Buxton et al., 1988) than decarboxylation by  $\text{SO}_4^{\bullet-}$  ( $10^6\text{--}10^9 \text{ M}^{-1}\cdot\text{s}^{-1}$ ) (Neta et al., 1977) could explain the higher reactivity of NOM to  $\bullet\text{OH}$ . Instead of a decrease in the  $\text{O}/\text{C}_{\text{wa}}$  of the extractable produced molecules highly expected due to decarboxylation, an increase was observed (Table A2-9). This increase could be attributed to the prevalence of hydroxylation in radical oxidation processes. Interestingly, the  $\text{O}/\text{C}_{\text{wa}}$  of extracted produced molecules by  $\text{SO}_4^{\bullet-}$  oxidation was even higher than that of  $\bullet\text{OH}$ . The higher  $\text{O}/\text{C}_{\text{wa}}$  could probably correlate with the detection of assigned S-containing molecules, probably formed through  $\text{SO}_4^{\bullet-}$  addition. However, further investigation is necessary to confirm this hypothesis. The molecular formula assignment remains a challenge in the analysis of FT-ICR MS data, especially with the inclusion of non-oxygen heteroatoms (i.e., S, N) and the increase of molecular mass (Herzprung et al., 2016; Ohno et al., 2013). The investigation on the transformation of single model compound with  $\text{SO}_4^{\bullet-}$  might be able to provide additional insights. However, the possible reaction pathway through  $\text{SO}_4^{\bullet-}$  addition was not further discussed as not being the focus of this investigation.

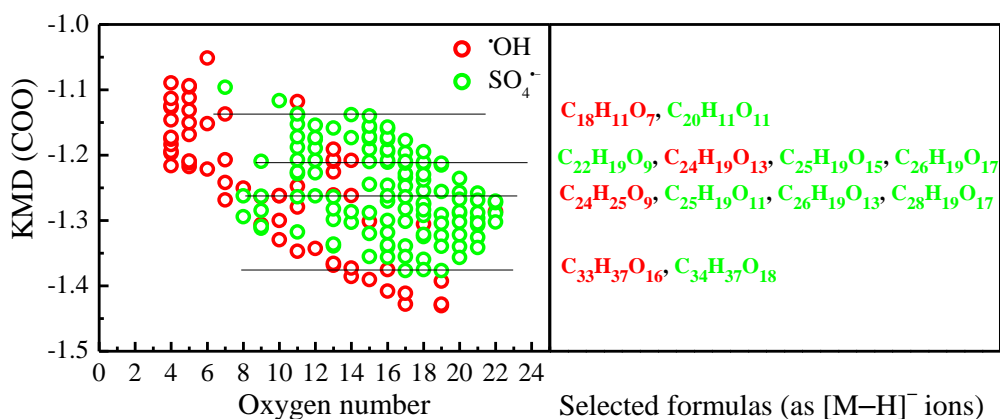


**Figure 3-4. KMD (COO) of molecules exclusively reactive with  $\cdot\text{OH}$  or  $\text{SO}_4^{\cdot-}$  as a function of oxygen number in the NOM isolate of S-HPOA. The selected molecular formulas were presented as an illustration.**

### 3.3.3.3 DBE.

A higher value of  $m/z_{\text{wa}}$ ,  $C_{\text{wa}}$ , and  $\text{DBE}_{\text{wa}}$  were observed with molecules exclusively reactive to  $\text{SO}_4^{\cdot-}$  (563.80, 25.88, and 15.66 for S-HPOA) as compared to those of  $\cdot\text{OH}$  (447.53, 21.87, and 10.86 for S-HPOA) (Table A2-8). The difference in DBE is also be illustrated in Figure 3-5, Figure A2-8, and Figure A2-9, where DBE was plotted against the number of carbon atoms with reference to the O/C ratio. Specifically, the DBE of the vast majority of molecules exclusively reactive to  $\cdot\text{OH}$  was lower than the  $\text{DBE}_{\text{wa}}$  of the molecules exclusively reactive towards  $\text{SO}_4^{\cdot-}$  (15.66 for S-HPOA), as illustrated by the black dash line in Figure 3-5. Interestingly, the larger value of DBE (i.e., larger than 15.66 in Figure 3-5b) were contributed by molecules with a larger number of carbon atoms (i.e., 20–37). Theoretically, the oxidation of  $\text{SO}_4^{\cdot-}$  towards larger molecules (i.e., with larger number of carbon atoms) was unfavorable due to the higher electrosteric repulsion phenomenon between the two (Baalousha et al., 2018; Shen et al., 2015). These findings demonstrated the critical role of electron density in  $\text{SO}_4^{\cdot-}$  reaction (as reflected by DBE), where the high electron density of a molecule would counterbalance the steric repulsion and successfully trigger  $\text{SO}_4^{\cdot-}$  oxidation. The current results clearly showed that molecules with higher DBE and  $m/z$  or C

number, and higher O/C were preferentially degraded by  $\text{SO}_4^{\bullet-}$ . The involvement of larger size molecules with high electron density during  $\text{SO}_4^{\bullet-}$  oxidation would be expected to slow down the reaction (Dong et al., 2010), in accordance with the observed lower reactivity. Interestingly, the molecules produced through  $\text{SO}_4^{\bullet-}$  oxidation exhibited lower  $\text{DBE}_{\text{wa}}$ ,  $m/z_{\text{wa}}$ , or  $C_{\text{wa}}$  than those generated with  $\cdot\text{OH}$  (Table S9), indicating a higher degree of oxidation by  $\text{SO}_4^{\bullet-}$  and consistent with the more significant  $\text{UV}_{254}$  decrease (Figure 3-1a). However, since the exclusively reactive molecules only account for 10–20% of total reactive molecules, distinct reaction pathways associated with shared (major) reactive sites would also be expected to shape the different reactivity between NOM and the radicals. Therefore, the reaction pathways of the major reactive sites were explored in the following section.

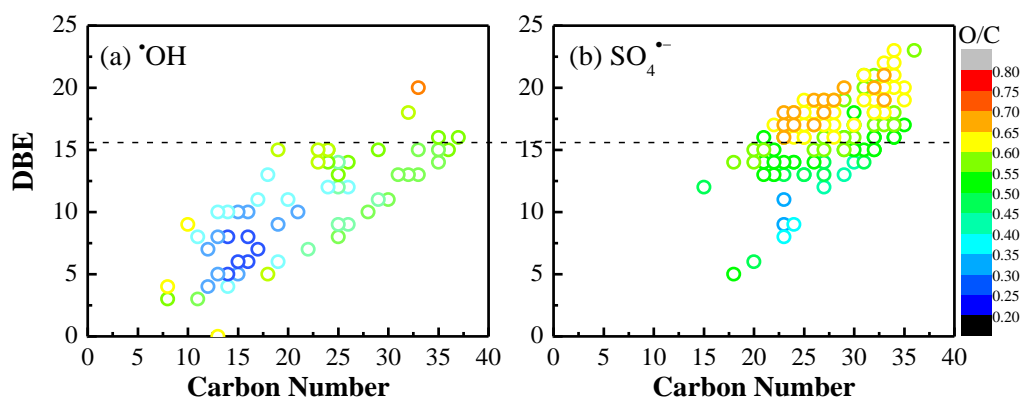


**Figure 3-5. DBE of molecules exclusively reactive to (a)  $\cdot\text{OH}$  or (b)  $\text{SO}_4^{\bullet-}$  as a function of number of carbon atoms based on O/C in S-HPOA. The dashed line indicates the comparison at a DBE value of 15.66 ( $\text{DBE}_{\text{wa}}$  of the molecules exclusively reactive to  $\text{SO}_4^{\bullet-}$ )**

### 3.3.4 Reaction pathways of major reactive molecules.

Lignins (i.e., as predominant reactive molecules in both reaction processes, Figure 3-2a and Figure 3-2c) have been reported as the primary contributors to both UV-light absorbing property and the electron-donating capacity (EDC) of NOM (Aeschbacher et al., 2012; Wenk et al., 2013). The changes in EDC and  $\text{UV}_{254}$  (UV light absorbance

at 254 nm) of the three NOM isolates were measured. Both EDC and  $UV_{254}$  values, in all three NOM isolates, were more efficiently depleted by  $SO_4^{\bullet-}$  than  $\bullet OH$  (Figure A2-10). To differentiate the reaction pathways, changes in EDC and  $UV_{254}$  were further explored by plotting the normalized EDC decrease versus the corresponding normalized  $UV_{254}$  decay (Figure 3-6). In  $\bullet OH$ -based AOPs, the EDC of R-HPO and C-HPO decreased slower than  $UV_{254}$ ; contrariwise, a slightly faster decrease in EDC was observed for S-HPOA (Figure 3-6a). Interestingly, a faster decrease in EDC than in  $UV_{254}$  was recorded with all three NOM isolates in  $SO_4^{\bullet-}$ -based AOPs (Figure 3-6b). The discrepancy in the EDC- $UV_{254}$  correlations between these radical-based AOPs indicated a difference in reaction pathways. Specifically, the  $SO_4^{\bullet-}$  reaction was initiated with one electron transfer from phenolic  $-OH$  moieties leading to the oxidation of phenolic structures, while the UV light absorbing property was preserved (Zhang et al., 2019). The  $\bullet OH$  reaction would lead to the destruction of aromatic moieties; however, the preservation of phenolic structures probably involved a radical addition to nonphenolic aromatic moieties (Neta et al., 1974). Consequently, the higher reaction rate of  $\bullet OH$  radical addition (diffusion limited) (Buxton et al., 1988) than electron transfer to  $SO_4^{\bullet-}$  ( $10^6$ – $10^9$   $M^{-1}\cdot s^{-1}$ ) (Neta et al., 1977) would lead to the higher reactivity of NOM to  $\bullet OH$ .

The slightly faster decrease of EDC than  $UVA_{254}$  observed with S-HPOA in the presence of  $\bullet OH$  (i.e., an opposite trend from R-HPO and C-HPO) was probably caused by its higher degree of aromatic substitution as suggested by the higher SUVA and EDC values (Table A2-1). As a consequence, the oxidation of phenolic structures would be predominant due to the lower available sites for radical addition. This result could also explain the smaller difference in the reactivity between  $\bullet OH$  and  $SO_4^{\bullet-}$  for S-HPOA as compare to R-HPO or C-HPO (Figure 3-1).

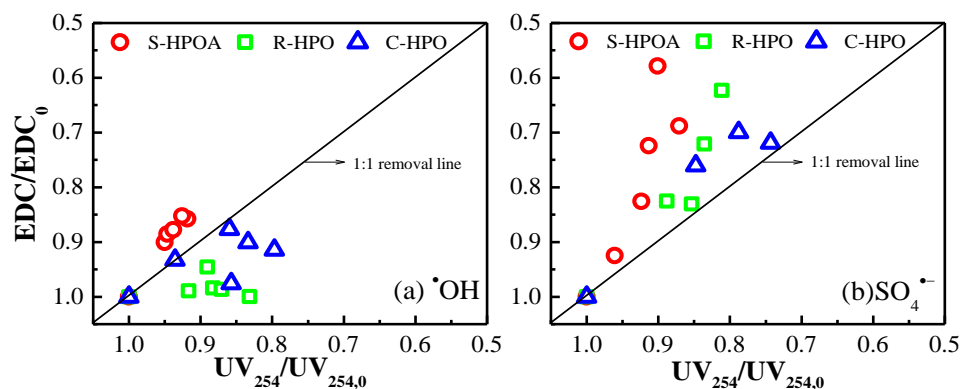


**Figure 3-6. Relationship between normalized UVA<sub>254</sub> and EDC decrease of different NOM isolates in (a)  $\cdot\text{OH}$  and or (b)  $\text{SO}_4^{\cdot-}$  reaction processes. Conditions: Incident UV intensity =  $0.9 \text{ mW}\cdot\text{cm}^{-2}$ ,  $[\text{TOC}]_0 = 3.89 \pm 0.18 \text{ mgC}\cdot\text{L}^{-1}$ , and  $[\text{H}_2\text{O}_2]_0$  or  $[\text{PDS}]_0 = 0.00\text{--}0.10 \text{ mM}$ , at unadjusted pH ( $4.65 \pm 0.09$ ) and room temperature ( $20^\circ\text{C}$ ).**

### 3.4 Summary

The current study significantly advanced our fundamental knowledge on the reactivity of NOM with radical species through the identification of  $\cdot\text{OH}$ - and  $\text{SO}_4^{\cdot-}$ - reactive sites using an ultrahigh resolution FT-ICR MS. Understanding the reactivity and changes in the molecular composition of NOM with  $\cdot\text{OH}$  or  $\text{SO}_4^{\cdot-}$ -based treatment is useful to predict its behavior in engineered and natural aquatic systems. For instance, the photoreactivity of NOM could be decreased after reaction with  $\cdot\text{OH}$  or  $\text{SO}_4^{\cdot-}$  because molecules with higher DBE (i.e., which are preferentially degraded) were reported as more photoreactive (Gonsior et al., 2009). A proper radical-based treatment strategy for the degradation of target sites in complex organic matrices could be more efficiently implemented. For example,  $\text{SO}_4^{\cdot-}$ -based oxidation process could be adopted for the decrease of carboxyl-rich molecules (e.g. removal of membrane foulants (Lin et al., 2001)) because of its observed higher affinity to  $-\text{COOH}$ ; while  $\cdot\text{OH}$ -based oxidation process could be selected for the removal of organics with abundant aliphatic structures.

The structures of the molecules are yet to be confirmed, although their formulas have been unambiguously assigned. More complex water matrices representing natural waters (i.e., containing  $\text{Cl}^-$ ,  $\text{HCO}_3^-$ , or varying pH conditions) should also be considered in future studies. Besides, extending this study to a larger pool of NOM isolates (i.e., various origins and molecular composition) would refine and extent our knowledge on the selective reactivity of radicals with NOM molecules.

## **Chapter 4. Organic Matter interfacial interactions with MnO<sub>2</sub> and its influence on catalytic oxidation processes**

Suona Zhang, Leonardo Gutierrez, Xi-Zhi Niu, Fei Qi and Jean-Philippe Croué

Chemosphere, Volume 209, October 2018, Pages 950–959

<https://doi.org/10.1016/j.chemosphere.2018.06.145>

## 4.1 Introduction

Manganese (Mn) oxides occur in the environment due to biological activity and weathering of Mn-containing minerals (Post, 1999). Due to their structures and chemical reactivity, these naturally abundant metal oxides as well as their synthetic counterparts exhibit a high potential as absorbents, oxidants, catalysts, and cation exchange reagents in aquatic systems (Driehaus et al., 1995; Golden et al., 1986; Whitney, 1975). MnO<sub>2</sub> (i.e., one of the most common Mn oxides) participates in a wide range of processes leading to the transformation of organic contaminants and heavy metals, and has also gained attention as a catalyst due to its environmentally friendly and ubiquitous nature (Barrett et al., 2005; Tong et al., 2003; Zhang et al., 2013). These catalytic oxidation processes have been reported to degrade contaminants by the generation of reactive species when used in combination with oxidants, e.g., peroxymonosulfate (PMS), hydrogen peroxide (H<sub>2</sub>O<sub>2</sub>), and ozone (O<sub>3</sub>) (Saputra et al., 2013; Tong et al., 2003; Yu et al., 2014). Recently, MnO<sub>2</sub> has been tested as a ceramic membrane coating material. Catalytic processes occurring at MnO<sub>2</sub> surface generated reactive species responsible for foulants oxidation (Corneal et al., 2011; Corneal et al., 2010).

Interestingly, the ubiquitous presence of dissolved organic matter (i.e., DOM, a highly heterogeneous mixture of organic compounds of different chemical compositions, structures, and properties) exerts a significant impact on MnO<sub>2</sub>-participated processes (e.g., adsorption, oxidation, or catalysis) in both engineered and natural aquatic systems (Chen et al., 2002). For instance, DOM interfacial interactions with MnO<sub>2</sub> have been proposed to decrease the reaction rate of MnO<sub>2</sub> with pollutants. Specifically, DOM adsorption on MnO<sub>2</sub> would lead to a change in surface properties and to a decrease in available reactive sites (Feitosa-Felizzola et al., 2009; Zhang et al., 2003).

Remarkably, a preferential adsorption of high molecular weight organics enriched in aromatic moieties has been observed for synthetic and natural manganese oxides, where hydrophobic interactions were proposed as the dominant interacting mechanism (Allard et al., 2017). In addition, DOM would cause a drastic impact on the aggregation behaviour of MnO<sub>2</sub> nanoparticles in solution.

The influence of DOMs on the aggregation of (nano)particles, e.g., silver, gold, TiO<sub>2</sub>, aluminum oxide, iron oxide, and carbon nanotubes, have been extensively studied (Domingos et al., 2009; Furman et al., 2013; Ghosh et al., 2008; Liu et al., 2013; Saleh et al., 2010; Vindedahl et al., 2016). Briefly, DOM has been proposed to induce the stability of nanoparticles in solution by electrostatic and steric mechanisms. Conversely, DOM can also induce enhanced aggregation through the formation of hydrogen bonds between hydroxyl groups-enriched organic fractions, or by (multivalent) cation bridging mechanisms (Boyle et al., 1989; Shen et al., 2015). MnO<sub>2</sub> particles have been reported to readily aggregate in aqueous environments due to collision arising from Brownian diffusion and subsequent attachment controlled by Derjaguin-Landau-Verwey-Overbeek (DLVO) interactions (Hotze et al., 2010). Also, these particles were significantly stabilized by model constituents of humic substances (Suwannee River humic acid SR-HA and fulvic acid SR-FA) and non-humic substances (alginate and bovine serum albumin BSA). This enhanced stability was attributed to steric repulsion resulting from the adsorption of DOMs onto MnO<sub>2</sub> surface (Huangfu et al., 2013). Nevertheless, DOM composition and properties are highly variable and dependent on their origins; thus, the DOMs tested in previous investigations (e.g., alginate, BSA, SR-FA, and SR-HA) were far from representative of all natural DOMs due to the heterogeneity and complexity of the latter (Leenheer et al., 2003). Therefore, the use of DOMs isolated from different water sources would

provide a deeper insight into the interfacial interactions of MnO<sub>2</sub> with organic matter in natural aquatic environments and water treatment systems.

The objective of this investigation was to study the influence of organic matter characteristics on its interfacial interactions with MnO<sub>2</sub> and on catalytic oxidation processes. Four DOM fractions with different structural properties previously isolated from raw and treated surface waters and from a treated urban wastewater were selected. Time-Resolved Dynamic Light Scattering (TR-DLS) technique was selected to study the aggregation of MnO<sub>2</sub> nanoparticles in DOM-containing electrolyte solutions. Due to its sensitivity at a sub-nano Newton resolution, Atomic Force Microscopy (AFM) in contact mode was used to investigate the interaction forces between MnO<sub>2</sub> and DOMs. Also, H<sub>2</sub>O<sub>2</sub> was selected to study the influence of adsorbed DOM on the catalytic processes occurring at MnO<sub>2</sub> surface in the presence of oxidants. This investigation would provide a better nanoscale understanding of the impact of DOM on the biogeochemical cycle of Mn oxides in environmental and engineered systems.

## **4.2 Materials and methods**

### **4.2.1 Solution preparation and reagents**

Colloidal suspensions and electrolyte solutions used in this study were prepared with ultrapure water (18.2 M $\Omega$ ·cm resistivity, PURELAB Ultra, ELGA). NaCl and CaCl<sub>2</sub> solutions were prepared with analytical grade reagents, and were filtered through a 0.2  $\mu$ m membrane filter (Asordisc PSF, PALL, USA) prior to use. H<sub>2</sub>O<sub>2</sub> stock solution was prepared through dilution of H<sub>2</sub>O<sub>2</sub> of 30% (w/w) before measurements. Organic matter stocks were prepared by dissolving each DOM isolate in ultrapure water and stored in 4°C.

#### **4.2.2 Preparation of MnO<sub>2</sub> nanoparticles**

MnO<sub>2</sub> particles were synthesized by oxidizing manganese nitrate (Mn[NO<sub>3</sub>]<sub>2</sub>) with potassium permanganate (KMnO<sub>4</sub>). The resulting MnO<sub>2</sub> particles were ground into nanoscale particles with a BTRM 459 grinder (Rocklabs Limited, New Zealand). Details on MnO<sub>2</sub> synthesis and nanoparticle preparation were provided in Text A3-1.

#### **4.2.3 Origin and characteristics of the DOM isolates**

Four DOM isolates previously characterized and extracted from three surface waters (Croue et al., 1999; Hwang et al., 2001) and one urban wastewater effluent (Zheng et al., 2014) using the comprehensive isolation protocol previously described (Leenheer et al., 2000a), were selected for the current study. Hydrophobic DOM (HPO) fractions isolated using the XAD-8<sup>®</sup> resin were obtained from the high-humic content Gartempe River water (GRW-HPO), the Jeddah secondary-treated urban wastewater (JWW-HPO), and the ozonated Colorado River water (CRW-OC-HPO). The hydrophilic (HPI) DOM fraction from the Ribou River water (RRW-HPI) not adsorbed onto the XAD-8<sup>®</sup> and XAD-4<sup>®</sup> resin placed in series, was isolated using anion exchange resin. The summary of the major characteristics of the four DOM samples were provided in Table A3-1. CRW-OC-HPO, JWW-HPO, and RRW-HPI were further characterized using high-resolution mass spectrometry FTICR-MS. Negative Electrospray Ionization Fourier Transform Ion Cyclotron Resonance [ESI(-)] FTICR mass spectra were acquired using a 12T Bruker Solarix mass spectrometer (Bruker Daltonics, Bremen, Germany) and an Apollo II electrospray ionization (ESI) source in negative mode. The details for sample preparation and data processing were described elsewhere (Cawley, 2016; Tziotis et al., 2011).

#### **4.2.4 Measurement of zeta potential, hydrodynamic diameter, and aggregation kinetics of MnO<sub>2</sub> nanoparticles in DOM-containing electrolyte solutions**

UV-Vis spectra (200-800 nm wavelengths) for MnO<sub>2</sub> suspensions were obtained with a Cary 60 spectrophotometer (Agilent, USA). Hydrodynamic diameter and Zeta potential of MnO<sub>2</sub> nanoparticles were measured with a Zetasizer (nano ZS, Malvern, UK) using a laser at a wavelength of 633 nm and a scattering angle of 173°. Clear disposable zeta cells (1 mL, DTS1070, Malvern, UK) were used to determine the Zeta potential of the nanoparticles under a wide range of solution conditions, i.e., NaCl and CaCl<sub>2</sub> solution with ionic strength (IS) ranging from 1 to 100 mM. Solution pH was adjusted by the addition of NaOH and H<sub>2</sub>SO<sub>4</sub> at 10 mM NaCl and room temperature (~25°C). Detailed information on the procedures were provided in Text A3-2. TR-DLS measurements were performed using low volume disposable cuvettes (ZEN112, Malvern, UK). Sample preparation and measurement procedures were provided in SI section. Briefly, MnO<sub>2</sub> nanoparticles and DOM were simultaneously added to the selected electrolyte solution to a final concentration of 1 ppm and 10 mg C/L, respectively, gently shook, and placed in the Zetasizer equipment for immediate measurement (Gutierrez et al., 2015a). The change in hydrodynamic diameter of MnO<sub>2</sub> nanoparticles in electrolyte solutions or DOM-containing electrolyte solutions were recorded every 20 seconds and at a 1h timeframe. The experimental aggregation kinetic rate ( $\kappa_{11}$ : nm.min<sup>-1</sup>) of MnO<sub>2</sub> particles under each electrolyte solution condition was calculated as initial rate of increase in particles hydrodynamic diameter ( $D_h$ ) with respect to time, as previously described (Gutierrez et al., 2015a). Additionally, interaction energies (i.e., energy barriers) between MnO<sub>2</sub> nanoparticles in solution were modeled by classic DLVO theory, and described in Text A3-4. To study the impact of oxidants on the aggregation kinetics of MnO<sub>2</sub> in DOM-containing solutions

(i.e., influence of adsorbed DOM on the catalytic processes occurring at MnO<sub>2</sub> surface in the presence of oxidants), H<sub>2</sub>O<sub>2</sub> was added after 1h of MnO<sub>2</sub> /DOM aggregation in 30 mM NaCl solutions; where the subsequent change in D<sub>h</sub> was recorded as a function of time.

#### **4.2.5 Force measurements and data analysis**

Atomic force microscopy (Icon, Bruker, USA) in contact mode was used to study the interaction forces between DOM isolates and MnO<sub>2</sub>. Force-distance curves were generated at a sub-nano Newton resolution and at a nanometer scale. Probe and surface preparation procedures were provided in Text A3-3. A minimum of 30 force profiles were collected for each experimental condition. Approaching and retraction sections of the force profiles were recorded. Approaching curves were analyzed to study the repulsion forces or jump-to-contact events. Repulsion forces following an exponential decay were described by:  $F=F_0 \exp(-\kappa h)$ , where  $h$  is the separation distance,  $F$  is the interaction force between probe and surface,  $F_0$  is the pre-exponential constant defined as force in contact, and  $\kappa^{-1}$  is the interaction force decay length (Butt et al., 2005). Jump-to-contact events occurred when the gradient of the attractive forces exceeded the spring constant of the cantilever. Retracting force profiles were processed to calculate the maximum adhesion forces, defined as the maximum force before total detachment of the probe from the surface. Maximum adhesion forces provided information of the strength of the bond between MnO<sub>2</sub> surface and DOM isolates. Due to the heterogeneity of organic matter, adhesion forces were statistically analyzed by probability density function, where the mean ( $\mu$ ) and variance ( $\sigma$ ) were calculated.

## 4.3 Results and discussion

### 4.3.1 Characteristics of MnO<sub>2</sub> particles

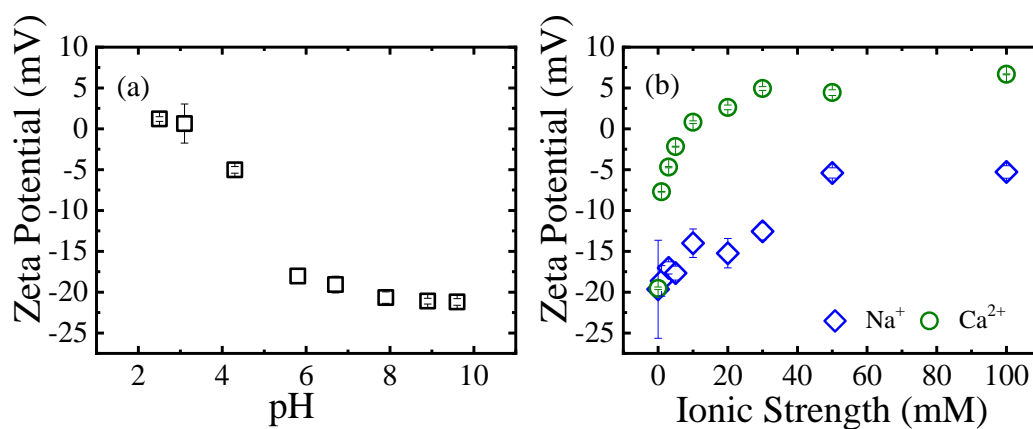


**Figure 4-1 Zeta potential of MnO<sub>2</sub> of as a function of: a) solution pH 2-10, and b) ionic strength (Na<sup>+</sup> and Ca<sup>2+</sup>) ranging from 1-100 mM and at unadjusted pH.**

The mean initial hydrodynamic diameter ( $D_{ho}$ ) of MnO<sub>2</sub> particles was  $130.3 \pm 5.8$  nm, with a mean Polydispersity Index (PdI) of 0.16; indicating a monodispersed nanoparticles population in solution. The XRD spectrum of the MnO<sub>2</sub> particles (Figure A3-1a) indicated a predominant crystalline structure of  $\alpha$ -MnO<sub>2</sub>. The UV-Vis absorbance profile (Figure A3-1b) showed the absence of a maximum absorbance peak which differed from that previously reported (Huangfu et al., 2013). This difference in absorbance profile indicated a specific molecular orbits arrangement, which would subsequently lead to a change in MnO<sub>2</sub> affinity to DOMs (Griffith et al., 1957). The isoelectric point of MnO<sub>2</sub> nanoparticles was calculated by zeta potential (ZP) measurements at different pH conditions. A negative value of ZP ( $-19.6 \pm 4.9$  mV) was observed for MnO<sub>2</sub> nanoparticles at unadjusted and basic pH values (i.e., 5.8-10), indicating a negative charge due to deprotonation of hydroxyl groups (Szekeres et al., 2012) (Figure 4-1a). The isoelectric point was calculated at approximate pH 3.25, which was in good agreement with that reported in previous studies (McBride, 1989).

Both  $\text{Na}^+$  and  $\text{Ca}^{2+}$  cations influenced the ZP of  $\text{MnO}_2$ . The ZP of  $\text{MnO}_2$  was negative throughout the whole IS range tested and decreased with increasing  $\text{Na}^+$  concentration in solution (Figure 4-1b), indicating simple charge screening. Nevertheless, the ZP of  $\text{MnO}_2$  was more impacted in the presence of  $\text{Ca}^{2+}$  in solution. Specifically, at low concentrations of  $\text{Ca}^{2+}$ , i.e., 0.33mM, the charge significantly decreased compared to that in  $\text{Na}^+$  solutions. Remarkably, charge reversal was observed at 3.33 mM  $\text{CaCl}_2$ . This result indicated a more efficient charge neutralizing effect by  $\text{Ca}^{2+}$  than  $\text{Na}^+$  at same ionic strength, and also suggests cation complexation between  $\text{Ca}^{2+}$  and  $\text{MnO}_2$ . Inner-sphere tetradentate or monodentate complexes would form via interaction between  $\text{Ca}^{2+}$  and hydroxyl groups on  $\text{MnO}_2$  (Sverjensky, 2006).

### 4.3.2 Aggregation kinetics of $\text{MnO}_2$ nanoparticles

#### 4.3.2.1 Aggregation of $\text{MnO}_2$ nanoparticles in electrolyte solution

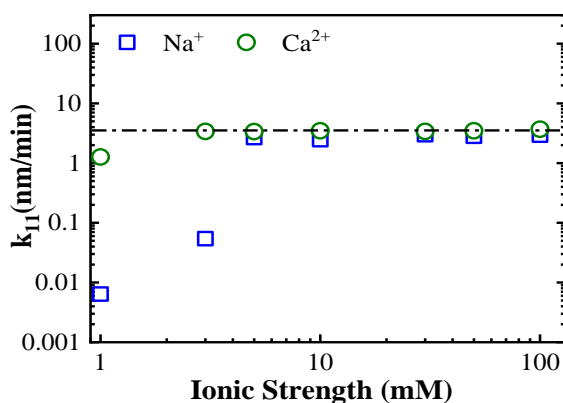


**Figure 4-2. Aggregation rate constants  $\kappa_{11}$  of  $\text{MnO}_2$  nanoparticles in  $\text{Na}^+$  or  $\text{Ca}^{2+}$  solutions at unadjusted pH ( $5.8 \pm 0.3$ )**

$\text{MnO}_2$  particles readily aggregated in the presence of both  $\text{NaCl}$  and  $\text{CaCl}_2$  at varying concentrations (Figure 4-2). Linear aggregation kinetics curves were observed, indicating the presence of a monodispersed population of  $\text{MnO}_2$  nanoparticles in solution (Figure A3-2). The presence of cations in solution induced charge screening

(Figure 4-2) and consequently a decrease in energy barrier between MnO<sub>2</sub> particles. Specifically, electrostatic repulsion between nanoparticles decreased with increasing cation concentration, leading to a decrease in total DLVO interaction energy (Text A3-4). Additionally, due to the hydrophobic nature of MnO<sub>2</sub> (Lu et al., 2016b), short-ranged hydrophobic interactions between MnO<sub>2</sub> nanoparticles would play a key role for the readily aggregation observed.

Critical coagulation concentration (CCC) was observed at approximately 5 mM for NaCl solutions, and fast aggregation rate constant ( $\kappa_{\text{fast}}$ ) was calculated as approximately 3.5 nm/min. CCC for NaCl and  $\kappa_{\text{fast}}$  were lower compared to that reported in the literature (i.e., CCC: ~28 mM NaNO<sub>3</sub> and  $\kappa_{\text{fast}}$ : 40 nm/min) (Huangfu et al., 2013). This difference was probably caused by the experimental conditions or the synthesis procedure of the particles. Specifically, a significantly lower zeta potential (-18.63 mV vs -41.96 mV) and a larger diameter (130 nm vs 55 nm) measured in current study for MnO<sub>2</sub> nanoparticles would lead to a lower energy barrier compared to that previously reported (Huangfu et al., 2013). Therefore, a lower concentration of salt was required to reach fast aggregation regime, i.e., lower CCC. Remarkably, DLVO theory (Figure A3-3) predicted a small energy barrier preventing aggregation (i.e., reaction-limited regime) for 1 mM NaCl, and no energy barrier (i.e., diffusion-limited regime) at 5 mM NaCl. These results confirm the suitability of DLVO theory for (bare) hard particles in solution under the influence of electrostatic and vdW interactions.

In CaCl<sub>2</sub> solutions, CCC occurred at lower concentrations (<1mM) than in NaCl solutions, which was consistent with the ZP trend observed (Figure 4-1b). Specifically, MnO<sub>2</sub> nanoparticles displayed a significantly lower negative charge in Ca<sup>2+</sup> solutions

than in  $\text{Na}^+$  solutions, resulting in weaker electrostatic repulsive forces. The absence of energy barrier at 1 mM  $\text{Ca}^{2+}$  (Figure A3-3) was consistent with the lower CCC in  $\text{Ca}^{2+}$  solutions. Also, the formation of surface complexes between  $\text{Ca}^{2+}$  and negatively-charged groups on  $\text{MnO}_2$  surface would enhance the aggregation of nanoparticles. Similar trends in both aggregation behaviour and surface charge have been previously observed (Chowdhury et al., 2013; Huynh et al., 2011).

#### ***4.3.2.2 Aggregation of $\text{MnO}_2$ in DOM-containing NaCl solutions***

The aggregation kinetics of  $\text{MnO}_2$  particles was considerably decreased in DOM-containing NaCl solution (Figure A3-3a and Figure A3-4). This stabilization effect would be caused by DOM adsorption on  $\text{MnO}_2$ , leading to a change in  $\text{MnO}_2$  surface properties. Specifically, DOM would provide an additional charge contribution to  $\text{MnO}_2$  surface (i.e., increased electrostatic repulsion and DLVO interaction). Also, adsorbed DOM would induce steric repulsive forces preventing the aggregation of particles. This stabilization effect caused by DOM have been reported in previous studies conducted with  $\text{TiO}_2$  (Domingos et al., 2009), aluminum oxide (Ghosh et al., 2008), viruses (Gutierrez et al., 2012), and other engineered particles (Basnet et al., 2013; Liu et al., 2013). At low NaCl concentrations, the  $\kappa_{11}$  constants of DOM-coated  $\text{MnO}_2$  nanoparticles were >2 orders of magnitude lower than those of bared  $\text{MnO}_2$  nanoparticles. No clear CCC was observed for RRW-HPI and CRW-OC-HPO, indicating unfavorable aggregation between DOM-coated  $\text{MnO}_2$  particles. Conversely, GRW-HPO-coated nanoparticles exhibited a  $\kappa_{\text{fast}}$  of 0.1 nm/min at high  $\text{Na}^+$  concentration; while no aggregation was detected for  $\text{MnO}_2$  particles in JWW-HPO-containing NaCl solutions. The aggregation rate constants  $\kappa_{11}$  of all DOM-coated  $\text{MnO}_2$  nanoparticles were lower than  $\kappa_{\text{fast}}$  of bared  $\text{MnO}_2$  nanoparticles (i.e.,

approximately 3.5 nm/min) during the whole NaCl concentration range tested (Figure 4-3 and Figure 4-1a), indicating the high stabilization effect of adsorbed DOM.

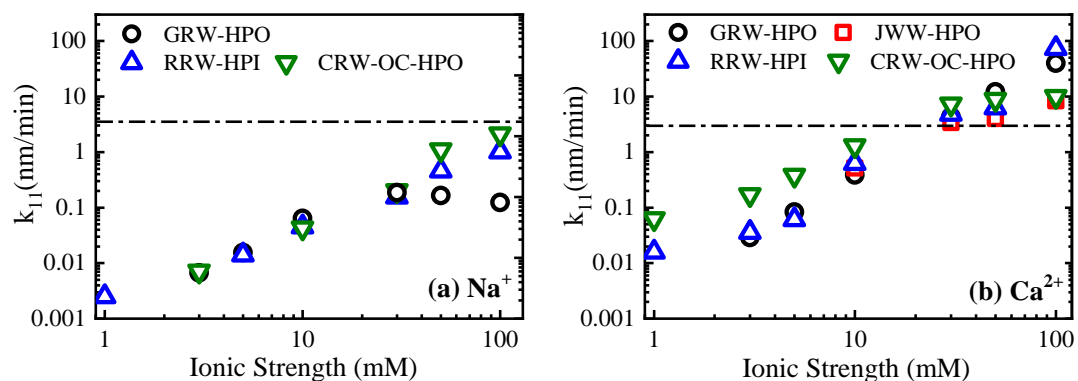


**Figure 4-3. Aggregation rate constants  $\kappa_{11}$  of  $\text{MnO}_2$  in the presence of 10 mg C/L DOM in a)  $\text{Na}^+$  or b)  $\text{Ca}^{2+}$  solutions and at unadjusted pH**

Interestingly, JWW-HPO-coated  $\text{MnO}_2$  particles exhibited a considerably higher stability than those of river DOM-coated  $\text{MnO}_2$  particles (RRW-HPI, GRW-HPO, and CRW-OC-HPO); probably due to the difference in their origins and physicochemical characteristics. River HPO fractions mainly contains lignin derivatives while wastewater DOM isolate was affected by microbial activities. Additionally,  $\text{MnO}_2$  particles were less stable at higher ionic strength ( $>30$  mM NaCl) in the presence of DOMs of lower  $\text{SUVA}_{254}$  (i.e., RRW-HPI and CRW-OC-HPO, both of lower aromatic character) than their more hydrophobic counterparts (i.e., GRW-HPO and JWW-HPO). Van Krevelen diagrams based on FTICR-MS results, confirmed the stronger hydrophobic character of JWW-HPO (i.e., molecular composition showing higher H/C and lower O/C ratios) than CRW-OC-HPO and RRW-HPI (Figure A3-5). The lower molecular weight and less complex polymeric structure of RRW-HPI and CRW-OC-HPO would induce a lower steric stabilization effect at higher ionic strength in solution. A direct correlation between the average molecular weight ( $M_w$ ) and SUVA has been previously established for NOM isolates (Violleau, 1999). FTICR-MS confirmed the

significant presence of high molecular structures ( $m/z > 400$ ) in the JWW-HPO fraction. A high-SUVA DOM fraction showing similar structural composition as GRW-HPO (i.e., Suwannee River fulvic acid) was found to incorporate higher  $m/z$  molecules than RRW-HPI and CRW-OC-HPO (Hertkorn et al., 2008). Nevertheless, another hypothesis that would explain the more efficient stabilization effect of the hydrophobic (HPO) isolates on  $MnO_2$  nanoparticles would be the coating efficiency (i.e., coating completeness) of organics on  $MnO_2$  surface (Aubry et al., 2013). Due to unfavorable polar interactions, the hydrophilic fractions (RRW-HPI and CRW-OC-HPO) would not be able to fully coat the surface of the  $MnO_2$  nanoparticles, as opposed to the hydrophobic isolates (GRW-HPO and JWW-HPO). Thus, a more efficient DOM coating would provide a higher stabilization effect to  $MnO_2$  nanoparticles. A preferential adsorption of organics enriched in aromatic moieties (e.g., HPO isolates) has been observed for synthetic and natural Mn oxides, where hydrophobic interactions were proposed as the dominant interacting mechanism (Allard et al., 2017). This hypothesis was further explored in section 4.3.2.4.

#### ***4.3.2.3 Aggregation of $MnO_2$ in DOM-containing $CaCl_2$ solutions***

Higher aggregation rates (i.e., of up to 2 orders of magnitude) were observed for  $MnO_2$  nanoparticles in DOM-containing  $CaCl_2$  solutions than in DOM-containing NaCl solutions (Figure 4-3b and Figure A3-6). DOM-coated nanoparticles were more stable than bared  $MnO_2$  nanoparticles at low  $CaCl_2$  concentrations (i.e.,  $\leq 3.33$  mM  $CaCl_2$ , equivalent to  $\leq 10$  mM IS). At this low ionic strength, the aggregation kinetic rates  $k_{11}$  of  $MnO_2$ -coated CRW-OC-HPO particles were higher than the other three DOM-coated  $MnO_2$  particles; probably due to weaker steric interactions (i.e., smaller  $M_w$  and less complex polymeric structure) and lower electrostatic repulsive forces (i.e., more efficient charge screening/bridging by  $Ca^{2+}$ ) of the former. Conversely, the

aggregation rates  $\kappa_{11}$  for all DOM-coated MnO<sub>2</sub> particles were higher than  $\kappa_{\text{fast}}$  of bared MnO<sub>2</sub> particles at high CaCl<sub>2</sub> concentration (i.e.,  $\geq 10$  mM CaCl<sub>2</sub>, equivalent to  $\geq 30$  mM IS), indicating enhanced aggregation and the key role of both Ca<sup>2+</sup> and DOM characteristics. Cation (Ca<sup>2+</sup>) bridging would form between deprotonated carboxyl groups on DOM in solution and on DOM adsorbed on MnO<sub>2</sub> nanoparticles, leading to the formation of larger DOM/MnO<sub>2</sub> aggregates as measured by DLS (Chen et al., 2006; Dong et al., 2013). Compared to Na<sup>+</sup> solutions, the presence of Ca<sup>2+</sup> had a deeper relative impact on the aggregation kinetics of MnO<sub>2</sub> in GRW-HPO, JWW-HPO, and RRW-HPI-containing solutions at high ionic strength, possibly due to a higher content of carboxyl groups in their structures. The magnitude of the electrophoretic mobility (i.e., indicator of ionized functional groups content) of these isolates followed the trend: GRW-HPO > JWW-HPO > RRW-HPI > CRW-OC-HPO (Aubry et al., 2013; Gutierrez et al., 2015a; Gutierrez et al., 2015b; Hwang et al., 2001).

#### ***4.3.2.4 Influence of DOM characteristics on MnO<sub>2</sub> catalytic oxidation efficiency***

First, the aggregation of bared MnO<sub>2</sub> particles in the presence of H<sub>2</sub>O<sub>2</sub> was studied. H<sub>2</sub>O<sub>2</sub> was added after 1h of MnO<sub>2</sub> aggregation in 30 mM NaCl solutions; where the subsequent change in  $D_h$  was recorded as a function of time (Figure 4-4). A significant change in the aggregation profile of bared MnO<sub>2</sub> particles was observed after the addition of H<sub>2</sub>O<sub>2</sub>. The aggregation profile was highly scattered (i.e., following no aggregation trend) and showed a considerable increase in the hydrodynamic diameter of particles as large as 3000 nm (Figure 4-4). Using statistical analysis by probability density functions, the mean hydrodynamic diameter of MnO<sub>2</sub> nanoparticles upon H<sub>2</sub>O<sub>2</sub> addition was calculated as 836.8 nm ( $\sigma$ : 0.41 and  $R^2$ : 0.95) (Figure A3-7a). The highly scattered MnO<sub>2</sub>/H<sub>2</sub>O<sub>2</sub> aggregation profile would be caused by the change in surface property of the particles as well as in solution conditions. Specifically, a higher

concentration of  $\text{Mn}^{2+}$  (i.e., 20  $\mu\text{g/l}$ ) was recorded upon  $\text{H}_2\text{O}_2$  addition than in oxidant-free solution (i.e., below 1  $\mu\text{g/l}$ ). This  $\text{Mn}^{2+}$  release in solution would lead to aggregation by charge neutralization or complexation mechanisms. Other reactive species may have been produced during the catalytic oxidation processes; thus, inducing instability in  $\text{MnO}_2$  particles in solution. In a previous investigation, several reductants ( $\text{O}_2^{\cdot-}$ ,  $\text{HO}_2^-$ , and  $\text{H}^{\cdot}$ ) were generated in a  $\text{MnO}_2$  catalyzed system with  $\text{H}_2\text{O}_2$  (i.e., in addition to the strong oxidant  $\cdot\text{OH}$ ), which even exhibited the capacity to induce contaminants desorption from substrates (Do et al., 2009). Also, a significant change in surface charge (i.e., from negative to positive, Figure A3-8) was observed probably due to interaction between deprotonated hydroxyl groups and  $\text{Mn}^{2+}$  or  $\text{H}_2\text{O}_2$ .

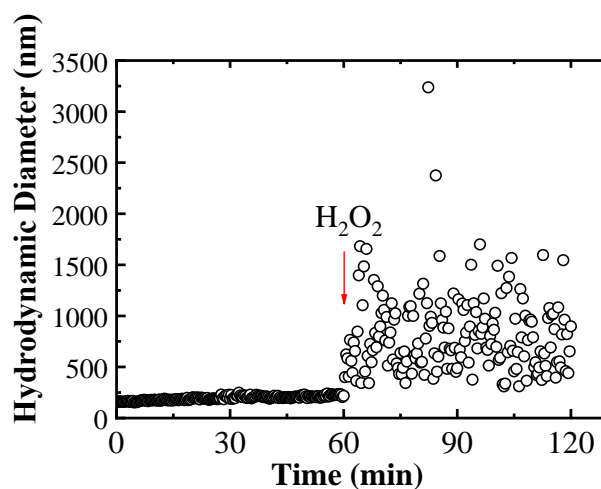


**Figure 4-4. Aggregation kinetic profiles of bared  $\text{MnO}_2$  particles in 30mM NaCl solution. 1 mM  $\text{H}_2\text{O}_2$  were added after 1h of  $\text{MnO}_2$  aggregation.**

The influence of  $\text{H}_2\text{O}_2$  in the aggregation of  $\text{MnO}_2$  nanoparticles in DOM-containing electrolyte solution was also investigated.  $\text{H}_2\text{O}_2$  was added after 1h of  $\text{MnO}_2/\text{DOM}$  aggregation in 30 mM NaCl solutions; where the subsequent change in  $D_h$  was recorded as a function of time (Figure 4-5). The addition of  $\text{H}_2\text{O}_2$  did not affect the stability of JWW-HPO-coated  $\text{MnO}_2$  nanoparticles ( $\mu$ : 135.3 nm,  $\sigma$ : 0.06,  $R^2$ : 0.98)

(Figure 4-5(a)). However, upon addition of H<sub>2</sub>O<sub>2</sub> the aggregation profile of GRW-HPO-coated MnO<sub>2</sub> particles showed scattered; where the mean D<sub>h</sub> of the aggregates increased to 332 nm ( $\sigma$ : 0.33, R<sup>2</sup>: 0.96) (Figure A3-7(b)). Nevertheless, the aggregation of GRW-HPO-coated MnO<sub>2</sub> nanoparticles was less affected by the addition of H<sub>2</sub>O<sub>2</sub> (Figure 4-5 (b)) than bared MnO<sub>2</sub> nanoparticles (Figure 4-4). Contrariwise, the stability of the HPI fractions-coated MnO<sub>2</sub> nanoparticles was considerably more impacted by the addition of H<sub>2</sub>O<sub>2</sub> than their hydrophobic counterparts. Specifically, the aggregation profiles recorded were highly scattered (Figure 4-5c-d) and similar to that of bared MnO<sub>2</sub> particles (Figure 4-4). The mean D<sub>h</sub> of RRW-HPI was calculated as 772.6 nm ( $\sigma$ : 0.44, R<sup>2</sup>: 0.94) while the mean D<sub>h</sub> of CRW-OC-HPO was 641.6 nm ( $\sigma$ : 0.31, R<sup>2</sup>: 0.95).

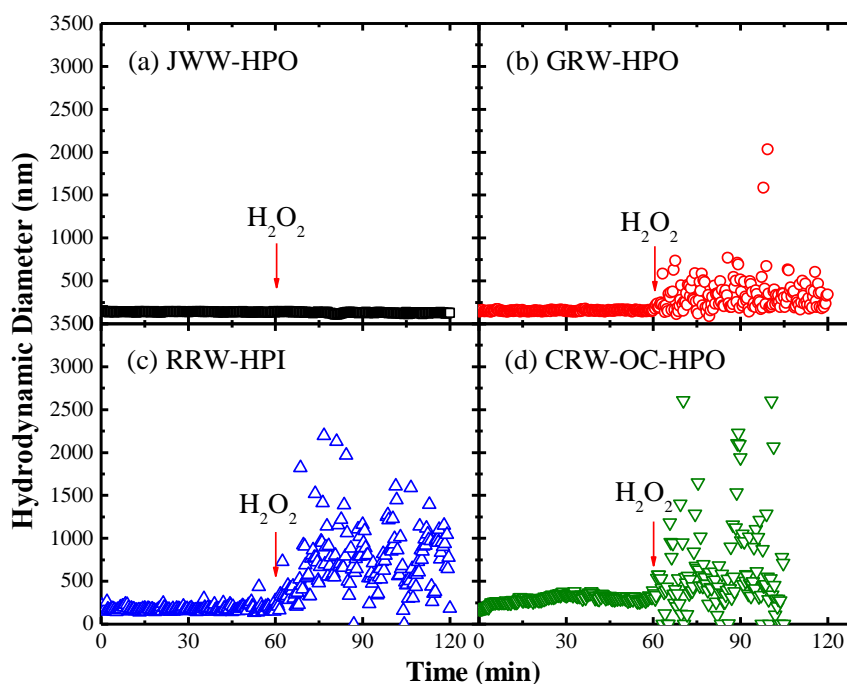


**Figure 4-5. Aggregation profiles of MnO<sub>2</sub> particles in 10 mg C/L DOM-containing NaCl solutions, at unadjusted pH. 1mM H<sub>2</sub>O<sub>2</sub> was added after 1h of MnO<sub>2</sub> /DOM aggregation.**

Considering that H<sub>2</sub>O<sub>2</sub> had no measurable impact on DOM (i.e., based on H<sub>2</sub>O<sub>2</sub> demand, TOC, and UV<sub>254</sub> analyses, results not shown) these results suggest favorable hydrophobic interactions between HPO fractions and MnO<sub>2</sub> leading to a more efficient DOM coating (i.e., blocking surface reactive sites) and a reduced possibility of: a) contact between MnO<sub>2</sub> and H<sub>2</sub>O<sub>2</sub>, and b) release of Mn<sup>2+</sup> and other reactive species. Remarkably, JWW-HPO would be more efficient in coating the surface of MnO<sub>2</sub> than GRW-HPO. The specific structure of JWW-HPO would favor its adsorption to MnO<sub>2</sub> and would create a more efficient protective coating layer against H<sub>2</sub>O<sub>2</sub>. These results were consistent with the stabilization effect shown by the two HPO fractions in NaCl solutions (Figure 4-3a). Conversely, the more hydrophilic organic fractions (i.e., RRW-HPI and CRW-OC-HPO) would not efficiently adsorb on the MnO<sub>2</sub> surface due to unfavorable polar interactions; thus, exposing available reactive sites. Nevertheless, the possibility of GRW-HPO, RRW-HPI, and CRW-OC-HPO desorption from MnO<sub>2</sub> surface due to MnO<sub>2</sub>/H<sub>2</sub>O<sub>2</sub> oxidation processes and subsequent generation of reactive species cannot be fully discarded (Do et al., 2009). This DOM desorption would expose reactive sites on MnO<sub>2</sub> surface; consequently, inducing aggressive aggregation of MnO<sub>2</sub> nanoparticles (Figure 4-5b-d). Thus, to further study this reversibility of DOM adsorption on MnO<sub>2</sub> surface (i.e., direct indicative of the strength of the bond), the interaction forces between MnO<sub>2</sub> and DOM were studied by AFM.

### **4.3.3 Interfacial interactions between MnO<sub>2</sub> and DOMs**

The investigation of DOMs interfacial interactions with MnO<sub>2</sub> by AFM highly assisted in explaining the more favorable interactions shown between MnO<sub>2</sub> and HPO fractions leading to a higher stability in NaCl solutions and a lower reactivity in the presence of H<sub>2</sub>O<sub>2</sub>, as compared to their more hydrophilic counterparts. The interaction forces between DOMs and MnO<sub>2</sub> were analyzed in both approaching and retracting regimes,

providing important information on the strength of the interaction (e.g., attractive forces during approach and adhesion forces during retraction) as a function of their physicochemical characteristics. JWW-HPO and CRW-OC-HPO were selected for AFM analysis due to their different: a) characteristics, b) impact on MnO<sub>2</sub> aggregation behavior, and c) reactivity with H<sub>2</sub>O<sub>2</sub>.

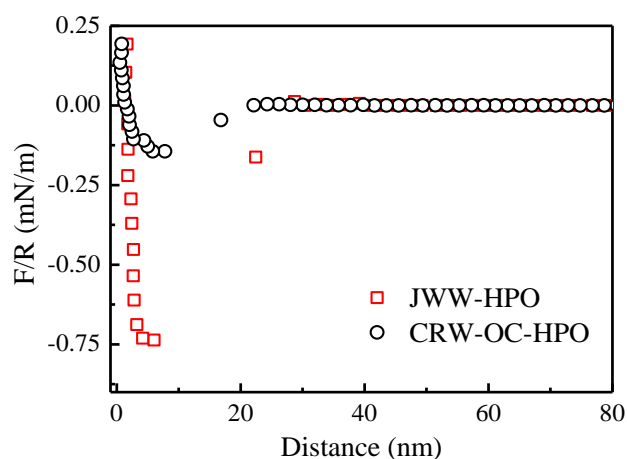


**Figure 4-6. Representative approaching curve profiles between CRW-OC-HPO or JWW-HPO-coated silica colloidal probe and MnO<sub>2</sub> surface at 10 mM Na<sup>+</sup> and at unadjusted pH.**

Attractive forces leading to jump-to-contact events between MnO<sub>2</sub> and CRW-OC-HPO or JWW-HPO were recorded in both NaCl and CaCl<sub>2</sub> solutions, at every ionic strength tested (Table 4-1). In the current experimental setup, electrostatic repulsion forces between MnO<sub>2</sub> surface and CRW-OC-HPO or JWW-HPO were not clearly detected in the approaching curve due to their low surface charges; thus, resulting in low electrostatic interactions (i.e., as opposed to previous studies using organic fractions and highly negatively-charged mica surface) (Aubry et al., 2013). Specifically, electrostatic interactions following Coulomb's Law, depict a proportional relationship between repulsive force and the product of the charges.

However, JWW-HPO exhibited stronger attracting forces to MnO<sub>2</sub> than CRW-OC-HPO in every NaCl concentration tested (Table 4-1). These strong attractive forces (i.e., possibly arising from favorable hydrophobic interactions) would explain the high affinity shown by JWW-HPO to MnO<sub>2</sub>, resulting in a favorable adsorption and in a more efficient organic coating. Also, Ca<sup>2+</sup> exerted a deeper impact on JWW-HPO attractive forces to MnO<sub>2</sub>. Ca<sup>2+</sup> would decrease intramolecular and intermolecular repulsion by an efficient charge screening and complexation with negatively-charged functional groups on JWW-HPO structure. This would result in conformational changes in the organic polymeric layer leading to a more compact structure as conceptually modeled elsewhere; consequently, favoring JWW-HPO interactions with MnO<sub>2</sub> (Avena et al., 1999; Lead et al., 2000; Murphy et al., 1994; Xu et al., 2005).

**Table 4-1. Mean values ( $\mu$ ) of attracting forces (mN/m) measured during DOM-coated silica colloidal probe approaching to MnO<sub>2</sub> surface at different solution chemistries. Variance ( $\sigma$ ) are shown in parentheses.**

DOM	Na <sup>+</sup>			Ca <sup>2+</sup>		
	1 mM	10 mM	100 mM	0.33 mM	3.33 mM	33.3 mM
JWW-HPO	0.53(0.06)	0.59(0.19)	0.49(0.24)	1.50(0.09)	1.11(0.32)	1.40(0.10)
CRW-OC-HPO	0.17(0.04)	0.20(0.04)	0.19(0.04)	0.18(0.10)	0.18(0.10)	0.32(0.02)

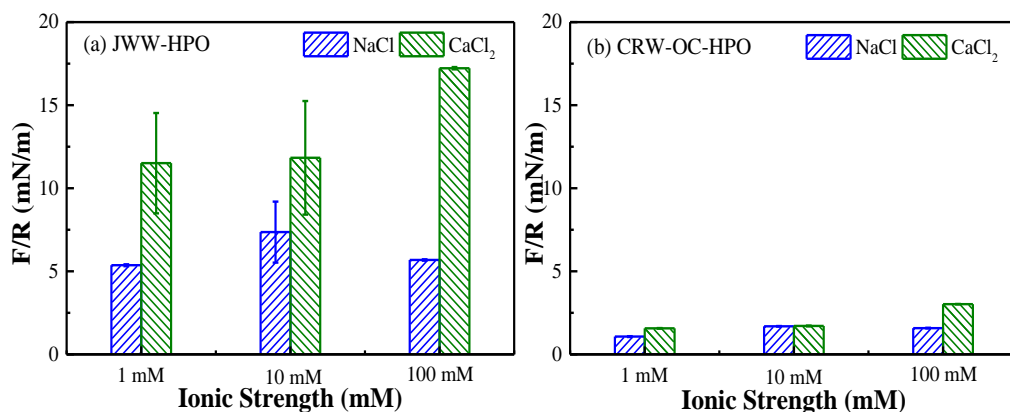


**Figure 4-7. Maximum adhesion forces between MnO<sub>2</sub> and a) JWW-HPO, and b) CRW-OC-HPO in NaCl or CaCl<sub>2</sub> solution at different ionic strengths and unadjusted pH.**

Analogously, stronger adhesion forces were recorded in the retracting regime between JWW-HPO and MnO<sub>2</sub> under all NaCl solution conditions (Figure 4-6). This direct correlation between attracting forces and adhesion forces have been previously reported (Cappella et al., 1999). Unfavorable polar interactions between MnO<sub>2</sub> and CRW-OC-HPO would induce these lower adhesion forces. Also, sulfur-containing moieties present in JWW-HPO would favor the formation of strong bonds with metal surfaces (Tao et al., 2014). The magnitude of adhesion forces between surfaces is a direct indicative of the strength of the bond (Butt et al., 2005). This latter observation would explain the significantly higher reactivity between CRW-OC-HPO-coated MnO<sub>2</sub> nanoparticles and H<sub>2</sub>O<sub>2</sub>. This lower adhesion forces (i.e., weaker bonds) would result in higher possibilities of CRW-OC-HPO desorption from MnO<sub>2</sub> surface due to oxidation processes and subsequent generation of reactive species, as hypothesized in section 4.3.2.4. Contrariwise, the stronger bonds displayed between JWW-HPO and MnO<sub>2</sub> would indicate irreversible adsorption and thus, low possibilities of DOM desorption from substrate (Gutierrez et al., 2015b; Zaouri et al., 2017). This latter result would be consistent with the extremely low JWW-HPO-coated MnO<sub>2</sub> nanoparticles

reactivity towards  $\text{H}_2\text{O}_2$  in solution (i.e., low impact of  $\text{H}_2\text{O}_2$  on JWW-HPO-coated  $\text{MnO}_2$  nanoparticles aggregation) (Figure 4-5(a)). Also, the adhesion forces between JWW-HPO and  $\text{MnO}_2$  were more influenced by the presence of  $\text{Ca}^{2+}$  in solution (Figure 4-7). Cation bridging between deprotonated hydroxyl groups on  $\text{MnO}_2$  surface and carboxyl groups in JWW-HPO structure as well as conformational changes in its polymeric structure would favor JWW-HPO adhesion to  $\text{MnO}_2$  surface (Pettibone et al., 2008). In conclusion, the specific characteristics of  $\text{MnO}_2$  and DOM (i.e., charge, structure, composition, hydrophobicity, and functional groups) played a crucial role during interfacial interactions; where the strength of the interaction (i.e., strength of the bond) would determine the reversibility of adsorption of the organic.

#### **4.4 Summary**

With the use of sensitive tools at a nanoscale resolution, this study provided fundamental information on: a) the interfacial interactions between  $\text{MnO}_2$  and naturally occurring DOMs of different origins and characteristics under varying solution conditions, and b) the impact of the physicochemical characteristics of DOMs on  $\text{MnO}_2$ -participated catalytic oxidation processes.

- Bare  $\text{MnO}_2$  nanoparticles readily aggregated in both monovalent and divalent cation solutions due to hydrophobic and low electrostatic interactions. Classic DLVO theory successfully described  $\text{MnO}_2$  aggregation behavior and CCCs.
- In NaCl solutions, DOM isolates adsorbed on  $\text{MnO}_2$  nanoparticles surface; conferring them stability mainly by electrostatics (additional charge contribution) and steric repulsive forces originating from the polymeric structure of the DOM. This stabilization effect was more efficient for JWW-

HPO and GRW-HPO, possibly due to their higher molecular weight and more complex polymeric structure.

- In DOM-containing  $\text{CaCl}_2$  solutions, the aggregation rates of  $\text{MnO}_2$  nanoparticles increased because of a more efficient charge screening and cation ( $\text{Ca}^{2+}$ ) bridging mechanisms. This increase was correlated to the carboxyl groups content on each DOM fraction. At high  $\text{Ca}^{2+}$  concentrations, enhanced aggregation was observed for all DOM isolates.
- JWW-HPO adsorbed onto  $\text{MnO}_2$  completely hindered  $\text{H}_2\text{O}_2$  catalytic oxidation processes on  $\text{MnO}_2$  surface by blocking reactive sites; while GRW-HPO reduced these oxidation processes. Conversely, RRW-HPI and CRW-OC-HPO did not impact  $\text{H}_2\text{O}_2$  oxidation reaction on  $\text{MnO}_2$ ; thus, exerting little or no effect on the high aggregation of  $\text{MnO}_2$  nanoparticles. A more efficient HPO DOM coating or a possible HPI DOM desorption from  $\text{MnO}_2$  surface during catalytic oxidation processes would explain these observations.
- Results from AFM confirmed the stronger interactions between  $\text{MnO}_2$  and JWW-HPO, evidenced by high attractive forces during approach (i.e., suggesting the influence of hydrophobic interactions) and high adhesion forces during retraction (i.e., direct indicative of the strength of the bond) in both monovalent and divalent cation solutions. Weaker attractive and adhesion forces were observed between  $\text{MnO}_2$  and CRW-OC-HPO, possibly due to unfavorable polar interactions.

The current results provided a fundamental understanding at the nanoscale of the efficiency of  $\text{MnO}_2$ -participated adsorption, oxidation, and catalysis processes in the presence of DOM of different physicochemical characteristics in aqueous environment.

## **Chapter 5. SO<sub>4</sub><sup>2-</sup>-based catalytic ceramic UF membrane for organics removal and flux restoration**

The contents of Chapter 5 & Appendix 4 are unable to be reproduced here as they are under embargo due to current consideration for publication in the journal *Chemical Engineering Journal*.

## 5.1 Introduction

Currently, ultrafiltration (UF) is widely implemented as an efficient membrane technology in water treatment (Gao et al., 2011; Wolf et al., 2005). Often used as a pretreatment step, UF exhibits a high capacity for the removal of suspended particles, colloids, and microorganisms (Winter et al., 2016). Nevertheless, the removal of small organic pollutants by UF is inefficient (Yoon et al., 2006). More importantly, the inevitable fouling caused by Natural Organic Matter (i.e., NOM, ubiquitously present in aquatic environments) remains a substantial drawback for this technology. Frequent membrane cleanings are required for restoring the permeate flux caused by fouling. Remarkably, the development of catalytic membranes to address the issue of organic fouling has attracted increasing research interests in recent years.

Catalytic membranes are commonly prepared through surface modification with functionalized materials. Ceramic membranes have nowadays gained increasing interests in both lab-scale research and full-scale water treatment processes due to their stronger thermal, mechanical and chemical properties (Kim et al., 2008; Lehman et al., 2009). Specifically, ceramic membranes are more suitable for the preparation of catalytic membranes due to their stronger chemical stability as compared to their polymeric counterparts. Thus, ceramic membrane filtration integrated with Advanced Oxidation Processes (AOP) generating Reactive Oxygen Species (i.e., ROS, such as  $\cdot\text{OH}$ ,  $\text{O}_2^{\cdot-}$ , and  $^1\text{O}_2$ ) when used in combination with oxidants or light irradiation is a promising robust technology for tackling organic fouling. Briefly, Byun et al. modified the surface of ceramic membranes with different metal oxides coatings by the layer-by-layer self-assembly technique and observed the highest flux recovery and permeate quality with Mn oxide-coated membrane in combination with ozone treatment (Byun et al., 2011). The Mn oxide-coated membrane was successfully prepared by spreading

the metal oxide onto the membrane surface, followed by a sintering process. The modified membrane was demonstrated as capable of mitigating both irreversible and reversible fouling, as well as to enhance the removal of *p*-chloronitrobenzene when coupled with ozone (Cheng et al., 2017b). Besides ozone-based AOPs, photo-Fenton oxidation has also been integrated with ceramic membrane filtration and goethite as a catalyst via a cross-linking method. The hybrid process slowed down the fouling kinetics by bovine serum albumin (BSA) and humic acid (HA) with a mineralization rate of over 80% (Sun et al., 2018).

Catalytic membranes have also shown more efficient flux recovery when using specific oxidants as cleaning agents. For instance, an iron oxide membrane achieved a flux recovery of 97% for HA, 86% for BSA, and 88% for sodium alginate (SA) when H<sub>2</sub>O<sub>2</sub> was used as a cleaning reagent (De Angelis et al., 2016). Also, transition metal (i.e., Mn, Cu, Fe, and Co) oxide-coated ceramics showed higher cleaning efficiencies than uncoated ceramic membranes fouled by dyes when peroxymonosulfate (PMS) was used as the cleaning agent (Zhao et al., 2019). The improved performance in fouling mitigation, permeate quality, and flux recovery was ultimately attributed to the degradation of organics (i.e., NOM and organic pollutants) by ROS generated in the catalytic membrane system. Therefore, ROS-based oxidation processes play a crucial role in the performance of catalytic membranes.

Sulfate radical (SO<sub>4</sub><sup>•-</sup>)-based AOPs have been widely studied as an alternative oxidation technology in the past few years. According to previous studies, this process is capable of degrading a wide variety of organic pollutants due to its high reduction potential (Lutze et al., 2015b). Recently, a MnO<sub>2</sub>-integrated ceramic membrane was synthesized and used for degrading organic pollutants (Wu et al., 2019). Up to 98.9%

removal of 4-hydroxybenzoic acid was achieved through filtration, mainly relying on  $\text{SO}_4^{\bullet-}$  generated in the PMS/catalytic membrane. Although fouling mitigation was also observed in that PMS/catalytic membrane system, the transformation or removal of NOM directly linked to fouling was not investigated. Interestingly,  $\text{SO}_4^{\bullet-}$  has been shown highly efficient in the mineralization of NOM in a Co/PMS system (Zhang et al., 2019). Therefore, a significant NOM transformation or removal in an  $\text{SO}_4^{\bullet-}$ -based catalytic membrane system would be highly expected; thus, contributing to improved permeate quality, decreased fouling during filtration, and more efficient cleaning processes.

The main goal of this study was to investigate the performance of an  $\text{SO}_4^{\bullet-}$ -based catalytic membrane filtration process. Rather than focusing on the removal of pollutants, the main focus was set on NOM transformation, fouling behavior, and cleaning efficiency. A novel  $\text{MnO}_2\text{-Co}_3\text{O}_4$  composite was used as a catalytic material for ceramic membrane surface modification, where  $\text{SO}_4^{\bullet-}$  was generated in the presence of PMS. This Co-based composite catalyst was selected for  $\text{SO}_4^{\bullet-}$  production because of the reported high catalytic efficiency of Co oxide in PMS decomposition (Anipsitakis et al., 2005). Also, this hybrid metal oxide has exhibited high efficiency in the activation of ozone into radicals (Guo et al., 2016). The catalytic membrane was prepared through the filtration of a  $\text{MnO}_2\text{-Co}_3\text{O}_4$  nanoparticle suspension, followed by sintering and sonication. The  $\text{SO}_4^{\bullet-}$  production on the catalytic membrane was confirmed by using *p*CBA and NB as a probe compound. Fouling tests were conducted with feedwater prepared with a mixture of well-characterized NOM isolates of different physicochemical properties from various aquatic environments. The change of organics before and after filtration was studied using classic NOM characterization techniques (i.e., UV-vis spectrometer, Fluorometer, TOC analyzer). The performance

of the modified ceramic membrane towards fouling and cleaning efficiency using PMS solution were also investigated. The results of this study would significantly assist in the optimization of  $\text{SO}_4^{2-}$ -based catalytic membrane processes for future successful industrial implementation. .

## 5.2 Experimental Section

### 5.2.1 Chemicals and materials

Methanol (MeOH) of HPLC grade was purchased from Honeywell Burdick & Jackson, and hydrochloric acid (HCl, 32%) was supplied by UNIVAR. All the solutions: PMS (Oxone,  $2\text{KHSO}_5 \cdot \text{KHSO}_4 \cdot \text{K}_2\text{SO}_4$ , Sigma-Aldrich), *p*-chlorobenzoic acid (*p*CBA, Acros Organics), nitrobenzene (NB, Sigma-Aldrich), and sodium hydroxide (NaOH, UNIVAR) were prepared with ultrapure water (PURELAB Ultra, ELGA).  $\text{MnO}_2$ - $\text{Co}_3\text{O}_4$  nanoparticles were synthesized through the oxidation of cobaltous nitrate ( $\text{Co}(\text{NO}_3)_2 \cdot 6\text{H}_2\text{O}$ ) by potassium permanganate ( $\text{KMnO}_4$ ), and then rigorously characterized as previously reported (Guo et al., 2016). The ceramic membranes were obtained from TAMI Industries (France), and their characteristics were shown in Table A4-1.

The feedwater was reconstituted using extracted hydrophobic and colloidal NOM isolates: hydrophobic fractions from Suwannee River (HPO-SRNOM, USA) and Blavet River (HPO-Blavet, France) (Croue et al., 2000), and soluble colloidal fractions from a river in the Brittany Region (Colloids-Brittany, France) (Lee et al., 2006) and from a nanofiltration (NF) unit (soluble fraction of the biofilm) in the Mery Sur Oise Drinking Water Treatment Plant in Paris (Colloids-Mery, France) (Croué unpublished data). The percentage of colloids in the mixture was approximately 10%; thus, highly representative of natural aquatic environments (Wershaw et al., 2005).

These NOM fractions have been characterized in earlier studies. HPO fractions isolated from Suwannee and Blavet rivers have been defined as a typical humic-like substance with a significant content of aromatic and phenolic carbon and high C/O, C/H, and C/N ratios. Conversely, the Colloids-Brittany fraction isolated according to Leenheer et al. (Leenheer et al., 2000b) protocol incorporates larger molecular structures characterized by higher nitrogen content and low content of aromatic/phenolic carbon. Amino sugars, proteins, and polysaccharides (i.e., peptidoglycan-type structure) are present in this biopolymer structure, conferring it considerable hydrophilic properties. The soluble fraction of the foulant layer recovered from the surface of a nanofiltration membrane, Colloids-Mery, was separated from the insoluble fraction of the scrapped foulant by centrifugation and further lyophilized. The molecular composition of Colloids-Mery resembles the one described for Colloids-Brittany, however, Fourier transformed infrared analysis showed that the former contains a higher proportion of polysaccharides (Figure A4-1, to be compared with results shown in Lee et al. (2006) for Colloids-Brittany) based on the relative abundance of polysaccharides (C-O stretching of alcohols around  $1000\text{ cm}^{-1}$ ) to proteins (amide I band, C=O stretching around  $1650\text{ cm}^{-1}$ ).

### **5.2.2 Preparation and characterization of $\text{MnO}_2\text{-Co}_3\text{O}_4$ coated ceramic membrane**

Prior to use, a sequential cleaning with NaOH,  $\text{HNO}_3$  and DI water was conducted with the obtained membranes as described elsewhere (Lu et al., 2016a). Following the cleaning procedures,  $\text{MnO}_2\text{-Co}_3\text{O}_4$ -coated ceramic membrane was prepared as follows:  $\text{MnO}_2\text{-Co}_3\text{O}_4$  nanoparticles were dissolved in ultrapure water to obtain a stock nanoparticle suspension of 0.2g/L. Predetermined amount of the stock solution was diluted with 200 ml of ultrapure water and the obtained nanoparticle solution was

filtered through the ceramic membrane at 1 bar. At the end of the filtration, a theoretical value of 0.5–4 mg nanoparticles were loaded onto the ceramic disc. The coated membrane was thereafter sintered at 550 °C for an hour under air atmosphere and then treated with sonication for approximately 15 seconds with an operational frequency of 44 kHz. Various analytical techniques were employed for the characterization of the catalytic membrane. To check the influence of coating on membrane permeability, permeate flux of both original and coated membrane was recorded with pure water.

### 5.2.3 Experimental procedures

Fouling tests were conducted using 100 mL of NOM solution as feedwater in a dead-end mode filtration setup (Figure A4-2) at a constant pressure of 1 bar. Instead of buffering solution, NaOH was used for pH adjustment where needed to avoid the influence of other radical species such as carbonate/bicarbonate radicals formed through oxidation of carbonate/bicarbonate by  $\text{SO}_4^{\bullet-}$ . The mass of permeate was tracked using an electronic balance and the output data was recorded through a data acquisition system. Based on the collected data, the change in permeate flux could be calculated. Specifically, permeate flux (( $J$ ,  $\text{L m}^{-2} \text{h}^{-1}$ )) could be obtained from Equation 5.1:

$$J = \frac{V}{At} \quad \text{Equation 5.1}$$

Where  $V$  (L) is the volume of permeate,  $A$  ( $\text{m}^2$ ) is the effective membrane area, and  $t$  (h) is the filtration time.

Flux decline ( $F_d$ , %) can thus be calculated as

$$F_d(\%) = \left(1 - \frac{J}{J_0}\right) \times 100 \quad \text{Equation 5.2}$$

Where  $J$  ( $\text{L m}^{-2} \text{h}^{-1}$ ) and  $J_0$  ( $\text{L m}^{-2} \text{h}^{-1}$ ) is the permeate flux at the end and the beginning of each filtration cycle.

Retention rate ( $R$ , %) of organic foulants can be found from:

$$R(\%) = \left(1 - \frac{C_p}{C_0}\right) \times 100 \quad \text{Equation 5.3}$$

Where  $C_p$  is the  $\text{UV}_{254}$  or TOC in permeate, and  $C_0$  is the initial  $\text{UV}_{254}$  or TOC in feedwater. Different cleaning methods were used for the flux restoration of the fouled membrane. Backwash was achieved by flushing the inverted fouled ceramic in the membrane cell with an operational pressure of 1.25 bar. Chemical cleaning was performed by either filtering 100 ml of 10 mM PMS solution through fouled membrane or by soaking fouled ceramics in 10 mM HCl, NaOH or PMS solution at room temperature ( $20 \pm 1$  °C). The average permeate flux with pure water with the cleaned membrane was expressed as  $J_c$  ( $\text{L m}^{-2}\text{h}^{-1}$ ). Flux recovery rate was thus calculated as

$$Fr(\%) = \left(\frac{J_c}{J_0}\right) \times 100 \quad \text{Equation 5.4}$$

Membrane resistance ( $R_s$ ,  $\text{m}^{-1}$ ) was calculated based on the following equation:

$$R_s(\text{m}^{-1}) = \frac{\Delta P}{\mu J} \quad \text{Equation 5.5}$$

Where  $\Delta P$  is the operational pressure (Pa),  $\mu$  is the dynamic viscosity (Pa·s) of the NOM solution, and  $J$  is the permeate flux ( $\text{L m}^{-2}\text{h}^{-1}$ ).

#### 5.2.4 Analytical methods

Hydrodynamic diameter and Zeta potential of  $\text{MnO}_2\text{-Co}_3\text{O}_4$  nanoparticles were measured with a Zetasizer (nano ZS, Malvern, UK) as previously described (Zhang et al., 2018). The catalytic behavior of the nanoparticles was explored by looking at the rate of PMS decomposition, where PMS residual was measured using a method in a previous study (Zhang et al., 2019). The oxidation state of each element on the membrane was characterized by X-ray photoelectron spectroscopy (XPS, PerkinElmer, USA) and the topography were studied using atomic force microscopy (AFM, Bruker, USA), respectively.

The change in *p*CBA and NB concentration with filtration at an 1 min interval were studied with an HPLC unit equipped with a  $250 \text{ mm} \times 4.6 \text{ mm}$  C18 5- $\mu\text{m}$  reverse phase column (Alltima<sup>TM</sup>, GRACE) and UV detector (Agilent 1100 series, USA). The concentration of the probe compounds after filtration were presented as an average of the multiple results within 5 min. The detecting wavelength was set as 238 nm and 270 nm for *p*CBA and NB, respectively. UV light absorbance at 254 nm ( $\text{UV}_{254}$ ) of different solutions were analyzed using a Cary 60 spectrophotometer (Agilent, USA). The total organic carbon content in feedwater and permeate was measured with Shimadzu TOC-L analyzer (SHIDMAZU, Japan). Fluorescence excitation and emission matrices (EEM) was acquired with a Fluorescence spectrometer (Cary Eclipse, Varian) based on the method from Chen et al. (2003). Specifically, the measurements were taken with a scan rate of 1200 nm/min and excitation/emission slit

bandwidth of 5nm, respectively. The excitation wavelength started from 220 nm to 400 nm with a 5 nm increment, and the emission spectra were recorded from 290 nm to 550 nm with a 2 nm increment. The metal leaching content were analysed using an inductively coupled plasma mass spectrometry (ICP-MS, Agilent Technology) with a detection limit of 0.0001mg/L.

### **5.3 Results and Discussion**

#### **5.3.1 Characterization of MnO<sub>2</sub>-Co<sub>3</sub>O<sub>4</sub> nanoparticles and catalytic membrane**

##### *5.3.1.1 Characterization of MnO<sub>2</sub>-Co<sub>3</sub>O<sub>4</sub> nanoparticles*

The size of the coating material has been reported as related to the intrinsic resistance of the coated membrane due to pore blocking effect (Cheng et al., 2017b); therefore, the hydrodynamic diameter of the MnO<sub>2</sub>-Co<sub>3</sub>O<sub>4</sub> nanoparticles was investigated by Dynamic Light Scattering (DLS) measurements. The results showed a hydrodynamic diameter of  $136.86 \pm 4.33$  nm with a Polydispersity Index (PDI) value of  $0.14 \pm 0.03$ , indicating a monodispersed nanoparticle population in solution. As the mean pore size of the original ceramic membrane was 8.6 nm (50 kDa, Table A4-1), the deposition of the nanoparticles onto the surface of the membrane would be favorable during the preparation of catalytic membranes through filtration of nanoparticle suspension.

A negative value ( $-19.83 \pm 0.51$ ) of Zeta Potential (ZP) was observed for MnO<sub>2</sub>-Co<sub>3</sub>O<sub>4</sub> nanoparticles at unadjusted pH ( $5.8 \pm 0.3$ ), indicating a negatively-charged surface. The change in ZP as a function of solution pH was also recorded (Figure A4-3). Interestingly, the isoelectric point of MnO<sub>2</sub>-Co<sub>3</sub>O<sub>4</sub> was not observed even at a solution pH as low as 2. The isoelectric point of TiO<sub>2</sub>/ZrO<sub>2</sub> (i.e., the filtration layer of the pristine ceramic membrane) was recorded at pH ~6 (Fu et al., 1996). These results indicated that repulsive electrostatic interactions between coated membranes and

NOM would be expected at approximately neutral pH conditions, where NOM is also negatively charged.

The catalytic activity of MnO<sub>2</sub>-Co<sub>3</sub>O<sub>4</sub> nanoparticles has also been investigated by studying the decomposition of PMS under different conditions. In the current study, an enhanced PMS decay (i.e., high decay rate) was recorded due to catalytic decomposition by the MnO<sub>2</sub>-Co<sub>3</sub>O<sub>4</sub> nanoparticles. Further details regarding the catalytic activity of the coated membranes and their production of radical species are discussed in section 5.3.2.

#### ***5.3.1.2 Characterization of catalytic membrane***

As indicated by the optical images of the pristine and coated ceramics (Figure A4-4), MnO<sub>2</sub>-Co<sub>3</sub>O<sub>4</sub> nanoparticles were successfully dispersed onto the membrane surface through filtration of nanoparticles suspension. Sonication was applied to remove loosely-bound nanoparticles. Remarkably, following sonication of 15 sec (i.e., at an operational frequency of 40 kHz), the dispersed nanoparticles mostly remained stable on the surface. The elemental composition of the nanoparticles was also investigated through XPS analysis (Text A4-1., Figure A4-5).

Atomic Force Microscopy (AFM) was used to investigate the topography and chemical mapping (i.e., phase imaging) of the surface of the membranes. Briefly, the surface of both membranes was physically heterogeneous at the nano-scale (Figure A4-4b). However, the MnO<sub>2</sub>-Co<sub>3</sub>O<sub>4</sub> coating slightly decreased the surface roughness as indicated by its lower roughness ( $R_{\text{RMS}}$ :  $45.1 \pm 5.9$  versus  $50.9 \pm 5.5$  nm). This lower roughness would be caused by the entrapment of nanoparticles in the valleys on the membrane surface; thus, increasing the stability of the nanoparticles on the membrane surface. Phase images (i.e., chemical mapping of surfaces based on the differences in

elemental composition) showed the difference in the elemental composition of pristine and coated membranes; thus, indicating successful adsorption of the nanoparticles on the ceramic membranes (Figure A4-4c). Moreover, the occurrence of different oxidation states of Mn (i.e., Mn(IV) and Mn(III)) and Co (i.e., Co(III) and Co(II)) was confirmed through XPS analysis (Text A4-1.). The permeability with pure water was also measured and compared between pristine and coated membranes. The incorporation of 1 mg MnO<sub>2</sub>-Co<sub>3</sub>O<sub>4</sub> nanoparticles showed a minor effect on the permeability of membranes (i.e., 370.5 Lm<sup>-2</sup>h<sup>-1</sup>bar<sup>-1</sup> and 340.33 Lm<sup>-2</sup>h<sup>-1</sup>bar<sup>-1</sup> for pristine and coated membranes, respectively)(Figure A4-6).

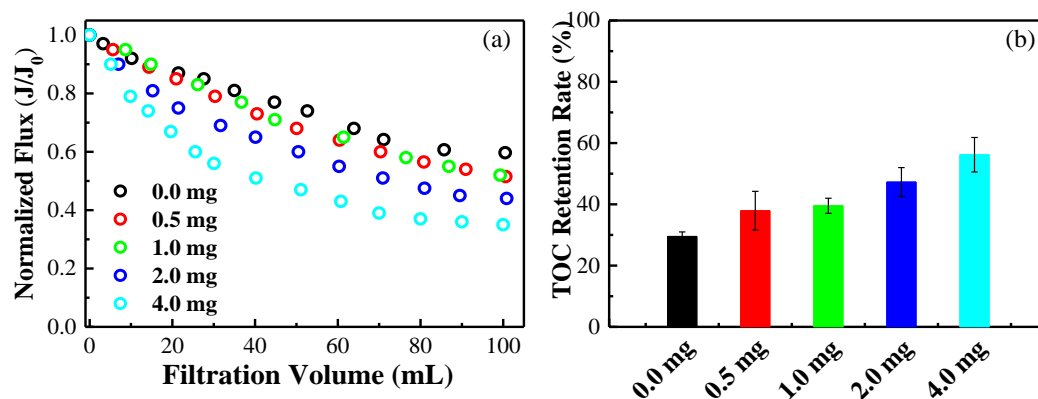


**Figure 5-1. (a) Normalized flux decline, and (b) TOC retention rate for coated membranes with different MnO<sub>2</sub>-Co<sub>3</sub>O<sub>4</sub> loadings (0.0–4.0 mg). Fouling experiments were conducted with NOM-containing feed water (~5mgC/L NOM mixture with ~10% colloids and ~90% HPO fractions) at unadjusted pH of 6.3 ± 0.2 and operating pressure of 1bar.**

With the filtration of pure water, a coating of 0.5–4.0 mg catalyst showed a minor influence on the pure water flux or intrinsic membrane resistance (i.e., < 10%, Table A4-2) as compared to the pristine membrane. With the filtration of NOM (~5 mgC/L) solutions, the water flux and TOC retention rate for both pristine and coated membranes were also measured. The NOM solution used was a mixture of previously isolated colloidal (~10%) and hydrophobic fractions (~90%) selected based on their

fouling behaviors (will be discussed in 5.3.3.1) and environmental relevance. Following the filtration of 100 mL NOM solution, a 40% decrease in water flux (Figure 5-1), a 67% increase in membrane resistance (Table A4-2) and a 30% NOM retention rate (Figure 5-1) were recorded with the pristine membrane. With the incorporation of  $\text{MnO}_2\text{-Co}_3\text{O}_4$  nanoparticles, a decrease in water flux (Figure 5-1a, and profiles of original flux were present in Figure A4-7) and an increase in membrane resistance (Table A4-2) as well as NOM retention rate (Figure 5-1b) were observed. Moreover, an increase in the nanoparticle loadings led to a more pronounced change in these parameters. For instance, a coating of 0.5 mg nanoparticles only led to a 48% decrease in water flux, a 94% increase in membrane resistance, and a 38% NOM retention rate. However, a 65% decrease in water flux, a 185% increase in membrane resistance, and a 56% NOM retention rate were achieved with a 4 mg  $\text{MnO}_2\text{-Co}_3\text{O}_4$  nanoparticle coating. The results clearly indicate that increasing nanoparticle load could induce an additional decrease in water flux and an increase in membrane resistance as well as NOM retention rate. To minimize the influence of the coating on water flux and maximize the catalytic ability, a coating of 1mg  $\text{MnO}_2\text{-Co}_3\text{O}_4$  nanoparticles (i.e.,  $0.06 \text{ mg/cm}^2$ ) was selected for the following experimental conditions and analysis.

### 5.3.2 Catalytic performance of the coated membrane

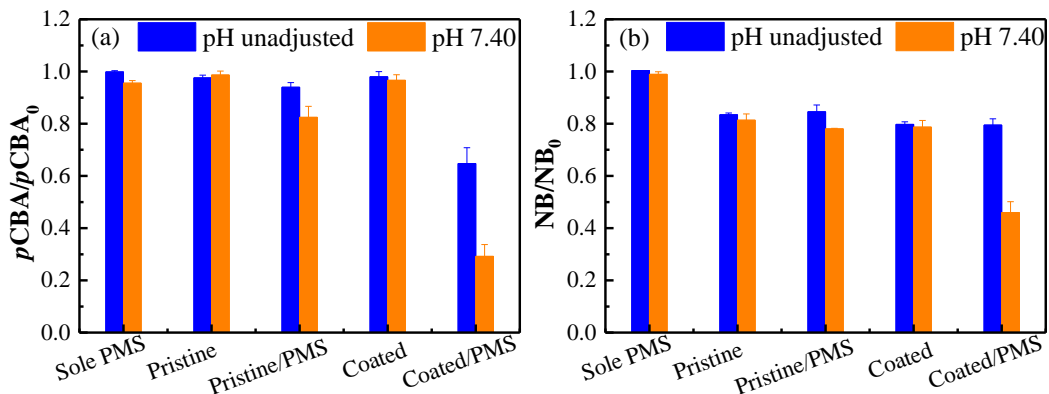


**Figure 5-2. (a) *p*CBA and (b) NB removal during filtration with pristine and coated membranes with or without PMS addition. Conditions: [*p*CBA]<sub>0</sub> = 2 μM, [NB]<sub>0</sub> = 2 μM, [PMS]<sub>0</sub> = 1 mM, TMP = 1.0 bar, temperature = 20 ± 1°C, pH = 5.20 ± 0.20 without PMS addition and 3.40 ± 0.10 with PMS addition without pH adjustment, pH was adjusted to 7.40 ± 0.20 with 0.01M NaOH for both sole and catalytic filtration process.**

The generation of reactive species was confirmed through the filtration of probe compound-containing solution in the presence of 1mM PMS. The removal efficiency of *p*CBA and NB (i.e., used as SO<sub>4</sub><sup>-</sup> and ·OH probe compounds, respectively) under different experimental conditions were shown in Figure 5-2. The removal of *p*CBA by sole PMS or adsorption was negligible under both pH conditions (i.e., pH 3.40 and 7.40), while approximately 20% adsorption efficiency was observed with NB. Adsorption of NB onto MnO<sub>x</sub>- or TiO<sub>2</sub>- based catalyst have also been reported in previous studies (Ma et al., 2005; Yang et al., 2007). Upon addition of PMS (i.e., probe compound-containing solution), a significant increase in *p*CBA removal was observed with the coated membrane as compared to the pristine membrane (Figure 5-2a). In addition, the removal efficiency was enhanced with an increase in pH. The removal rate increased from 35% at pH 3.40 to 70% at pH 7.40. This improved catalytic performance was probably caused by an enhancement in radical production and/or the increase in the reactivity of *p*CBA at higher pH conditions (Benner et al., 2009). Specifically, the deprotonated form of *p*CBA at a pH significantly higher than its pK<sub>a</sub> (i.e., 3.98) is more reactive to radicals. The removal of NB through the hybrid PMS-catalytic membrane process was insignificant at pH 3.40; however, this removal increased to 54% with a pH adjusted to 7.40. The increase in NB removal at higher pH could probably be attributed to the favorable conversion of OH<sup>-</sup> to ·OH under caustic conditions. Overall, these findings suggested that reactive species were generated through the catalytic decomposition of PMS by the MnO<sub>2</sub>-Co<sub>3</sub>O<sub>4</sub> nanoparticles coated on the membrane. In addition, the higher removal of *p*CBA than NB indicated the

predominance of  $\text{SO}_4^{\bullet-}$  in the catalytic membrane system. The results also implied that organic pollutants susceptible to these radical species could be potentially removed by the catalytic membrane.

### 5.3.3 Fouling behavior of catalytic membrane

#### 5.3.3.1 Fouling behavior of different NOM solutions

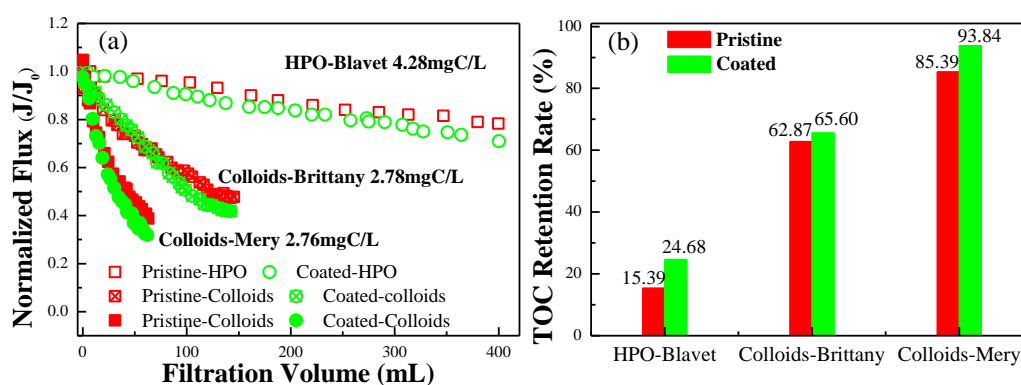


**Figure 5-3. (a) Fouling profile and (b) TOC retention rate for both pristine and coated membranes caused by different NOM solutions: 4.28 mgC/L HPO-Blavet (pH 5.87), 2.78 mgC/L Colloids-Brittany (pH 6.74), and 2.76 mgC/L Colloids-Mery (pH 6.45) at a transmembrane pressure of 1 bar.**

Fouling tests for both pristine and coated membranes were conducted with different NOM solutions prepared using ultrapure water (Figure 5-3). Different fouling profiles were observed with the selected three NOM solutions. Fouling was minor with the presence of sole hydrophobic fractions, for instance, flux decline was lower than 30% with the filtration of 400 mL of NOM solution. However, a 55% decrease in the normalized flux could be achieved with the filtration of 150 mL of Colloids-Brittany solution. Interestingly, even higher fouling was observed with Colloids-Mery, causing an approximately 65% decrease in permeate flux with a 60 mL filtration volume. The stronger fouling behavior caused by colloids as compared to HPO fractions has been reported in previous studies (Zheng et al., 2014). The higher fouling potential of

Colloids-Mery in the current study was probably due to its higher content of polysaccharides (5.2.1), leading to an enhanced interaction with the membrane surface through hydrogen-bonding (Zaouri et al., 2017). Overall, the influence of the coating on water flux was insignificant, consistent with previous findings (Figure 5-3a). The lowest fouling potential of HPO fractions could be attributed to its smaller molecular size (i.e., < 3nm (Aoustin et al., 2001)) as compared to the pore size of the membrane (i.e., 8.6 nm, Table A4-1); thus, the HPO molecules would easily transport through the membrane without causing significant fouling. Conversely, the colloidal molecules with a much larger molecular size would more likely be retained by the membrane (i.e., adsorbed on membrane surface or within membrane pores). For instance, the TOC retention rate was highest for Colloids-Mery and lowest for HPO-Blavet (Figure 5-3b). In addition, more TOC was removed with the coated membrane for all the three NOM solutions, also experiencing a slightly higher extent of fouling as compared to the pristine membrane. This observation indicated a potential correlation between TOC retention rate and fouling in the sole membrane filtration process.

### 5.3.3.2 Transformation of organic foulants .

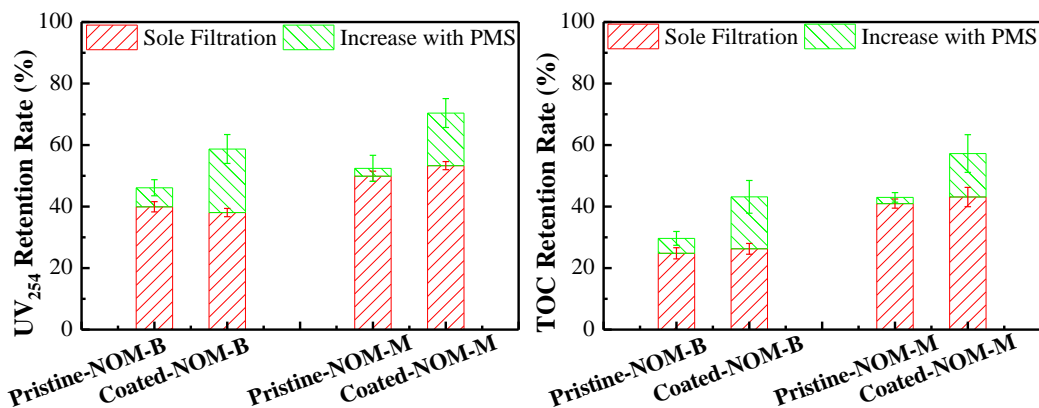


**Figure 5-4. (a) UV<sub>254</sub> and (b) TOC removal rate with pristine and coated membranes. NOM solution-B: 0.56 mgC/L Colloids-Brittany + 4.45 mgC/L HPO-SRNOM, and NOM solution-M: 0.55mgC/L Colloids-Mery + 4.45 mgC/L**

**HPO-SRNOM. Experimental conditions: Operational pressure =1.0 bar, temperature  $20\pm 1^\circ\text{C}$ , pH ~ 6 without PMS addition and  $3.40\pm 0.10$  with 1 mM PMS addition.**

The change in  $UV_{254}$  of the NOM solution (i.e., mixture of Colloids and HPO-SRNOM) following membrane filtration was investigated as aromaticity has been reported to play an important role in membrane fouling (Aoustin et al., 2001). The varying trend of  $UV_{254}$  values of the NOM solutions before and after filtration was measured for both pristine and coated membranes under varying conditions. The initial  $UV_{254}$  value for both NOM solutions was similar at approximately  $0.18\text{ (cm}^{-1}\text{)}$ . The absorbance was predominantly contributed by the HPO fractions due to the negligible UV absorbance of the colloidal fractions (i.e.,  $SUVA < 0.4\text{ m}^{-1}(\text{mgC/L})^{-1}$ ). Under sole membrane filtration (red bar in Figure 5-4a), a decrease in  $UV_{254}$  value in the permeate was observed for both pristine and coated membranes. The difference in the  $UV_{254}$  retention rate between pristine and coated membranes was insignificant. Interestingly, a higher removal in  $UV_{254}$  was recorded for NOM solution-M (i.e.,  $0.55\text{ mgC/L Colloids-Mery} + 4.45\text{ mgC/L HPO-SRNOM}$ ) than for NOM solution-B ( $0.56\text{ mgC/L Colloids-Brittany} + 4.45\text{ mgC/L HPO-SRNOM}$ ) i.e., 50% and 40%, respectively. As Colloids-Mery showed higher fouling potential than Colloids-Brittany, the higher  $UV_{254}$  removal for NOM solution-M than solution-B could be caused by the increased retention of HPO fractions due to enhanced interactions with Colloids-Mery. With the addition of 1mM PMS in the feedwater, the  $UV_{254}$  removal efficiency was further increased (green bar in Figure 5-4a). This increase was higher for coated membrane than pristine membrane; specifically, 20.7% versus 6.2% for NOM solution-B, and 17.1% versus 2.6% for NOM solution-M, respectively. This could be attributed to the enhanced reaction between NOM and  $\text{SO}_4^{\cdot-}$  generated in the catalytic membrane system. The slightly enhanced  $UV_{254}$  removal with the pristine membrane was

probably due to the reaction of electron-rich moieties with PMS (Zhao et al., 2019), as its production of radical species was detected as negligible (Figure 5-2).

The TOC removal rate of the two NOM solutions through either sole membrane filtration or hybrid oxidation-filtration process was also measured. Consistent with the trend observed with the  $UV_{254}$  retention rate, the TOC retention rate (red bar in Figure 5-4b) was higher for NOM solution-M than NOM solution-B under sole membrane filtration. Consistently, the difference in the change of specific UV absorbance at 254 nm (i.e., SUVA) value before and after filtration was insignificant between NOM solution-M and NOM solution-B (Table A4-3). Specifically, a decrease of 15 to 20% of the SUVA was observed with sole membrane filtration under all conditions. However, the difference in TOC retention rate between NOM solution-M and NOM solution-B was higher than that of  $UV_{254}$ . This could also be explained by the distinct fouling potential of the two colloidal fractions in each NOM solution. Not only the moieties with larger molecular size (colloids and high MW UV light-absorbing structures) could be easily withheld, the relatively smaller molecular weight moieties (i.e., less enriched in aromatic structures) could also be screened out due to a probably more efficient interaction of HPO molecules with Colloids-Mery. Similarly, the TOC removal efficiency was significantly increased during the hybrid oxidation-filtration process, i.e., 16.9% versus 4.8% for NOM solution-B, and 14.1% versus 2.0% for NOM solution-M. Moreover, the removal rate of SUVA was also higher with PMS/coated membrane than PMS/pristine membrane process (i.e., 29% versus 16%, Table A4-3), indicating a more efficient removal of aromatic structures of the former. Overall, the enhanced removal of aromatics, as well as TOC, would be attributed to the transformation or removal of the organic foulants through reaction with the generated  $SO_4^{\bullet-}$ .

Although an increased removal efficiency for *p*CBA and NB was observed at pH 7.40, the change in the removal efficiency of UV<sub>254</sub> and TOC was negligible when pH was increased to 7.40 (i.e., within 7%, Figure A4-8). This could be ascribed to the highly heterogeneous nature of NOM as compared to simple compounds. Specifically, the change in reactivity with pH would not be as significant as a simple compound (i.e., *p*CBA, Figure 5-2). The results indicated that the performance of the catalytic membrane would be stable at a pH range from 3.40–7.40, and the catalytic membrane would also be applicable in multiple aquatic environments (e.g., natural water, wastewater, etc). These results also confirmed that the increase in UV<sub>254</sub> or TOC removal rate with PMS addition was a product of radical production instead of pH change.

### 5.3.3.3 Change of fouling profile

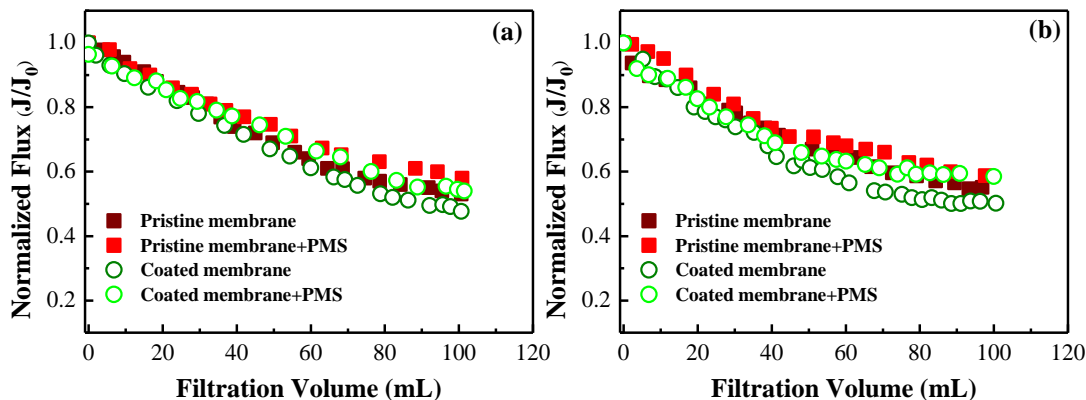


**Figure 5-5. Normalized water flux of the pristine and coated membrane with or without PMS addition in (a) NOM solution-B and (b) NOM solution-M. NOM solution-B: 0.56 mgC/L Colloids-Brittany + 4.45 mgC/L HPO-SRNOM, NOM solution-M: 0.55 mgC/L Colloids-Mery + 4.45 mgC/L HPO-SRNOM. Experimental conditions: Operational pressure =1.0 bar, temperature  $20 \pm 1$  °C, pH ~ 6 without PMS addition, and  $3.40 \pm 0.10$  with 1 mM PMS addition.**

The water flux of the pristine and coated membrane with or without PMS addition in NOM solution-B or NOM solution-M were also studied at unadjusted pH. As shown

in Figure 5-5 (i.e., results selected as representative of multiple tests showing the same trend), an approximately 50% flux decline was measured for both membranes upon filtration of 100 mL NOM solution-B or NOM solution-M. With the addition of 1mM PMS, the flux increase was only 8% for the coated membrane, slightly higher than the pristine membrane (i.e., 4%). Moreover, the influence of pH on fouling mitigation was negligible (Figure A4-9, fouling profile obtained at pH 7.40). Despite a higher removal in UV<sub>254</sub> or TOC in the PMS/coated membrane process, the improvement in fouling mitigation was insignificant possibly due to the formation of lower molecular weight organics (i.e., as reflected by the blue shift of the peaks in fluorescence spectra, Text A4-2) adsorbing onto the internal wall of the membrane pores and consequently causing more fouling through pore constriction. Specifically, the fouling could be caused by the interaction of treated NOM molecules with the membrane through hydrogen-bonding due to the formation of hydroxylated products with SO<sub>4</sub><sup>-</sup> oxidation (Zhang et al., 2019).

The fouling mitigation effect of catalytic membranes has been less investigated as compared to its performance on organic pollutant removal (Cheng et al., 2017b; Guo et al., 2016). Interestingly, an insignificant flux increase (i.e., approximately 10%) has also been observed with an Mn oxide integrated catalytic ceramic membrane (Wu et al., 2019). However, the possible reasons causing this minor effect were not provided. To explain the observations in the current study, fouling mechanisms under varying conditions were investigated using filtration models. Membrane fouling can be classified into four categories: Complete pore blocking, intermediate pore blocking, standard pore constriction, and cake layer filtration (Shen et al., 2010). The equations and descriptions for different filtration models were listed in Table A4-4. The R<sup>2</sup> values obtained from the fitting of the experimental data using the fouling model

equations were summarized in Table 5-1. As reflected by the  $R^2$  values in Table 1, the standard blocking model displayed the best fitting to the experimental data under all experimental conditions, where an  $R^2$  value of up to 1.000 was calculated. These results indicated the predominance of pore constriction caused by the deposition of foulants onto the internal wall of the membrane pores. Nevertheless, other fouling mechanisms may also play a role in fouling evolution (Table 5-1). The reaction with  $SO_4^{\bullet-}$  would more likely occur for organics adsorbed at the membrane surface where the  $MnO_2-Co_3O_4$  nanoparticles would mainly be present (section 5.3.1), and radical species were generated. Consequently, the oxidation of the organics trapped within membrane pores might not be efficient, probably due to its short-lived nature or unfavorable radical diffusion (e.g., quenching by NOM molecules in liquid phase). Consequently, the overall percentage of the organics exposed to radical would be small because the majority of the organics would deposit on the internal wall of the membrane pore channel as revealed by the predominant fouling mechanism. Specifically, only larger molecules i.e., Colloids-HPO complex could react with radicals due to their higher possibility of deposition onto the membrane surface. However, the increased fouling caused by the formation of smaller molecules and their subsequent adsorption on the pore channel could not be reflected by these fitting results, as a fouling mechanism of standard pore constriction was already predominant during sole filtration (i.e., absence of PMS in NOM solution, Table 5-1).

**Table 5-1.  $R^2$  values from the fitting of the experimental data with filtration models ( $R^2$ : coefficient of determination for different modelings; STDEV: Standard deviation in  $R^2$  of duplicate modeling. The experimental data used for modeling was obtained from fouling tests using NOM solution-M)**

Complete Blocking		Intermediate Blocking		Standard Blocking		Cake Layer Filtration	
$R^2$	STDEV	$R^2$	STDEV	$R^2$	STDEV	$R^2$	STDEV

Pristine	0.889	0.00	0.906	0.00	1.000	0.00	0.905	0.02
Pristine/PMS	0.792	0.00	0.771	0.04	0.999	0.00	0.812	0.01
Coated	0.876	0.03	0.872	0.03	1.000	0.00	0.879	0.05
Coated/PMS	0.862	0.06	0.882	0.05	1.000	0.00	0.889	0.03

### 5.3.4 Cleaning efficiency of catalytic membranes

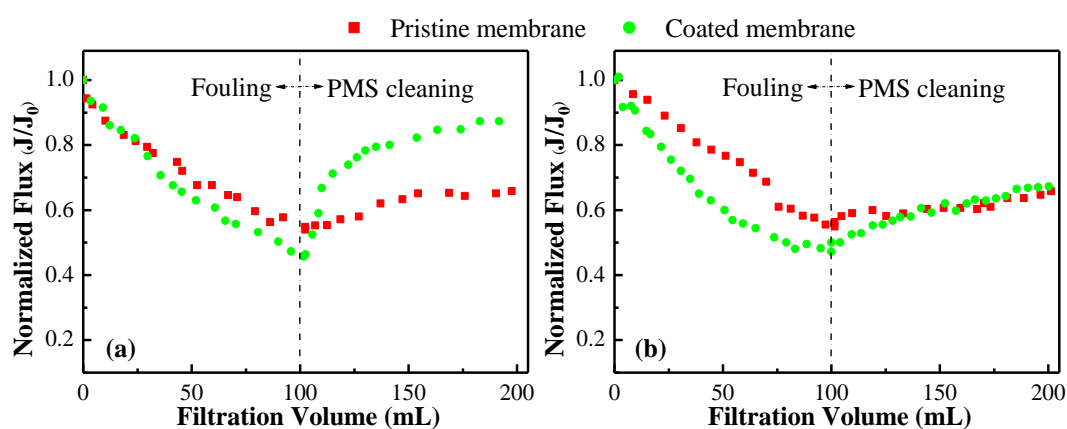


**Figure 5-6. Change in normalized water flux during fouling test and PMS cleaning for (a) NOM solution-B and (b) solution-M fouled membrane. Conditions: Fouling tests were conducted with 100 mL of feed water containing 0.56mgC/L Colloids-Brittany + 4.45 mgC/L HPO-SRNOM for (a) and 0.55mgC/L Colloids-Mery + 4.45 mgC/L HPO-SRNOM for (b). Cleaning was performed with 100 mL of 10 mM PMS solution at  $\text{pH } 3.20 \pm 0.10$ .**

The performance of PMS cleaning for both the pristine and coated membrane was studied through flux restoration. PMS cleaning was conducted by the filtration of 10 mM PMS solution through the fouled membrane at pH 3.20. As shown in Figure 5-6 (i.e., representative results of multiple cleaning tests), a higher flux recovery was obtained with the coated membrane for both NOM solutions. In addition, the flux recovery was faster at the beginning of the cleaning phase and then slowed down. Specifically, the flux was recovered from 46% to 82% for NOM solution-B and from

50% to 62% for NOM solution-M with the filtration of 50 mL of PMS solution. However, the flux was only increased by approximately 5% with another 50 mL PMS solution. This low flux recovery was probably due to a faster reaction of HPO fractions (i.e., major fraction of NOM solution) with  $\text{SO}_4^{\bullet-}$  at the initial phase, as previously reported (Zhang et al., 2019). Moreover, PMS cleaning for the NOM solution-B fouled membrane was more efficient as compared to that fouled by NOM solution-M. Prolonged cleaning time was applied to further improve the cleaning efficiency as the increase in flux slowed down during the cleaning. As an alternative, PMS cleaning was conducted by soaking the fouled membrane in 10 mM PMS solution for different time durations. The results for the membrane fouled by NOM solution-M (i.e., selected as a representative experimental result) showed a slower flux restoration. After a soaking time of 10 min, equivalent to the time frame for filtering 100 mL of 10 mM PMS solution through the membrane, the water flux was recovered by  $19 \pm 0.1\%$  (Figure A4-11), which was higher than that of the former cleaning method (i.e., 12%). The observation seems to indicate that the reaction of NOM with radicals was more favorable under static conditions.

Full flux recovery was achieved when the soaking time was prolonged to 2 hours, which equals to a flux increase of approximately 50% (Figure 5-7a). The efficiency of other cleaning methods, i.e., backwashing, HCl, and NaOH cleaning was also investigated. As it was shown in Figure 5-7a, PMS cleaning exhibited a significant increase in water flux as compared to other cleaning means. In addition, the flux recovery by PMS cleaning for the pristine membrane was lower than the coated membrane (i.e., 75% versus 97%). The increase in water flux for the pristine membrane could be attributed to the reaction of NOM with PMS (Zhao et al., 2019). However, the significantly improved cleaning efficiency for the coated membrane

would be attributed to the catalytic process, where reactive radical species (i.e., mainly  $\text{SO}_4^{\bullet-}$ ) were produced through  $\text{MnO}_2\text{-Co}_3\text{O}_4$  nanoparticles-catalyzed PMS decomposition. The organic foulants could be transformed/degraded and removed by the generated  $\text{SO}_4^{\bullet-}$  with sufficient exposure time, leading to the observed cleaning performance of the coated membrane.

The applicability of PMS cleaning was further evaluated by performing different fouling cycles with both pristine and coated membranes. The filtration of 100 mL NOM solution-M (pH 6.28) followed by PMS cleaning with a soaking time of 2 hours were included in each cycle. The normalized water flux decreased to approximately 55% at the end of fouling test (cycle 1) (Figure 5-7b). Following PMS cleaning, a full flux recovery was observed with the coated membrane, and a flux recovery of 82% was observed with the pristine membrane, leading to a lower initial flux at the beginning of the second filtration cycle. The flux recovery was negligible with PMS cleaning for the pristine membrane at cycle 2; however, the normalized flux increased to 80% for the coated membrane. These results indicated that the catalytic membrane not only exhibited better performance with PMS cleaning but also remained relatively stable in performance within 3 cycles of filtration.

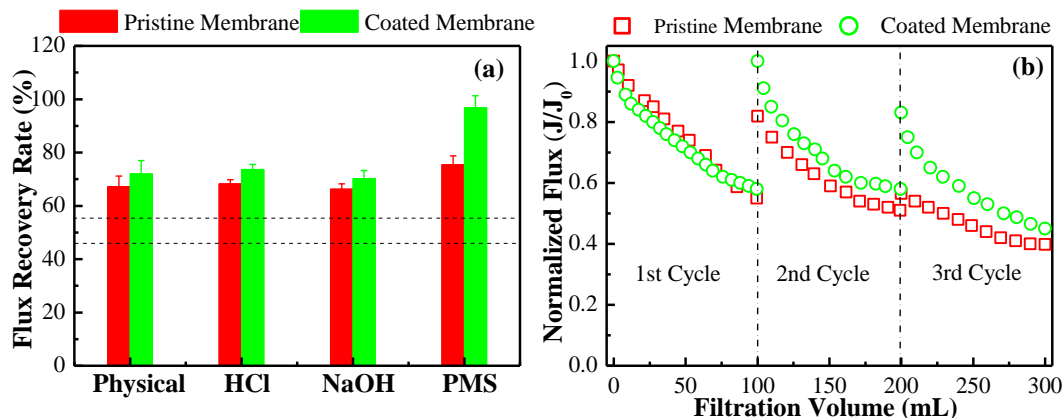


**Figure 5-7. Flux recovery rate with (a) multiple cleaning methods and (b) fouling profiles during filtration cycles with PMS cleaning applied between each fouling cycle for both pristine and coated membranes. Feedwater for fouling tests was prepared with a mixture of 0.55 mgC/L Colloids-Mery and 4.45 mgC/L HPO-SRNOM (pH 6.28). The black dash lines in Figure 5-7a indicate the range of the values in normalized water flux before cleaning.**

### 5.3.5 Metal leaching

The content of leached metals in permeate, i.e., Mn and Co, from MnO<sub>2</sub>-Co<sub>3</sub>O<sub>4</sub> nanoparticles was measured under different experimental conditions (Table A4-5). The leaching level was higher at acidic conditions (i.e., pH 3.40) than in basic environments (i.e., pH 7.40). Besides, metal leaching increased after the first cycle of PMS cleaning and decreased after the second cycle of PMS cleaning. Overall, the concentration of leached Mn ranged from 0.002–0.04 mg/L, accounting for 0.2%–3.7% of MnO<sub>2</sub>-Co<sub>3</sub>O<sub>4</sub> nanoparticles coated on the membrane (1 mg). The concentration of leached Co was measured as 0.008–0.1 mg/L, accounting for 1.4%–10% of the weight of the coated catalyst. The concentration of leached Mn in the current experiments falls within the range of Mn detected in freshwaters, 0.001–0.2 mg/L (WHO, 2004). Leached Co level is higher than that reported for surface water or groundwater ranging from <1µg/L to 1–10µg/L (Kim et al., 2006), suggesting the need for developing efficient Co-based catalyst with less metal leaching.

#### 5.4 Summary

MnO<sub>2</sub>-Co<sub>3</sub>O<sub>4</sub> coated ceramic UF membrane was prepared through a membrane filtration of nanoparticles suspensions followed by sintering and sonication. The incorporation of 1 mg nanoparticles (i.e., 0.06 mg/cm<sup>2</sup>) onto the membrane slightly decreased the surface roughness and showed an insignificant impact on the membrane permeability with pure water. The catalytic property of the MnO<sub>2</sub>-Co<sub>3</sub>O<sub>4</sub> coated membrane was confirmed with the remarkable removal of pCBA during the hybrid oxidation and filtration process. SO<sub>4</sub><sup>•-</sup> was found as the predominant radical species in the catalytic membrane system because of the higher removal efficiency of pCBA than NB. Compared with the pristine membrane, the coated membrane showed a more robust removal of organic foulants with PMS added in the feedwater as well as a higher cleaning efficiency with PMS as a cleaning agent. However, the improvement in permeate flux during fouling tests with PMS added in feedwater was insignificant, probably due to the unfavorable radical oxidation of the organic molecules adsorbed onto the internal walls of membrane pores under the current experimental conditions. The current study provided a comprehensive insight into the performance of SO<sub>4</sub><sup>•-</sup>-based catalytic membrane process. However, further studies are highly required to improve the performance of the catalytic membrane on fouling control. A coating on the membrane surface, as well as onto the inner walls of membrane pores could be developed to increase the efficiency of radical production. In addition, the development of highly efficient catalysts with lower or no metal leaching is highly beneficial and required for the successful implementation of SO<sub>4</sub><sup>•-</sup>-based catalytic membrane process in industrial processes.

## Chapter 6. Conclusions and Future Perspectives

The thesis systematically provides new insights into the reactivity of NOM in advanced oxidation processes and the performance of a  $\text{SO}_4^{\bullet-}$ -based catalytic membrane for NOM transformation, fouling mitigation and TOx removal in water treatment.

Radical species play a critical role in the performance of the catalytic membrane according to previous studies on  $\cdot\text{OH}$ -based catalytic membrane. The information on the reactivity of NOM with  $\text{SO}_4^{\bullet-}$  ultimately provided guidance for the applicability of  $\text{SO}_4^{\bullet-}$ -based catalytic membrane associated with organic foulant transformation and consequently fouling mitigation. The reaction of NOM with  $\text{SO}_4^{\bullet-}$  was distinguished into two phases where an initial fast reaction phase was observed followed by a slow reaction phase. The second-order-rate constant of fast reacting NOM was calculated at an order of  $10^8 \text{ M}^{-1}\text{s}^{-1}$ . The knowledge also implied the application of  $\text{UVA}_{254}$  decrease of NOM as a surrogate indicator of TOx removal efficiency in permeate. The reaction was initiated with the depletion of EDC at fast reacting phase and eventually led to significant carbon removal at slow reacting phase.

A molecular-level investigation on the reactivity of NOM with  $\cdot\text{OH}$  and  $\text{SO}_4^{\bullet-}$  using FT-ICR MS advanced our fundamental understanding on their distinct radical-specific reactivity. Generally, a faster reaction of NOM was observed with  $\cdot\text{OH}$  as compared to  $\text{SO}_4^{\bullet-}$ . The higher reaction rate was attributed to the different reaction sites as well as reaction pathways. Approximately 10–20% of reactive sites were identified as exclusively reactive to specific radical using FT-ICR MS.  $\cdot\text{OH}$  would react with more aliphatic molecules with higher H/C and lower DBE besides electron-rich moieties.

However,  $\text{SO}_4^{\bullet-}$  preferentially targeted at molecules with higher electron density, i.e., with lower H/C, higher O/C, DBE and  $m/z$ . The difference in the reactive sites and the associated reaction pathways would lead to the observed different reactivity. The preferential selection of molecules enriched with  $-\text{COOH}$  by  $\text{SO}_4^{\bullet-}$  provided molecular-level evidence for its higher carbon removal as compared to  $\cdot\text{OH}$  as well as the potential of application of  $\text{SO}_4^{\bullet-}$ -based catalytic membrane.

Catalyst applied for catalytic membrane preparation is also critical for the performance of the modified membrane by impacting the efficiency of radical production. Besides catalytic capability, the interfacial interaction between the catalyst and NOM should also be taken into account in the selection of catalyst due to its direct relationship with catalytic membrane fouling as well as available reactive sites. The information could be obtained by indirectly tracking the influence of NOM on catalyst nanoparticle aggregation using TR-DLS, and directly measuring the interaction force using AFM. Using the analytic techniques, the interaction between NOM with  $\text{MnO}_2$  nanoparticles (i.e., a potential catalyst for  $\text{SO}_4^{\bullet-}$  production) was found correlated with solution chemistry and NOM characteristics. Specifically, the interaction was enhanced with the presence of  $\text{Ca}^{2+}$  due to cation bridging. In addition, NOM with more complex and polymeric structure was found more attractive to  $\text{MnO}_2$  surface and consequently more efficient in blocking reactive sites.

The investigation on the performance of the  $\text{SO}_4^{\bullet-}$ -based catalytic membrane (i.e., with  $\text{MnO}_2\text{-Co}_3\text{O}_4$  as catalytic material) reflected its good application potential for the improvement on permeate quality and fouling mitigation. Removal of *p*CBA as a  $\text{SO}_4^{\bullet-}$  probe compound also implied the capability to remove other  $\text{SO}_4^{\bullet-}$ -susceptible TOrCs during the application of the catalytic membrane in water treatment. Due to the

reactivity of feed water NOM with  $\text{SO}_4^{\cdot-}$ , significant removal of chromophoric NOM as well as carbon was observed. This contributes to the improved permeate quality as well as flux recovery after PMS cleaning. However, its contribution to fouling control was not obvious probably due to the pore constriction fouling mechanisms unfavourable for NOM-radical reaction. Further study targeting at the optimization of the  $\text{SO}_4^{\cdot-}$ -based catalytic membrane process is strongly recommended.

Future perspectives were proposed based on the major findings of the current PhD project as follows. Novel membrane modification technique could be developed to realize a coating onto membrane surface as well as the internal wall of membrane pores to obtain a more efficient radical production. To better understand the efficiency of NOM transformation during catalytic membrane process, a study on the distribution of radical species at membrane surface as well as within membrane pores could be conducted. In addition, the different in the reaction of NOM with radical species under static and dynamic conditions could also be investigated. Though metal leaching level in the thesis complies with the currently available regulations, catalyst showing no leaching or metal-free while with comparable catalytic ability could be developed for the better application of catalytic membrane.

## Appendix 1 Supporting Information-Chapter 2

### Text A1-1. Evolution of fluorophores as a function of PMS exposure in Co(II)/PMS system

Fluorescence excitation-emission matrixes (EEM) of the DOM fractions were shown in Figure A1-11. Two fluorescence peaks ( $E_m \sim 450$  nm) were detected for all DOMs and were ascribed to humic-like substances containing fluorophores associated with the activation of aromatic rings. Peak location and peak intensity for each DOM were summarized in Table A1-2. Interestingly, S-HPOA (i.e., showing the highest SUVA value, Table A1-1) exhibited the lowest fluorescence intensity for both peaks. This observation has been widely reported and attributed to DOM of larger molecular weight and higher light absorbing capacities being more likely to reabsorb the emission energy, resulting in a lower fluorescence intensity.

The peak with lower excitation wavelength ( $E_x = 230$  nm) was selected to determine the fluorescent decrease for each sample during the oxidation process due to its: 1) higher fluorescence intensity compared to the peak with higher excitation wavelength, and 2) identical decrease rate with the peak with higher excitation wavelength (Figure A1-12). Similar with EDC or  $UVA_{254}$  decrease, two stages of fluorescence decrease could be distinguished with the increase of PMS exposure, except for S-HPOA (Figure A1-13). The slight fluorescence increase of S-HPOA at lower PMS exposure was probably due to: i) the transformation of phenol groups into quinone structures which are reported as more fluorescent (Cory et al., 2005); or ii) the breakdown of the higher molecular weight polycondensates into smaller MW fractions which showed higher fluorescence intensity. Similar observation for fluorescence changes of this DOM fraction upon chlorination has been previously reported (Korshin et al., 1999).

Considering the similar decreasing trend observed between UVA<sub>254</sub> and FI, the correlation between chromophore and fluorophores was studied and shown in Figure A1-14. Interestingly, an identical correlation was found between UVA and FI, except for S-HPOA and B-HPOA at lower PMS exposures, which would be caused by a smaller decrease or slight increase in fluorescence signal at lower PMS exposure due to the abovementioned reasons. These results clearly indicated the insensitivity of the measurement based on fluorescence signal and the suitability of UV indices used as an indicator for humic substances.

#### **Text A1-2. Calculation of PMS exposures under different initial PMS concentrations**

The decomposition of PMS (i.e, ranging from 0.00 to 1.00 mM) was measured and plotted against time. A pseudo-first-order decomposition was found and expressed by Equation A1-1, where k was the pseudo-first-order rate constant (Table A1-5). The effective contact time ( $t_c$ , Table A1-4) for each condition was determined from the decomposition equation (Equation A1-1), based on the assumption that complete PMS consumption was reached when PMS residual ([PMS]) was approximately 5% of [PMS]<sub>0</sub>. It should be noted that the effective contact time ( $t_c$ ) is a theoretical calculated value rather than an experimental value. Therefore, PMS exposure was calculated following the PMS decomposition equation (Equation A1-1) from 0 to  $t_c$ , which could be expressed as Equation A1-2. The values of PMS exposures were calculated and shown in Table A1-5. The calculation was only conducted in S-HPOA containing system as the PMS decomposition was similar in the presence of different DOMs.

$$[PMS] = [PMS]_0 e^{-kt} \quad \text{Equation A1-1}$$

$$\text{PMS exposure} = [PMS]_0 \int_0^{t_c} e^{-kt} dt \quad \text{Equation A1-2}$$

**Table A1-1. Characteristics of selected DOM fractions**

DOM	TOC <sup>a</sup> (mgC·L <sup>-1</sup> )	UV <sub>254</sub> (cm <sup>-1</sup> )	SUVA (L·mgC <sup>-1</sup> ·m <sup>-1</sup> )	EDC (mAU·s)	EDC <sub>n</sub> <sup>b</sup> (mAU·s·L·mgC <sup>-1</sup> )
S-HPOA	3.96	0.1893	4.78	1.79E+05	4.52E+04
B-FLV	3.98	0.1617	4.06	1.07E+05	2.69E+04
R-HPO	3.74	0.1196	3.22	5.60E+04	1.50E+04
C-HPO	3.93	0.0840	2.14	2.45E+04	6.24E+03

<sup>a</sup> Concentration of total organic carbon used in the current study.

<sup>b</sup> Normalized EDC results with DOC concentration.

**Table A1-2. Peak location and maximum fluorescence intensity of each peak for the DOM fractions**

NOM	Peak I		Peak II		Peak I/Peak II	
	Ex/Em(nm)	Intensity	Ex/Em(nm)	Intensity	$\Delta$ Ex (nm) <sup>a</sup>	Intensity ratio
S-HPOA	230/450	16.37	335/450	8.60	105	1.90
B-FLV	230/440	26.99	325/440	12.18	95	2.22
R-HPO	230/435	26.79	315/435	11.60	85	2.30
C-HPO	230/430	11.74	310/425	3.27	80	3.59

<sup>a</sup> Difference between the excitation wavelengths of the two peaks.

**Table A1-3. Second order rate constants of *p*CBA, *t*-BuOH, and EtOH with  $\cdot$ OH and SO<sub>4</sub><sup>•-</sup>**

Radicals	<i>p</i> CBA	<i>t</i> -BuOH	EtOH
$\cdot$ OH	5.2 × 10 <sup>9</sup> M <sup>-1</sup> s <sup>-1</sup> (Pi et al., 2005)	<i>t</i> -BuOH + $\cdot$ OH ~ (3.8–7.6) × 10 <sup>9</sup> M <sup>-1</sup> s <sup>-1</sup> (Cong et al., 2015)	EtOH + $\cdot$ OH ~ 1.2–2.8 × 10 <sup>9</sup> M <sup>-1</sup> s <sup>-1</sup> (Hussain et al., 2014)
SO <sub>4</sub> <sup>•-</sup>	3.6 × 10 <sup>8</sup> M <sup>-1</sup> s <sup>-1</sup> (Neta et al., 1977)	<i>t</i> -BuOH + SO <sub>4</sub> <sup>•-</sup> ~ 4.0–9.1 × 10 <sup>5</sup> M <sup>-1</sup> s <sup>-1</sup> (Hussain et al., 2014)	EtOH + SO <sub>4</sub> <sup>•-</sup> ~ 1.6–7.7 × 10 <sup>7</sup> M <sup>-1</sup> s <sup>-1</sup> (Hussain et al., 2014)

**Table A1-4. Calculation of PMS exposures with an initial PMS concentration of 1 mM at different reaction time in S-HPOA containing system**

$$(\text{PMS exposure (M}\cdot\text{s)} = [\text{PMS}]_0 \int_0^t e^{-kt} dt)$$

Reaction time (s)	0	10	30	60	120	240	360	480	600
k (s <sup>-1</sup> )	/	8×10 <sup>-4</sup>	8×10 <sup>-4</sup>	8×10 <sup>-4</sup>	3×10 <sup>-4</sup>				
PMS exposure (M·s)	0	0.0100	0.0296	0.0586	0.1179	0.2316	0.3412	0.4470	0.5491

**Table A1-5. Calculation of PMS exposures with different initial PMS concentrations in S-HPOA containing system (PMS exposure (M·s) = [PMS]<sub>0</sub> ∫<sub>0</sub><sup>t<sub>c</sub></sup> e<sup>-kt</sup> dt)**

[PMS] <sub>0</sub> (mM)	0.00	0.02	0.04	0.06	0.08	0.10	0.20	0.60	1.00
k (min <sup>-1</sup> )	/	0.110	0.050	0.039	0.035	0.030	0.016	0.010	0.006
t <sub>c</sub> (min)	0.00	26.60	62.39	77.88	86.60	93.60	187.45	282.84	473.00
PMS exposure (M·s)	0.00	0.01	0.05	0.09	0.14	0.16	0.72	2.87	8.04

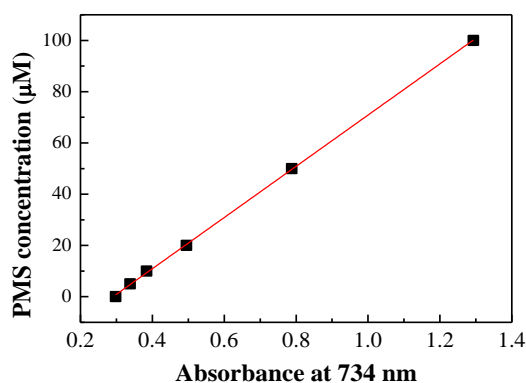


**Figure A1-1. Calibration curve for PMS determination (PMS (µM) = 99.92 A<sub>734</sub> - 29.052, R<sup>2</sup>=0.9998)**

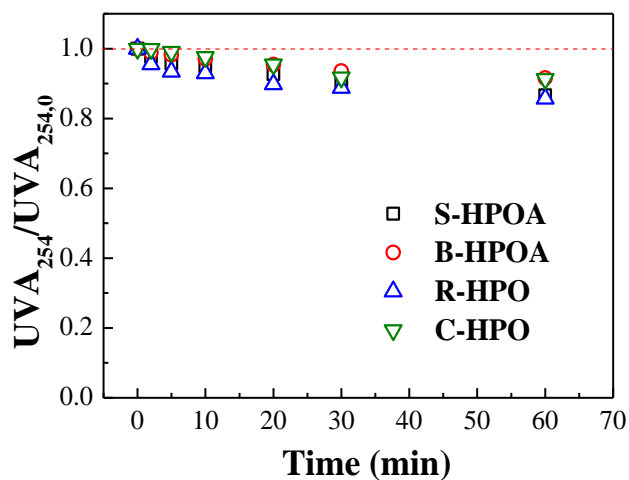


**Figure A1-2. UVA<sub>254</sub> decrease of different DOM fractions in the solely presence of PMS as a function of time. Conditions: [PMS]<sub>0</sub> = 1.0 mM; DOM = 3.90 ± 0.11 mgC/L; pH = 8.00 ± 0.05(borate buffer); T = 20°C.**

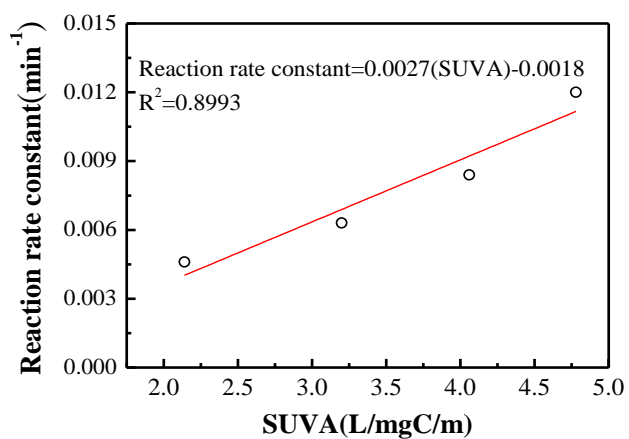


**Figure A1-3. Correlation between the reaction rate constant of CDOM<sub>slow</sub> and SUVA for each DOM fraction. Conditions: [PMS]<sub>0</sub> = 1.0 mM; Co(II) = 1.0 μM; DOM = 3.90 ± 0.11 mgC/L; pH = 8.00 ± 0.05 (10 mM borate buffer); T = 20°C.**

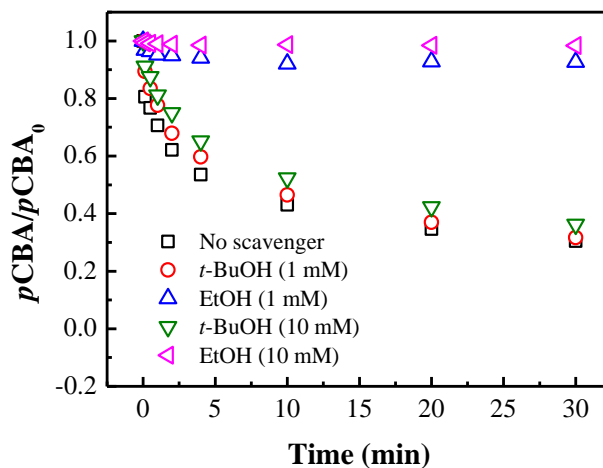


**Figure A1-4. Removal of pCBA in the presence and absence of scavengers in PMS/Co(II) system. Conditions:  $[PMS]_0 = 1.0 \text{ mM}$ ;  $Co(II) = 1.0 \mu\text{M}$ ;  $[pCBA]_0 = 10 \mu\text{M}$ ;  $pH = 8.00 \pm 0.05$  (borate buffer) ;  $T = 20^\circ\text{C}$ .**

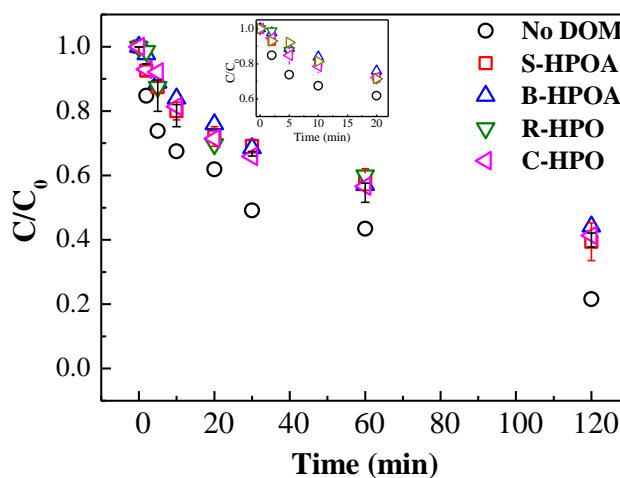


**Figure A1-5. PMS decomposition in Co(II)/PMS system with or without DOM isolates. Conditions:  $[PMS]_0 = 1.00 \text{ mM}$ ;  $Co(II) = 1.00 \mu\text{M}$ ;  $DOM = 3.90 \pm 0.11 \text{ mgC/L}$ ;  $pH = 8.00 \pm 0.05$  (10 mM borate buffer);  $T = 20^\circ\text{C}$ .**

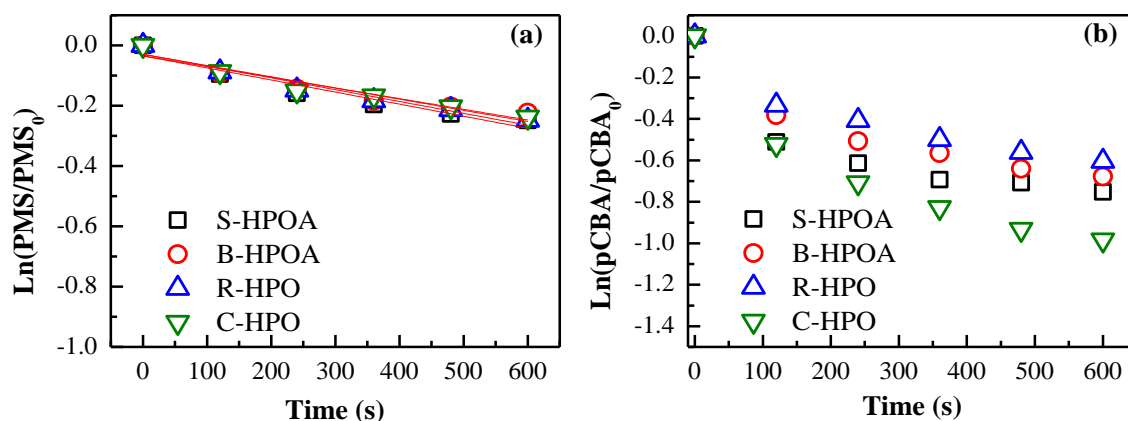


**Figure A1-6. (a) PMS decomposition and (b) pCBA decrease in Co(II)/PMS system containing different DOM isolates. Conditions:  $[PMS]_0 = 1.00$  mM;  $Co(II) = 1.00$   $\mu$ M;  $[pCBA]_0 = 1.0$   $\mu$ M;  $DOM = 3.90 \pm 0.11$  mgC/L;  $pH = 8.00 \pm 0.05$  (10 mM borate buffer);  $T = 20^\circ C$ .**

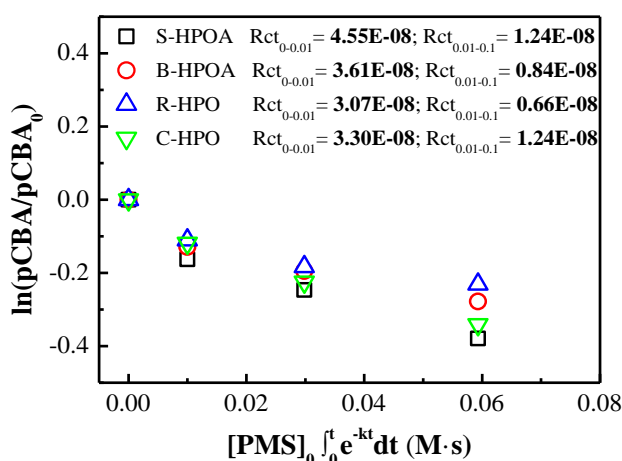


**Figure A1-7. Correlation between pCBA decay and PMS exposure ( $<0.1$  M·s) in Co(II)/PMS system containing different DOM fractions. Conditions:  $[PMS]_0 = 1.00$  mM;  $Co(II) = 1.00$   $\mu$ M;  $[pCBA]_0 = 1.0$   $\mu$ M;  $DOM = 3.90 \pm 0.11$  mgC/L;  $pH = 8.00 \pm 0.05$  (10 mM borate buffer);  $T = 20^\circ C$ .  $Rct_{0-0.01}$  and  $Rct_{0.01-0.1}$  represent the calculated Rct values at a PMS exposure of 0-0.01M·s and 0.01-0.1M·s, respectively.**

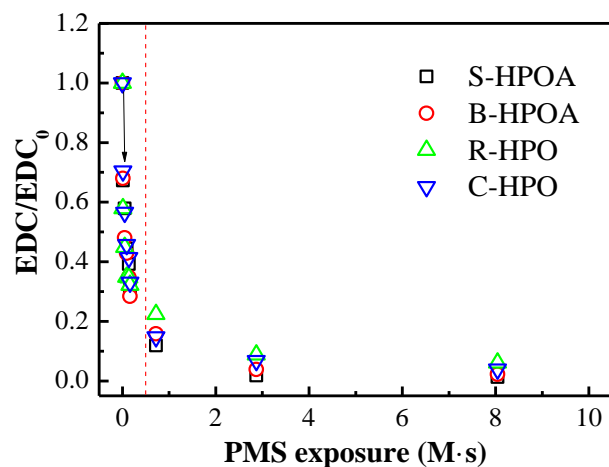


**Figure A1-8. EDC decrease of different DOM isolates in Co(II)/PMS system as a function of PMS exposures. Conditions: PMS exposure = 0.00–8.04 M·s; Co(II) = 1.0  $\mu$ M; DOM = 3.90  $\pm$  0.11 mgC/L; pH = 8.00  $\pm$  0.05(borate buffer); T = 20°C.**

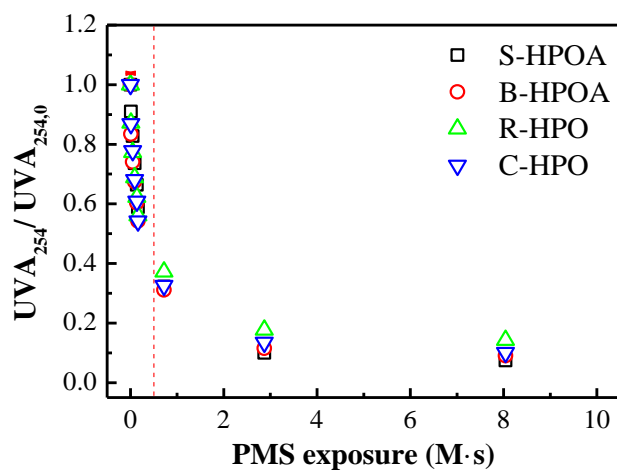


**Figure A1-9. UVA<sub>254</sub> decrease of different DOM samples in Co(II)/PMS system as a function of PMS exposures. Conditions: PMS exposure = 0.00–8.04 M·s; Co(II) = 1.0  $\mu$ M; DOM = 3.90  $\pm$  0.11 mgC/L; pH = 8.00  $\pm$  0.05(borate buffer); T = 20°C.**

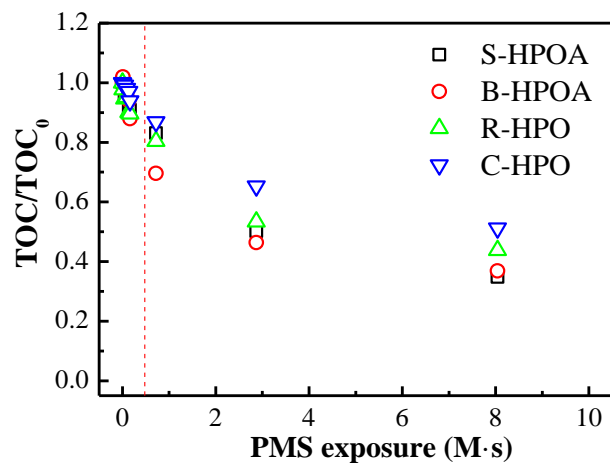


**Figure A1-10. TOC removal of different DOM samples in Co(II)/PMS system as a function of PMS exposures. Conditions: PMS exposure = 0.00–8.04 M·s; Co(II) = 1.0  $\mu$ M; DOM = 3.90  $\pm$  0.11 mgC/L; pH = 8.00  $\pm$  0.05(borate buffer); T = 20°C.**

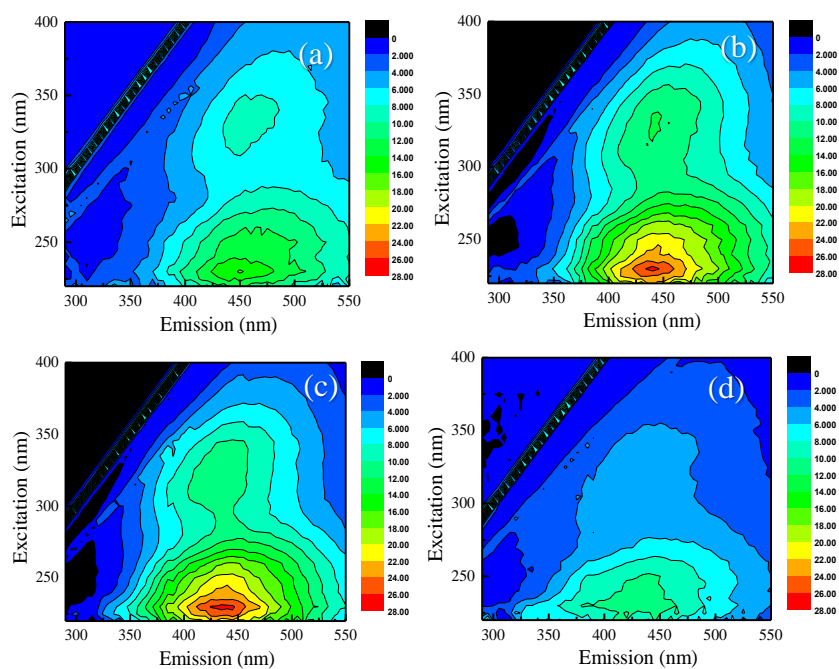


**Figure A1-11. EEM spectra of (a) S-HPOA, (b) B-HPOA, (c) R-HPO, and (d) C-HPO. DOC = 3.90  $\pm$  0.11 mgC/L; pH = 8.00  $\pm$  0.05 (10 mM borate buffered); T = 20°C.**

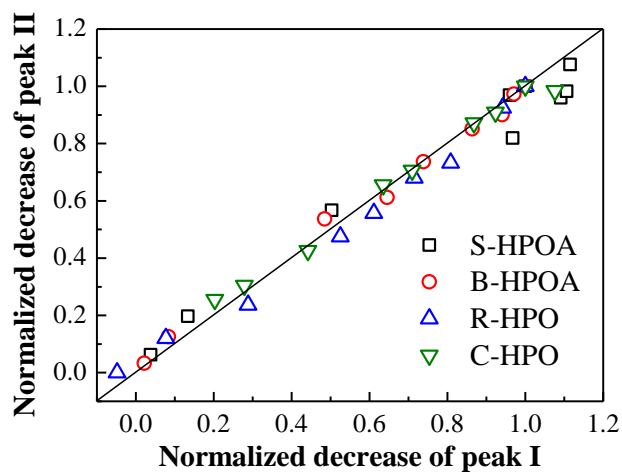


**Figure A1-12. Correlation of fluorescence between Peak I and Peak II during Co(II)/PMS oxidation process.**

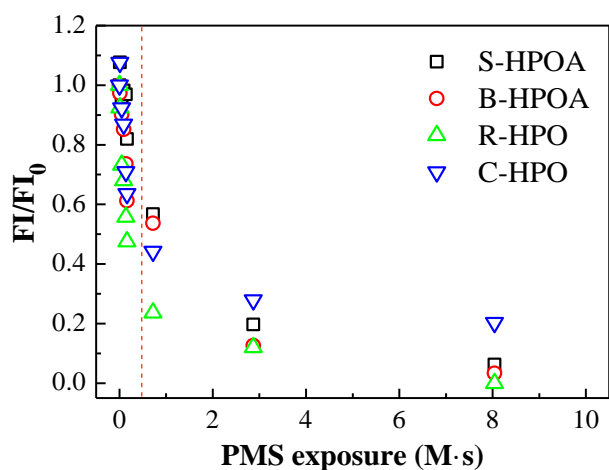


**Figure A1-13. FI decrease of different DOM samples in Co(II)/PMS reaction system as a function of PMS exposures. Conditions: PMS exposure = 0.00–8.04 M·s; Co(II) = 1.0  $\mu$ M; DOM = 3.90  $\pm$  0.11 mgC/L; pH = 8.00  $\pm$  0.05(borate buffer); T = 20°C.**

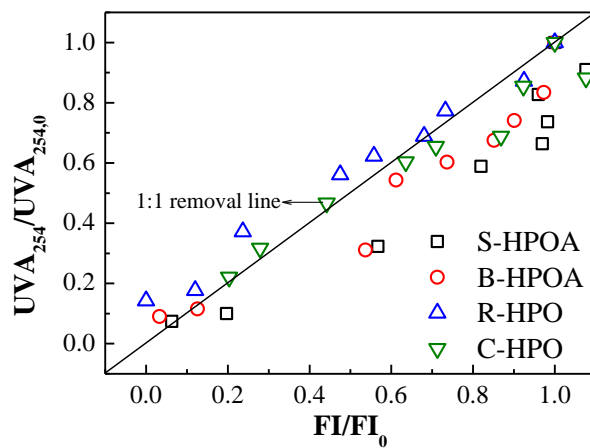


**Figure A1-14. Correlation between the relative residual  $UV_{254}$  and FI of different DOM samples in Co(II)/PMS system. Conditions: PMS exposure = 0.00–8.04 M·s; Co(II) = 1.0  $\mu$ M; DOM =  $3.90 \pm 0.11$  mgC/L; pH =  $8.00 \pm 0.05$ (borate buffer); T = 20°C.**

## Appendix 2 Supporting Information-Chapter 3

### Text A2-1.

1. As illustrated in Figure A2-1, a total of three 15 W low-pressure Hg UV-lamps (UV Technik Meyer, Germany) were installed in the collimated beam device. A petri dish placed under the collimator was used as UV-AOPs reactor. The petri dish was mounted on top of a xy-cross slide table with a magnetic stirrer (Cimarec i Micro Stirrers and a Telemodul 20 C controller, Thermo Scientific). The distance between the lamp and the surface of the slide table was measured as ca. 30 cm. A certified UV-C radiometer (UV-surface-D, sglux, Germany) was used for the determination of the average UV-C intensity ( $\sim 0.9 \text{ mW}\cdot\text{cm}^{-2}$ ) across the petri dish. The UV-C intensity was further corrected with radiometer, divergence, reflection, petri and water factor for each experiment system (Bolton et al., 2003).

2. The steady state radical concentration, i.e,  $[\cdot\text{OH}]_{\text{ss}}$  or  $[\text{SO}_4^{\cdot-}]_{\text{ss}}$ , were measured using *p*CBA as probe compounds ( $k_{\cdot\text{OH}, p\text{CBA}} = 5.2 \times 10^9 \text{ M}^{-1} \text{ s}^{-1}$ , (Pi et al., 2005)  $k_{\text{SO}_4^{\cdot-}, p\text{CBA}} = 3.6 \times 10^8 \text{ M}^{-1} \text{ s}^{-1}$ ). Nitrobenzene (NB) was also used for the detection of  $[\cdot\text{OH}]_{\text{ss}}$  produced in UV/PDS system due to its low reaction rate with  $\text{SO}_4^{\cdot-}$  ( $k_{\text{SO}_4^{\cdot-}, \text{NB}} < 10^6 \text{ M}^{-1} \text{ s}^{-1}$ , (Neta et al., 1977)  $k_{\cdot\text{OH}, \text{NB}} = 3.2 \times 10^9 \text{ M}^{-1} \text{ s}^{-1}$ ). The calculations of the radical concentrations were shown in the following equations. Experiments were conducted in 30mL unbuffered solution with an incident UV intensity of  $0.9 \text{ mW}\cdot\text{cm}^{-2}$ , a NOM concentration of  $\sim 4 \text{ mgC}\cdot\text{L}^{-1}$  and an initial oxidant concentration of 0.0, 0.1 or 1.0 mM. A petridish with a diameter of 84 mm was used as the reactor.

(1). In direct UV photolysis system,

$$-\ln\left(\frac{[pCBA]_t}{[pCBA]_0}\right) = k_{UV,direct} \times t \quad \text{Equation A2-1}$$

where  $[pCBA]_t$  is the concentration of  $pCBA$  at time  $t$ ,  $[pCBA]_0$  is the initial  $pCBA$  concentration and  $k_{UV,direct}$  is the direct photolysis rate constant of  $pCBA$  by UV irradiation. The  $k_{UV,direct}$  value obtained in the equation would be used in the following equations.

(2). In UV/H<sub>2</sub>O<sub>2</sub> system,

$$-\ln\left(\frac{[pCBA]_t}{[pCBA]_0}\right) = (k_{\cdot OH, pCBA} [\cdot OH]_{ss} + k_{UV,direct}) \times t \quad \text{Equation A2-2}$$

where  $k_{\cdot OH, pCBA}$  is the second order rate constant between  $\cdot OH$  and  $pCBA$ , and  $[\cdot OH]_{ss}$  is the steady-state concentration of  $\cdot OH$ .

3. In UV/PDS system,

$$-\ln\left(\frac{[pCBA]_t}{[pCBA]_0}\right) = (k_{\cdot OH, pCBA} [\cdot OH]_{ss} + k_{SO_4^{\cdot-}, pCBA} [SO_4^{\cdot-}]_{ss} + k_{UV,direct}) \times t \quad \text{Equation A2-3}$$

where  $k_{SO_4^{\cdot-}, pCBA}$  is the second order rate constant between  $SO_4^{\cdot-}$  and  $pCBA$ , and  $[SO_4^{\cdot-}]_{ss}$  is the steady-state concentration of  $SO_4^{\cdot-}$ . The value of  $[\cdot OH]_{ss}$  could be calculated from Equation A2-4.

$$-\ln\left(\frac{[NB]_t}{[NB]_0}\right) = k_{\cdot OH, NB} [\cdot OH]_{ss} \times t \quad \text{Equation A2-4}$$

where  $k_{\cdot\text{OH},\text{NB}}$  is the second order rate constant between  $\cdot\text{OH}$  and NB.

4. The acidified samples were concentrated with solid phase extraction (SPE) using Bond Elut PPL cartridges (6 mL, 1 g, Agilent Technologies) for FT-ICR MS analysis. Briefly, the cartridges were conditioned sequentially with 10 mL of methanol, 10 mL of ethyl acetate, and 10 mL ultrapure water (acidified to pH~2 with HCl). The acidified NOM samples were loaded onto the cartridges at a flow rate of  $\sim 3\text{ mL}\cdot\text{min}^{-1}$  with a vacuum pump. To minimize the interference of salt, the loaded cartridges were rinsed with 10 mL of acidified ultrapure water and left vacuum-dried before elution. 10 mL of LCMS grade methanol was used for NOM elution and the eluted samples were dried with nitrogen gas and stored at  $-20^\circ\text{C}$  in the dark.

5. The study on the reaction pathways taking place for the major reactive molecules was achieved by another set of experiments conducted with 30 mL solution in a petridish (84 mm in diameter). An incident UV intensity of  $\sim 0.9\text{ mW}\cdot\text{cm}^{-2}$  and a series of initial oxidant concentrations (i.e., 0.00, 0.02, 0.04, 0.06, 0.08, 0.10 mM) was applied. The initial UV fluence was calculated as 1268, 1311, and 1353  $\text{mJ}\cdot\text{cm}^{-2}$  for S-HPOA-, R-HPO-, and C-HPO-containing solutions, respectively. The change in  $\text{UV}_{254}$  was recorded and corrected by subtracting the contribution of oxidants and sole UV irradiation at the end of 30 min reaction. Samples for Electron Donating Capacity (EDC) analysis were collected and kept in Amber vials without quencher addition to avoid any interference with EDC signal. The change in  $\text{UV}_{254}$  or EDC was negligible with sole  $\text{H}_2\text{O}_2$  or PDS oxidation in 30 min.

6. The instrument was externally and internally calibrated with 10 mM sodium formate and a known homologous series of NOM, respectively. An excellent sensitivity with a mass error of less than 0.2 ppm was achieved after calibration. The molecular formula

for each  $m/z$  peak with a signal-to-noise ratio (S/N) larger than 5 was assigned using Bruker Daltonics data analysis software version 4.0. The formulas calculation were conducted based on the elemental rules of  $^{12}\text{C}_{1-100}^{1}\text{H}_{2-202}^{16}\text{O}_{1-102}^{14}\text{N}_{0-3}^{32}\text{S}_{0-2}$  and the elemental ratio restrictions of  $0.33 < \text{H/C} < 2.0$  and  $0.23 < \text{O/C} < 1.2$ . The criteria that the mass error between the measured and the calculated chemical formula should be below 1 ppm was also applied in the calculation. The assignment of formulas above 500 Da was achieved through identification of homologous series differing only by integer multiples of  $-\text{CH}_2$  units. The calculation of the molecular characteristics and categorization of the assigned molecules were detailed in the following sections.

7. Van Krevelen diagram obtained by plotting H/C against O/C of all the assigned formulas for each sample for the visualization of the distribution and class of the molecules. The VK diagram was then divided into different regions representing all together seven classes of compounds commonly found in NOM, i.e., aromatic structures ( $\text{H/C} = 0.2\text{--}0.7$ ,  $\text{O/C} = 0.0\text{--}0.67$ ), unsaturated hydrocarbons ( $\text{H/C} = 0.7\text{--}1.5$ ,  $\text{O/C} = 0.0\text{--}0.1$ ), lignis/CRAM-like structures ( $\text{H/C} = 0.7\text{--}1.5$ ,  $\text{O/C} = 0.1\text{--}0.67$ ), tannins ( $\text{H/C} = 0.6\text{--}1.5$ ,  $\text{O/C} = 0.67\text{--}1.0$ ), lipids ( $\text{H/C} = 1.5\text{--}2.0$ ,  $\text{O/C} = 0.0\text{--}0.3$ ), aliphatic proteins ( $\text{H/C} = 1.5\text{--}2.2$ ,  $\text{O/C} = 0.3\text{--}0.67$ ), and carbohydrates ( $\text{H/C} = 1.5\text{--}2.4$ ,  $\text{O/C} = 0.67\text{--}1.2$ ). The calculation of various molecular characteristics were illustrated as follows:

1). Double bond equivalent:

$$DBE = 1/2 \times (2 \times C + N - H + 2) \quad \text{Equation A2-5}$$

2). The weight averaged values for specific molecular characteristic ( $X_{wa}$ ) were calculated as follows:

$$X_{wa} = \sum_{i=1}^n X_i \times I_{Ri} \quad \text{Equation A2-6}$$

$$I_{Ri} = I_i / \sum_{i=1}^n I_i \quad \text{Equation A2-7}$$

where  $X_i$  and  $I_{Ri}$  represents the value of a specific molecular characteristic and the relative intensity of formula  $i$  in a sample,  $I_{Ri}$  was calculated by normalizing the intensity of formula  $i$  ( $I_i$ ) by the total intensity of all the assigned formulas in a sample ( $\sum_{i=1}^n I_i$ ).

3). The value of KMD (COO) was calculated using the following equations:

$$\text{KMD (COO)} = \text{Observed nominal mass} - \text{Kendrick Mass (COO)} \quad \text{Equation A2-8}$$

$$\text{Exact } m/z \text{ of the peak} = \text{calculated } m/z + 1.00784 - 0.000549 \quad \text{Equation A2-9}$$

$$\text{Kendrick Mass (COO)} = \text{exact } m/z \text{ of the peak} \times (\text{nominal mass of COO} / \text{exact mass of COO}) \quad \text{Equation A2-10}$$

where the observed nominal mass is the integer value of the observed mass, nominal mass of COO is 44.00000, and exact mass of COO is 43.98983.

8. Molecular formulas were compared between treated and original samples to determine reactive, resistant and produced molecules. Specifically, molecules that disappeared after reaction was identified as reactive, molecules remaining unchanged after reaction were identified as resistant, and molecules newly formed were identified as produced. Similarly, the exclusively reactive molecules were determined

by comparing reactive molecules between  $\cdot\text{OH}$  and  $\text{SO}_4^{\cdot-}$  oxidation processes. Molecules only found in  $\cdot\text{OH}(\text{SO}_4^{\cdot-})$ -oxidation process were defined as exclusively reactive to  $\cdot\text{OH}/(\text{SO}_4^{\cdot-})$ .

### Text A2-2.

As was shown in the van Krevelen diagram (Figure A2-2), the distribution of the assigned formulas were comparable and CHO molecules were the major components for all three NOM isolates. The majority (95.7%, 96.0%, and 97.5% for S-HPOA, R-HPO and C-HPO, respectively) of assigned molecules belong to aromatic structures, lignis/CRAM-like structures ( $H/C = 0.7-1.5$ ,  $O/C = 0.1-0.67$ ), tannin ( $H/C = 0.6-1.5$ ,  $O/C = 0.67-1.0$ ) and ( $H/C = 0.2-0.7$ ,  $O/C = 0.0-0.67$ ). This is probably due to the fact that the aquatic NOMs shared the similar sources of organic input (i.e., terrestrial input) and the same protocol of extraction. However, different N or S contents were found among the organics. Specifically, the respective N and S content were 0.06% and 0.10% for S-HPOA, 0.38% and 0.07% for R-HPO, and, 0.12% and 0.07% for C-HPO. This is probably attributed to the different degree of microbial activity in each aquatic system. The weight averaged DBE ( $DBE_{wa}$ , Table A2-2) were 10.73, 9.73, and 9.30 for S-HPOA, R-HPO, and C-HPO, respectively. The trend for the variation of the  $DBE_{wa}$  among the three NOM isolates were consistent with that of SUVA values (Table A2-2). The weight averaged  $m/z$  ( $m/z_{wa}$ , Table A2-2) was approximately 430, 424, and 437 for S-HPOA, R-HPO, and C-HPO, respectively. The results were notably smaller than those previously reported, for instance, 1,100 Da for humic substances from Suwannee River. (Lee et al., 2006) This may be ascribed to the difference in the technique for size measurement. Collectively, a variation in characteristics of the selected NOM samples would represent a wider spectrum of aquatic environment. The good agreement of the findings in the current study with a previous study using a 12T mass spectrometer indicated the consistency and reliability of this instrument.

**Table A2-1. Bulk properties of NOM isolates**

NOM	TOC <sup>a</sup> mgC·L <sup>-1</sup>	UV <sub>254</sub> cm <sup>-1</sup>	SUVA <sup>b</sup> L·mgC <sup>-1</sup> ·m <sup>-1</sup>	EDC <sup>c</sup> mAU·s	EDC <sub>n</sub> <sup>d</sup> mAU·s·L·mgC <sup>-1</sup>
S-HPOA	3.89	0.189	4.94	1.76E+05	4.74E+04
R-HPO	4.09	0.129	3.20	6.64E+04	1.63E+04
C-HPO	3.86	0.078	1.98	3.76E+04	9.74E+03

<sup>a</sup> Concentration of total organic carbon for each NOM isolate in the experiment (mgC·L<sup>-1</sup>).

<sup>b</sup> Specific UV absorbance at 254nm (SUVA, L·mgC<sup>-1</sup>·m<sup>-1</sup>).

<sup>c</sup> Electron donating capacity (EDC, mAU·s).

<sup>d</sup> Normalized EDC results with TOC concentration.

**Table A2-2. Molecular characteristics of NOM isolates studied in the experiment**

NOM	DBE <sub>wa</sub> <sup>a</sup>	m/z <sub>wa</sub> <sup>a</sup>	H/C <sub>wa</sub> <sup>a</sup>	O/C <sub>wa</sub> <sup>a</sup>	C <sub>wa</sub> % <sup>a</sup>	H <sub>wa</sub> % <sup>a</sup>	O <sub>wa</sub> % <sup>a</sup>	N <sub>wa</sub> % <sup>a</sup>	S <sub>wa</sub> % <sup>a</sup>
S-HPOA	10.73	430.51	1.05	0.51	39.15	40.78	19.90	0.06	0.10
S-HPOA <sup>b</sup>	11.00	432.60			39.70	42.17	17.94	0.15	0.04
R-HPO	9.73	424.70	1.11	0.53	37.65	42.15	19.75	0.38	0.07
R-HPO <sup>b</sup>	9.90	435.20			37.60	42.44	19.30	0.58	0.08
C-HPO	9.30	437.76	1.19	0.52	36.96	44.05	18.80	0.12	0.07
C-HPO <sup>b</sup>	9.60	453.80			37.04	44.81	17.97	0.14	0.04

<sup>a</sup> Weight averaged values of different characteristics for the assigned formulas from FT-ICR MS (see Equation A2-6 and Equation A2-7 for calculation.)

<sup>b</sup> Results from Niu et al (Niu et al., 2018).

**Table A2-3. Rate constant (*k*) and correlation coefficient (*R*<sup>2</sup>) of pseudo-first-order kinetics of UV<sub>254</sub> decrease and steady-state radical concentration. (Conditions: Incident UV intensity = 0.9 mW·cm<sup>-2</sup>, [TOC]<sub>0</sub> = 3.89 ± 0.18 mgC·L<sup>-1</sup>, [H<sub>2</sub>O<sub>2</sub>]<sub>0</sub> or [PDS]<sub>0</sub> = 1.00 mM, [pCBA]<sub>0</sub> or [NB]<sub>0</sub> = 1.00 μM at unadjusted pH ([pH]<sub>0</sub>(H<sub>2</sub>O<sub>2</sub>) = 4.65±0.09, [pH]<sub>0</sub>(PDS) = 4.66±0.18) and room temperature (20°C).)**

UV <sub>254</sub>		[SO <sub>4</sub> <sup>·-</sup> ] <sub>ss</sub>		UV <sub>254</sub>		[·OH] <sub>ss</sub>	
<i>k</i> (min <sup>-1</sup> )	<i>R</i> <sup>2</sup>	<i>M</i> (×10 <sup>-12</sup> )		<i>k</i> (min <sup>-1</sup> )	<i>R</i> <sup>2</sup>	<i>M</i> (×10 <sup>-12</sup> )	

S-HPOA	0.029±0.006	0.995±0.011	1.625±0.191	0.014±0.001	0.999±0.004	0.650±0.085
R-HPO	0.046±0.006	0.991±0.000	3.230±0.552	0.023±0.001	1.000±0.002	0.625±0.148
C-HPO	0.044±0.005	0.959±0.001	6.180±1.089	0.024±0.000	0.994±0.007	1.005±0.106

**Table A2-4. Statistics on molecules reactive or resistant to  $\cdot\text{OH}$  and  $\text{SO}_4^{\cdot-}$ .**

Sample			Number	N% <sup>a</sup>	I% <sup>b</sup>
S-HPOA	$\cdot\text{OH}$	reactive	750	0.380	0.197
		resistant	1224	0.620	0.803
	$\text{SO}_4^{\cdot-}$	reactive	811	0.411	0.223
		resistant	1163	0.589	0.777
R-HPO	$\cdot\text{OH}$	reactive	1329	0.460	0.205
		resistant	1557	0.540	0.795
	$\text{SO}_4^{\cdot-}$	reactive	1437	0.498	0.235
		resistant	1449	0.502	0.765
C-HPO	$\cdot\text{OH}$	reactive	1037	0.413	0.160
		resistant	1476	0.587	0.840
	$\text{SO}_4^{\cdot-}$	reactive	1231	0.490	0.246
		resistant	1282	0.510	0.754

<sup>a</sup>: Number percentage

<sup>b</sup>: Intensity percentage

**Table A2-5. Removal efficiency of different NOM classes by  $\cdot\text{OH}$  and  $\text{SO}_4^{\cdot-}$ .**

Sample	Aromatics%	Lignins%	Tannins%
--------	------------	----------	----------

S-HPOA	$\cdot\text{OH}$	53	41	3
	$\text{SO}_4^{\cdot-}$	62	44	3
R-HPO	$\cdot\text{OH}$	80	46	24
	$\text{SO}_4^{\cdot-}$	81	79	41
C-HPO	$\cdot\text{OH}$	75	42	9
	$\text{SO}_4^{\cdot-}$	83	65	8

**Table A2-6. Comparison of molecular characteristics between reactive and resistant molecules in  $\cdot\text{OH}$  and  $\text{SO}_4^{\cdot-}$ -based AOPs.**

NOM			m/z <sub>wa</sub>	C <sub>wa</sub>	DBE <sub>wa</sub>	H/C <sub>wa</sub>	O/C <sub>wa</sub>
S-HPOA	$\cdot\text{OH}$	reactive	537.65	26.13	14.05	1.015	0.465
		resistant	410.25	18.85	9.96	1.053	0.549
	$\text{SO}_4^{\cdot-}$	reactive	551.72	26.48	14.69	0.974	0.485
		resistant	401.96	18.51	9.63	1.066	0.546
R-HPO	$\cdot\text{OH}$	reactive	481.06	22.99	11.99	1.044	0.470
		resistant	410.17	18.73	9.14	1.132	0.547
	$\text{SO}_4^{\cdot-}$	reactive	483.63	22.96	12.04	1.038	0.483
		resistant	406.62	18.57	9.02	1.037	0.546
C-HPO	$\cdot\text{OH}$	reactive	518.13	25.78	11.42	1.189	0.417
		resistant	422.46	19.45	8.90	1.189	0.536
	$\text{SO}_4^{\cdot-}$	reactive	524.59	26.64	11.55	1.1278	0.4550
		resistant	416.28	19.10	8.56	1.2089	0.5387

**Table A2-7. Percentage of molecules with different molecular compositions reactive to  $\cdot\text{OH}$  and  $\text{SO}_4^{\cdot-}$ .**

Sample		CHO%	CHON%	CHOS%	CHONS %
S-HPOA	$\cdot\text{OH}$	94	3	1	2
	$\text{SO}_4^{\cdot-}$	94	3	1	2
R-HPO	$\cdot\text{OH}$	53	37	9	1
	$\text{SO}_4^{\cdot-}$	55	38	7	0
C-HPO	$\cdot\text{OH}$	63	24	13	0
	$\text{SO}_4^{\cdot-}$	67	24	9	0

**Table A2-8. Molecular characteristics of molecules exclusively reactive to  $\cdot\text{OH}$  or  $\text{SO}_4^{\cdot-}$ .**

Sample		H/C <sub>wa</sub>	O/C <sub>wa</sub>	DBE <sub>wa</sub> <sup>a</sup>	DBE <sub>wa</sub> <sup>b</sup>	m/z <sub>wa</sub>	C <sub>wa</sub>
S-HPOA	$\cdot\text{OH}$	1.11	0.45	8.36	10.86	447.53	21.87
	$\text{SO}_4^{\cdot-}$	0.86	0.55	7.40	15.66	563.80	25.88
R-HPO	$\cdot\text{OH}$	1.06	0.50	7.86	11.06	456.06	21.01
	$\text{SO}_4^{\cdot-}$	1.02	0.55	9.54	11.86	484.52	22.13
C-HPO	$\cdot\text{OH}$	1.03	0.47	6.69	10.47	400.97	18.99
	$\text{SO}_4^{\cdot-}$	1.02	0.52	13.11	11.53	470.65	22.06

<sup>a</sup>: DBE<sub>wa</sub> of molecules in Area I.

<sup>b</sup>: DBE<sub>wa</sub> of total exclusively reactive molecules in Figure 3-3.

**Table A2-9. Characteristics of molecules produced through  $\cdot\text{OH}$  or  $\text{SO}_4^{\cdot-}$  oxidation.**

Sample		m/z <sub>wa</sub>	C <sub>wa</sub>	H/C <sub>wa</sub>	O/C <sub>wa</sub>	DBE <sub>wa</sub>
S-HPOA	$\cdot\text{OH}$	562.74	23.55	1.08	0.68	11.89

	$\text{SO}_4^{\cdot-}$	509.85	20.15	1.14	0.75	9.82
R-HPO	$\cdot\text{OH}$	487.81	22.50	1.03	0.53	12.73
	$\text{SO}_4^{\cdot-}$	461.82	19.48	1.12	0.64	10.41
C-HPO	$\cdot\text{OH}$	490.86	21.93	1.07	0.56	11.73
	$\text{SO}_4^{\cdot-}$	482.12	19.24	1.08	0.72	10.26

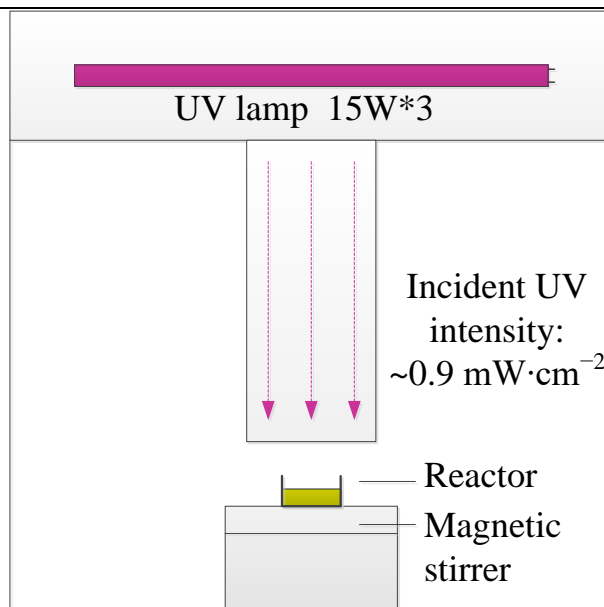


**Figure A2-1. Schematic representative of the collimated beam device (front view).**

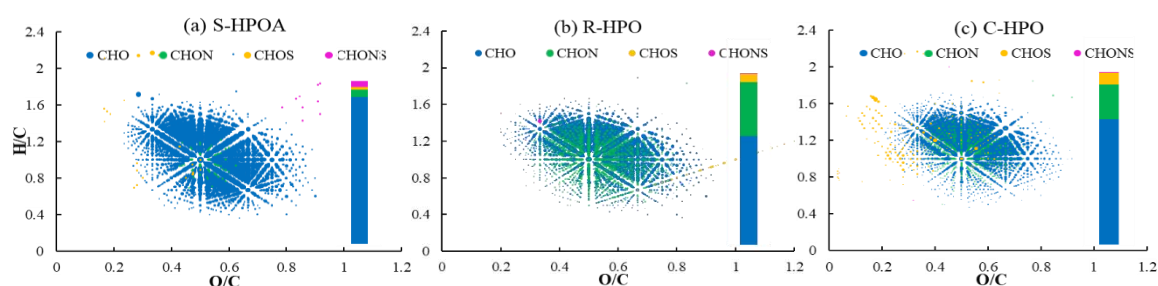


**Figure A2-2. van Krevelen diagrams of the formulas assigned from FTICR-MS peaks of three NOM isolates: (a) S-HPOA, (b) R-HPO, and (c) C-HPO. Relative abundance of molecules containing respective CHO (blue), CHON (green), CHOS (orange) and CHONS (pink) groups were reflected by the height of stacked columns. Bubble sizes reflect the relative intensities of respective mass peaks.**

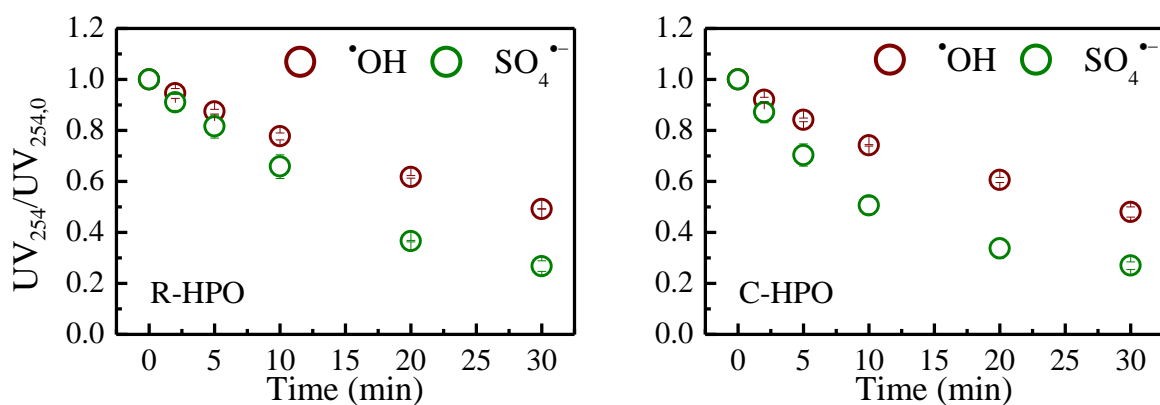


**Figure A2-3. UV<sub>254</sub> decrease of R-HPO (Ribou reservoir hydrophobic fraction) and C-HPO (Colorado river hydrophobic fraction) with  $\cdot\text{OH}$  or  $\text{SO}_4^{\bullet-}$  treatment. Conditions: Incident UV intensity =  $0.9 \text{ mW}\cdot\text{cm}^{-2}$ ,  $[\text{TOC}]_0 = 3.89 \pm 0.18 \text{ mgC}\cdot\text{L}^{-1}$ ,  $[\text{H}_2\text{O}_2]_0$  or  $[\text{PDS}]_0 = 1.00 \text{ mM}$ , at unadjusted pH ( $[\text{pH}]_0(\text{H}_2\text{O}_2) = 4.65 \pm 0.09$ ,  $[\text{pH}]_0(\text{PDS}) = 4.66 \pm 0.18$ ) and room temperature ( $20^\circ\text{C}$ ).**

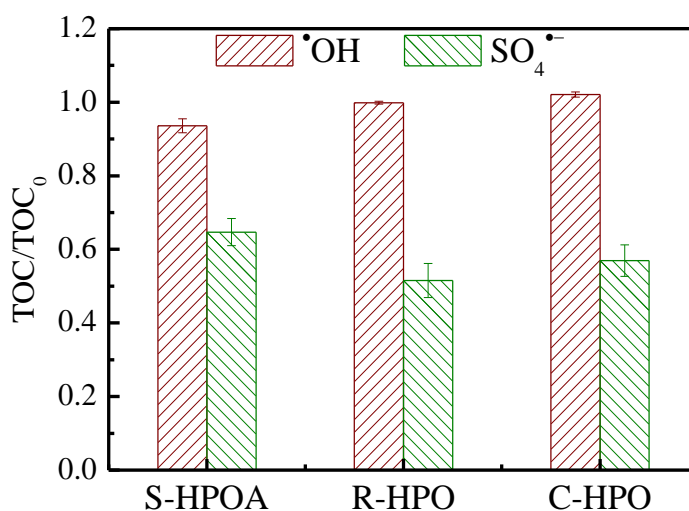


**Figure A2-4. TOC change of three NOM isolates with  $\cdot\text{OH}$  or  $\text{SO}_4^{\bullet-}$  treatment for 30 min. Conditions: Incident UV intensity =  $0.9 \text{ mW}\cdot\text{cm}^{-2}$ ,  $[\text{TOC}]_0 = 3.89 \pm 0.18 \text{ mgC}\cdot\text{L}^{-1}$ ,  $[\text{H}_2\text{O}_2]_0$  or  $[\text{PDS}]_0 = 1.00 \text{ mM}$ , at unadjusted pH ( $[\text{pH}]_0(\text{H}_2\text{O}_2) = 4.65 \pm 0.09$ ,  $[\text{pH}]_0(\text{PDS}) = 4.66 \pm 0.18$ ) and room temperature ( $20^\circ\text{C}$ ).**

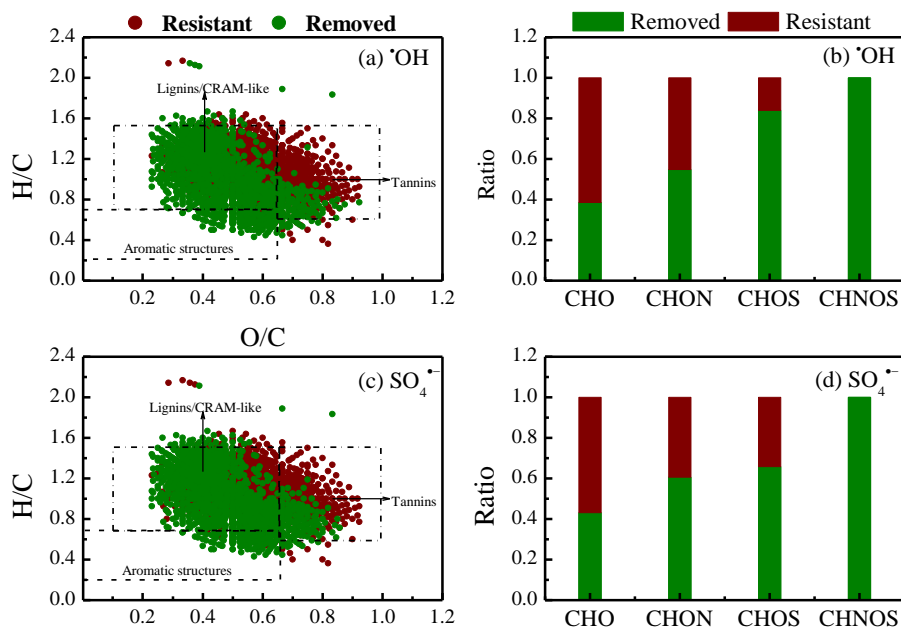


**Figure A2-5. (a,c) van Krevelen diagrams and (b,d) molecular compositions of R-HPO after  $\cdot\text{OH}$  or  $\text{SO}_4^{\cdot-}$  treatment. Green points/bars represent formulas disappeared after reaction (reactive), and red points/bars reflect formulas remaining unchanged after reaction (resistant).**

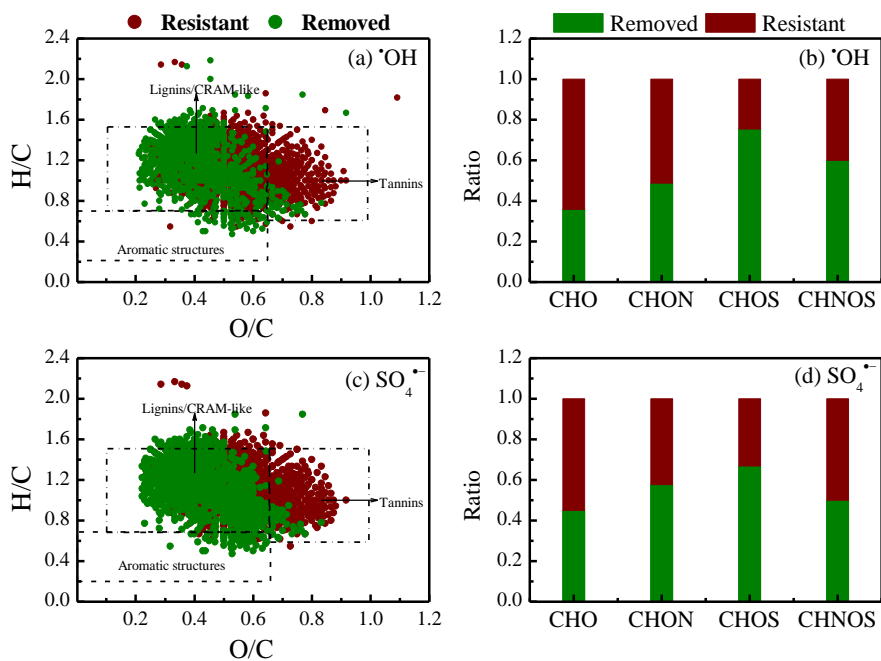


**Figure A2-6. (a,c) van Krevelen diagrams and (b,d) molecular compositions of C-HPO after  $\cdot\text{OH}$  or  $\text{SO}_4^{\cdot-}$  treatment. Green points/bars represent formulas disappeared after reaction (reactive), and red points/bars reflect formulas remaining unchanged after reaction (resistant).**

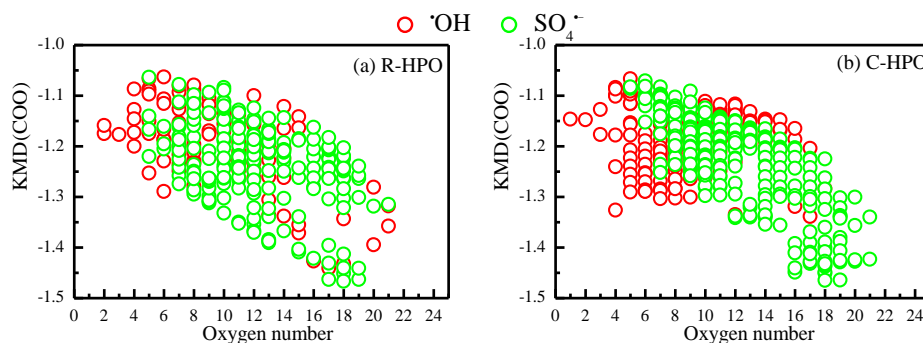


**Figure A2-7.** KMD (COO) of molecules exclusively reactive with  $\cdot\text{OH}$  or  $\text{SO}_4^{\cdot-}$  as a function of oxygen number in the NOM isolate of (a) R-HPO and (b) C-HPO.

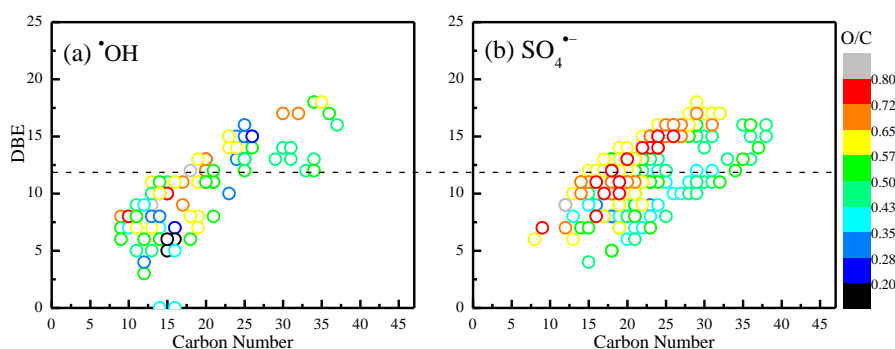


**Figure A2-8.** DBE of molecules exclusively reactive to (a)  $\cdot\text{OH}$  or (b)  $\text{SO}_4^{\cdot-}$  as a function of carbon number in the NOM isolate of R-HPO. The dash line was drawn at approximately a DBE value of 11.86 ( $\text{DBE}_{\text{wa}}$  of the molecules exclusively reactive to  $\text{SO}_4^{\cdot-}$ ).

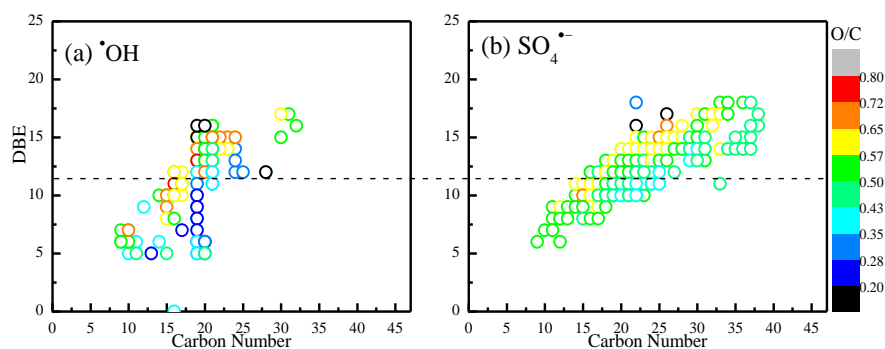


**Figure A2-9.** DBE of molecules exclusively reactive to (a)  $\cdot\text{OH}$  or (b)  $\text{SO}_4^{\cdot-}$  as a function of carbon number in the NOM isolate of C-HPO. The dash line was drawn at approximately a DBE value of 11.53 ( $\text{DBE}_{\text{wa}}$  of the molecules exclusively reactive to  $\text{SO}_4^{\cdot-}$ ).

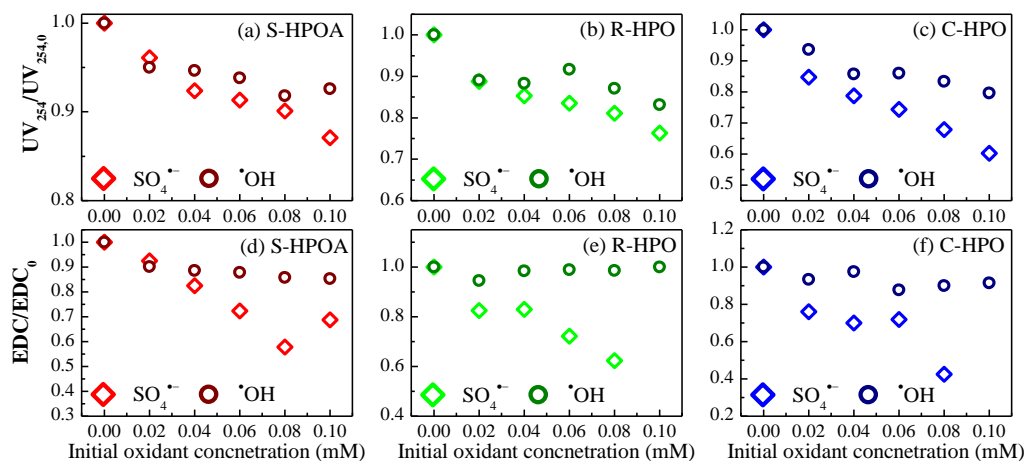


**Figure A2-10. Normalized decrease of (a), (b), and (c) UVA<sub>254</sub> and (d), (e), and (f) EDC of different NOM isolates after reaction with •OH and SO<sub>4</sub><sup>•-</sup>. Conditions: Incident UV intensity = 0.9 mW·cm<sup>-2</sup>, [TOC]<sub>0</sub> = 3.89 ± 0.18 mgC·L<sup>-1</sup>, and [H<sub>2</sub>O<sub>2</sub>]<sub>0</sub> or [PDS]<sub>0</sub> = 0.00–0.10 mM, at unadjusted pH ([pH]<sub>0</sub>(H<sub>2</sub>O<sub>2</sub>) = 4.65±0.09, [pH]<sub>0</sub>(PDS) = 4.66±0.18) and room temperature (20°C).**

## Appendix 3 Supporting Information-Chapter 4

### Text A3-1. Synthesis of MnO<sub>2</sub> and nano-scaled particle preparation

MnO<sub>2</sub> particles were synthesized by reducing manganese nitrate (Mn(NO<sub>3</sub>)<sub>2</sub>) with potassium permanganate (KMnO<sub>4</sub>). Briefly, Mn(NO<sub>3</sub>)<sub>2</sub> was added into KMnO<sub>4</sub> solution drop by drop under dynamic magnetic stirring. The resulting suspension was continuously and vigorously stirred. The sediments were collected and dried at 373 K. Finally, the precursor was calcined in air atmosphere at 723 K and stored in a desiccator. The resulting MnO<sub>2</sub> particles were ground into nanoscale particles in a grinder for 5-8 min for several runs (ROCKLABS BTRM 459, Rocklabs Limited, Auckland, New Zealand). Nanoparticle suspensions were prepared by adding DDI water. The suspension was sonicated (UNISONICS, Australia) for 1 h, followed by 1 h of settling. An aliquot of the supernatant was collected to prepare MnO<sub>2</sub> stock solution by adding DDI water. Size and electrophoretic mobility of MnO<sub>2</sub> particles were measured with a Zetasizer (nano ZS, Malvern, UK) using a laser at a wavelength of 633 nm and a scattering angle of 173°. UV-Vis spectra of MnO<sub>2</sub> suspensions were recorded with an Agilent Cary 60 spectrophotometer from 200-800 nm.

### **Text A3-2. Measurements of Zeta potential and hydrodynamic diameter**

Samples for Zeta potential measurement were prepared by adding a specific concentration of electrolyte solution in a clean cuvette containing a predetermined volume of diluted nanoparticle suspension and OMs to a final volume of 1 mL. The obtained solution was then pipetted into the zeta cell and then placed into the light scattering compartment, where the measurement was immediately performed. A minimum of three measurements per sample were conducted for each solution condition and the data sets were subjected to statistic processing.

The initial hydrodynamic diameter ( $D_{ho}$ ) of  $MnO_2$  nanoparticles was measured immediately before every TR-DLS experiment as a baseline. Samples analyzed by TR-DLS were prepared by adding 1 ppm of  $MnO_2$  nanoparticles to electrolyte solutions to a final ionic strength ranging from 1 to 100 mM  $Na^+$  or  $Ca^{2+}$ , and to a final DOM concentration of 0 or 10 mg C/L for DOM-containing electrolyte solutions. The sample was gently shook and immediately placed into the Zetasizer for measurement.

### **Text A3-3. Preparation of MnO<sub>2</sub>-coated silica surface and DOM-coated AFM probe**

The MnO<sub>2</sub> surface used was prepared using Pulse-Laser Deposition (PLD) technique as previously described (Lu et al., 2016b). Briefly, a layer of approximately 10 nm of MnO<sub>2</sub> was deposited on a smooth silica wafer (RRMS: 0.3 nm) using a COMPexPro201, Coherent. The MnO<sub>2</sub> coating was further confirmed by Scanning Transmission Electron Microscopy (STEM) (Titan 80-300, FEI), and the elements of the MnO<sub>2</sub>-coated surface were confirmed with the Energy Dispersive Spectroscopy (EDS) accessory of the STEM as shown in a previous study (Lu et al., 2016b). A Silica AFM colloidal probe (i.e., termed as Silica AFM Probe) was prepared by gluing a silica colloid to the tip of an AFM cantilever. The diameter of the silica colloid was measured by SEM for further normalization of interfacial forces (F/R: units of mN/m) as previously described (Gutierrez et al., 2015a). This silica AFM probe was coated with a specific DOM isolate according to the layer-by-layer protocol (Aubry et al., 2013). Briefly, a silica AFM probe was placed in an iron oxide solution for eight hours. After rinsing in MQ water, the probe was immersed into a 50 mg C/L DOM solution and allowed to coat for 8 hours. The probe was removed from the DOM solution and rinsed with MQ water prior to use. The sensitivity of the cantilever was measured using a mica surface prior to each experiment. The cantilever spring constant was measured by thermal tuning method, where deflection (V) was converted to force (nN) according to Hooke's Law (Aubry et al., 2013). The MnO<sub>2</sub> surface, i.e. MnO<sub>2</sub>-coated silica wafer, was carefully rinsed before each experiment.

#### Text A3-4. DLVO interaction between bare particles

Total DLVO interaction energy (J) between bare particles is the sum of  $V_{\text{vdw}}$ , i.e., van der Waals attractive interaction energy (J), and  $V_{\text{EDL}}$ , i.e., electron double layer repulsion energy (J).

$$V_{\text{vdw}}(J) = -\frac{Aa}{12h(1+14h/\lambda)} \quad \text{Equation A3-1}$$

Where A is the Hamaker constant of the particle in aqueous media, a is the particle radius,  $\lambda$  is the dielectric wavelength, and h is the separation distance between two particles (nm).

$$V_{\text{EDL}}(J) = \frac{\pi\epsilon_r\epsilon_0a_1a_2(\psi_{01}^2 + \psi_{02}^2)}{(a_1 + a_2)} \left[ \frac{2\psi_{01}\psi_{02}}{(\psi_{01}^2 + \psi_{02}^2)} \ln\left(\frac{1 + \exp(-\kappa h)}{1 - \exp(-\kappa h)}\right) + \ln(1 - \exp(-2\kappa h)) \right] \quad \text{Equation A3-2}$$

$\epsilon_r$  is the relative permittivity of water,  $\epsilon_0$  is the permittivity of free space,  $\psi$  is the surface potential (V),  $\kappa$  is Debye length ( $\text{m}^{-1}$ ). In the current study,  $a_1=a_2$  and  $\psi_{01}=\psi_{02}$  due to the presence of only one population of nanoparticles, i.e.,  $\text{MnO}_2$ . Energy barrier is defined as the maximum DLVO interaction at a specific separation distance.

**Table A3-1. Major characteristics of HPO and HPI DOM fractions**

Isolate	Sampling location	$\times$ C/O	$\times$ C/N	$\surd$ Arom-C (%)	#SUVA <sub>254</sub>
GRW-HPO	Gartempe River (Lathus - Vienne, France)	1.6	28.9	22	4.4
CRW-OC-HPO	Colorado River (La Verne, MWDC, CA USA) Post-ozonated water (pilot unit)	1.8	43.7	nd	1.4
JWW-HPO	Jeddah treated urban wastewater (Jeddah, Saudi Arabia)	2.8	7.6	24	2.9
RRW-HPI	Ribou Reservoir (Cholet-Maine et Loire, France)	1.0	8.5	7	1.2

$\times$ : Mass ratio

$\surd$ : Aromatic-C content from Solid-State  $^{13}\text{C}$ -NMR

#: Unit:  $\text{L mg C}^{-1} \text{ m}^{-1}$

nd: Not determined

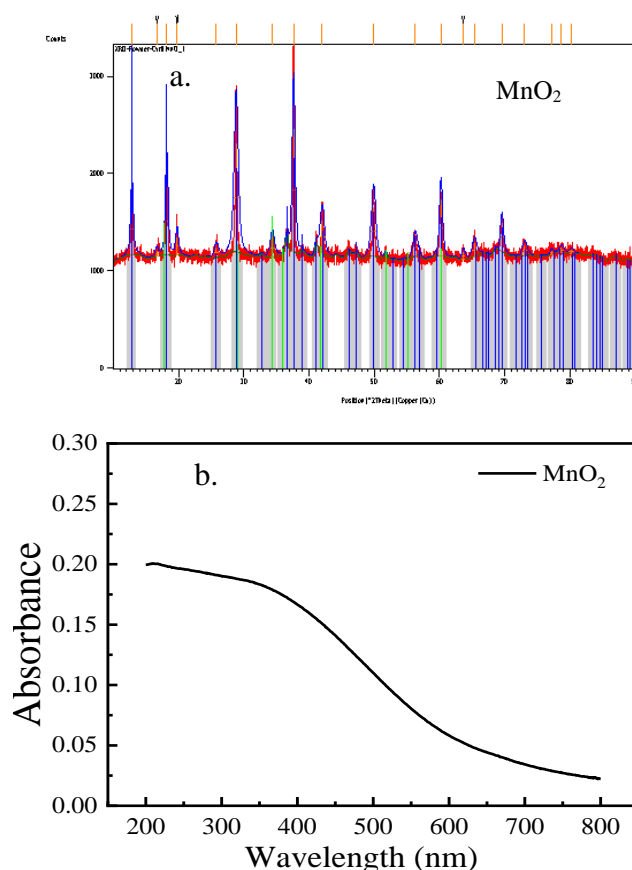


**Figure A3-1. (a) XRD and (b) UV-Vis spectra of MnO<sub>2</sub> particles**

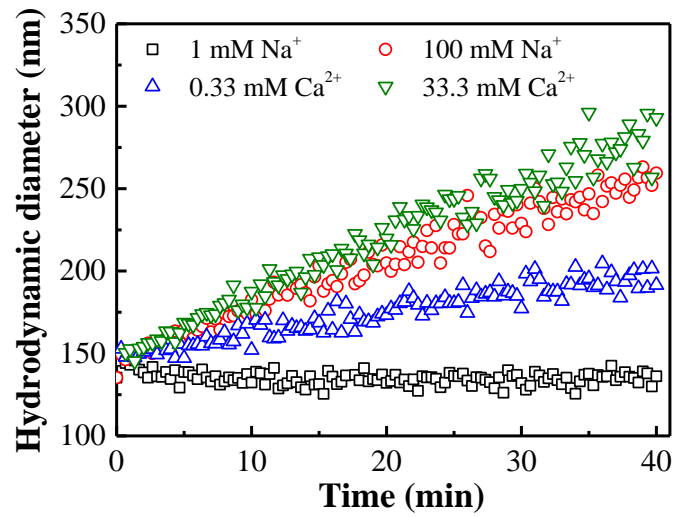


**Figure A3-2. Aggregation kinetics of MnO<sub>2</sub> particles under different Na<sup>+</sup> or Ca<sup>2+</sup> concentrations at unadjusted pH (5.8) and at 25°C**

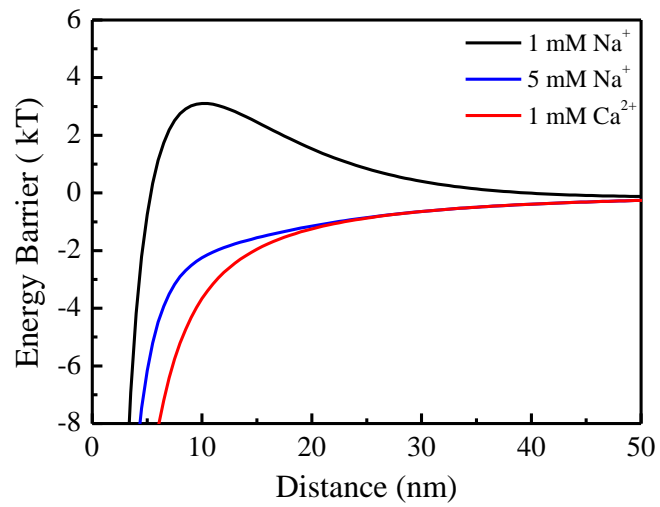


**Figure A3-3. DLVO interaction energy profiles between bared MnO<sub>2</sub> particles as a function of separation distance under different solution condition at unadjusted pH (5.8)**

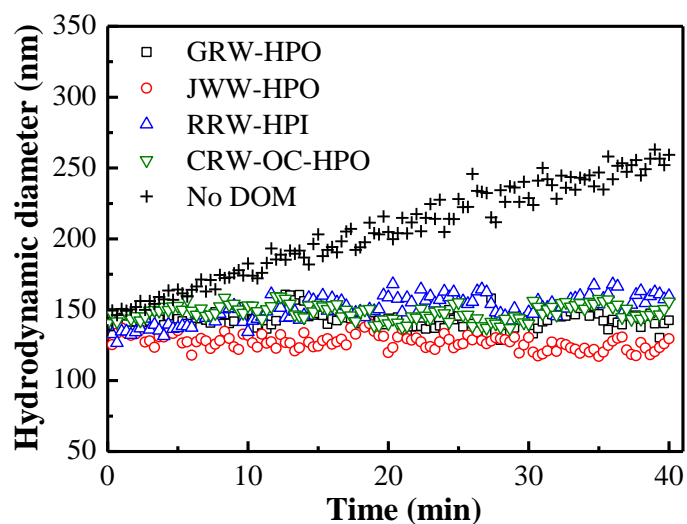


**Figure A3-4. Aggregation kinetics of MnO<sub>2</sub> particles in the presence of 10 mg C/L DOM and in 30 mM NaCl solution at unadjusted pH (5.8) and at 25°C**

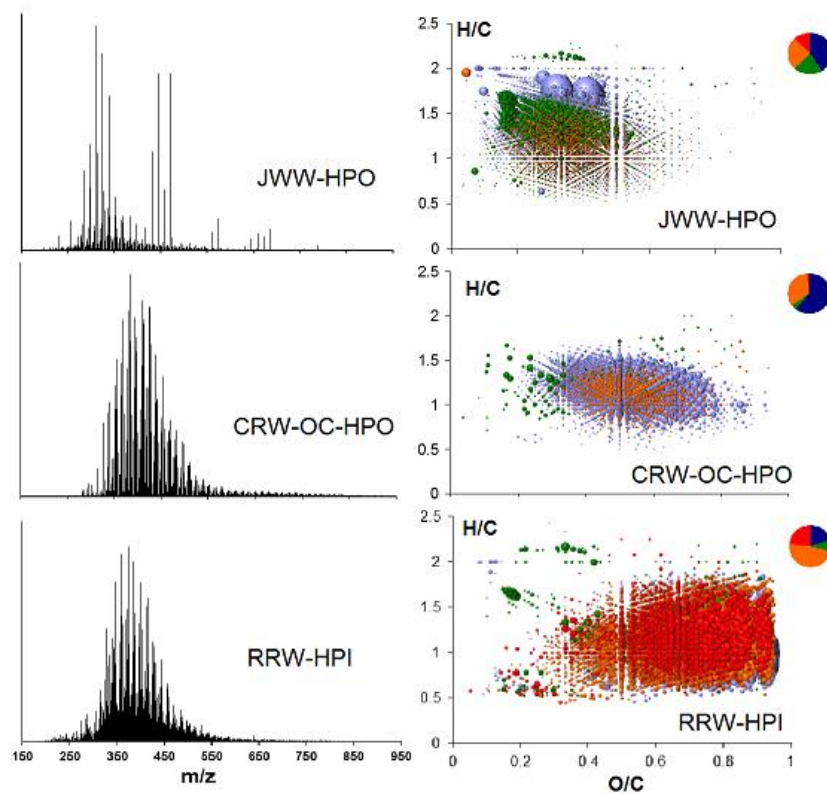


**Figure A3-5. Mass spectra (left) and van Krevelen Diagrams (right) for JWW-HPO, CRW-OC-HPO, and RRW-HPI. Colors reflect the molecular series, i.e., CHO: blue, CHOS: green, CHNO: orange, and CHNOS: red. Bubble areas reflect the relative average intensities of the respective mass peaks**

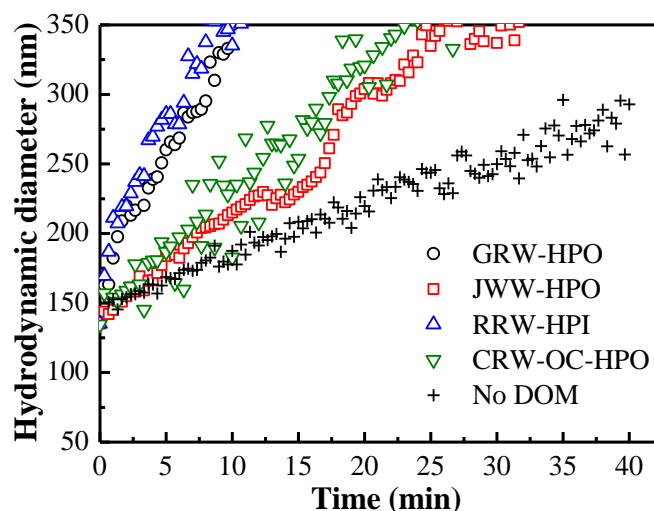


**Figure A3-6. Aggregation kinetics of MnO<sub>2</sub> particles in the presence of 10 mg C/L DOM and in 33.3 mM CaCl<sub>2</sub> solution at unadjusted pH (5.8) and at 25°C**

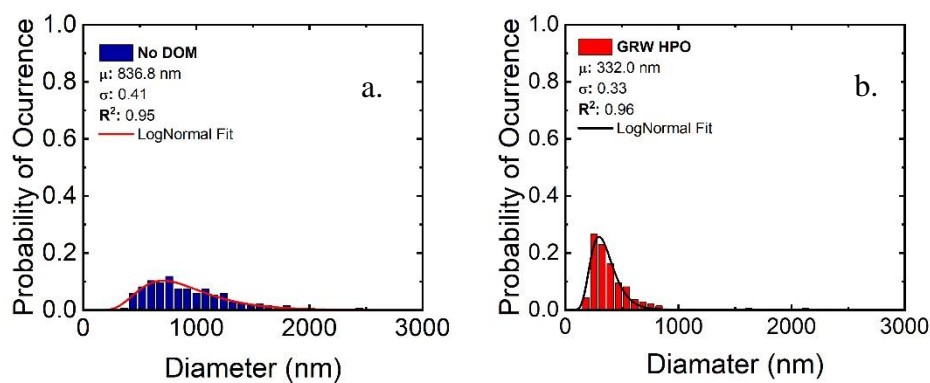


**Figure A3-7. Probability density function describing the mean hydrodynamic diameter ( $\mu$ ) and variance ( $\sigma$ ) of MnO<sub>2</sub> nanoparticles in the (a) absence of DOM in solution and in (b) GRW-HPO-containing solutions, after contact with H<sub>2</sub>O<sub>2</sub>.**

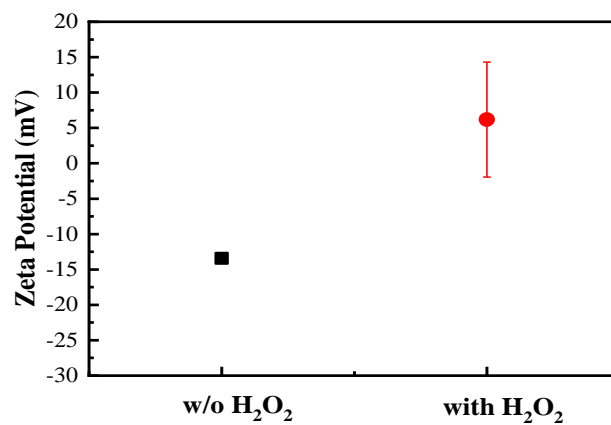


**Figure A3-8. Change of Zeta Potential of MnO<sub>2</sub> particles in 30 mM NaCl solution at unadjusted pH, before and after 1 mM H<sub>2</sub>O<sub>2</sub> addition**

## Appendix 4 Supporting Information-Chapter 5

### Text A4-1.

The XPS spectrum for Mn2p and Co2p of the coated membrane was shown in Figure A4-5. For the XPS spectra of Co2p (Figure A4-5(a)), two main peaks centered at 780.6 and 795.8 eV could be assigned to Co2p<sub>3/2</sub> and Co2p<sub>1/2</sub>, respectively. With deconvolution, the existence of Co(III) and Co(II) could be confirmed with assignment of the two peaks at 780.5 and 795.5 eV, and another two peaks at 782.9 and 797.1 eV. Similarly, two major spin-orbit lines of 2p<sub>3/2</sub> at 641.7 eV and 2p<sub>1/2</sub> at 654.0 eV with the difference as 12.3 eV was detected with XPS spectra of Mn (Figure A4-5(b)). Two peaks at 642.7 and 654.6 eV representative of the Mn(IV), and the other two peaks at 640.8 and 652.9 eV characteristic of Mn(III) could be obtained after deconvolution. The observations were consistent with those previously reported (Todorova et al., 2012; Wang et al., 2015). No significant difference in the XPS spectra was observed with the sonicated catalytic membrane (Figure A4-5(c) and (d)), indicating the negligible impact of sonication on the oxidation state of Co and Mn within the coating layer.

#### **Text A4-2.**

To further differentiate the influence on NOM transformation between pristine and coated membranes in the presence of PMS, fluorescence EEM spectra were collected for feedwaters (B and M), permeate from pristine and coated membranes in the presence of 1 mM PMS in feedwater. As was shown in Figure A4-10a and d, both types of feed water showed similar fluorescent peaks representative of hydrophobic NOM fractions (i.e., major fluorescent compositions in the NOM solution). A decrease in the intensity of fluorescent peaks was observed after membrane filtration with PMS added in feedwater. However, a higher decrease was recorded with the coated membrane as compared to the pristine membrane. Moreover, a significant peak shift from longer (448/446 nm) to shorter emission (436/420 nm) wavelength was detected with both NOM solutions treated by PMS-coated membrane process, which was however negligible with the PMS-pristine membrane process (Figure A4-10g and h). The blue shift indicated the breakdown of larger molecular weight structures and the formation smaller molecules. The higher decrease in the fluorescent intensity and the more pronounced blue shift of fluorescent peaks indicated the enhanced transformation of NOM due to its reaction with the generated sulfate radical in the PMS-catalytic membrane system

**Table A4-1. Characteristics of original ceramic membranes.**

Dimension	Discs with diameter of 47 mm
Filtration area	17.35 (cm <sup>2</sup> )
Active layer material	TiO <sub>2</sub> /ZrO <sub>2</sub>
Support layer material	TiO <sub>2</sub>
Thickness	2.46mm
Membrane pore size	50 kDa (8.6 nm)
Maximum operating pressure	4 bar

**Table A4-2. Flux and resistance of membrane with different catalyst loadings (0–4mg) before ( $J_0$  and  $R_0$ ) and after ( $J_f$  and  $R_f$ ) fouling. Fouling experiments were conducted with NOM-containing feed water (~5mgC/L NOM mixture with ~10% colloids and ~90% HPO fractions) at unadjusted pH of  $6.3 \pm 0.2$  and operating pressure of 1bar.**

	0 mg	0.5 mg	1 mg	2 mg	4 mg
$J_0$ (Lm <sup>-2</sup> h <sup>-1</sup> )	377.63	388.01	379.71	350.66	346.51
$R_0$ (10 <sup>12</sup> m <sup>-1</sup> )	1.07	1.04	1.07	1.15	1.17
$J_f$ (Lm <sup>-2</sup> h <sup>-1</sup> )	225.45	199.83	197.45	154.29	121.28
$R_f$ (10 <sup>12</sup> m <sup>-1</sup> )	1.79	2.02	2.05	2.62	3.34

**Table A4-3. SUVA value ( $\text{m}^{-1}(\text{mg/L})^{-1}$ ) of feedwater and permeate under different experimental conditions: NOM solution-B: 0.56 mgC/L Colloids-Brittany + 4.45 mgC/L HPO-SRNOM, and NOM solution-M: 0.55mgC/L Colloids-Mery + 4.45 mgC/L HPO-SRNOM. Experimental conditions: Operational pressure = 1.0 bar, temperature  $20 \pm 1^\circ\text{C}$ , pH ~ 6 without PMS addition and  $3.40 \pm 0.10$  with 1 mM PMS addition.**

Samples	NOM solution-B	NOM solution-M
Feed water	3.65	3.76
Permeate-pristine	2.92	3.19
Permeate-pristine/PMS	2.80	3.14
Permeate-coated	3.07	3.08
Permeate-coated/PMS	2.65	2.66

**Table A4-4. Equations and descriptions of different filtration models.**

Filtration model	Equation	Description
Complete pore blocking	$J = -AV + J_0$	Foulants with comparable size seal pore upon reaching it.
Intermediate pore blocking	$J_0/V = 1/t + B$	Foulants either seal pores or deposit on already sealed pores.
Standard pore constriction	$\ln J = -CV + \ln J_0$	Foulants deposit on the internal pore wall, causing a reduced pore diameter.
Cake layer filtration	$(1/J) = DV + (1/J_0)$	Foulants are retained due to size exclusion and form a cake at membrane surface.

**Table A4-5. Leaching of cobalt and manganese ions from the coated membrane under different conditions.**

No.	Feed water description	Co		Mn	
		mg/L	%*	mg/L	%*
1	Nanoparticle suspension	0.028	2.80	0.0013	0.13
2	NOM+PMS(1mM) pH3.40	0.100	10.0	0.0370	3.70
3	NOM+PMS(1mM) pH7.40	0.020	2.00	0.0063	0.63
4	NOM-1st cycle no PMS(10mM) cleaning	0.008	0.82	0.0025	0.25
5	NOM-2nd cycle after PMS(10mM) cleaning	0.039	3.90	0.0100	1.00
6	NOM-3rd cycle after PMS(10mM) cleaning	0.014	1.40	0.0021	0.21

\*Percentage calculated based on total  $\text{MnO}_2\text{-Co}_3\text{O}_4$  catalyst (1mg) coated on membrane.

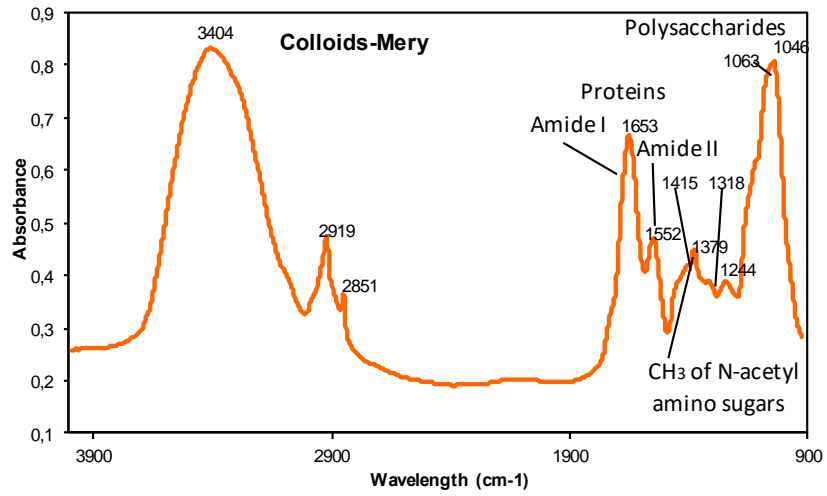


**Figure A4-1. FTIR spectra of Colloids-mery**

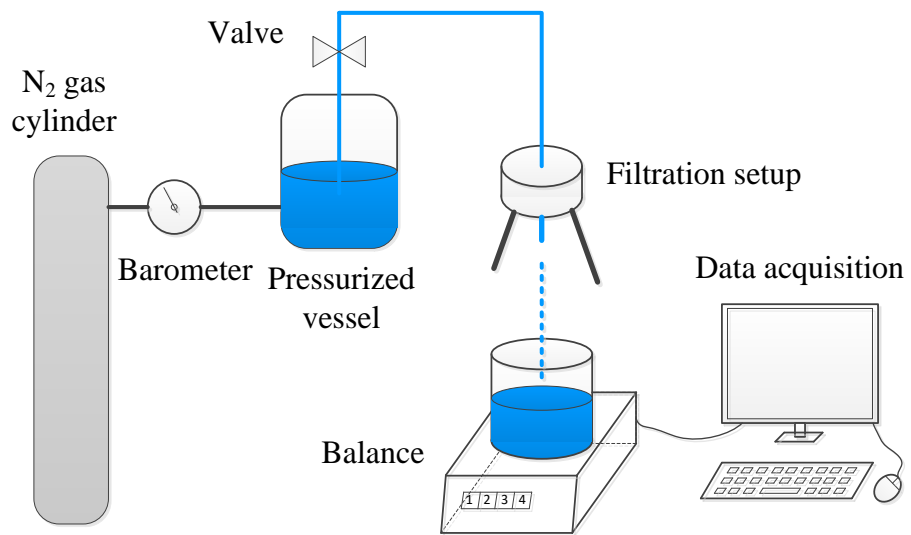


**Figure A4-2. Schematic representative of membrane filtration set-up**

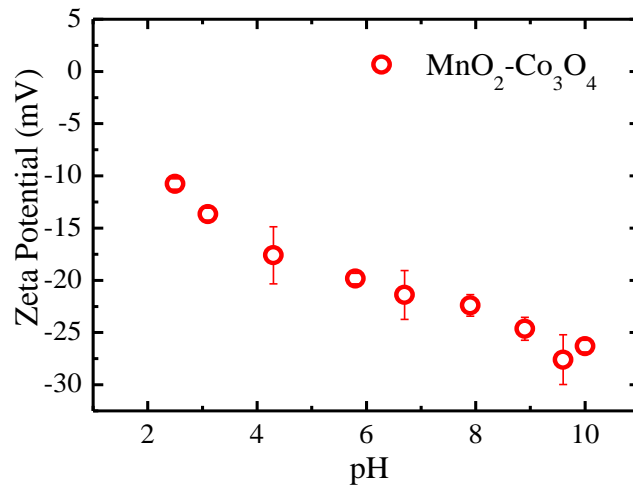


**Figure A4-3. Zeta potential of  $\text{MnO}_2\text{-Co}_3\text{O}_4$  particles as a function of solution pH.**

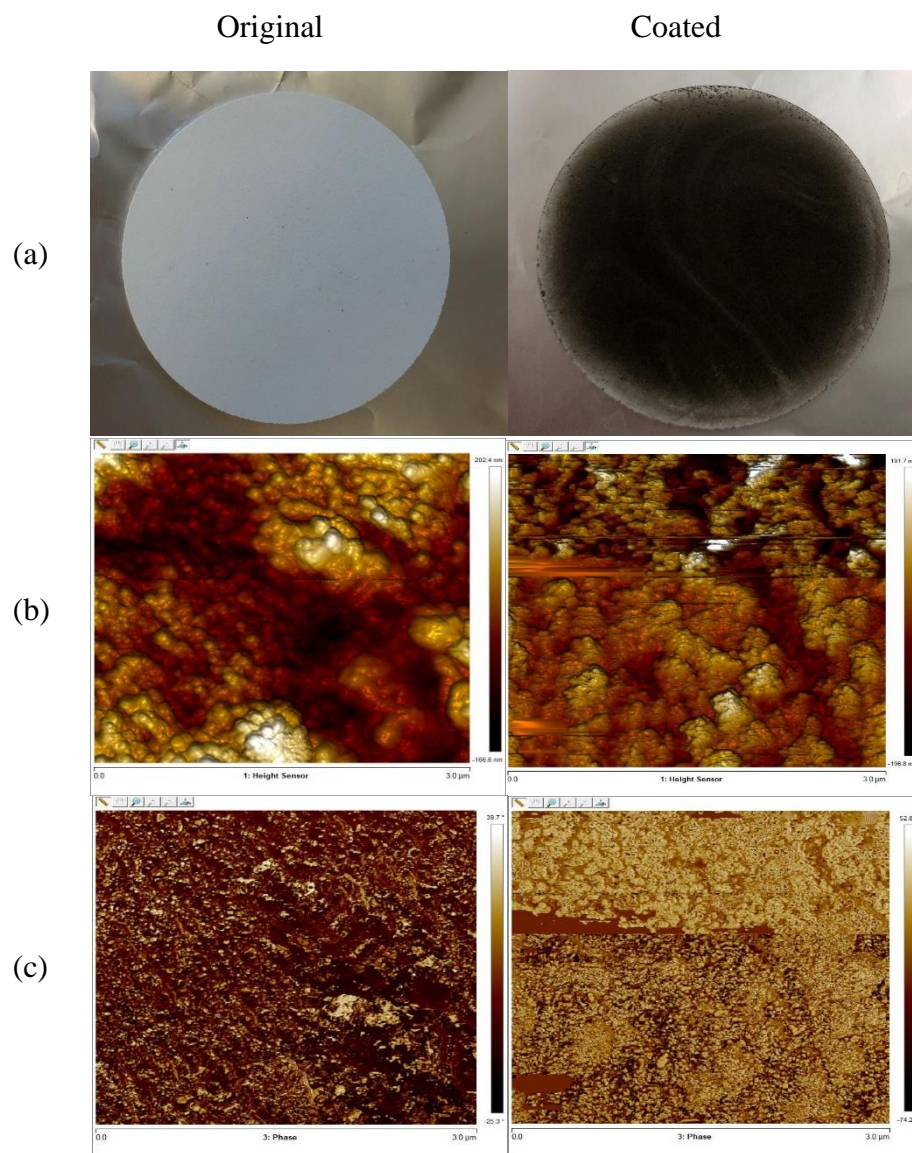


**Figure A4-4. Optical pictures (a), topography (3D-height sensor) images (b) and phase images (c) of original (left) and MnO<sub>2</sub>-Co<sub>3</sub>O<sub>4</sub>-coated membranes (right). Images were acquired by AFM scan (tapping mode) in air with a scan area of 3 μm × 3 μm.**

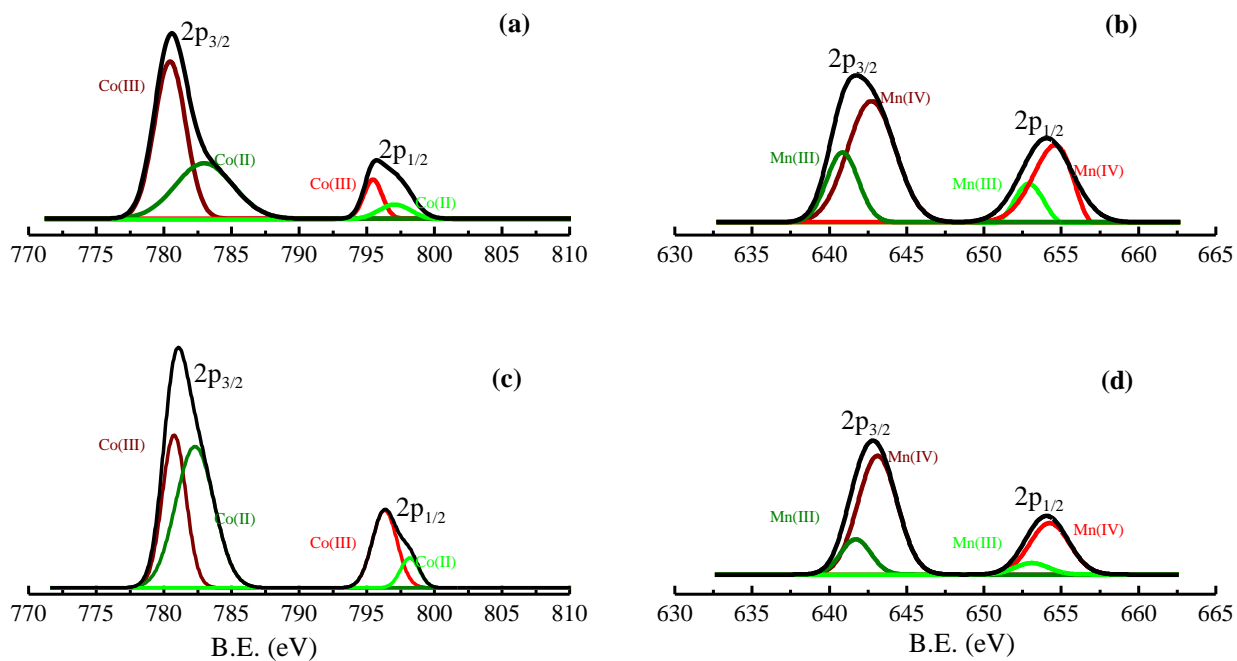


**Figure A4-5. XPS spectra of Co2p and Mn2p for coated membrane without (a, b) and with sonication (c, d).**

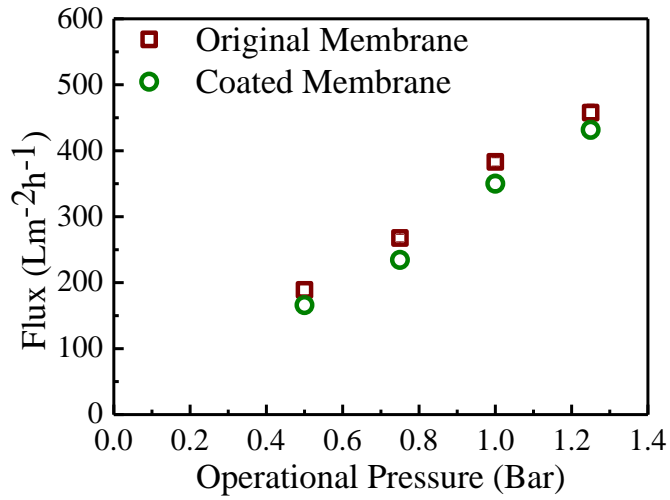


**Figure A4-6. Comparison of original and coated ceramic membrane (1mg MnO<sub>2</sub>-Co<sub>3</sub>O<sub>4</sub> nanoparticles) for pure water permeability (TMP: 1 bar, Temperature: 20 ± 1 °C).**

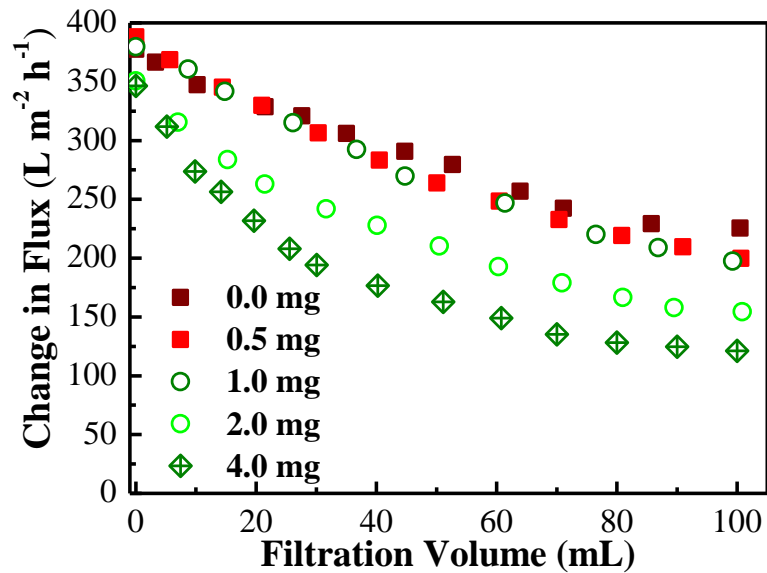


**Figure A4-7. Flux decline for coated membranes with different MnO<sub>2</sub>-Co<sub>3</sub>O<sub>4</sub> loadings (0.0–4.0 mg). Fouling experiments were conducted with NOM-containing feed water (~5mgC/L NOM mixture with ~10% colloids and ~90% HPO fractions) at unadjusted pH of 6.3±0.2 and operating pressure of 1bar.**

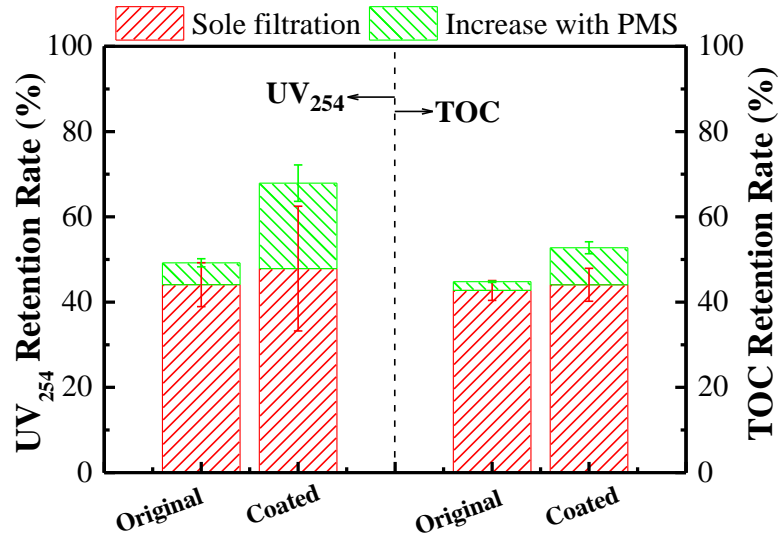


Figure A4-8. UV<sub>254</sub> and TOC removal rate after filtration of 100 mL NOM solution for both original and coated membranes. NOM solution: Colloids-Mery 0.55mgC/L + HPO SRNOM 4.45 mgC/L. Experimental conditions: Operational pressure =1.0 bar, temperature 20 ± 1 °C, pH was adjusted with NaOH to 7.40 ± 0.2.

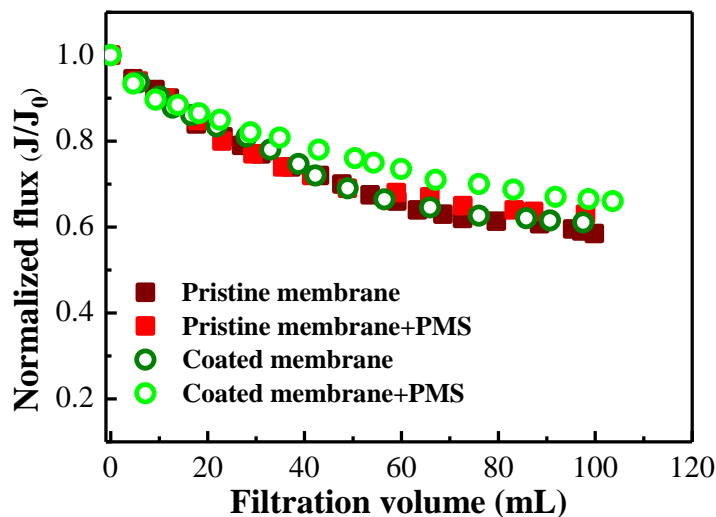
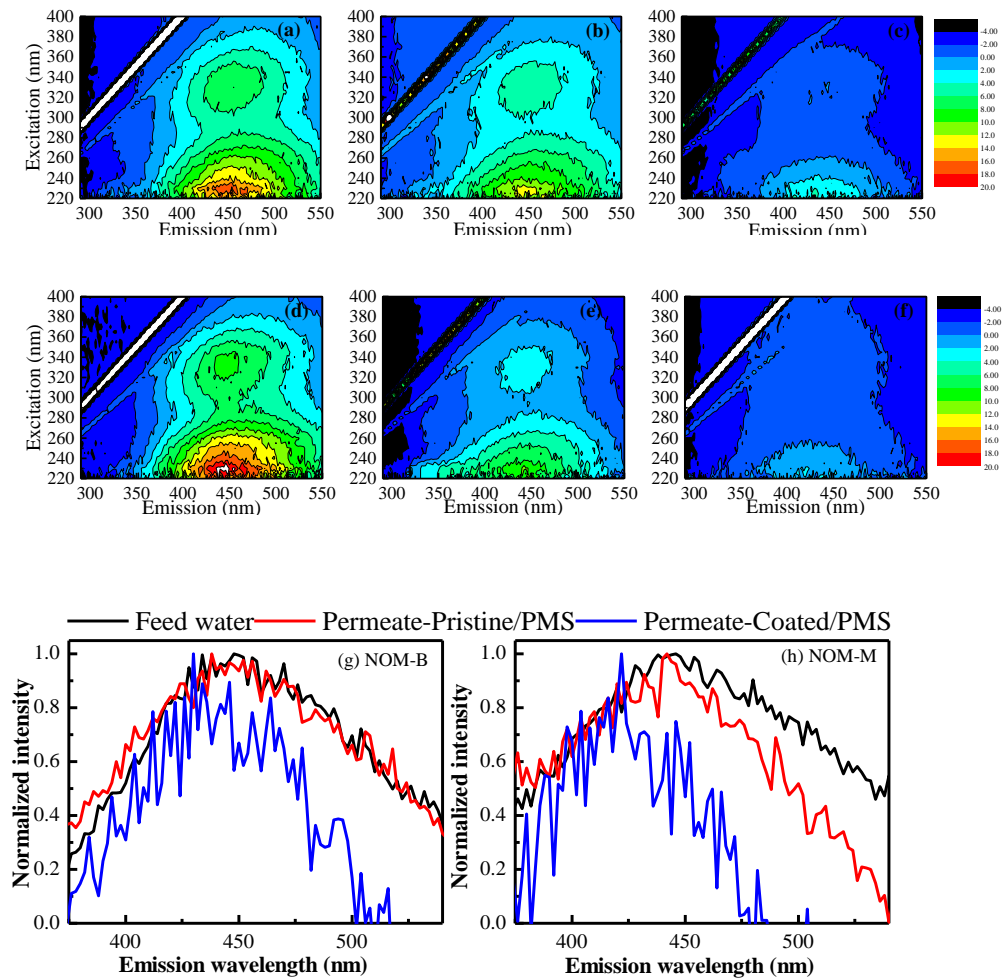
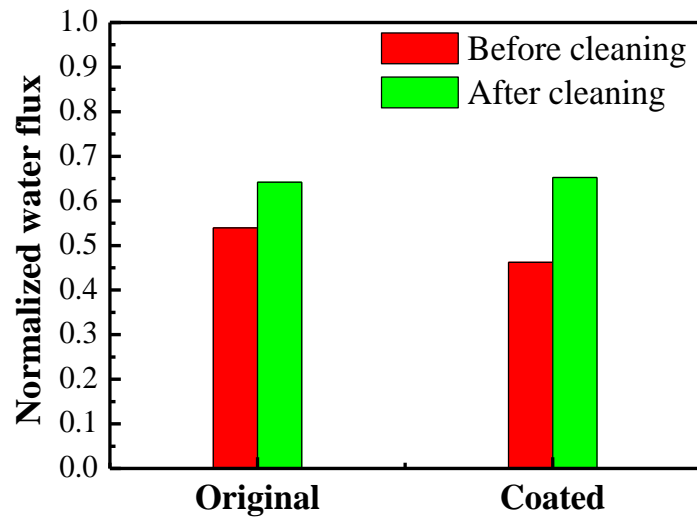


Figure A4-9. Normalized water flux of the original and coated membrane with or with PMS addition in NOM solution-M (Colloids-Mery 0.55 mgC/L + HPO SRNOM 4.45 mgC/ L). Experimental conditions: Operational pressure =1.0 bar, temperature 20 ± 1 °C, pH was adjusted with NaOH to 7.40±0.2.



**Figure A4-10. Fluorescence EEM spectra of (a) NOM solution-B and (d) solution-M, permeate from pristine membrane with PMS added in (b) NOM solution-B and (e) solution-M, and permeate from coated membrane with PMS added in (c) NOM solution-B and (f) solution-M. Emission spectra of (g) NOM solution-B and (h) solution-M before and after filtration under different conditions at an excitation wavelength of 230 nm.**



**Figure A4-11. Flux recovery by soaking fouled membrane in 10 mM PMS solution (pH  $3.20 \pm 0.10$ ) for 10 min. Conditions: fouling tests were conducted with 100 mL of NOM solution-M (Colloids-Mery 0.55mgC/L and HPO SRNOM 4.45 mgC/L).**

## Appendix 5 Permission from the Publisher

 **Copyright Clearance Center** **RightsLink®** [Home](#) [Create Account](#) [Help](#) 

 **Title:** Reactivity of chromophoric dissolved organic matter (CDOM) to sulfate radicals: Reaction kinetics and structural transformation

**Author:** Suona Zhang, Valentin Rouge, Leonardo Gutierrez, Jean-Philippe Croue

**Publication:** Water Research

**Publisher:** Elsevier

**Date:** 15 October 2019

© 2019 Elsevier Ltd. All rights reserved.

**LOGIN**

If you're a **copyright.com** user, you can login to RightsLink using your copyright.com credentials. Already a **RightsLink** user or want to [learn more?](#)

Please note that, as the author of this Elsevier article, you retain the right to include it in a thesis or dissertation, provided it is not published commercially. Permission is not required, but please ensure that you reference the journal as the original source. For more information on this and on your other retained rights, please visit: <https://www.elsevier.com/about/our-business/policies/copyright#Author-rights>

[BACK](#)

[CLOSE WINDOW](#)

Copyright © 2019 [Copyright Clearance Center, Inc.](#) All Rights Reserved. [Privacy statement.](#) [Terms and Conditions.](#) Comments? We would like to hear from you. E-mail us at [customercare@copyright.com](mailto:customercare@copyright.com)

 **Copyright Clearance Center** **RightsLink®** [Home](#) [Create Account](#) [Help](#) 

 **Title:** The characteristics of organic matter influence its interfacial interactions with MnO<sub>2</sub> and catalytic oxidation processes

**Author:** Suona Zhang, Leonardo Gutierrez, Xi-Zhi Niu, Fei Qi, Jean-Philippe Croue

**Publication:** Chemosphere

**Publisher:** Elsevier

**Date:** October 2018

© 2018 Elsevier Ltd. All rights reserved.

**LOGIN**

If you're a **copyright.com** user, you can login to RightsLink using your copyright.com credentials. Already a **RightsLink** user or want to [learn more?](#)

Please note that, as the author of this Elsevier article, you retain the right to include it in a thesis or dissertation, provided it is not published commercially. Permission is not required, but please ensure that you reference the journal as the original source. For more information on this and on your other retained rights, please visit: <https://www.elsevier.com/about/our-business/policies/copyright#Author-rights>

[BACK](#)

[CLOSE WINDOW](#)

Copyright © 2019 [Copyright Clearance Center, Inc.](#) All Rights Reserved. [Privacy statement.](#) [Terms and Conditions.](#) Comments? We would like to hear from you. E-mail us at [customercare@copyright.com](mailto:customercare@copyright.com)

# Appendix 6 Attribution Statements

## Statement of Contribution to Co-authored Published Paper

Chapter 2 includes the co-authored paper “Reactivity of chromophoric dissolved organic matter (CDOM) to sulfate radicals: Reaction kinetics and structural transformation”, published on Water Research. The bibliographic details of the co-authored paper, including all authors are:

Zhang, S.; Rougé, V.; Gutierrez, L.; Croué, J.-P. (2019). Reactivity of chromophoric dissolved organic matter (CDOM) to sulfate radicals: Reaction kinetics and structural transformation. Water Research, 163, 114846.

I, Suona Zhang, as the primary author, conducted all the experimental work and data analysis, including creating figures and tables, and writing and editing the manuscript.

I, as a Co-Author, endorsed that this level of contribution by the candidate indicated above is appropriate.

Valentin Rougé

Leonardo Gutierrez

Jean-Philippe Croué

## Statement of Contribution to Co-authored Published Paper

Chapter 3 includes the co-authored paper “Molecular Insights into the Reactivity of Aquatic Natural Organic Matter towards  $\cdot\text{OH}$  and  $\text{SO}_4^{\cdot-}$  Using FT-ICR MS”, to be submitted to *Environmental Science & Technology*. The bibliographic details of the co-authored paper, including all authors are:

Zhang, S.; Hao, Z.; Liu, J.; Gutierrez, L., Croué, J.-P. (2020). Molecular Insights into the Reactivity of Aquatic Natural Organic Matter towards  $\cdot\text{OH}$  and  $\text{SO}_4^{\cdot-}$  Using FT-ICR MS. to be submitted to *Environmental Science & Technology*.

I, Suona Zhang, as the primary author, conducted all the experimental work and data analysis, including creating figures and tables, and writing and editing the manuscript.

I, as a Co-Author, endorsed that this level of contribution by the candidate indicated above is appropriate.

Zhineng Hao

Jingfu Liu

Leonardo Gutierrez

Jean-Philippe Croué

## Statement of Contribution to Co-authored Published Paper

Chapter 4 includes the co-authored paper “Organic Matter interfacial interactions with MnO<sub>2</sub> and its influence on catalytic oxidation processes, published on Chemosphere. The bibliographic details of the co-authored paper, including all authors are:

Zhang, S.; Gutierrez, L.; Niu, X-Z.; Qi, F.; Croué, J.-P. (2018). Organic Matter interfacial interactions with MnO<sub>2</sub> and its influence on catalytic oxidation processes. Chemosphere, 209, 950–959.

I, Suona Zhang, as the primary author, conducted all the experimental work and data analysis, including creating figures and tables, and writing and editing the manuscript.

I, as a Co-Author, endorsed that this level of contribution by the candidate indicated above is appropriate.

Leonardo Gutierrez

Xi-Zhi Niu

Fei Qi

Jean-Philippe Croué

## Statement of Contribution to Co-authored Published Paper

Chapter 5 includes the co-authored paper “SO<sub>4</sub><sup>2-</sup>-based catalytic ceramic UF membrane for organics removal and flux restoration”, to be submitted to *Chemical Engineering Journal*. The bibliographic details of the co-authored paper, including all authors are:

Zhang, S.; Gutierrez, L.; Qi, F.; Croué, J.-P. (2020). SO<sub>4</sub><sup>2-</sup>-based catalytic ceramic UF membrane for organics removal and flux restoration. To be submitted to *Chemical Engineering Journal*.

I, Suona Zhang, as the primary author, conducted all the experimental work and data analysis, including creating figures and tables, and writing and editing the manuscript.

I, as a Co-Author, endorsed that this level of contribution by the candidate indicated above is appropriate.

Leonardo Gutierrez

Fei Qi

Jean-Philippe Croué

## List of References

- Aeschbacher, M., Graf, C., Schwarzenbach, R. P., & Sander, M. (2012). Antioxidant properties of humic substances. *Environmental Science & Technology*, 46(9), 4916-4925
- Allard, S., Gutierrez, L., Fontaine, C., Croué, J.-P., & Gallard, H. (2017). Organic matter interactions with natural manganese oxide and synthetic birnessite. *Science of The Total Environment*, 583, 487-495
- Anipsitakis, G. P., & Dionysiou, D. D. (2003). Degradation of Organic Contaminants in Water with Sulfate Radicals Generated by the Conjunction of Peroxymonosulfate with Cobalt. *Environmental Science & Technology*, 37(20), 4790-4797
- Anipsitakis, G. P., Dionysiou, D. D., & Gonzalez, M. A. (2006). Cobalt-Mediated Activation of Peroxymonosulfate and Sulfate Radical Attack on Phenolic Compounds. Implications of Chloride Ions. *Environmental Science & Technology*, 40(3), 1000-1007
- Anipsitakis, G. P., Stathatos, E., & Dionysiou, D. D. (2005). Heterogeneous activation of Oxone using  $\text{Co}_3\text{O}_4$ . *Journal of Physical Chemistry B*, 109(27), 13052-13055
- Aoustin, E., Schäfer, A. I., Fane, A. G., & Waite, T. D. (2001). Ultrafiltration of natural organic matter. *Separation and Purification Technology*, 22-23, 63-78
- Aubry, C., Gutierrez, L., & Croue, J. P. (2013). Coating of AFM probes with aquatic humic and non-humic NOM to study their adhesion properties. *Water Research*, 47(9), 3109-3119
- Autin, O., Hart, J., Jarvis, P., MacAdam, J., Parsons, S. A., & Jefferson, B. (2013). The impact of background organic matter and alkalinity on the degradation of the pesticide metaldehyde by two advanced oxidation processes: UV/ $\text{H}_2\text{O}_2$  and UV/ $\text{TiO}_2$ . *Water Research*, 47(6), 2041-2049
- Avena, M. J., Vermeer, A. W. P., & Koopal, L. K. (1999). Volume and structure of humic acids studied by viscometry pH and electrolyte concentration effects. *Colloids and Surfaces A: Physicochemical and Engineering Aspects*, 151(1-2), 213-224
- Baalousha, M., Afshinnia, K., & Guo, L. (2018). Natural organic matter composition determines the molecular nature of silver nanomaterial-NOM corona. *Environmental Science: Nano*, 5(4), 868-881

- Barrett, K. A., & McBride, M. B. (2005). Oxidative Degradation of Glyphosate and Aminomethylphosphonate by Manganese Oxide. *Environmental Science & Technology*, 39(23), 9223-9228
- Basnet, M., Ghoshal, S., & Tufenkji, N. (2013). Rhamnolipid Biosurfactant and Soy Protein Act as Effective Stabilizers in the Aggregation and Transport of Palladium-Doped Zerovalent Iron Nanoparticles in Saturated Porous Media. *Environmental Science & Technology*, 47(23), 13355-13364
- Benner, J., & Ternes, T. A. (2009). Ozonation of Metoprolol: Elucidation of Oxidation Pathways and Major Oxidation Products. *Environmental Science & Technology*, 43(14), 5472-5480
- Bolton, J. R., & Linden, K. G. (2003). Standardization of Methods for Fluence (UV Dose) Determination in Bench-Scale UV Experiments. *Journal of Environmental Engineering*, 129(3), 209-215
- Bortolomeazzi, R., Sebastianutto, N., Toniolo, R., & Pizzariello, A. (2007). Comparative evaluation of the antioxidant capacity of smoke flavouring phenols by crocin bleaching inhibition, DPPH radical scavenging and oxidation potential. *Food Chemistry*, 100(4), 1481-1489
- Boyle, M., Frankenberger, W. T., & Stolzy, L. H. (1989). The Influence of Organic Matter on Soil Aggregation and Water Infiltration. *Journal of Production Agriculture*, 2(4), 290-299
- Butt, H.-J., Cappella, B., & Kappl, M. (2005). Force measurements with the atomic force microscope: Technique, interpretation and applications. *Surface Science Reports*, 59(1-6), 1-152
- Buxton, G. V., Greenstock, C. L., Helman, W. P., & Ross, A. B. (1988). Critical Review of rate constants for reactions of hydrated electrons, hydrogen atoms and hydroxyl radicals ( $\cdot\text{OH}/\text{O}^-$  in Aqueous Solution. *Journal of Physical and Chemical Reference Data*, 17(2), 513-886
- Byun, S., Davies, S. H., Alpatova, A. L., Corneal, L. M., Baumann, M. J., Tarabara, V. V., & Masten, S. J. (2011). Mn oxide coated catalytic membranes for a hybrid ozonation-membrane filtration: Comparison of Ti, Fe and Mn oxide coated membranes for water quality. *Water Research*, 45(1), 163-170
- Cabaniss, S. E. (2011). Forward Modeling of Metal Complexation by NOM: II. Prediction of Binding Site Properties. *Environmental Science & Technology*, 45(8), 3202-3209

- Cappella, B., & Dietler, G. (1999). Force-distance curves by atomic force microscopy. *Surface Science Reports*, 34(1), 1-104
- Cawley, K. M. (2016). Molecular characterization of dissolved organic matter from subtropical wetlands: a comparative study through the analysis of optical properties, NMR and FTICR/MS. *Biogeosciences*, 13(8), 2257
- Chen, J., Gu, B., LeBoeuf, E. J., Pan, H., & Dai, S. (2002). Spectroscopic characterization of the structural and functional properties of natural organic matter fractions. *Chemosphere*, 48(1), 59-68
- Chen, K. L., Mylon, S. E., & Elimelech, M. (2006). Aggregation Kinetics of Alginate-Coated Hematite Nanoparticles in Monovalent and Divalent Electrolytes. *Environmental Science & Technology*, 40(5), 1516-1523
- Chen, W., Westerhoff, P., Leenheer, J. A., & Booksh, K. (2003). Fluorescence Excitation–Emission Matrix Regional Integration to Quantify Spectra for Dissolved Organic Matter. *Environmental Science & Technology*, 37(24), 5701-5710
- Cheng, X., Liang, H., Ding, A., Tang, X., Liu, B., Zhu, X., Li, G. (2017). Ferrous iron/peroxymonosulfate oxidation as a pretreatment for ceramic ultrafiltration membrane: Control of natural organic matter fouling and degradation of atrazine. *Water Research*, 113, 32-41
- Cheng, X., Liang, H., Qu, F., Ding, A., Chang, H., Liu, B., Li, G. (2017). Fabrication of Mn oxide incorporated ceramic membranes for membrane fouling control and enhanced catalytic ozonation of p-chloronitrobenzene. *Chemical Engineering Journal*, 308, 1010-1020
- Chon, K., Salhi, E., & von Gunten, U. (2015). Combination of UV absorbance and electron donating capacity to assess degradation of micropollutants and formation of bromate during ozonation of wastewater effluents. *Water Research*, 81, 388-397
- Chowdhury, I., Duch, M. C., Mansukhani, N. D., Hersam, M. C., & Bouchard, D. (2013). Colloidal Properties and Stability of Graphene Oxide Nanomaterials in the Aquatic Environment. *Environmental Science & Technology*, 47(12), 6288-6296
- Chu, W., Li, D., Gao, N., Templeton, M. R., Tan, C., & Gao, Y. (2015). The control of emerging haloacetamide DBP precursors with UV/persulfate treatment. *Water Research*, 72, 340-348

- Cong, J., Wen, G., Huang, T., Deng, L., & Ma, J. (2015). Study on enhanced ozonation degradation of para-chlorobenzoic acid by peroxymonosulfate in aqueous solution. *Chemical Engineering Journal*, 264, 399-403
- Corneal, L. M., Baumann, M. J., Masten, S. J., Davies, S. H. R., Tarabara, V. V., & Byun, S. (2011). Mn oxide coated catalytic membranes for hybrid ozonation-membrane filtration: Membrane microstructural characterization. *Journal of Membrane Science*, 369(1-2), 182-187
- Corneal, L. M., Masten, S. J., Davies, S. H. R., Tarabara, V. V., Byun, S., & Baumann, M. J. (2010). AFM, SEM and EDS characterization of manganese oxide coated ceramic water filtration membranes. *Journal of Membrane Science*, 360(1-2), 292-302
- Cory, R. M., & McKnight, D. M. (2005). Fluorescence Spectroscopy Reveals Ubiquitous Presence of Oxidized and Reduced Quinones in Dissolved Organic Matter. *Environmental Science & Technology*, 39(21), 8142-8149
- Croué, J.-P., Violleau, D., & Labouyrie, L. (2000). *Disinfection by-product formation potentials of hydrophobic and hydrophilic natural organic matter fractions: a comparison between a low-and a high-humic water*. Paper presented at the ACS Symposium Series.
- Croué, J.-P., Korshin, G. V., & Benjamin, M. M. (2000). *Characterization of natural organic matter in drinking water*: American Water Works Association.
- Croué, J. P., Korshin Gregory, V., & Benjamin, M. M. (1999). *Isolation, Fractionation and Characterization of Natural Organic Matter in Drinking Water*. USA: AWWA Research Foundation and American Water Works Association.
- De Angelis, L., & de Cortalezzi, M. M. F. (2016). Improved membrane flux recovery by Fenton-type reactions. *Journal of Membrane Science*, 500, 255-264
- Do, S.-H., Batchelor, B., Lee, H.-K., & Kong, S.-H. (2009). Hydrogen peroxide decomposition on manganese oxide (pyrolusite): Kinetics, intermediates, and mechanism. *Chemosphere*, 75(1), 8-12
- Domingos, R. F., Tufenkji, N., & Wilkinson, K. J. (2009). Aggregation of Titanium Dioxide Nanoparticles: Role of a Fulvic Acid. *Environmental Science & Technology*, 43(5), 1282-1286
- Dong, H., & Lo, I. M. C. (2013). Influence of calcium ions on the colloidal stability of surface-modified nano zero-valent iron in the absence or presence of humic acid. *Water Research*, 47(7), 2489-2496

- Dong, M. M., Mezyk, S. P., & Rosario-Ortiz, F. L. (2010). Reactivity of Effluent Organic Matter (EfOM) with Hydroxyl Radical as a Function of Molecular Weight. *Environmental Science & Technology*, 44(15), 5714-5720
- Driehaus, W., Seith, R., & Jekel, M. (1995). Oxidation of arsenate(III) with manganese oxides in water treatment. *Water Research*, 29(1), 297-305
- Elovitz, M. S., & von Gunten, U. (1999). Hydroxyl Radical/Ozone Ratios During Ozonation Processes. I. The Rct Concept. *Ozone: Science & Engineering*, 21(3), 239-260
- Feitosa-Felizzola, J., Hanna, K., & Chiron, S. (2009). Adsorption and transformation of selected human-used macrolide antibacterial agents with iron(III) and manganese(IV) oxides. *Environ Pollut*, 157(4), 1317-1322
- Fichot, C. G., Benner, R., Kaiser, K., Shen, Y., Amon, R. M. W., Ogawa, H., & Lu, C.-J. (2016). Predicting Dissolved Lignin Phenol Concentrations in the Coastal Ocean from Chromophoric Dissolved Organic Matter (CDOM) Absorption Coefficients. *Frontiers in Marine Science*, 3(7)
- Fischer, H., & Radom, L. (2001). Factors Controlling the Addition of Carbon-Centered Radicals to Alkenes—An Experimental and Theoretical Perspective. *Angewandte Chemie International Edition*, 40(8), 1340-1371
- Fu, X., Clark, L. A., Yang, Q., & Anderson, M. A. (1996). Enhanced Photocatalytic Performance of Titania-Based Binary Metal Oxides: TiO<sub>2</sub>/SiO<sub>2</sub> and TiO<sub>2</sub>/ZrO<sub>2</sub>. *Environmental Science & Technology*, 30(2), 647-653
- Furman, O., Usenko, S., & Lau, B. L. T. (2013). Relative Importance of the Humic and Fulvic Fractions of Natural Organic Matter in the Aggregation and Deposition of Silver Nanoparticles. *Environmental Science & Technology*, 47(3), 1349-1356
- Gao, W., Liang, H., Ma, J., Han, M., Chen, Z.-l., Han, Z.-s., & Li, G.-b. (2011). Membrane fouling control in ultrafiltration technology for drinking water production: A review. *Desalination*, 272(1), 1-8
- Gerrity, D., Gamage, S., Jones, D., Korshin, G. V., Lee, Y., Pisarenko, A., Snyder, S. A. (2012). Development of surrogate correlation models to predict trace organic contaminant oxidation and microbial inactivation during ozonation. *Water Research*, 46(19), 6257-6272
- Ghauch, A., Baalbaki, A., Amasha, M., El Asmar, R., & Tantawi, O. (2017). Contribution of persulfate in UV-254 nm activated systems for complete

- degradation of chloramphenicol antibiotic in water. *Chemical Engineering Journal*, 317, 1012-1025
- Ghosh, S., Mashayekhi, H., Pan, B., Bhowmik, P., & Xing, B. (2008). Colloidal Behavior of Aluminum Oxide Nanoparticles As Affected by pH and Natural Organic Matter. *Langmuir*, 24(21), 12385-12391
- Golden, D. C., Chen, C. C., & Dixon, J. B. (1986). Synthesis of Todorokite. *Science*, 231(4739), 717-719
- Gonsior, M., Peake, B. M., Cooper, W. T., Podgorski, D., D'Andrilli, J., & Cooper, W. J. (2009). Photochemically Induced Changes in Dissolved Organic Matter Identified by Ultrahigh Resolution Fourier Transform Ion Cyclotron Resonance Mass Spectrometry. *Environmental Science & Technology*, 43(3), 698-703
- Griffith, J. S., & Orgel, L. E. (1957). Ligand-field theory. *Quarterly Reviews, Chemical Society*, 11(4), 381-393
- Guan, Y.-H., Ma, J., Ren, Y.-M., Liu, Y.-L., Xiao, J.-Y., Lin, L.-q., & Zhang, C. (2013). Efficient degradation of atrazine by magnetic porous copper ferrite catalyzed peroxymonosulfate oxidation via the formation of hydroxyl and sulfate radicals. *Water Research*, 47(14), 5431-5438
- Guo, L., Lehner, J. K., White, D. M., & Garland, D. S. (2003). Heterogeneity of natural organic matter from the Chena River, Alaska. *Water Research*, 37(5), 1015-1022
- Guo, Y., Xu, B., & Qi, F. (2016). A novel ceramic membrane coated with MnO<sub>2</sub>-Co<sub>3</sub>O<sub>4</sub> nanoparticles catalytic ozonation for benzophenone-3 degradation in aqueous solution: Fabrication, characterization and performance. *Chemical Engineering Journal*, 287, 381-389
- Gutierrez, L., Aubry, C., Cornejo, M., & Croue, J.-P. (2015). Citrate-Coated Silver Nanoparticles Interactions with Effluent Organic Matter: Influence of Capping Agent and Solution Conditions. *Langmuir*, 31(32), 8865-8872
- Gutierrez, L., Aubry, C., Valladares Linares, R., & Croue, J.-P. (2015). Natural organic matter interactions with polyamide and polysulfone membranes: Formation of conditioning film. *Colloids and Surfaces A: Physicochemical and Engineering Aspects*, 477, 1-8
- Gutierrez, L., & Nguyen, T. H. (2012). Interactions between Rotavirus and Suwannee River Organic Matter: Aggregation, Deposition, and Adhesion Force Measurement. *Environmental Science & Technology*, 46(16), 8705-8713

- He, X., de la Cruz, A. A., & Dionysiou, D. D. (2013). Destruction of cyanobacterial toxin cylindrospermopsin by hydroxyl radicals and sulfate radicals using UV-254nm activation of hydrogen peroxide, persulfate and peroxymonosulfate. *Journal of Photochemistry and Photobiology A: Chemistry*, 251, 160-166
- Hem, L. J., & Efraïmsen, H. (2001). Assimilable organic carbon in molecular weight fractions of natural organic matter. *Water Research*, 35(4), 1106-1110
- Hertkorn, N., Frommberger, M., Witt, M., Koch, B. P., Schmitt-Kopplin, P., & Perdue, E. M. (2008). Natural Organic Matter and the Event Horizon of Mass Spectrometry. *Analytical Chemistry*, 80(23), 8908-8919
- Herzprung, P., Hertkorn, N., von Tümpling, W., Harir, M., Friese, K., & Schmitt-Kopplin, P. (2016). Molecular formula assignment for dissolved organic matter (DOM) using high-field FT-ICR-MS: chemical perspective and validation of sulphur-rich organic components (CHOS) in pit lake samples. *Analytical and Bioanalytical Chemistry*, 408(10), 2461-2469
- Hotze, E. M., Phenrat, T., & Lowry, G. V. (2010). Nanoparticle Aggregation: Challenges to Understanding Transport and Reactivity in the Environment *Journal of Environmental Quality*, 39, 1909-1924
- Huangfu, X., Jiang, J., Ma, J., Liu, Y., & Yang, J. (2013). Aggregation Kinetics of Manganese Dioxide Colloids in Aqueous Solution: Influence of Humic Substances and Biomacromolecules. *Environmental Science & Technology*, 47(18), 10285-10292
- Hussain, I., Zhang, Y., & Huang, S. (2014). Degradation of aniline with zero-valent iron as an activator of persulfate in aqueous solution. *RSC Advances*, 4(7), 3502-3511
- Huynh, K. A., & Chen, K. L. (2011). Aggregation Kinetics of Citrate and Polyvinylpyrrolidone Coated Silver Nanoparticles in Monovalent and Divalent Electrolyte Solutions. *Environmental Science & Technology*, 45(13), 5564-5571
- Hwang, C., Kranser, S. W., Amy, G., Bruchet, A., Croue, J. P., & Leenheer Jerry, A. (2001). *Polar NOM: Characterization, DBPs, Treatment*: AWWA Research Foundation.
- Kim, J., Davies, S. H. R., Baumann, M. J., Tarabara, V. V., & Masten, S. J. (2008). Effect of ozone dosage and hydrodynamic conditions on the permeate flux in a hybrid ozonation–ceramic ultrafiltration system treating natural waters. *Journal of Membrane Science*, 311(1), 165-172

- Korshin, G. V., Kumke, M. U., Li, C.-W., & Frimmel, F. H. (1999). Influence of Chlorination on Chromophores and Fluorophores in Humic Substances. *Environmental Science & Technology*, 33(8), 1207-1212
- Lavonen, E. E., Kothawala, D. N., Tranvik, L. J., Gonsior, M., Schmitt-Kopplin, P., & Köhler, S. J. (2015). Tracking changes in the optical properties and molecular composition of dissolved organic matter during drinking water production. *Water Research*, 85, 286-294
- Le Roux, J., Nihemaiti, M., & Croué, J.-P. (2016). The role of aromatic precursors in the formation of haloacetamides by chloramination of dissolved organic matter. *Water Research*, 88, 371-379
- Lead, J. R., Wilkinson, K. J., Starchev, K., Canonica, S., & Buffle, J. (2000). Determination of diffusion coefficients of humic substances by fluorescence correlation spectroscopy: Role of solution conditions. *Environmental Science & Technology*, 34(7), 1365-1369
- Lee, N., Amy, G., & Croué, J.-P. (2006). Low-pressure membrane (MF/UF) fouling associated with allochthonous versus autochthonous natural organic matter. *Water Research*, 40(12), 2357-2368
- Lee, N., Amy, G., Croué, J.-P., & Buisson, H. (2005). Morphological analyses of natural organic matter (NOM) fouling of low-pressure membranes (MF/UF). *Journal of Membrane Science*, 261(1), 7-16
- Leenheer, J. A., & Croué, J.-P. (2003). Peer Reviewed: Characterizing Aquatic Dissolved Organic Matter. *Environmental Science & Technology*, 37(1), 18A-26A
- Leenheer, J. A., Croué, J.-P., Benjamin, M., Korshin Gregory, V., Hwang Cordelia, J., Bruchet, A., & Aiken George, R. (2000). Comprehensive Isolation of Natural Organic Matter from Water for Spectral Characterizations and Reactivity Testing *Natural Organic Matter and Disinfection By-Products* (Vol. 761, pp. 68-83): American Chemical Society.
- Leenheer, J. A., Croué, J.-P., Benjamin, M., Korshin, G. V., Hwang, C. J., Bruchet, A., & Aiken, G. R. (2000). Comprehensive Isolation of Natural Organic Matter from Water for Spectral Characterizations and Reactivity Testing *Natural Organic Matter and Disinfection By-Products* (Vol. 761, pp. 68-83): American Chemical Society.

- Lehman, S. G., & Liu, L. (2009). Application of ceramic membranes with pre-ozonation for treatment of secondary wastewater effluent. *Water Research*, *43*(7), 2020-2028
- Li, T., Jiang, Y., An, X., Liu, H., Hu, C., & Qu, J. (2016). Transformation of humic acid and halogenated byproduct formation in UV-chlorine processes. *Water Research*, *102*, 421-427
- Li, W.-T., Cao, M.-J., Young, T., Ruffino, B., Dodd, M., Li, A.-M., & Korshin, G. (2017). Application of UV absorbance and fluorescence indicators to assess the formation of biodegradable dissolved organic carbon and bromate during ozonation. *Water Research*, *111*, 154-162
- Lin, C.-F., Liu, S.-H., & Hao, O. J. (2001). Effect of functional groups of humic substances on uf performance. *Water Research*, *35*(10), 2395-2402
- Liu, J., Legros, S., von der Kammer, F., & Hofmann, T. (2013). Natural Organic Matter Concentration and Hydrochemistry Influence Aggregation Kinetics of Functionalized Engineered Nanoparticles. *Environmental Science & Technology*, *47*(9), 4113-4120
- Lu, D., Cheng, W., Zhang, T., Lu, X., Liu, Q., Jiang, J., & Ma, J. (2016). Hydrophilic Fe<sub>2</sub>O<sub>3</sub> dynamic membrane mitigating fouling of support ceramic membrane in ultrafiltration of oil/water emulsion. *Separation and Purification Technology*, *165*, 1-9
- Lu, D., Zhang, T., Gutierrez, L., Ma, J., & Croué, J.-P. (2016). Influence of Surface Properties of Filtration-Layer Metal Oxide on Ceramic Membrane Fouling during Ultrafiltration of Oil/Water Emulsion. *Environmental Science & Technology*, *50*(9), 4668-4674
- Luo, S., Wei, Z., Dionysiou, D. D., Spinney, R., Hu, W.-P., Chai, L., Xiao, R. (2017). Mechanistic insight into reactivity of sulfate radical with aromatic contaminants through single-electron transfer pathway. *Chemical Engineering Journal*, *327*, 1056-1065
- Lutze, H. V., Bircher, S., Rapp, I., Kerlin, N., Bakkour, R., Geisler, M., Schmidt, T. C. (2015). Degradation of Chlorotriazine Pesticides by Sulfate Radicals and the Influence of Organic Matter. *Environmental Science & Technology*, *49*(3), 1673-1680

- Lutze, H. V., Kerlin, N., & Schmidt, T. C. (2015). Sulfate radical-based water treatment in presence of chloride: Formation of chlorate, inter-conversion of sulfate radicals into hydroxyl radicals and influence of bicarbonate. *Water Research*, 72, 349-360
- Lv, J., Li, D., Luo, L., Wu, T., & Zhang, S. (2017). Molecular transformation of natural and anthropogenic dissolved organic matter under photo-irradiation in the presence of nano TiO<sub>2</sub>. *Water Research*, 125, 201-208
- Lv, J., Zhang, S., Wang, S., Luo, L., Cao, D., & Christie, P. (2016). Molecular-Scale Investigation with ESI-FT-ICR-MS on Fractionation of Dissolved Organic Matter Induced by Adsorption on Iron Oxyhydroxides. *Environmental Science & Technology*, 50(5), 2328-2336
- Ma, J., Sui, M., Zhang, T., & Guan, C. (2005). Effect of pH on MnOx/GAC catalyzed ozonation for degradation of nitrobenzene. *Water Research*, 39(5), 779-786
- Madhavan, V., Levanon, H., & Neta, P. (1978). Decarboxylation by SO<sub>4</sub><sup>•-</sup> Radicals. *Radiation Research*, 76(1), 15-22
- McBride, M. B. (1989). Oxidation of dihydroxybenzenes in aerated aqueous suspensions of birnessite. *Clays Clay Miner*, 37(4), 341-347
- Mebrahtu, G., & Zerabruk, S. (2011). Concentration and health implication of heavy metals in drinking water from urban areas of Tigray region, Northern Ethiopia. *Momona Ethiopian Journal of Science*, 3(1), 105-121
- Miklos, D. B., Hartl, R., Michel, P., Linden, K. G., Drewes, J. E., & Hübner, U. (2018). UV/H<sub>2</sub>O<sub>2</sub> process stability and pilot-scale validation for trace organic chemical removal from wastewater treatment plant effluents. *Water Research*, 136, 169-179
- Milne, C. J., Kinniburgh, D. G., Van Riemsdijk, W. H., & Tipping, E. (2003). Generic NICA–Donnan model parameters for metal-ion binding by humic substances. *Environmental Science & Technology*, 37(5), 958-971
- Murphy, E. M., Zachara, J. M., Smith, S. C., Phillips, J. L., & Wietsma, T. W. (1994). Interaction of Hydrophobic Organic Compounds with Mineral-Bound Humic Substances. *Environmental Science & Technology*, 28(7), 1291-1299
- Neta, P., & Fessenden, R. W. (1974). Hydroxyl radical reactions with phenols and anilines as studied by electron spin resonance. *The Journal of Physical Chemistry*, 78(5), 523-529
- Neta, P., Huie, R. E., & Ross, A. B. (1988). Rate constants for reactions of inorganic radicals in aqueous solution. *Journal of Physical and Chemical Reference Data*, 17(3), 1027-1284

- Neta, P., Madhavan, V., Zemel, H., & Fessenden, R. W. (1977). Rate constants and mechanism of reaction of sulfate radical anion with aromatic compounds. *Journal of the American Chemical Society*, *99*(1), 163-164
- Nihemaiti, M., Miklos, D. B., Hübner, U., Linden, K. G., Drewes, J. E., & Croué, J.-P. (2018). Removal of trace organic chemicals in wastewater effluent by UV/H<sub>2</sub>O<sub>2</sub> and UV/PDS. *Water Research*, *145*, 487-497
- Niu, X.-Z., Harir, M., Schmitt-Kopplin, P., & Croué, J.-P. (2018). Characterisation of dissolved organic matter using Fourier-transform ion cyclotron resonance mass spectrometry: Type-specific unique signatures and implications for reactivity. *Science of The Total Environment*, *644*, 68-76
- Ohno, T., & Ohno, P. E. (2013). Influence of heteroatom pre-selection on the molecular formula assignment of soil organic matter components determined by ultrahigh resolution mass spectrometry. *Analytical and Bioanalytical Chemistry*, *405*(10), 3299-3306
- Organization, W. H. (2004). Manganese in drinking-water: Background document for development of WHO Guidelines for Drinking-water Quality: World Health Organization.
- Park, J.-S., Choi, H., & Cho, J. (2004). Kinetic decomposition of ozone and para-chlorobenzoic acid (pCBA) during catalytic ozonation. *Water Research*, *38*(9), 2285-2292
- Pettibone, J. M., Cwiertny, D. M., Scherer, M., & Grassian, V. H. (2008). Adsorption of Organic Acids on TiO<sub>2</sub> Nanoparticles: Effects of pH, Nanoparticle Size, and Nanoparticle Aggregation. *Langmuir*, *24*(13), 6659-6667
- Pi, Y., Schumacher, J., & Jekel, M. (2005). The Use of para-Chlorobenzoic Acid (pCBA) as an Ozone/Hydroxyl Radical Probe Compound. *Ozone: Science & Engineering*, *27*(6), 431-436
- Post, J. E. (1999). Manganese oxide minerals: Crystal structures and economic and environmental significance. *Proceedings of the National Academy of Sciences*, *96*(7), 3447-3454
- Ramseier, M. K., & Gunten, U. v. (2009). Mechanisms of phenol ozonation—kinetics of formation of primary and secondary reaction products. *Ozone: Science & Engineering*, *31*(3), 201-215

- Rosario-Ortiz, F. L., Wert, E. C., & Snyder, S. A. (2010). Evaluation of UV/H<sub>2</sub>O<sub>2</sub> treatment for the oxidation of pharmaceuticals in wastewater. *Water Research*, 44(5), 1440-1448
- Saleh, N. B., Pfefferle, L. D., & Elimelech, M. (2010). Influence of Biomacromolecules and Humic Acid on the Aggregation Kinetics of Single-Walled Carbon Nanotubes. *Environmental Science & Technology*, 44(7), 2412-2418
- Saputra, E., Muhammad, S., Sun, H., Ang, H. M., Tadé, M. O., & Wang, S. (2013). Different Crystallographic One-dimensional MnO<sub>2</sub> Nanomaterials and Their Superior Performance in Catalytic Phenol Degradation. *Environmental Science & Technology*, 47(11), 5882-5887
- Sarathy, S., & Mohseni, M. (2008). The fate of natural organic matter during UV/H<sub>2</sub>O<sub>2</sub> advanced oxidation of drinking water. *Canadian Journal of Civil Engineering*, 36(1), 160-169
- Sarathy, S. R. (2009). *Effects of UV/H<sub>2</sub>O<sub>2</sub> advanced oxidation on physical and chemical characteristics of natural organic matter in raw drinking water sources*. (Text). Retrieved from <https://open.library.ubc.ca/collections/24/items/1.0058674>
- Shen, M.-H., Yin, Y.-G., Booth, A., & Liu, J.-F. (2015). Effects of molecular weight-dependent physicochemical heterogeneity of natural organic matter on the aggregation of fullerene nanoparticles in mono- and di-valent electrolyte solutions. *Water Research*, 71, 11-20
- Shen, Y., Zhao, W., Xiao, K., & Huang, X. (2010). A systematic insight into fouling propensity of soluble microbial products in membrane bioreactors based on hydrophobic interaction and size exclusion. *Journal of Membrane Science*, 346(1), 187-193
- Siegrist, R. L., Crimi, M., & Simpkin, T. J. (2011). *In situ chemical oxidation for groundwater remediation* (Vol. 3): Springer Science & Business Media.
- Sleighter, R. L., & Hatcher, P. G. (2007). The application of electrospray ionization coupled to ultrahigh resolution mass spectrometry for the molecular characterization of natural organic matter. *Journal of Mass Spectrometry*, 42(5), 559-574
- Sun, S., Yao, H., Fu, W., Hua, L., Zhang, G., & Zhang, W. (2018). Reactive Photo-Fenton ceramic membranes: Synthesis, characterization and antifouling performance. *Water Research*, 144, 690-698

- Sun, Y., Cho, D.-W., Graham, N. J. D., Hou, D., Yip, A. C. K., Khan, E., Tsang, D. C. W. (2019). Degradation of antibiotics by modified vacuum-UV based processes: Mechanistic consequences of H<sub>2</sub>O<sub>2</sub> and K<sub>2</sub>S<sub>2</sub>O<sub>8</sub> in the presence of halide ions. *Science of The Total Environment*, 664, 312-321
- Sverjensky, D. A. (2006). Prediction of the speciation of alkaline earths adsorbed on mineral surfaces in salt solutions. *Geochimica et Cosmochimica Acta*, 70(10), 2427-2453
- Szekeres, M., & Tombácz, E. (2012). Surface charge characterization of metal oxides by potentiometric acid–base titration, revisited theory and experiment. *Colloids and Surfaces A: Physicochemical and Engineering Aspects*, 414(Supplement C), 302-313
- Tao, X., Wang, J., Ying, Z., Cai, Q., Zheng, G., Gan, Y., Cui, Y. (2014). Strong Sulfur Binding with Conducting Magnéli-Phase TinO<sub>2n-1</sub> Nanomaterials for Improving Lithium–Sulfur Batteries. *Nano Letters*, 14(9), 5288-5294
- Tian, J., Wu, C., Yu, H., Gao, S., Li, G., Cui, F., & Qu, F. (2018). Applying ultraviolet/persulfate (UV/PS) pre-oxidation for controlling ultrafiltration membrane fouling by natural organic matter (NOM) in surface water. *Water Research*, 132, 190-199
- Todorova, S., Naydenov, A., Kolev, H., Holgado, J. P., Ivanov, G., Kadinov, G., & Caballero, A. (2012). Mechanism of complete n-hexane oxidation on silica supported cobalt and manganese catalysts. *Applied Catalysis A: General*, 413-414, 43-51
- Tong, S.-p., Liu, W.-p., Leng, W.-h., & Zhang, Q.-q. (2003). Characteristics of MnO<sub>2</sub> catalytic ozonation of sulfosalicylic acid and propionic acid in water. *Chemosphere*, 50(10), 1359-1364
- Tziotis, D., Hertkorn, N., & Schmitt-Kopplin, P. (2011). Kendrick-analogous network visualisation of ion cyclotron resonance Fourier transform mass spectra: improved options for the assignment of elemental compositions and the classification of organic molecular complexity. *European Journal of Mass Spectrometry*, 17(4), 415-421
- Varanasi, L., Coscarelli, E., Khaksari, M., Mazzoleni, L. R., & Minakata, D. (2018). Transformations of dissolved organic matter induced by UV photolysis, Hydroxyl radicals, chlorine radicals, and sulfate radicals in aqueous-phase UV-Based advanced oxidation processes. *Water Research*, 135, 22-30

- Vindedahl, A. M., Strehlau, J. H., Arnold, W. A., & Penn, R. L. (2016). Organic matter and iron oxide nanoparticles: aggregation, interactions, and reactivity. *Environmental Science: Nano*, 3(3), 494-505
- Violleau, D. (1999). *Intérêt du fractionnement et de l'extraction des matières organiques naturelles d'eaux de surface pour l'étude de leurs propriétés structurales et de leur pouvoir complexant vis-à-vis du cuivre*. Available from <http://www.theses.fr/1999POIT2360>
- Wacławek, S., Lutze, H. V., Grübel, K., Padil, V. V. T., Černík, M., & Dionysiou, D. D. (2017). Chemistry of persulfates in water and wastewater treatment: A review. *Chemical Engineering Journal*, 330, 44-62
- Wang, K., Shi, Z., Wang, Y., Ye, Z., Xia, H., Liu, G., & Qiao, G. (2015). Co<sub>3</sub>O<sub>4</sub> nanowires@MnO<sub>2</sub> nanolayer or nanoflakes core-shell arrays for high-performance supercapacitors: The influence of morphology on performance. *Journal of Alloys and Compounds*, 624, 85-93
- Wang, W.-L., Zhang, X., Wu, Q.-Y., Du, Y., & Hu, H.-Y. (2017). Degradation of natural organic matter by UV/chlorine oxidation: Molecular decomposition, formation of oxidation byproducts and cytotoxicity. *Water Research*, 124, 251-258
- Wang, Y., Le Roux, J., Zhang, T., & Croué, J.-P. (2014). Formation of Brominated Disinfection Byproducts from Natural Organic Matter Isolates and Model Compounds in a Sulfate Radical-Based Oxidation Process. *Environmental Science & Technology*, 48(24), 14534-14542
- Wenk, J., Aeschbacher, M., Salhi, E., Canonica, S., von Gunten, U., & Sander, M. (2013). Chemical Oxidation of Dissolved Organic Matter by Chlorine Dioxide, Chlorine, And Ozone: Effects on Its Optical and Antioxidant Properties. *Environmental Science & Technology*, 47(19), 11147-11156
- Wershaw, R. L., Leenheer, J. A., & Cox, L. G. (2005). Characterization of dissolved and particulate natural organic matter (NOM) in Neversink Reservoir, New York.
- Westerhoff, P., Chao, P., & Mash, H. (2004). Reactivity of natural organic matter with aqueous chlorine and bromine. *Water Research*, 38(6), 1502-1513
- Westerhoff, P., Mezyk, S. P., Cooper, W. J., & Minakata, D. (2007). Electron Pulse Radiolysis Determination of Hydroxyl Radical Rate Constants with Suwannee River Fulvic Acid and Other Dissolved Organic Matter Isolates. *Environmental Science & Technology*, 41(13), 4640-4646

- Whitney, P. R. (1975). Relationship of manganese-iron oxides and associated heavy metals to grain size in stream sediments. *Journal of Geochemical Exploration*, 4(2), 251-263
- Winter, J., Uhl, W., & Bérubé, P. R. (2016). Integrated oxidation membrane filtration process – NOM rejection and membrane fouling. *Water Research*, 104, 418-424
- Wolf, P. H., Siverns, S., & Monti, S. (2005). UF membranes for RO desalination pretreatment. *Desalination*, 182(1), 293-300
- Wu, H., Xu, X., Shi, L., Yin, Y., Zhang, L.-C., Wu, Z., Sun, H. (2019). Manganese oxide integrated catalytic ceramic membrane for degradation of organic pollutants using sulfate radicals. *Water Research*, 167, 115110
- Xiao, R., Ye, T., Wei, Z., Luo, S., Yang, Z., & Spinney, R. (2015). Quantitative Structure–Activity Relationship (QSAR) for the Oxidation of Trace Organic Contaminants by Sulfate Radical. *Environmental Science & Technology*, 49(22), 13394-13402
- Xie, P., Ma, J., Liu, W., Zou, J., & Yue, S. (2015). Impact of UV/persulfate pretreatment on the formation of disinfection byproducts during subsequent chlorination of natural organic matter. *Chemical Engineering Journal*, 269, 203-211
- Xie, P., Ma, J., Liu, W., Zou, J., Yue, S., Li, X., Fang, J. (2015). Removal of 2-MIB and geosmin using UV/persulfate: Contributions of hydroxyl and sulfate radicals. *Water Research*, 69, 223-233
- Xu, L. C., & Logan, B. E. (2005). Interaction forces between colloids and protein-coated surfaces measured using an atomic force microscope. *Environmental Science and Technology*, 39(10), 3592-3600
- Yang, W., Zhou, H., & Cicek, N. (2014). Treatment of Organic Micropollutants in Water and Wastewater by UV-Based Processes: A Literature Review. *Critical Reviews in Environmental Science and Technology*, 44(13), 1443-1476
- Yang, Y., Cao, Y., Jiang, J., Lu, X., Ma, J., Pang, S., Guan, C. (2019). Comparative study on degradation of propranolol and formation of oxidation products by UV/H<sub>2</sub>O<sub>2</sub> and UV/persulfate (PDS). *Water Research*, 149, 543-552
- Yang, Y., Lu, X., Jiang, J., Ma, J., Liu, G., Cao, Y., Luo, C. (2017). Degradation of sulfamethoxazole by UV, UV/H<sub>2</sub>O<sub>2</sub> and UV/persulfate (PDS): Formation of oxidation products and effect of bicarbonate. *Water Research*, 118, 196-207

- Yang, Y., Ma, J., Qin, Q., & Zhai, X. (2007). Degradation of nitrobenzene by nano-TiO<sub>2</sub> catalyzed ozonation. *Journal of Molecular Catalysis A: Chemical*, 267(1), 41-48
- Ye, T., Wei, Z., Spinney, R., Tang, C.-J., Luo, S., Xiao, R., & Dionysiou, D. D. (2017). Chemical structure-based predictive model for the oxidation of trace organic contaminants by sulfate radical. *Water Research*, 116, 106-115
- Yoon, Y., Westerhoff, P., Snyder, S. A., & Wert, E. C. (2006). Nanofiltration and ultrafiltration of endocrine disrupting compounds, pharmaceuticals and personal care products. *Journal of Membrane Science*, 270(1), 88-100
- Yu, C., Li, G., Wei, L., Fan, Q., Shu, Q., & Yu, J. C. (2014). Fabrication, characterization of  $\beta$ -MnO<sub>2</sub> microrod catalysts and their performance in rapid degradation of dyes of high concentration. *Catalysis Today*, 224, 154-162
- Yuan, Z., He, C., Shi, Q., Xu, C., Li, Z., Wang, C., Ni, J. (2017). Molecular Insights into the Transformation of Dissolved Organic Matter in Landfill Leachate Concentrate during Biodegradation and Coagulation Processes Using ESI FT-ICR MS. *Environmental Science & Technology*, 51(14), 8110-8118
- Zafiriou, O. C., Jousset-Dubien, J., Zepp, R. G., & Zika, R. G. (1984). Photochemistry of natural waters. *Environmental Science & Technology*, 18(12), 358A-371A
- Zaouri, N., Gutierrez, L., Dramas, L., Garces, D., & Croue, J.-P. (2017). Interfacial interactions between *Skeletonema costatum* extracellular organic matter and metal oxides: Implications for ceramic membrane filtration. *Water Research*, 116, 194-202
- Zhang, H., & Huang, C.-H. (2003). Oxidative Transformation of Triclosan and Chlorophene by Manganese Oxides. *Environmental Science & Technology*, 37(11), 2421-2430
- Zhang, H., Zhang, Y., Shi, Q., Hu, J., Chu, M., Yu, J., & Yang, M. (2012). Study on Transformation of Natural Organic Matter in Source Water during Chlorination and Its Chlorinated Products using Ultrahigh Resolution Mass Spectrometry. *Environmental Science & Technology*, 46(8), 4396-4402
- Zhang, H., Zhang, Y., Shi, Q., Ren, S., Yu, J., Ji, F., Yang, M. (2012). Characterization of low molecular weight dissolved natural organic matter along the treatment trait of a waterworks using Fourier transform ion cyclotron resonance mass spectrometry. *Water Research*, 46(16), 5197-5204

- Zhang, S., Gutierrez, L., Niu, X.-Z., Qi, F., & Croue, J.-P. (2018). The characteristics of organic matter influence its interfacial interactions with MnO<sub>2</sub> and catalytic oxidation processes. *Chemosphere*, 209, 950-959
- Zhang, S., Rouge, V., Gutierrez, L., & Croue, J.-P. (2019). Reactivity of chromophoric dissolved organic matter (CDOM) to sulfate radicals: Reaction kinetics and structural transformation. *Water Research*, 163, 114846
- Zhang, T., Chen, Y., & Leiknes, T. (2016). Oxidation of refractory benzothiazoles with PMS/CuFe<sub>2</sub>O<sub>4</sub>: kinetics and transformation intermediates. *Environmental Science & Technology*, 50(11), 5864-5873
- Zhang, T., & Sun, D. D. (2013). Removal of arsenic from water using multifunctional micro-/nano-structured MnO<sub>2</sub> spheres and microfiltration. *Chemical Engineering Journal*, 225, 271-279
- Zhang, Z., & Edwards, J. O. (1992). Chain lengths in the decomposition of peroxomonosulfate catalyzed by cobalt and vanadium. Rate law for catalysis by vanadium. *Inorganic Chemistry*, 31(17), 3514-3517
- Zhao, Q., Lu, D., Jiang, H., Zhao, Y., Sun, Y., Li, Z., Ma, J. (2019). Peroxymonosulfate-based cleaning technology for metal oxide-coated ceramic ultrafiltration membrane polluted by Alcian Blue 8GX dye: Radical and non-radical oxidation cleaning mechanism. *Journal of Membrane Science*, 573, 210-217
- Zheng, X., Khan, M. T., & Croué, J.-P. (2014). Contribution of effluent organic matter (EfOM) to ultrafiltration (UF) membrane fouling: Isolation, characterization, and fouling effect of EfOM fractions. *Water Research*, 65, 414-424
- Zhou, L., Sleiman, M., Ferronato, C., Chovelon, J.-M., & Richard, C. (2017). Reactivity of sulfate radicals with natural organic matters. *Environmental Chemistry Letters*, 15(4), 733-737
- Zhou, Y., Jiang, J., Gao, Y., Ma, J., Pang, S.-Y., Li, J., Yuan, L.-P. (2015). Activation of Peroxymonosulfate by Benzoquinone: A Novel Nonradical Oxidation Process. *Environmental Science & Technology*, 49(21), 12941-12950

*Every reasonable effort has been made to acknowledge the owners of copyright material. I would be pleased to hear from any copyright owner who has been omitted or incorrectly acknowledged.*